BLACK START RESTORATION FOR ELECTRIC DISTRIBUTION SYSTEMS AND MICROGRIDS

A Dissertation

by

BO CHEN

Submitted to the Office of Graduate and Professional Studies of
Texas A&M University
in partial fulfillment of the requirements for the degree of

DOCTOR OF PHILOSOPHY

Chair of Committee,	Karen L. Butler-Purry
Committee Members,	Le Xie
	I-Hong Hou
	Sergiy Butenko
Head of Department,	Miroslav M. Begovic

May 2017

Major Subject: Electrical Engineering

ABSTRACT

Modern power systems face increased risk of wide area blackouts caused by extreme weather events, man-made errors, cyber-attacks, and other threats. In order to promptly restore power after a blackout, an efficient black start restoration methodology should be developed. Emerging smart grid technologies such as remote control switches (RCSs) and distributed energy resources (DERs) present significant potential that can be leveraged for developing advanced black start restoration methodologies.

In this dissertation research, a new black start restoration (BSR) method, which could be used in distribution management system (DMS) or microgrid control center (MGCC), was presented. The BSR problem was formulated as a dynamic optimization problem in order to coordinate the dispatching actions of DERs and the switching actions of RCSs over multiple decision time steps. Several linearization techniques were presented to re-formulate the dynamic optimization model as a mixed-integer linear programming (MILP) model. The rolling-horizon functionality was used to reduce the computation time. The MILP mode was simulated in MATLAB® using YALMIP Toolbox and solved in the IBM CPLEX™ solver.

Several case studies were conducted to illustrate how the new BSR method works on the modified IEEE 13 node and 123 node systems installed with dispatchable distributed generations (DGs), renewable DGs, energy storage systems (ESSs), and RCSs. OpenDSS was used to simulate power flow, and PSCAD™/EMTDC™ was used to simulate frequency response. The new BSR method was able to generate black start sequences in

response to varying operating conditions such as balanced and unbalanced conditions, cold load pick up (CLPU) conditions, and different fault scenarios.

The performance of the new BSR method was analyzed through extensive case studies. It was observed that using properly selected rolling-horizon parameters could reduce the computation time and achieve near-optimal solutions. However, some operating conditions resulted in infeasible solutions, such as limited DG ramp rate and capacity, heavy loading conditions, and excessive fluctuation of renewable DG outputs and load demands.

The new BSR method can be further improved by incorporating a method for determining the rolling-horizon parameters without conducting exhaustive case studies and developing an integrated structure to coordinate with DG primary controls.

DEDICATION

To my family

ACKNOWLEDGEMENTS

First and foremost, I would like to thank my advisor, Dr. Karen L. Butler-Purry, for her guidance, support, and patience throughout my Ph.D. study. The guidance and encouragement from Dr. Butler-Purry help me overcome many difficulties during my years of research. From each meeting with Dr. Butler-Purry, I can always learn new things to improve my professional skills and capability of conducting independent research.

I would like to thank my committee members, Dr. Le Xie, Dr. I-Hong Hou, and Dr. Sergiy Butenko, for their time in serving on my committee. Thanks also go to the department faculty and staff for making my time at Texas A&M University a great experience.

I also would like to thank all of my friends and colleagues at the Power System Automation Laboratory for their support and friendships. Thanks also go to my colleagues at Argonne National Laboratory for their valuable input and thoughtful discussions.

Finally, I would like to thank my wife, Ang Li, for her support, patience, and love. My special thanks go to my parents, for their endless support.

CONTRIBUTORS AND FUNDING SOURCES

Contributors

Part 1, faculty committee recognition

This work was supervised by a dissertation committee consisting of Professor Karen L. Butler-Purry, Professor Le Xie, and Professor I-Hong Hou of the Department of Electrical and Computer Engineering and Professor Sergiy Butenko of the Department of Industrial and Systems Engineering.

Part 2, student/collaborator contributions

All work for the dissertation was completed independently by the student.

Funding Sources

This work was supported in part by Norman Hackerman Advanced Research Program Project 000512-0111-2009 and NSF grants EECS-1028246 and EEC-1062603.

TABLE OF CONTENTS

Page

LIST OF FIGURES

Page

LIST OF TABLES

Page

1 INTRODUCTION

1.1 Introduction

Modern power systems are threatened by increased frequency and severity of extreme weather events, which can cause a catastrophic impact on energy infrastructures[1-3]. For instance, more than 6.5 million people lost power during Hurricane Irene and more than 8 million people were affected by Superstorm Sandy [3, 4]. Similarly, over 1 million people in the state of Florida lost access to electricity during Hurricane Matthew [5]. In 2016, as of September, a total of 12 extreme weather events have been reported to cause losses exceeding $1 billion across the United States [6]. The inflation–adjusted cost of weather–related outages is between $25 billion and $70 billion annually [3]. Unfortunately, the frequency and severity of weather-related events continue to increase due to the changing global climate, which makes power systems prone to experience more weather-related outages [1]. Even though the modern power systems are designed to meet the "N–1" or "N–2" criteria to achieve a certain level of robustness, an excessive number of contingencies induced by extreme weather events will likely bring down part or the entire power system. For example, Hurricane Sandy was an "N–90" event [7]. In addition, rapidly growing demand and economical operation of power systems under a deregulated environment will force power systems to operate with limited stability margins, hence increasing the risk of system collapse and cascading failures [8]. Furthermore, recent research has shown that coordinated cyber-physical attacks and terrorism attacks are becoming potential threats that can cause large-area power blackouts [9, 10]. Natural

disasters and coordinated cyber–physical attacks can also deteriorate the functionality of communication networks, which are critical to performing supervising and controlling during the restoration process [11].

Distribution networks contribute over 90% customer outage–minutes in the United States [12]. Power outages in distribution systems can be caused by unscheduled events (e.g., fallen trees, lightning, storms, equipment failure) and scheduled events (e.g., regular maintenance, equipment installation) [13]. The modern electricity-driven lifestyle is vulnerable to power disruptions. When a power outage occurs, customers will lose electricity access and experience an extended impact on social, political and economic activities [14]. Conventional distribution systems are solely energized by substations. When a general blackout occurs, distribution systems will be fully de-energized, and they must be restored by energizating the substations first. For a blackout caused by extreme weather events, it will take several hours or even days to fully restore the system.

Emerging technologies such as distribution energy sources (DERs) and remote controllable switches (RCSs) demonstrate great potential that can be leveraged for developing advanced black start restoration (BSR) methodologies for distribution systems and microgrids [15, 16]. Specifically, some distributed generations (DGs) and energy storage systems (ESSs) can be started to energize critical loads during a power blackout. RCSs can be strategically opened or closed to interconnect these power sources with customer loads. The temporarily developed system can be operated as a dynamic microgrid [17]. For a large-scale system with many DERs, multiple microgrids can be

formed [17-19]. The customer loads within a microgrid can be continuously supported by properly operating the DERs within the same microgrid.

Most of the existing service restoration methods for distribution systems and microgrids only take into consideration a single local power outage and assume substations are intact. However, a general blackout can cause multiple outages at different locations including substations. The research on black start for distribution systems and microgrids is limited. The main shortcoming of many of the existing BSR methods is that they only generate restoration solutions that represent a single operating point [20-26]. However, the restoration sequence, which is critical to successfully implementing the restoration process, is needed. The presence of multiple DERs and time-varying load demand further necessitates the capability of a BSR method to generate feasible restoration sequences.

In this dissertation research, a new integrated BSR method for distribution systems and microgrids was presented. The new BSR method was formulated as a dynamic optimization problem, which could coordinate the dispatching actions of DERs and the switching actions of RCSs over multiple discrete time steps. The new BSR method can be implemented on a notional computer in distribution management system (DMS) or microgrid control center (MGCC). The new method was able to generate restoration sequences in response to varying operating conditions through a series of case studies. The system can be energized by implementing the restoration sequence step by step, while satisfying various operational constraints during the restoration process.

The major contributions in this dissertation research are in the following four areas.

Firstly, the BSR problem was formulated as a dynamic optimization problem, which can determine the dispatching actions of DERs and the switching actions of RCSs over multiple discrete time steps. Unlike many of the existing BSR methods that can only generate single-step solutions, the new BSR method can generate a sequence of control actions that optimally coordinate DERs and RCSs at each time step. The system operator can carry out the control actions specified in the restoration sequence to energize the system step by step, while ensuring the operational constraints are satisfied during the restoration process.

Secondly, multiple isolated microgrids could be developed by sequentially grouping DERs and loads. A set of topological rules were defined for RCSs and translated into the dynamic optimization problem formulation to ensure that each microgrid is operated in the tree topology, and multiple DERs can be dispatched to balance time-varying load demand within each isolated microgrid.

Thirdly, the nonlinear dynamic optimization model was linearized as a mixed-integer linear programming (MILP) model, which can be effectively solved by commercial software such as CPLEX and GUROBI. In addition, several linear models were proposed to address the practical concerns associated with black start and unbalanced operating conditions, such as cold load pick up (CLPU) issues and DG current unbalance limits. A rolling-horizon approach was implemented to reduce the computation time.

Fourthly, a comprehensive study was conducted to examine how the new BSR method works. In this dissertation research, the new BSR method was applied on balanced and unbalanced three-phase systems with dispatchable distributed generations (DGs), energy

storage systems (ESSs), renewable DGs, and RCSs. The new BSR method was able to generate restoration sequences in response to varying operating conditions. The performance of the new BSR method using different rolling-horizon parameters under different operating conditions was analyzed through a set of extensive case studies. The results indicated that the new BSR method could provide near-optimal solutions when the rolling-horizon parameters were properly selected.

1.2 Organization

This dissertation is organized into five sections. Section 2 introduces the existing BSR methods in the literature. Section 3 introduces the BSR problem and the BSR solution methodology. In section 4, the results of case studies and performance analysis are presented and discussed. The conclusions and future work are presented in section 5.

2 LITERATURE REVIEW

2.1 Introduction

The service restoration for power systems has been studied since more than 100 years ago [27]. Enormous efforts and resources have been devoted and invested in power systems to improve the efficiency and resiliency, making power system the most complex network ever built by mankind. Power systems are designed to meet the "N-1" or "N-2" criteria to achieve a certain level of robustness, meaning the system can survive from losing any one or two of its N components and keep operating within the stability margin [28]. However, as modern power systems are interconnected into a huge network that geographically stretches over thousands of miles, any extreme weather events or coordinated cyber-physical attacks can easily compromise multiple components simultaneously and result in large-scale power outages. Therefore, it is critical to develop a restoration methodology to improve the resilience of power systems.

Growing needs for improving power reliability and reducing dependence on fossil fuels have caused increasingly DERs installed in both transmission and distribution systems [29]. Declining prices and tax incentives also encourage people to use renewable energy resources in homes, buildings, public facilities and so on [30]. Also, given the fact that the microgrid market is growing fast in popularity, it is desired to fully leverage the value of DERs and microgrids. The integration of DERs and microgrids into distribution systems and microgrids provides a great opportunity for developing efficient restoration methodologies [30-32].

In this section, first of all, the concept of resilience is introduced, and the outage management procedures are presented. Next, conventional restoration methods in the literature are reviewed. The CLPU issues are introduced, and the existing methods for addressing CLPU issues are discussed. Then, several emerging smart grid technologies are introduced. Different types of DERs and microgrids are introduced and categorized based on their roles in performing black start restoration. Next, the existing restoration methods using DERs are reviewed. Finally, the problems with the existing methods are summarized, and the motivation for developing a new black start restoration methodology is introduced.

2.2 Resilience of Distribution Systems

C.S. Holling firstly defined resilience for ecological systems in 1973 as "a measure of the persistence of systems and of their ability to absorb change and disturbance and still maintain the same relationships between populations or state variables" [33]. This fundamental definition has been adapted for various systems. However, the resilience of power systems still lacks a commonly-accepted definition. Electric Power Research Institute (EPRI) identified three elements of the resilience for distribution systems (shown in Figure 2.1): prevention, recovery, and survivability [34]. Prevention refers to all means of tools and techniques for hardening the distribution systems to prevent or limit the damage caused by unexpected catastrophic events; for example, replacing aging poles and transformers, replacing overhead lines with underground lines, installing sectionalizing switches. Recovery refers to the use of tools and techniques for restoring the electricity service to affected customers as soon as possible. Many factors are involved in performing

recovery. For example, before a storm hits a power system, damage prediction and response should be performed in order to dispatch crews and resources to the field in advance. Then post-event damage assessment and service restoration will be initiated to restore the electricity service to affected customers using various tools and technologies. Survivability refers to the use of technologies to facilitate customers, communities, and facilities to perform partial function without accessing the grid power. For example, during a severe weather event, some critical loads (e.g., hospitals, traffic lights, prisons) can be continuously supplied by backup generators or batteries.

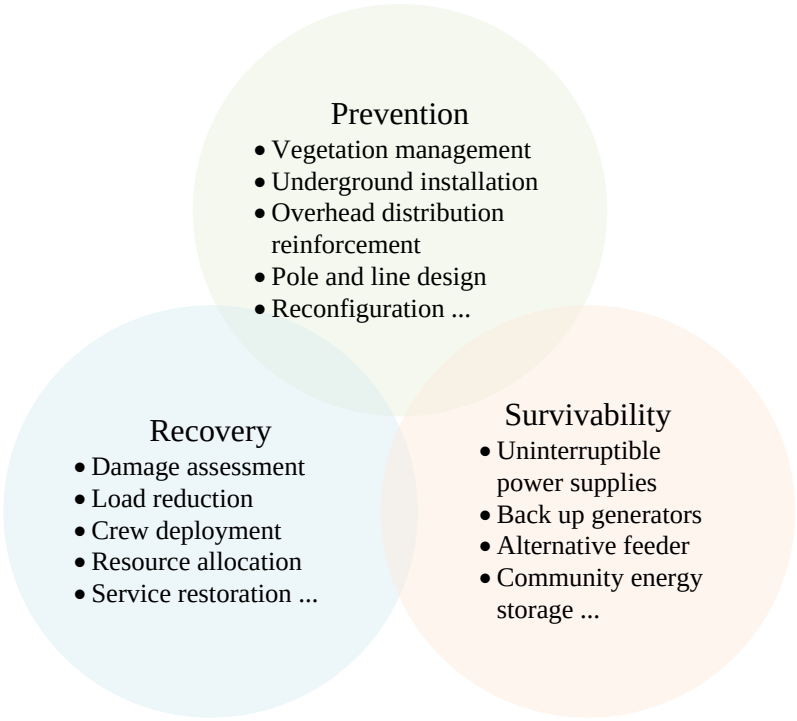

Figure 2.1. Three elements of resilience identified by EPRI for distribution systems [34]

All the three aforementioned factors should be taken into consideration in order to improve the overall resilience. It is worth noticing that some innovative tools and technologies can enhance two or three resilience factors once being deployed. For instance, installing sectionalizing switches can be beneficial for hardening the power lines, and it also enables the fast service restoration through reconfiguration during the post-event stage [35, 36]. Another example is the deployment of DERs and microgrids, which can be used for providing power to critical loads and help customers ride through the outage [1, 19, 20, 32]. However, in some cases, enhancing one resilience factor may cause a negative impact on other resilience factors. For example, replacing overhead lines with underground lines can significantly enhance the system robustness to certain disasters such as hurricanes and storms. However, once the underground lines are damaged for some reasons (e.g., earthquake), it will take much longer time for replacement and repair, hence prolonging the recovery duration [37].

Improving the power system resiliency against extreme events requires devoting efforts throughout the entire restoration process. The system resilience level as a function of time can be described by a conceptual curve, as shown in Figure 2.2, which is adapted from [38]. The vertical axis represents the system resilience level, which is determined by certain quantification measures. The horizontal axis represents the time, which can be hours or days, depending on the scale and severity of the event. Assuming an extreme weather event is in process between t_0 and t_e, the system infrastructure should be robust enough to withstand the initial disturbances without losing any customers, since the system is designed to meet "N-1" or "N-2" criteria. The resilience level under pre-event

conditions is denoted by R_0. During this stage, damage prediction should be performed, crews and resources (e.g., tools, vehicles, equipment) should be properly allocated. As the extreme event progresses, many facilities (e.g., power towers, transmission lines, substations) may be damaged or tripped to cause multiple contingencies. The system can no longer maintain the original resilience level. Accordingly, the resilience level drops from R_0 to R_{po}, and achieves the post-event degraded state at time t_{pe}. From t_e to t_r, the damage assessment will be performed and the restoration strategies will be developed accordingly. Based on various data sources, the faulty areas caused by the extreme events will be identified and located. From t_r to t_{pr}, all means of restoration strategies will be performed to restore the system from the post-event degraded state. As the extreme events progresses, new contingencies may occur and interrupt the pre-planned restoration strategies from time to time. So, it is critical to update the restoration plan accordingly to adapt to changing situations. At time t_{pr}, the resilience level will increase from R_{pe} to R_{pr} and achieve the post-restoration state. Considering some components can be damaged severely, it may be not possible to replace or repair them within a short time. So, the resilience level during the post-restoration stage may be lower than the pre-event resilience level R_0. Most customers should be restored using various tools and technologies during this stage. As all the affected components and customers are restored from t_{ir} to t_{pir}, the system will be fully recovered, and the resilience level increases from R_{pr} to R_0.

It is worth noticing that each stage may take different amount of time, depending on the severity and the type of the event. In addition, transition between different stages also requires different amount of time. We can see that the restoration stage from t_r to t_{pr}

plays an essential role in restoring the system back to normal conditions. In the next subsection, the outage management system used for service restoration will be introduced.

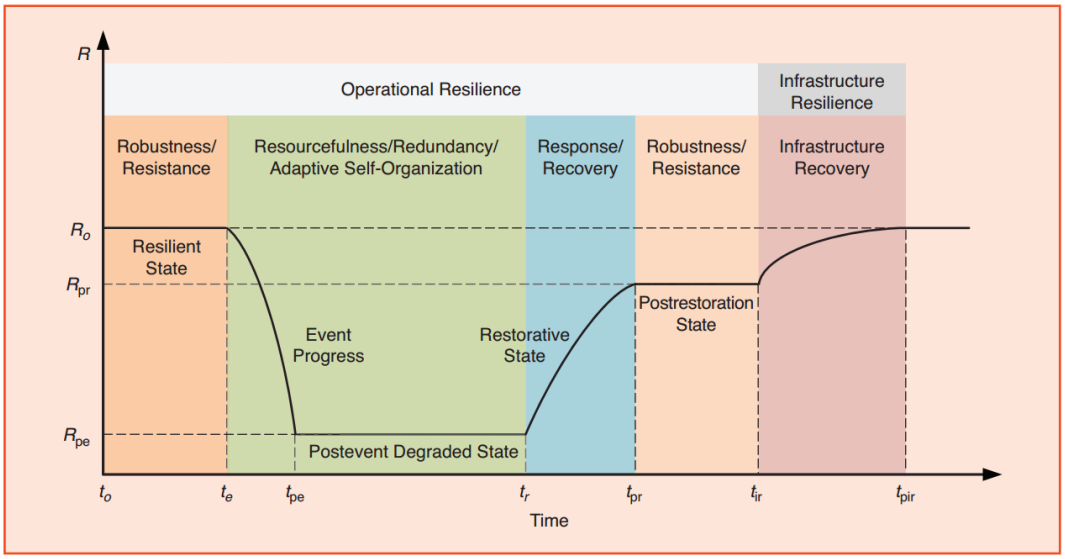

Figure 2.2. A conceptual resilience curve during and after an extreme event (Reprinted from [38])

2.3 Outage Management for Distribution Systems

Outage management system (OMS), as one of the core applications in the control center, is playing a mission-critical role for improving the power system resilience [39, 40]. Figure 2.3 demonstrates the typical functionalities of OMS for distribution systems [41, 42]. Once a power outage occurs, the OMS will receive information from the distribution supervisory control and data acquisition (SCADA) system, customer information system (CIS), interactive voice response (IVR), and smart meters through advanced metering infrastructure (AMI), reports from the crews, and other applications in distribution management system (DMS). Based on the collected information, OMS can

perform damage assessment and keep monitoring the system operating conditions. Given a damage assessment report, OMS can generate a set of restoration strategies, which can be performed by either RCSs deployed throughout the system or by dispatching the crews to the field. As the extreme event progresses, damage assessment and fault identification, isolated and restoration (FDIR) application are performed iteratively, until the system is fully recovered [43].

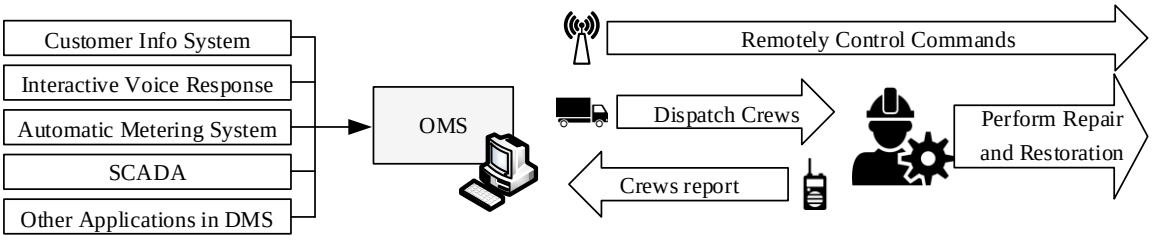

Figure 2.3. Outage management system for distribution systems

Conventional OMS can only handle normal day-to-day outages, which involve relatively small number of customers [44]. When the extreme events are expected to occur, much more efforts should be devoted to coping with multiple outages. Figure 2.4 shows a framework for large-scale outage management, which has two additional stages compared to conventional OMS: damage prediction and crew staging. Damage prediction and crew staging are essential for reducing the outage duration for major disaster events such as storms and hurricanes [45]. Based on the weather forecast and history information, an estimation is performed to find out any areas and components that are highly susceptible to the events. Then the required number of crews with particular skills and tools should be

estimated. In the crew staging stage, crews are dispatched to the estimated fault locations. The damage assessment and service restoration are performed immediately after the storms and hurricanes pass through.

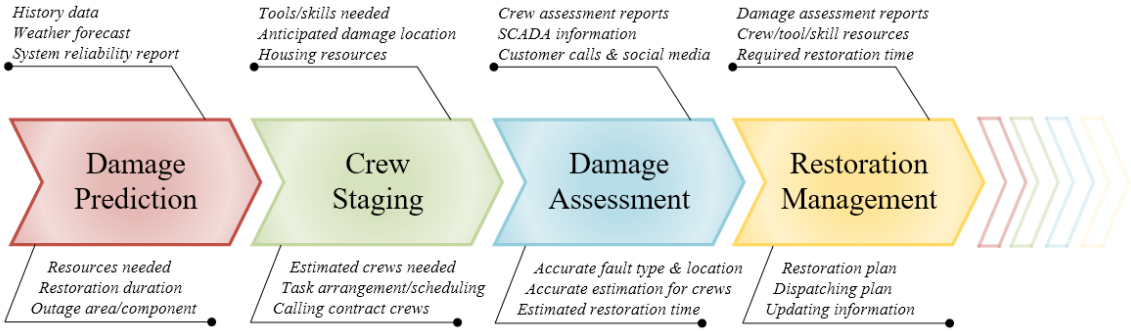

Figure 2.4. Framework for large-scale outage management [44]

The purpose of this dissertation is to develop an innovative black start restoration method, which can be integrated into the modern OMS and initiated right after the faulty areas are identified and isolated. The performance of the BSR methodology is critical for reducing the outage duration and in turn of great importance for improving power system resilience against local and large-scale power outages.

2.4 Conventional Service Restoration for Distribution Systems

Service restoration is a conventional topic that has been investigated by many researchers for the past few decades [46, 47]. Service restoration refers to the procedure of re-energizing a portion of the distribution system, which is isolated by protective devices after detecting a sustained fault. Note that black start is a special type of service

restoration. The system is usually assumed to be fully de-energized before performing black start.

2.4.1 Service Restoration Procedures

Conventional service restoration for distribution systems is performed through reconfiguration by remotely or manually changing the topology of the network, so as to transfer affected loads to other energized feeders while maintaining various operational constraints [47]. The outage duration will mainly depend on how long the event lasts and how fast the maintenance crew can pinpoint the fault and get to the location [48]. Figure 2.5 demonstrates the architecture of a simple active distribution system. General service restoration can be carried out by performing the following procedures [41, 42]:

Step 1) *Information Collection*. The outage management system (OMS) collects data from various types of entities such as the customer information system (CIS), interactive voice response (IVR), and advanced metering infrastructure (AMI), as well as the field measurements (e.g., protective relays, fault indicators, switchgear) through the supervisory control and data acquisition (SCADA) system.

Step 2) *Fault Location and Isolation.* After being hit by severe weather events, a power system can be subjected to multiple faults that occur at different components and locations. Based on the information collected from the protective relays and fault indicators, the fault locations can be pinpointed and isolated by opening the switches installed along the feeders. Then, the maintenance crews are dispatched to fix the failed components in the isolated faulty areas.

Step 3) *System Model Identification.* The resources that can potentially participate in the restoration are determined in this step by assessing the availability and controllability of various components such as DGs, lines, switches, and loads.

Step 4) *Service Restoration.* The restoration solutions are generated based on the updated system model. If a restoration solution cannot be successfully carried out for some reasons (e.g., loss of communication, or damaged by succeeding outages), system operators should return to Step (1) to collect up-to-date information, isolate the problematic components in Step (2), update the system model in Step (3), and generate a new solution in Step (4).

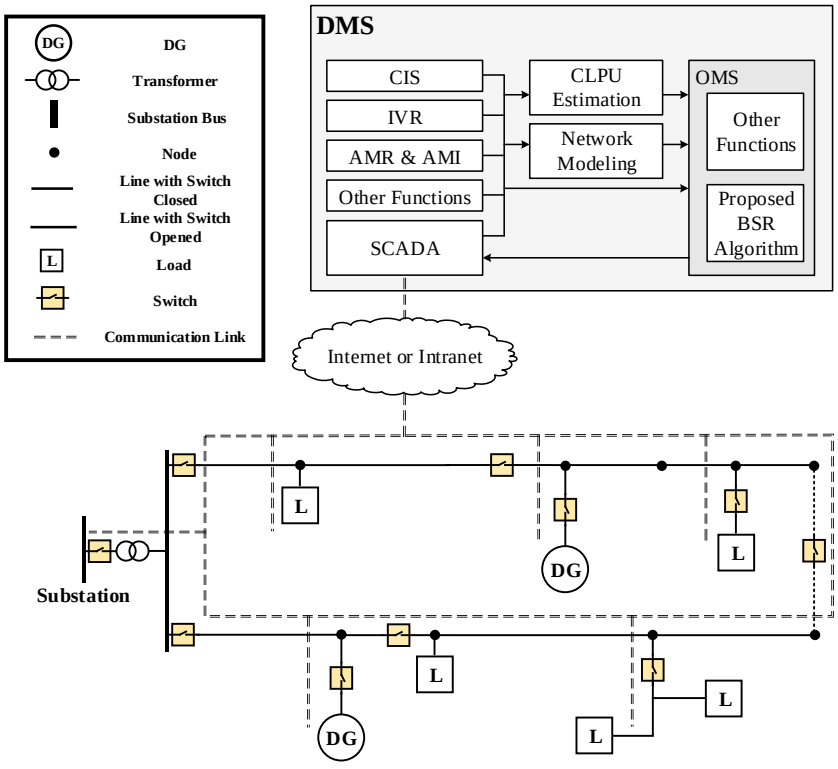

Figure 2.5. The architecture of an active distribution system [49]

Figure 2.6 shows an example of restoration procedures for a simple distribution system. In plot 1, the system is operated under normal condition with six aggregated loads energized by two different feeders (red feeder and green feeder). Note that distribution systems are normally operated in radial structure for protection purposes, as well as the operational and economic benefits [50]. Therefore, the normally-open tie switch between the red feeder and the green feeder is opened. Each load is solely energized by its upstreaming substation. In plot 2, when a fault occurs on the green feeder, the protective relay will be triggered to isolate the faulty area and cause all the connected loads on the green feeder to be de-energized. Note the green feeder is sectionalized by a sectionalizing switch in the middle. The affected customers that are downstream of the sectionalizing switch can be seen as healthy loads that should be restored as soon as possible. In plot 3, the sectionalizing switch is opened to isolate the faulty area. Then, the tie switch is closed to transfer the downstream loads to the red feeder. By doing so, the healthy costumer loads are restored quickly without waiting for the faulty area to be fixed. Meanwhile, OMS will perform damage assessment and dispatch crews to repair the faulty components. When the fault is cleared, the affected customers are transferred back to the green feeder, as shown in plot 4.

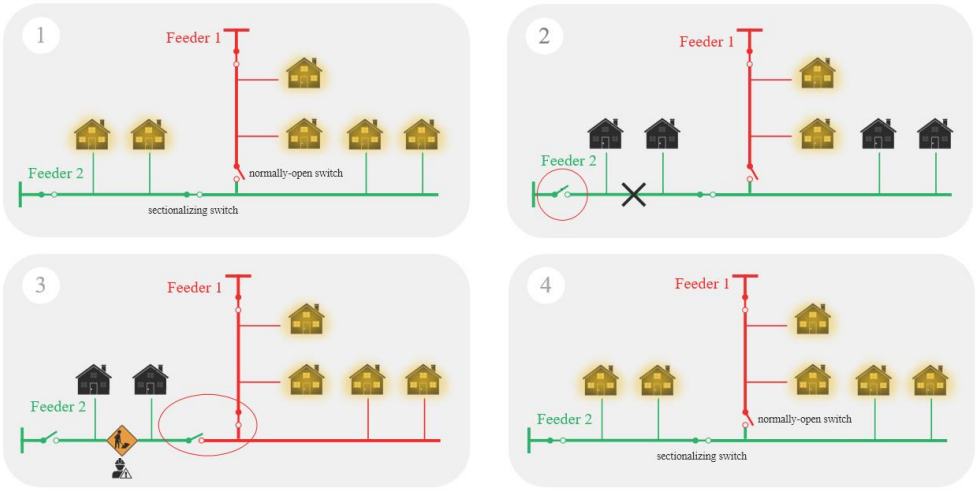

Figure 2.6. A simple case of service restoration using reconfiguration

2.4.2 Cold Load Pick Up Issues During Service Restoration

Cold load pick up (CLPU) issues have been identified as a critical concern that must be considered when restoring a distribution system after an extended outage [51, 52]. CLPU refers to the phenomenon that when restoring a load after an extended outage, a much higher demand than the pre-outage level will be resulted, because thermostatically controlled loads (e.g., air conditioners, heaters, and refrigerators) will start at the same time [52]. When a large number of thermostatically controlled loads are operated under normal conditions, their working cycles are diversified from each other. The aggregated loading level will be much lower than the total rated capacity. However, after an extended outage, the working cycles of these devices are reset and started at the same time when the power is restored. As a result, a much higher demand will present than normal conditions. Figure 2.7 shows the field measurement of the cold load pick-up for 625 houses, of which 525 have electric heating devices [53]. The field study was performed

during the night, and the outside temperature was +5 ℃ (1.0 p.u. is the base power consumption before the interruption). It can be seen that even for a short outage duration (e.g., 5 minutes), the pickup power would be around 2.1 p.u., and the CLPU duration was around 20 minutes.

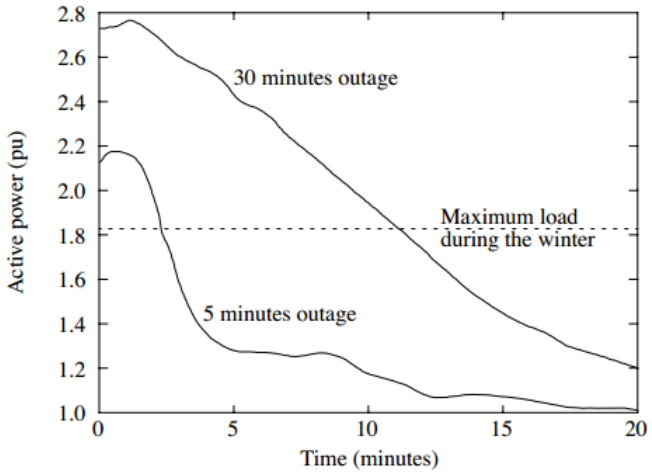

Figure 2.7. Field measurement of the cold load pick-up for 625 houses (Reprinted from [53])

After an extended outage, CLPU issues may prevent all the loads from being restored at the same time due to the capacity limit of transformers and lines. In practice, the solution is to sequentially restore the loads under CLPU conditions [54]. The feeders are divided into multiple segments by installing multiple sectionalizing switches, so the loads can be divided into multiple groups and brought online group by group. In [54], a step-by-step method is proposed for solving CLPU issues. The feeders were sectionalized into multiple segments that were energized sequentially. Similarly, in [55], a genetic algorithm is

proposed to generate the optimal restoration sequence, in order to address the CLPU issues.

2.4.3 Conventional Service Restoration Algorithms

Many algorithms have been proposed for solving conventional service restoration problems, such as heuristic algorithms [56], meta-heuristic algorithms [57], expert systems [58, 59], mathematical programming algorithms [60, 61], and multi-agent algorithms [43]. Minimizing the out-of-service loads is the objective of most of these algorithms. Some other objectives (e.g., the minimum number of switching operations and minimum outage duration) can also be incorporated into the objective function. Based on the implementation methodology, service restoration methods can be categorized into centralized methods and distributed methods. It is worth noticing that most of the conventional algorithms only take into consideration a single local power outage and assume substations are intact. Some of them (e.g., expert systems, heuristic methods) cannot be easily adapted to solve black start problem for distribution systems with DERs.

2.5 Black Start Restoration Considering DERs

Increased reliance on power supply reliability and economic efficiency makes the penetration of distributed energy resources (DERs) keep increasing within distribution systems and remote microgrids [62]. In this dissertation research, the term of DER refers to a board range of technologies. DERs not only include small power sources located within the distribution system or on customer's premises to supply the full or partial loads, but also include demand response measures [62]. Typical DERs include conventional non-

renewable distributed generation (DG), renewable DG, energy storage system (ESS), and demand response (DR) [63]. When a general blackout occurs, DERs can generate power to continuously energize the customer loads. Most commonly used DERs include diesel generators and batteries which can provide reliable power for home backup, critical loads (e.g., hospitals, schools, and data centers), and remote microgrids (e.g., island power systems, military base, remote communities) [64].

As shown in TABLE 2.1, DERs can be categorized into black start DGs, non-black start DGs, energy storage, and controllable loads, based on their roles in performing black start restoration. Note that controllable loads are categorized as a special type of DER, since they do not provide power. However, controllable loads can be shed or re-connected strategically to coordinate with other types of DERs, so as to enhance voltage profiles, release line congestion issues, and so on. The following subsections introduce each type of DERs listed in TABLE 2.1.

TABLE 2.1. DER CATEGORIES BASED ON THE ROLES IN BLACK START RESTORATION

DER Type	Black Start Capability	Dispatchable?	Examples
Black start DG	yes	yes	Combined heat and power (CHP), diesel generator, gas turbine generator, steam turbine generator, micro turbine, fuel cell.
Non-black start DG	no	yes	Micro turbine, small-hydro
		no	Wind generators, photovoltaics
Energy storage	yes, when discharging	yes	Battery, plug-in electric vehicle (PHEV), flywheel
Controllable loads	no	yes	Emergency demand response (DR) load (direct load control), economic DR load

2.5.1 Black Start DG

Black start resource in transmission systems is defined by North American Electric Reliability Corporation (NERC) as generation units and its ancillary equipment which can be self-started without external support [65]. This definition can be adapted for defining black start DGs in distribution systems and microgrids. Black start DGs refer to the power resources that can perform self-start and regulate frequency and voltage [66].

Typical black start DGs include combined heat and power unit (CHP), gas turbine, diesel generator and steam turbine. Micro turbines with storage devices installed on DC bus can also perform black start functionality with a rapid ramp rate (e.g. 0 to full load in 20-30 seconds) [67]. Black start DGs could be owned by utility, customers or other third-party utilities. Both utility-owned and customer-owned black start DGs can be used for providing standby restoration service for critical systems during outage conditions [68]. Some customer-owned microgrids can disconnect from the utility grid in case of a blackout. With a properly designed ancillary service market, these microgrids can also provide black start power to external network [1, 69]. In this dissertation research, a DG is categorized as a black start DG if [70]: 1): It is located within the microgrid or the distribution system; 2): It can communicate with the control center with its status, and 3): It can perform self-start and regulator voltage and frequency.

2.5.2 Non-Black Start DG

Non-black start DGs refers to the DGs that need external cranking power (e.g. battery banks, small diesel generators, and power from the grid) to start up [66]. Non-black start DGs can be further categorized into dispatchable DGs and non-dispatchable DGs.

Dispatchable DGs can output active power and reactive power at given set points. Whereas the power generated by non-dispatchable DGs is uncontrollable, such as wind generators and photovoltaics.

2.5.3 Energy Storage System

Energy storage system (ESS) (e.g., battery banks, flywheel, supercapacitors, compressed air and pumped hydro) is a special type of DERs, since it can act as a black start DG when discharging, and a controllable load when charging. Also, an ESS is capable of enhancing transient stability significantly if it is chosen to regulator the voltage and frequency, due to its fast response [16]. It is worth noticing that Plug-in Hybrid Electric Vehicle (PHEV) and Battery Electric Vehicle (BEV) are emerging techniques which can be used for black start restoration. A Large number of EVs can behavior as an ESS for load balancing and voltage and frequency regulation [71].

2.5.4 Demand Response

Demand response (DR) is defined by the Federal Energy Regulatory Commission (FERC) as the change in electric usage by end-user customers in response to the electricity price, in order to shifting load and maintain system reliability [72]. DR participation program can be generally categorized into economic DR and emergency DR (or Direct Load Control, DLC) based on if the response is voluntary [73]. Customer loads participating emergency DR programs can be seen as controllable loads. DLC in residential allows a utility to remotely control specific appliances, such as water heaters, heat pumps, and air conditioners. Participants get a lower energy price for the

inconvenience. In recent years, application of smart appliances gives the load more flexibility, which could be used in many applications such as ancillary services (frequency regulation, spinning reserves), renewable energy integration, etc.

2.5.5 Microgrid

A microgrid is defined by the U.S. Department of Energy as "a group of interconnected loads and distributed energy resources (DERs) with clearly defined electrical boundaries that acts as a single controllable entity with respect to the grid " [74]. A microgrid can operate in either grid-connected or island mode by connecting to or disconnecting from the main grid [74]. If a fault happens to the distribution system, the microgrids should be able to seamlessly transit from grid-connected mode to isolated mode, or perform black start if the transition is failed [75]. It is worth noticing that there are some remote microgrids that are permanently isolated from the main grid. These microgrids can be found in remote premises such as small islands, remote military bases and remote rural communities. The benefits provided by microgrids identified in the IEEE Standard 1547.4 include [75]: 1) Improve reliability by providing electricity to a portion of the main grid during a power outage; 2) Relieve distribution system overload problems by allowing a part of the main grid to intentionally island; 3) Relieve power quality issues (voltage distortion, voltage sag, flicker, lightning transients, etc.) by disconnecting from the main grid; and 4) Allow intentionally islanded customers to remaining powered when a maintenance is scheduled for the main grid.

The scale of a microgrid is spanning from a single customer with one DG to a whole substation that comprises multiple DGs, storages, and loads [75]. Figure 2.8 is a revised

version of the figure adapted from the IEEE standards 1547.4. The terminology “island” that used in the standard can be potentially treated as a microgrid since each island comprises generation and load with controllers and a point of common coupling (PCC). The microgrid control center (MGCC) is normally located at the point of common coupling (PCC). The MGCC is responsible for economic dispatch and emergency operation by controlling the elements (e.g., breakers, switches, DGs, and switchable loads) within the microgrid. This requires the MGCC to be able to interface with utility control centers and communicate with component controllers in the microgrid.

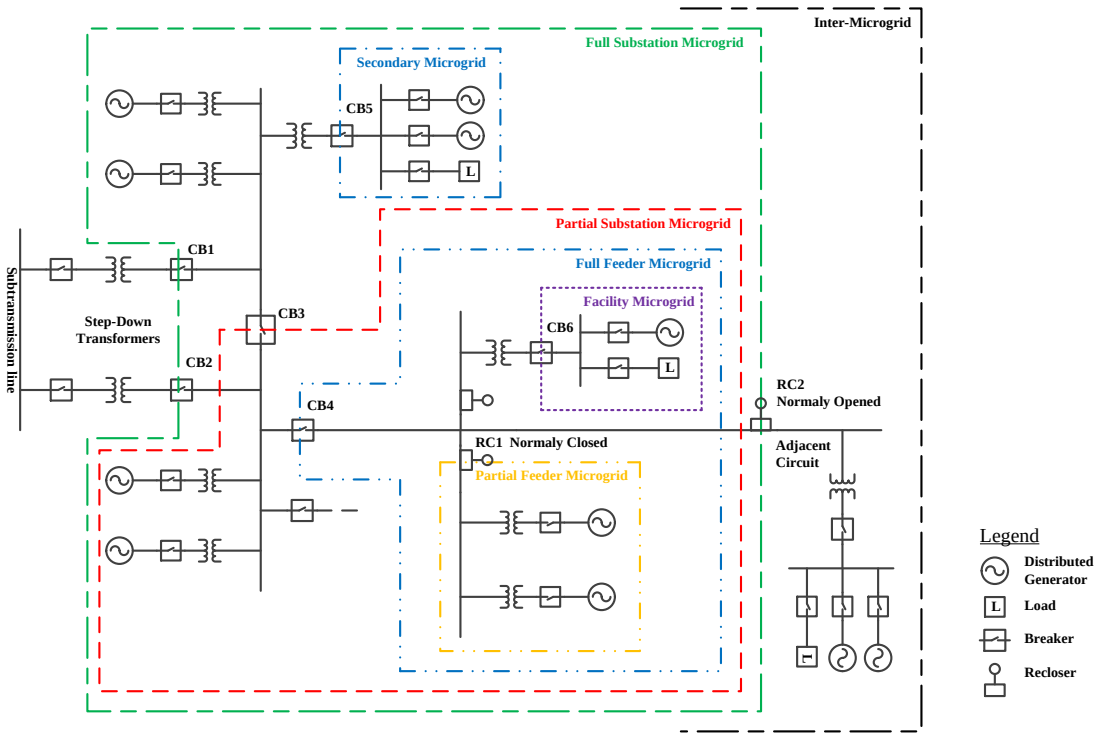

Figure 2.8 Identification of different microgrids based on IEEE Standard 1547.4 2011 [75]

2.6 BSR Methods Using DERs

Emerging DERs and RCSs in modern distribution systems demonstrate great potential that can be leveraged for developing new BSR methods. In this section, existing service restoration and BSR methods using DERs for both distribution systems and microgrids are reviewed.

2.6.1 Distribution Restoration Using DERs

Recently, some new service restoration methods were proposed to incorporate the operation of DERs installed in distribution systems [20-26]. The merits of incorporating DERs are summarized in [20-22]. Given the fact that DERs can provide power locally, some papers propose to form dynamic microgrids by grouping DERs and loads. For example, in [23], a distribution system was partitioned into several isolated microgrids based on power balancing and operational constraints. Authors in [24, 25] modeled microgrids as virtual substation feeders with voltage and frequency regulation capability. Therefore, some loads can be supplied by these microgrids and isolated from the main grid. Similarly, black start DGs can be also seen as virtual feeders. Authors in [76] proposed a branch and bound method to create cells in distribution systems using black start DERs. The switching sequence was considered in this paper. Authors in [77] proposed a method to partition a distribution system into several radial microgrids, considering renewable DERs and dispatchable DERs, and load profiles. The problem was formulated as a dynamic optimization problem. In [15, 78, 79], a similar partitioning method was proposed. The problem was formulated as a MILP problem and can be effectively solved using commercial solvers. Authors in [80] proposed a two-stage

heuristic method for restoring critical loads based on the concept of continuous operating time to ensure that all the critical loads can survive the expected outage duration. DG islanding operation is also studied in [81] using distributed multi-agent system. In [82], microgrids in a distribution system were employed to provide power locally to improve the voltage profile and facilitate the service restoration process. An operation strategy for networked microgrids is proposed in [83]. Based on the predicted load and RES data, microgrids can continuously energize the inside loads. A Tabu search based method is proposed in [84] to partition the system into multiple isolated microgrids.

CLPU issues must be considered after an extended outage [85]. Due to the limited transformer capacity, the high demand will prevent all loads from being restored at the same time [52]. A practical solution is to sectionalize a feeder into multiple sections and restore each section step by step. Doing so will apparently extend the restoration duration [54]. Black start DGs were used for service restoration to address the CLPU problem in [86, 87]. The basic idea was to energize local loads using DERs by grouping them into multiple microgrids isolated from the main grid. Therefore, CLPU issues can be addressed by properly grouping DERs and loads, such that the diversity of loads can be maintained and the restoration duration can be reduced. A major challenge is that the sequence for restoring multiple load groups should be properly addressed due to limited capacity of transformers, lines, and DERs. TABLE 2.2 summarizes the methods above, as well as their objective functions, constraints, and if they support forming isolated microgrids.

Some methods that can generate restoration sequences have been proposed. In [88, 89], the sequence for restoring loads was generated using dynamic programming. The

network topology was ignored. In [90, 91], the BSR problem was formulated as a MILP problem. Authors in [92] proposed a service restoration method to pick up the critical loads using the microgrids in the systems. The microgrids are assumed to be able to ride through the fault and support neighboring loads. A GridLAB-D based dynamic simulation was performed to verify the restoration plan. Heuristic and meta-heuristic methods used for generating sequences were presented in [93, 94].

TABLE 2.2. SERVICE RESTORATION AND BLACK START METHODS USING DERS

Ref No.	Method	Objective Function				Operational Constraints							DERs				Form MG	Seq.	DG Coord.	Black Start
		Max LR	*Min SO*	*Min LS*	*Min PL*	*PF*	*CL*	*VL*	*FL*	*RC*	*CLPU*	*LP*	*BDG*	*NBDG*	*MG*	*RES*				
[23]	**BE**	x			x		x	x							x		x			
[24]	**GA, PSO**				x	x	x	x		x					x	x	x			
[25]	**GT**	x	x			x	x	x		x					x		x			
[76]	**BB**	x				x	x	x	x	x		x	x	x			x			
[77]	**MINLP**			x		x	x	x		x			x			x	x			
[15]	**MILP**	x				x	x	x		x		x	x				x			x
[80]	**MC**	x				x	x	x		x		x			x		x			x
[79]	**TS**	x				x	x			x			x			x	x			
[81]	**MAS**					x	x	x	x	x			x							x
[82]	**MINLP**	x				x	x	x		x							x		x	x
[83]	**MILP**	x				x	x	x		x			x	x			x		x	x
[84]	**TS**	x			x	x	x	x	x	x				x		x	x			x
[54]	**AS**	x									x							x		
[86, 87]	**GA**			x			x	x			x	x	x							
[88, 89]	**DP**	x				x	x	x	x									x		
[90, 91]	**MILP**	**x**				x	x	x		x		x						x		
[92]	**STS**	x				x	x	x	x	x		x					x	x		x
[93]	**NDE**	x				x	x	x		x		x						x		
[94]	**GA**	x				x	x	x		x		x						x		

BE: branch exchange; **GA**: Genetic algorithm; **PSO**: particle swarm optimization; **GT**: Graph theory; **BB**: branch and bound; **LR**: Load restored; **SO**: Switching operations; **LS**: Load shed; **PL**: Power loss; **PF**: power flow; **CL**: current limit of branch; **VL**: voltage limit; **FL**: frequency limit; **RC**: radial topology constraint; **CLPU**: Cold load pickup; **LP**: Load priority; **BDG**: Black start DG; **NBDG**: Non-black start DG; **MG**: Microgrid; **RES**: Renewable energy sources; **MINLP**: Mixed-Integer Non-Linear Programming; **MILP**: Mixed-Integer Linear Programming; **MC**: Markov chain-based model; **TS**: Tabu search; **MAS**: Multi-agent system; **ILP**: Integer linear programming; **Sim**: Simulation; **AS**: Analytical solution; **DP**: Dynamic programming; **STS**: Spanning Tree Search; **NDE**: Node depth encoding

2.6.2 Microgrid Black Start Using DERs

Black start for microgrids refers to the process of restoring the microgrids without outside power supply. In this sense, the microgrids performing black start restoration should operate in island mode. According to the IEEE Standard 1547.4-2011, black start capability must be provided by microgrids capable of operating in island mode [75].

Conventional microgrids with black start capability can be found in remote premises that are permanently isolated from the main grid (e.g., small islands power systems, remote military bases and remote rural communities), and critical utilities within distribution systems (e.g., hospitals, data centers, and campuses). For remote permanently isolated microgrids, black start procedure should be initiated to restore the system after clearing the fault. For utility microgrids within distribution systems, in case of a power outage, they should support seamlessly transition from grid-connected mode to island mode to continuously energize customer loads or perform black start if the transition is failed [75]. Black start for small-scale microgrids is normally pre-planned and performed by following a set of operational rules [68]. For microgrids comprised of multiple DERs and loads, similar rules can be followed while coordinating DERs [95, 96]. The pre-planned black start strategies should be updated periodically to consider the expansion of generation and demand [68].

Current research on microgrid black start primarily focuses on the control strategy design and proof of feasibility for small scale microgrids using time domain simulation. The test systems and the methods for microgrid black start in the literature are summarized in TABLE 2.3. Feasibility of black start for microgrids was investigated in [16, 95, 97].

Black start strategies were evaluated based on the multi-master operation (MMO) mode, meaning all dispatchable DGs are operated separately to share the load demand. A set of pre-defined operational rules were defined. Rule-based methods for microgrid black start can be also found in [98-100]. In [98], battery, fuel cell, and renewable energy, were used for black start. In [100], a campus microgrid was shown to be able to support the loads outside of the microgrid. A multi-agent black start scheme was proposed in [101]. The multi-agent scheme was implemented in a distributed control manner, which could reduce the computational burden of MGCC, as well as the requirements for communication between the central agent (MGCC) and other agents (e.g., generation agent, load agent and breaker agent). However, bidirectional communication is still needed for negotiating between different agents. A black start method for microgrids was introduced in [102] based on a pre-planned procedure. Wind power was integrated into the black start process. Rule-based methods can be also found in [103, 104], in which multiple DERs were coordinated. The entire substation was operated as an isolated microgrid. Multiple sub-microgrids were formed firstly and then synchronized to the distribution feeders. The voltage constraint was verified by time domain simulation.

In summary, the existing black start methods for microgrids mainly focus on designing the rules and control strategies, which are valuable for developing advanced black start methods. Rule-based black start methods normally operate DGs in droop-control mode to implement a distributed control scheme. Whereas centralized control can achieve better results, if all the dispatchable DGs can be fully coordianted by MGCC. Hence, a robust communication network is required to support centralized control schemes. Since multiple

components may be affected by extreme weather events, system operating conditions can be changing continuously and unpredictable. The pre-planned solutions may be no longer feasible under varying operating conditions. Therefore, a BSR framework that can generate restoration solutions in response to varying operating conditions is needed.

TABLE 2.3. Previous WORK ON MICROGRID BLACK START PROBLEM

Ref No.	System parameters		Black start method		
	Voltage	Black start sources	Problem addressed	Algorithm	Features and Weaknesses
[16, 95, 97]	400V	Micro turbine, fuel cell, CHP, flywheel, battery, PV, controllable load	To proof the feasibility of using low-voltage microgrids for black start	Rule-based	Operational constraints and stability are examined by time domain simulation. Black start sequences are pre-defined based on the specific rules. DGs are coordinated through droop control.
[98]	220V	PV, Wind, Fuel cell, battery	Select voltage reference during black start in the absence of the main grid	Rule-based	Black start sequences are pre-defined based on the specific rules. Storage system is not well configured for compensating intermittent characteristic of renewables
[99]	20KV	Gas turbine, inverter-interfaced DGs	Evaluate the performance of communication, load control, and variable energy sources	Rule-based	Black start sequences are pre-defined based on simple rules. So it is not suitable for large scale microgrids. DGs are coordinated through droop control.
[100]	4.16KV	Gas turbine, Wind, PV, controllable load	Show the black start capability of IIT microgrid	Rule-based	Show the concept of DS restoration using MGs. DGs are coordinated through droop control.
[101]	120V	Micro turbine, PV, storage	Apply multi-agent method on microgrid black start problem	Multi-agent	The operational rules were built in each agent. The central agent acts as a control center. The rule-based weaknesses also apply for this method.
[102]	480V	Wind, Diesel Generator, ESS, and controllable load	Controller and operation guidelines design for microgrid black start	Pre-defined	The black start procedure is not suitable for large-scale microgrids. The wind speed was assumed to be constant. The uncertainty was not considered.
[103, 104]	Medium voltage	Micro-turbine, PV, controllable load	Prove the feasibility of black start for DS with a lot of controllable devices	Rule-based	Assumed conventional diesel and storage have sufficient capacity and control capability for maintaining voltage and frequency. The simple rules cannot specify the switching sequence for each device.

2.7 Motivation

This dissertation is motivated by the fact that an integrated BSR method is needed to coordinate DERs and switches during the black start process. The outage duration can be significantly reduced if microgrids can be developed with DERs continuously supporting the customers. The boundaries for each isolated microgrid can be dynamically developed by sequentially operating the switches. Therefore, the black start procedures must contain a sequence of control actions that are optimally scheduled over a time horizon. In addition, the BSR method should be able to adapt to varying system operating conditions (e.g., multiple faults, varying load demands, CLPU issues). However, such an integrated method that can address these concerns is still lacking in the literature.

2.7.1 Existing Problems

Existing methods for black start restoration at the distribution level can be categorized into two types: single-step methods (e.g., [23-25]) and sequence-generation methods (e.g., [54, 90, 92]). Single-step methods aim to generate a final configuration, which only specifies the status of each controllable component at a single operating point. Whereas the sequence-generation methods aim to generate a feasible restoration sequence, which represents a series of system operating points over multiple time steps.

Since single-step methods only generate a final configuration, a feasible black start sequence must be generated separately. In the context of varying load demand due to CLPU conditions, it is difficult to model the system load demand in the single-step method. It can be expected that using the peak load demand may result in sub-optimal solutions that are limited by permissive voltage ranges and line capacity constraints.

However, using the pre-fault load demand may lead to infeasible solutions, since the actual load demand may be much higher than the pre-fault load. Furthermore, many of the existing BSR methods can only determine the status of sectionalizing switches and tie switches [15, 77]. When a general blackout occurs, distribution substations may be out of power. Thus, reconfiguration-based methods cannot generate feasible solutions anymore, because no energization paths can be developed to bridge substations and loads [83, 92, 105]. Furthermore, single-step BSR methods cannot incorporate inter-temporal operational constraints for DERs (e.g., ramp rate constraint, ESS stage-of-charge (SOC) constraint).

Existing sequence-generation methods are normally performed in two stages. In the first stage, a final configuration is derived using the single-step method. Then, a sequence-generation algorithm is used to generate a feasible sequence that can energize the system from the pre-fault configuration to the final configuration [90]. Some sequence-generation methods use dynamic programming or genetic algorithm to generate the sequence without knowing the final configuration in advance [88, 94]. Existing sequence-generating algorithms work well for conventional distribution systems without DERs [90, 91]. However, the inter-temporal constraints introduced by operating DERs and time-varying loads require each control action to be carried out at a specified time. Existing sequence-generation methods cannot properly integrate the inter-temporal constraints or determine the timing for performing control actions.

Furthermore, many of the existing BSR methods are formulated based on several simplifications and assumptions, for example, balanced system conditions and constant

load demand. Although these simplifications and assumptions can significantly simplify the problem formulation, the feasibility of generated restoration solutions may be questionable when implementing the solutions on practical systems. Some heuristic models can be easily adapted to incorporate unbalanced operational conditions into the BSR method [25, 84], but they may not guarantee the optimality of the solutions.

In summary, many of the existing BSR methods are incapable of coordinating DERs and line switches while considering complicated load conditions throughout the black start process. The capability of generating restoration sequences is critical to successfully restoring a system starting from a fully de-energized state. In addition, several practical concerns (e.g., three-phase unbalanced operation, CLPU issues) should be addressed. To the best of the authors' knowledge, a restoration methodology that can meet these requirements is still lacking in the literature.

2.8 Section Summary

In this section, the concept of resilience was introduced first. As the core application for improving system resilience, OMS and its associated functionalities were introduced. Then, this section reviewed the existing black start restoration methods proposed for distribution systems and microgrids in the literature. Next, the motivation of this dissertation was introduced. It was concluded that an integrated black start restoration method is needed to fully coordinate DERs and switches during the restoration process.

3 PROBLEM FORMULATION AND SOLUTION METHODOLOGY

3.1 Introduction

Conventional distribution systems cannot perform black start restoration when a general blackout occur. This is because distribution substations, as the only power sources of conventional distribution systems, can only be energized by sub-transmission systems. Therefore, traditional black start restoration normally starts from large power plant restart and transmission system energization, then sub-transmission and distribution systems [106]. This top-down strategy will take several hours or even days to fully restore the system from a general blackout caused by extreme weather events [3, 4].

In recent years, many efforts have been made toward transforming conventional distribution systems to active distribution systems (ADSs) with the support of advanced communication technologies and emerging smart grid technologies. Specifically, distributed energy resources (DERs), which can supply power to local customers, make it possible to perform black start restoration in ADSs. Accordingly, many black start restoration (BSR) methods have been proposed in the literature. As discussed in Section 2, most of the existing BSR methods are developed based on the concept of "microgrid", which is defined as "a group of interconnected loads and distributed energy resources within clearly defined electrical boundaries" [74]. When a blackout occurs, DERs can be started to supply power to customers. Remote control switches (RCSs) can be used for interconnecting DERs and loads into microgrids, as well as defining electrical boundaries for each microgrid [17].

However, several problems with the existing BSR methods still remain unsolved. A feasible black start restoration sequence for coordinating DERs and RCSs is critical to successfully restoring a system. As concluded in Section 2, since single-step methods can only generate BSR solutions representing a single operating point, a feasible black start restoration sequence must be generated separately. In addition, it is difficult to model the system load demand in single-step methods, due to the fact that the load demand will change continuously under CLPU conditions. Furthermore, some inter-temporal operational constraints (e.g., ramp rate constraint for DERs, stage-of-charge (SOC) constraint for ESSs) cannot be incorporated in single-step methods. Regarding the existing sequence-generation methods, many of them were proposed for conventional distribution systems without DERs. Therefore, these methods can only determine the sequence of switches. Again, the inter-temporal operational constraints introduced for DERs and ESSs cannot be incorporated in the existing sequence-generation methods. Furthermore, many of the existing BSR methods are formulated based on several simplifications and assumptions, for example, balanced system conditions and constant load demand. Although these simplifications and assumptions can significantly simplify the problem formulation, the feasibility of generated restoration solutions can be questionable when implementing the solutions on practical systems. Therefore, the capability of the new BSR method to address three-phase unbalanced conditions and time-varying loads (e.g., CLPU conditions) is needed. In summary, the aforementioned problems require a new BSR method to be able to generate black start restoration sequences in response to varying operating conditions and coordinate DERs during the black start process.

In this section, the BSR problem is stated first. Then, the BSR problem is mathematically formulated as a dynamic optimization problem. Next, a mixed-integer linear programming (MILP) model is introduced to linearize the original nonlinear dynamic optimization problem. Finally, the solution methodology of the proposed BSR method is introduced.

3.2 BSR Problem Statement

Performing black start restoration on active distribution systems and microgrids presents many challenges. As concluded in Section 2, there are several problems with the existing BSR methods, hence hindering these methods from being applied to active distribution systems and microgrids directly. The BSR problem can be stated as four requirements, which will be introduced as follows.

Firstly, the proposed BSR method should be able to generate a black start restoration sequence. The restoration sequence should ensure that each type of black start resource (e.g., black start DGs, non-black start DGs, ESSs, controllable loads, switches) is operated properly. For example, black start DGs should self-start first. Non-black start DG should be started by external power. In addition, the restoration sequence should ensure that every time a control action is performed, all the operational constraints (e.g., voltage limit, line thermal limit, topological constraint) are satisfied.

Secondly, the proposed BSR method should be able to develop multiple isolated microgrids. Within each microgrid, there should be only one black start DG or energized substation operated as a slack bus. The DERs should be able to balance the load demand

within the corresponding microgrid all the time. In addition, the topological constraints should be satisfied for each microgrid.

Thirdly, the proposed BSR method should be able to dispatch all the dispatchable DERs in a way that the customer loads are restored as much as possible, while satisfying all the operational constraints.

Fourthly, the proposed BSR method should be able to address three-phase unbalanced conditions and time-varying loads (e.g., CLPU conditions).

The requirements on the new BSR method can be also illustrated through the following two examples. The first example demonstrates the scheme of forming microgrids within a distribution system. The second example shows how a sequence can impact the performance of a black start solution. Figure 3.1(a) demonstrates a simple system with two feeders. The substation is de-energized due to a general blackout. Note this system can also represent a microgrid operated in island mode. All the DERs in the system (e.g., DGs, battery, wind farm, customer microgrid) are disconnected to comply with the IEEE 1547.4 standard [75]. All the DGs, loads, and lines are remote controllable. Figure 3.1(b) shows a possible black start solution based on the concept of microgrid. It can be seen that the system is partitioned into two isolated microgrids, namely, Microgrid 1 and Microgrid 2. Microgrid 1 is formed by opening switches marked as 1, 2, 4, and 5; Microgrid 2 is formed by opening switches marked as 3 and 4. The switches within each microgrid are closed to interconnect DERs and loads. By forming the two microgrids, all the five loads can be restored, before the substation is energized by sub-transmission systems.

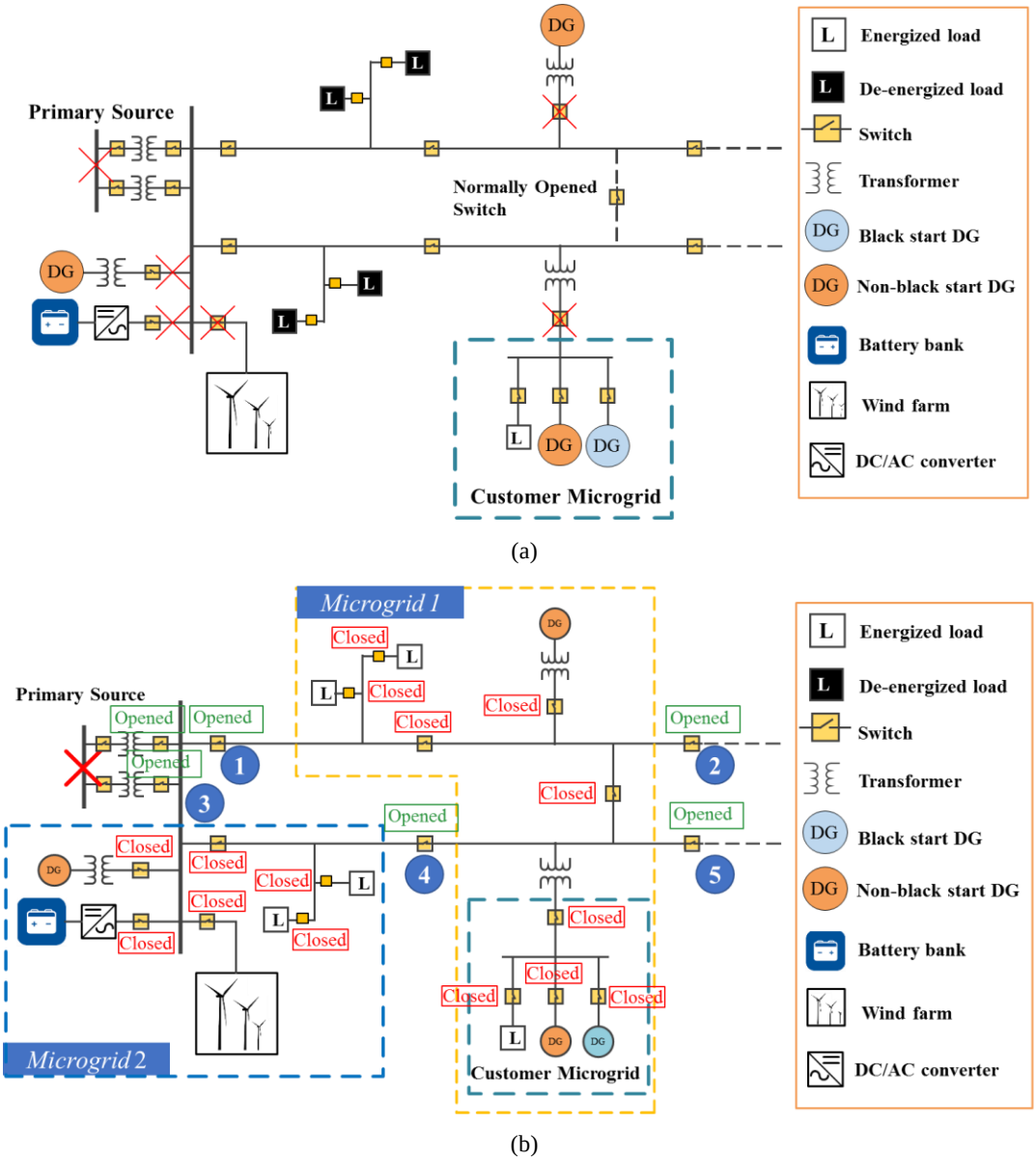

Figure 3.1. A simple distribution system to show the black start restoration based on the concept of microgrid. This system can also represent a microgrid. (a): System is in a blackout; (b): A possible restoration solution

Note that in practice, limited capacity of DERs may prevent all the loads from being restored, and only critical loads with higher priorities may be restored. In addition, multiple DERs in each microgrid should be coordinated to share the load demand. For

example, in Microgrid 1, the two dispatchable DGs should be properly dispatched to satisfy the operational constraints. Unlike Microgrid 1, in Microgrid 2, the battery is dispatchable and the wind farm is non-dispatchable. If the black start DG has limited capacity for regulating voltage and frequency, the battery may need to strategically charge and discharge to balance the time-varying loads and wind farm output.

An example black start sequence for restoring Microgrid 1 in Figure 3.1(b) is shown in TABLE 3.1. Figure 3.2(a) demonstrates the system configuration of Microgrid 1. The switches associated with transformers, lines, DGs, and loads are numbered in red boxes. At t_0, the customer microgrid, which survives from the general blackout, is prepared to provide black start services. Then, at t_1, the switch at location 1 is closed to energize the transformer. At t_2 and t_3, the tie-switch at location 2 and the sectionalizing switch at location 3 are closed sequentially to energize the feeder. Next, Load 1 at location 4 is energized at t_4. At t_5, the DG at location 5 are started to share the load demand by outputting power $P_5 + jQ_5$. At t_6, Load 2 at location 6 is energized, the dispatchable Dg at location 5 changes its output to $P_6 + jQ_6$. Note Load 2 is not energized together with Load 1. A possible reason is explained in Figure 3.2(b).

TABLE 3.1. AN EXAMPLE OF CONTROL SEQUENCE ASSOCIATED WITH FIGURE 3.2 (A)

Time	Control Actions
t_0	The customer microgrid is ready for performing service restoration
t_1	Close the switch at (1) to energize the transformer
t_2	Close the tie-switch at (2)
t_3	Close the sectionalizing switch at (3)
t_4	Energize Load 1 at (4)
t_5	Close the switch at (5) to start the DG, set the power output as $P_5 + jQ_5$
t_6	Restore Load 2 at (6), set the DG power output as $P_6 + jQ_6$
…	…

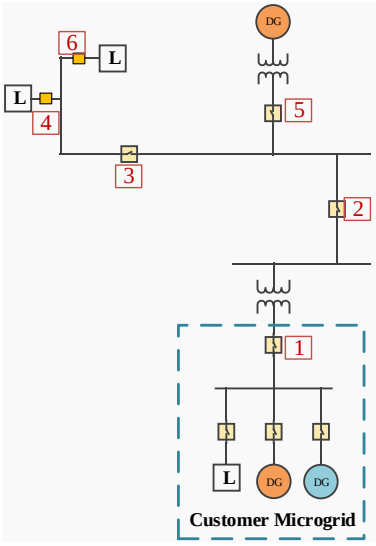

(a)

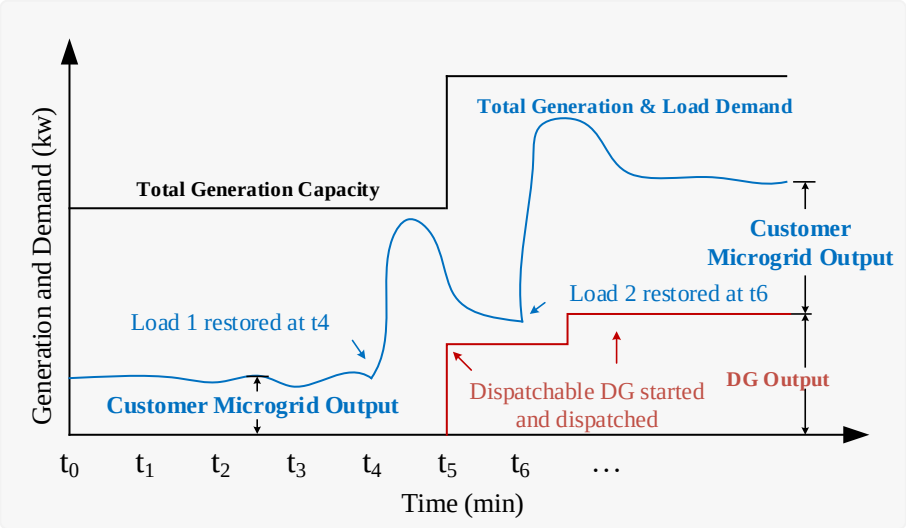

(b)

Figure 3.2. Microgrid 1 formed for the case shown in Figure 3.1. (a): Control sequence for restoring Microgrid 1; (b): Generation and load demand during the restoration process.

Figure 3.2(b) demonstrates the total generation capacity and load demand during the restoration process. The horizontal axis represents the time. Different control actions are performed at different time steps. The vertical axis represents the generation and load

profiles. It can be seen that the customer microgrid can pick up Load 1 at t_4, but no more capacity is available for picking up Load 2. Therefore, the DG is started at t_5, to provide additional generation capacity. Since the dispatchable DG is sharing the load demand of Load 1 and Load 2, less power will go through the tie-switch at location 2 from the customer microgrid. So, the line thermal limit for the transformer at location 1 is satisfied.

3.3 BSR Mathematical Problem Formulation

The aforementioned BSR problem can be mathematically formulated as a dynamic optimization problem. The dynamic optimization based formulation allows decisions to be made over multiple time steps [107]. At each time step, the set points for controllable components (e.g., controllable switches, dispatchable DGs, and controllable loads) can be defined and optimized to meet various operational constraints. The time horizon can be represented by a set of variables defined in discrete form; i.e., $z_t \in \{z_0, z_1, z_2, \dots, z_N\}$. Let N be the total number of time steps, then $N = T/\Delta t$, where Δt is the length of each time step. Define $x(z_t)$ as the state variable at time step z_t, and $u(z_t)$ as the control variable at time step z_t, $\tilde{f}[t, x(z_t), u(z_t)]$ as the transition equations determined by time step z_t, state variable $x(z_t)$ and control variable $u(z_t)$, and $\tilde{F}[z_t, x(z_t), u(z_t)]$ as the objective function. Then, the discrete-time dynamic optimization problem can be described as [107]:

$$maximize\ or\ minimize\ \sum_{Z_0}^{Z_N=\frac{T}{\Delta t}} \tilde{F}[z_t, x(z_t), u(z_t)]\Delta t \qquad (3.1)$$

$s.t.\ x(z_{t+1}) - x(z_t) = \tilde{f}[z_t, x(z_t), u(z_t)]$ → Equation of motion/transition equation

$(z_0) = A\ (A\ given),\ x(z_N) = Z(T\ given, Z\ free)$ → Transversality condition

Transition equation in the problem formulation defines the inter-temporal (or inter-step, inter-stage) constraints among various variables, hence relating the variables of different time steps [107]. For example, the difference of power output of DG between two consecutive steps should be smaller than a threshold (e.g., ramp rate constraint). Transversality conditions define the system operational conditions for each time step. For example, system model equations are typical transversality conditions. In order to facilitate the formulation of the BSR problem, three types of variables are normally defined to formulate dynamic optimization problems, namely, time variables, state variables, and control variables [107].

To better illustrate the problem formulation based on dynamic optimization, Figure 3.3 shows an example of how the proposed BSR method can generate a restoration sequence based on the values of decision variables. The system represents a simple distribution system or microgrid with dispatchable DGs. ESSs and renewable DGs should be incorporated into the problem formulation, but they are not shown in Figure 3.3. Components are numbered according to the node number. All lines and loads are assumed to be switchable and disconnected at Step 1. DG1 is a black start DG, and DG2 is a dispatchable DG without black start capability. A possible restoration solution is shown in Figure 3.3(a). At each step, the energization status of each component is shown. The active and reactive power output of each energized DG is shown as well. If two or more DGs are energized, they will be cooperatively dispatched. Figure 3.3(b) shows the configurations of the energized system at each step. At Step 1, $x_{1,1}^{G} = 1$, meaning DG1 is started to energize Node 1. At Step 2, $x_{12,2}^{BR} = 1$, meaning the switchable line between

Node 1 and Node 2 is closed to energize Node 2, which further enables Load 2 to be energized (i.e., $x_{2,2}^{L} = 1$). Similarly, Node 3 is energized at Step 3 by closing the line between Node 2 and Node 3. Meanwhile, DG3 is started to share the load demand, since its terminal node is energized. The proposed BSR method should be able to optimally coordinate all the controllable components to restore as much load as possible across given steps, and ensure all the constraints are satisfied.

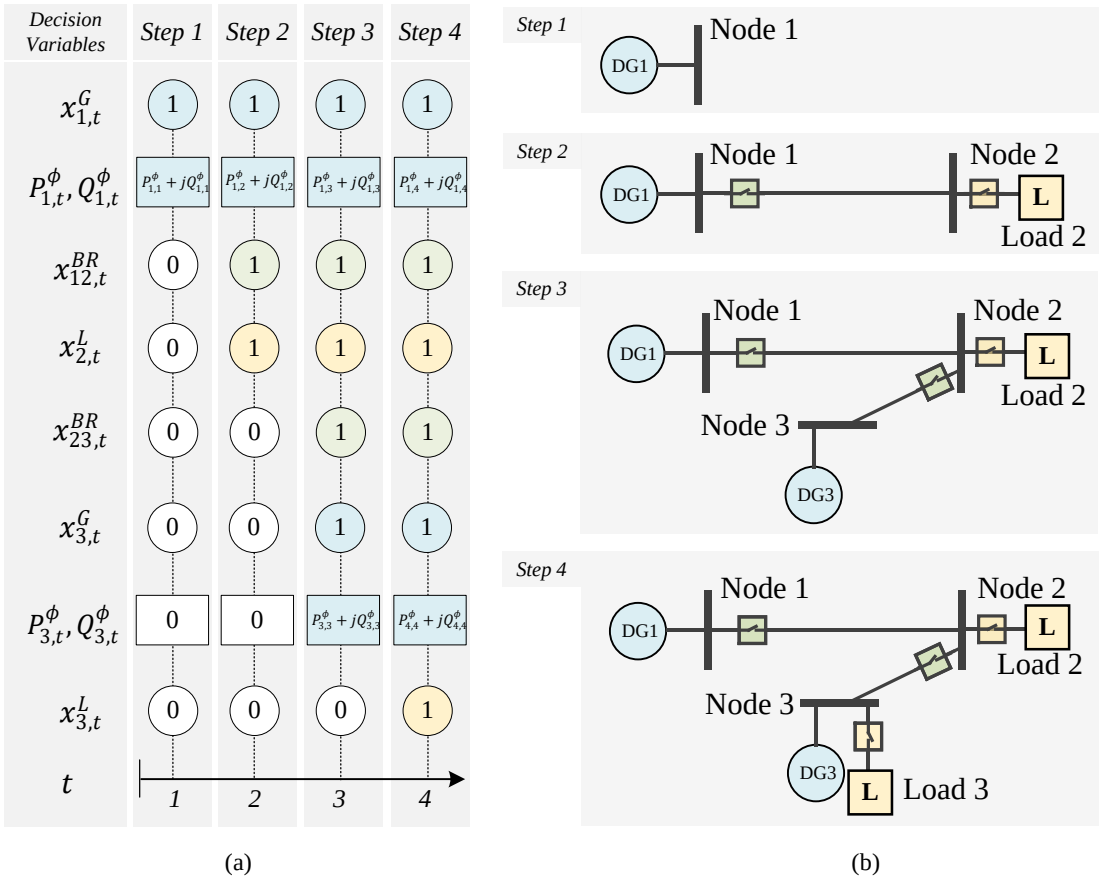

(a) (b)

Figure 3.3. Possible restoration sequence derived from the control variables that are solved by the proposed BSR model: (a) decision variables, (b) derived restoration sequence.

Mathematically, the BSR problem can be formulated as:

$$\min \mathrm{F}[\mathbf{x}(\mathrm{t}), \mathbf{u}(\mathrm{t})] \tag{3.2}$$

$$\text{s.t.} \quad \mathrm{G_i}[\mathbf{x}(\mathrm{t}), \mathbf{u}(\mathrm{t})] \leq 0, \mathrm{i} = 1, \ldots, \mathrm{m} \tag{3.3}$$

$$\mathrm{H_j}[\mathbf{x}(\mathrm{t}), \mathbf{u}(\mathrm{t})] = 0, \mathrm{j} = 1, \ldots, \mathrm{n} \tag{3.4}$$

$$t \in \{z_0, z_1, z_2, \ldots, z_N\}, \tag{3.5}$$

where $\boldsymbol{x}(t)$ and $\boldsymbol{u}(t)$ represent the vector of state variables and decision variables at each time instant, respectively; $F[\boldsymbol{x}(t), \boldsymbol{u}(t)]$ represents the objective function of the BSR problem, as a function of $\boldsymbol{x}(t)$ and $\boldsymbol{u}(t)$; Equation (3.3) represents m inequality constraints which can be capacity limits for DGs, magnitude limits for node voltage, etc.; Equation (3.4) represents n equality constraints such as power flow constraints. Both objective functions and constraints are introduced in the following subsections.

3.3.1 Objective Function of the BSR Problem

When a general blackout or partial power outage occurs, the most critical concern is to restore the affected customers. Therefore, the main objective is normally defined to maximize the total restored energy during the considered time horizon [77, 83]. Also, there are several other factors usually examined during the restoration process. For example, minimizing the restoration time for restoring a certain percentage of total system loads [108]; minimizing the number of switching operations [109]; and minimizing the total cost of restoration considering all the factors such as the cost of unserved energy, the cost of switching operations, and cost of the fuel used for dispatching DGs [110].

The objective function of the BSR problem can be formulated as:

$$\max \sum_{t\in\mathcal{T}} f\left(\boldsymbol{P}_{l,t}^{L}, \boldsymbol{P}_{g,t}^{\phi}, \boldsymbol{Q}_{g,t}^{\phi}, x_{ij,t}^{BR}, x_{l,t}^{L}, \Delta t\right), \tag{3.6}$$

where $t \in \mathcal{T} \coloneqq \{1,2,\dots,T\}$ is denoted as the set of steps, and T is the length of horizon. $\boldsymbol{P}_{l,t}^{L}$ is a vector representing three-phase load demand on node l at step t. Let $\mathcal{N} \coloneqq \{1,2,\dots,N_n\}$ represents the set of all the buses such as load buses and DG buses. $l \in \mathcal{L} \subseteq \mathcal{N}$ is the set of buses connected to loads. $\boldsymbol{P}_{g,t}^{\phi}, \boldsymbol{Q}_{g,t}^{\phi}$ are vectors representing three-phase active and reactive power generated by a DG on node g at step t. $g \in \mathcal{G} \subseteq \mathcal{N}$ is the set of substation buses and buses connected to dispatchable DGs. $x_{ij,t}^{BR}$ is the switching status of a switchable line between node i and node j, at step t. $x_{l,t}^{L}$ is the energization status of a load at node l, at step t. Δt is the length of the interval between two consecutive steps. $f(\blacksquare)$ is the function to represent the restored load (e.g., in kW) based on the control variables. Equation (3.6) represents the total amount of load restored at all the considered steps; i.e., the total restored energy (e.g., in kWh) over the considered horizon.

3.3.2 Constraints of the BSR Problem

A feasible black start solution should include a sequence of control actions that can be performed to energize the system step by step. In order to ensure the black start solutions are carried out securely and efficiently, various operational constraints should be defined for all the components (e.g., DGs, switches, transformers, lines, and loads) that are involved in the black start process. TABLE 3.2 lists the models and constraints that should be considered in the BSR problem.

TABLE 3.2. MODELS AND CONSTRAINTS OF THE BSR PROBLEM

Category	Models and Constraints	Description
System Model Constraints	Power Flow Model	Calculate voltage and line power, given an operating point
	Load Model: CLPU Load and ZIP Load	Calculate the load demand.
	Transformer/Voltage Regulator Model	Model the behavior of transformers and voltage regulators
	Black Start DG Model	Ensure that each component is connected and operated correctly
	Dispatchable DG Model	
	Renewable DG Model	
	ESS Model	
	Line Model	
	Initial Condition	Describe the initial state of the system
System Operational Constraints	Line kVA Capacity Constraint	Ensure the apparent power going through each energized line is maintained below the thermal threshold
	Voltage Limit Constraint	Ensure the voltage magnitude of each energized bus is maintained within a permissive range
	Max Step Load Constraint	Ensure the frequency stability
DG/ESS Operational Constraints	ESS Operation	Ensure each ESS is operated properly
	DG Current Unbalanced Operation	Protect each three-phase black start DG from being damaged by unbalanced conditions
	DG Capacity Constraint	Prevent a DG from being overloaded and changing its output too fast
	DG Ramp Rate Constraint	
Topological Constraints	Connectivity constraints Sequencing constraints	Ensure the BSR sequence is feasible. Components are correctly connected. Each isolated microgrid is in tree topology.

3.4 Assumptions

In practice, system operators should consider many factors during black start restoration, for example, work scheduling, crew dispatching, prediction error, and succeeding faults [69]. It is impossible to incorporate all the concerns into the problem formulation. For simplicity, several reasonable assumptions are made in this research to simplify the problem formulation.

1) The time interval between any two consecutive steps is assumed to be fixed.

2) All the loads are modeled as ZIP (constant impedance (Z), constant current (I), and constant power (P)) loads. If the loads are under CLPU conditions, they will be modeled as constant PQ loads.

3) A communication network is available during the restoration process and all the switches and DERs can be remotely controlled. This assumption ensures that the control commands can be performed timely for each time step. If a component is not controllable due to loss of communication, it will be classified as a failed component.

4) The predicted load profile and power output of renewable DGs are accurate.

5) The proposed method can generate restoration solutions that represent a series of operating points over multiple discrete time steps. In practice, the system operating conditions will change continuously from the operating point at one discrete step to the operating point at the next discrete step, due to continuously changing variables such as energized loads under CLPU conditions. Therefore, it is necessary to assume that the intermediate system operating conditions always satisfy the constraints.

3.5 MILP Formulation

In this section, the MILP formulation for the proposed BSR problem is presented. First, the nomenclature for various variables, parameters, and sets are introduced. Then, the objective function and various operational constraints are presented.

3.5.1 Nomenclature

3.5.1.1 Parameters

T	The length of the time horizon

Δt	The length of the time step
N_n	Total number of nodes
N_{br}	Total number of lines
N_l	Total number of loads
N_g	Total number of DGs

3.5.1.2 Sets

$\mathbb{C}$	Set of complex numbers. $\mathbb{C}^{3\times1}$ is the set of 3×1 vectors of complex number
$\mathbb{R}$	Set of real numbers. $\mathbb{R}^{3\times1}$ is the set of 3×1 vectors of real number
$\mathbb{Z}$	Set of integer numbers. $\mathbb{Z}_2^{3\times1}$ is the set of 3×1 vectors of binary integer
$\mathcal{T} \coloneqq \{1,2,\dots,T\}$	The set of time steps, T is the length of horizon.
$\Phi \coloneqq \{a,b,c\}$	The set of phases for single, two, and three-phase nodes and lines
$\mathcal{N} \coloneqq \{1,2,\dots,N_n\}$	The set of all the nodes such as load buses and DG buses.
$\mathcal{N}^F \subseteq \mathcal{N}$	The set of nodes that cannot be energized, e.g., fallen power poles
$\mathcal{L} \subseteq \mathcal{N}$	The set of nodes connected to loads
$\mathcal{L}^S \subseteq \mathcal{L}$	The set of loads that can be remotely switched on or off
$\mathcal{L}^F \subseteq \mathcal{L}$	The set of loads that cannot be restored in a short time
$\mathcal{G} \subseteq \mathcal{N}$	The set of nodes connected to DGs
$\mathcal{G}^S \subseteq \mathcal{G}$	The set of substation buses (i.e., slack buses) or DGs with black start capability

$\mathcal{G}^F \subseteq \mathcal{G}$	The set of DGs that cannot be utilized for service restoration.
$\mathcal{B} \coloneqq \begin{Bmatrix} (i,j): i \in \mathcal{N}, \\ j \in \mathcal{N},\ i \neq j \end{Bmatrix}$	The set of lines
$\mathcal{B}^S \subseteq \mathcal{B}$	The set of lines that can be remotely controlled.
$\mathcal{B}^F \subseteq \mathcal{B}$	The set of lines that are found to be damaged or disconnected and thus need to be isolated or fixed (e.g., trees lean on these lines, blown fuses).
$\mathcal{V} \subseteq \mathcal{B}$	The set of lines installed with voltage regulators and transformers
$\mathcal{E} \subseteq \mathcal{N}$	The set of ESS
$\mathcal{E}^F \subseteq \mathcal{N}$	The set of ESS not participating in BSR
$\mathcal{R}$	The set of voltage regulators

3.5.1.3 Superscripts and Subscripts

"S"	Superscript to indicate that a component/set is controllable, e.g., B^S
"F"	Superscript to indicate that a component/set is faulted, e.g., B^F
"N"	Superscript to indicate that a variable is related to node set, e.g., $s_{i,t}^N$
"BR"	Superscript to indicate that a variable is related to a line, e.g., $x_{ij,t}^{BR}$
"L"	Superscript to indicate that a variable is related to a load, e.g., $P_{l,t}^L$
"G"	Superscript to indicate that a variable is related to a DG, e.g., $P_{g,t}^G$
"i"	Subscript to represent the node number, e.g., $s_{i,t}^N$
"ij"	Subscript to represent the two end nodes of a line, e.g., $x_{ij,t}^{BR}$
"l"	Subscript to represent the load number, e.g., $x_{l,t}^L$

"g"	Subscript to represent the DG number, e.g., $x_{g,t}^{G}$

3.5.1.4 Variables

$s_{i,t}^{N} \in \{0,1\}$	Energization status of node i at step t
$x_{ij,t}^{BR} \in \{0,1\}$	Energization status of line (i,j) at step t
$x_{l,t}^{L} \in \{0,1\}$	Energization status of load l at step t
$x_{g,t}^{G} \in \{0,1\}$	Energization status of DG g at step t
$x_{e,t}^{ESS\_CH} \in \{0,1\}$	Charging action for ESS e at step t
$x_{e,t}^{ESS\_DISCH} \in \{0,1\}$	Discharging action for ESS e at step t
$\boldsymbol{P}_{g,t}^{\phi}, \boldsymbol{Q}_{g,t}^{\phi} \in \mathbb{R}^{3\times1}$	Three-phase active and reactive power provided by the DG at node $g \in \mathcal{G}$ for each phase at step t
$P_{e,t}^{ESS\_CH}, P_{e,t}^{ESS\_DISCH}$	Single-phase charging and discharging active power for ESS e at step t
$Q_{e,t}^{ESS\_CH}, Q_{e,t}^{ESS\_DISCH}$	Single-phase charging and discharging reactive power for ESS e at step t
$SOC_{e,t}^{ESS}$	State of charge (SOC) for a single-phase ESS e at step t
$\boldsymbol{P}_{ij,t}^{BR}, \boldsymbol{Q}_{ij,t}^{BR} \in \mathbb{R}^{3\times1}$	Three-phase active and reactive power going through the line between node i and node j at time step t
$\boldsymbol{P}_{l,t}^{L}, \boldsymbol{Q}_{l,t}^{L} \in \mathbb{R}^{3\times1}$	Three-phase active and reactive power of load l at time step t. Note they are determined by the control variables of load status $x_{i,t}^{L}$.
$\boldsymbol{V}_{i,t}$	Node voltage at time step t

$\boldsymbol{\beta}_{r,t}$	Tap ratio for voltage regulator r at time step t

Operators

$\odot$	Element-wise product for vectors and matrices
$\oslash$	Element-wise division for vectors and matrices

3.5.2 Objective Function

The objective function is defined to maximize the total restored energy of each step considering the weight factor of each load l (denoted as β_l^L):

$$\max \sum_{l\in\mathcal{L}} \sum_{t\in\mathcal{T}} \sum_{\phi\in\{a,b,c\}} \beta_l^L \cdot P_{l,t}^{\phi} \cdot \Delta t \tag{3.7}$$

and subject to the following constraints:

1) Linear three-phase power flow constraints

2) DG current unbalance constraints

3) Topological constraints

4) Initial condition constraints

5) Other constraints: line and transformer capacity constraint, DG output constraints, spinning reserve constraints, voltage limit constraints, ramp rate constraints, maximum load step constraints.

3.5.3 System Model

Distribution systems are operated three-phase unbalanced in nature [111]. For example, there are single-phase laterals and two-phase laterals connected to three-phase feeders to serve unbalanced loads (e.g., single-phase loads, two-phase loads, and three-phase loads). That said, in some distribution applications where only an approximate

answer is needed, it is acceptable to assume perfectly balanced three-phase systems [111]. For a balanced three-phase distribution system, it is assumed that all lines are three-phase and perfectly transposed, all loads are three-phase balanced loads, and all DERs are operated in three-phase balanced conditions. As mentioned in Section 2, many BSR methods proposed in the literature assume the distribution systems are three-phase balanced, considering that the top priority is to restore as much load demand as possible in emergency situations. Balanced operating conditions can significantly reduce the computation time required by the BSR method for solving the MILP model. On the other hand, the proposed BSR method can be used for three-phase unbalanced systems, if it is required to model the system as accurate as possible. The choice between using three-phase balanced model and three-phase unbalanced model depends on many factors, such as the requirements on the computation time and quality of solution. The task of selecting a proper system model is left to system operators, and it is out of the scope of this dissertation.

3.5.3.1 Power Flow Model

Many smart grid applications integrated in modern distribution management system (DMS) require the power flow to be calculated in real-time or near real-time. To approximate the node voltage magnitude and line power, a power flow model should be integrated into the proposed BSR formulation to ensure the feasibility of solutions.

A general form of power flow model for distribution systems can be formulated based on Kirchhoff's circuit law (KCL) [112]:

$$\begin{bmatrix} \boldsymbol{I}_S \\ \boldsymbol{I}_N \end{bmatrix} = \begin{bmatrix} \boldsymbol{Y}_{SS} & \boldsymbol{Y}_{SN} \\ \boldsymbol{Y}_{NS} & \boldsymbol{Y}_{NN} \end{bmatrix} \begin{bmatrix} \boldsymbol{V}_S \\ \boldsymbol{V}_N \end{bmatrix}, \tag{3.8}$$

where the subscript S represents the slack buses, and N represents the remaining buses. $\boldsymbol{V}_S$ and $\boldsymbol{V}_N$ are matrices representing the three-phase node voltages. $\boldsymbol{Y}_{SS}$, $\boldsymbol{Y}_{NN}$ are diagonal submatrices of the system admittance matrix. $\boldsymbol{Y}_{NS}$, $\boldsymbol{Y}_{SN}$ are off-diagonal submatrices of the system admittance matrix. $\boldsymbol{I}_S$ and $\boldsymbol{I}_N$ are matrices representing the three-phase node injected currents into slack buses and non-slack buses. Note the node injected current comprises of load currents and DER currents. The voltage-dependent ZIP loads, which can be represented as a non-linear function of $\boldsymbol{I}_S$, $\boldsymbol{I}_N$, $\boldsymbol{V}_S$, and $\boldsymbol{V}_N$, make the power flow model nonlinear [112].

Linear power flow for unbalanced three-phase distribution systems has been studied in the literature [113-116]. For each line $(i,k) \in \mathcal{B}$, apply Kirchhoff's voltage low, we have [111]:

$$\mathbf{V}_{\mathrm{k}} = \mathbf{V}_{\mathrm{i}} - \boldsymbol{z}_{\mathrm{ik}}\mathbf{I}_{\mathrm{ik}}, \tag{3.9}$$

where $\boldsymbol{V}_i = \left[V_i^a, V_i^b, V_i^c\right]^{\mathrm{T}} \in \mathbb{C}^{3\times 1}$ is the vector of complex numbers representing three-phase voltage at bus i. $\boldsymbol{V}_k = \left[V_k^a, V_k^b, V_k^c\right]^{\mathrm{T}} \in \mathbb{C}^{3\times 1}$, $\boldsymbol{I}_{ik} = \left[I_{ik}^a, I_{ik}^b, I_{ik}^c\right]^{\mathrm{T}} \in \mathbb{C}^{3\times 1}$, and $\boldsymbol{z}_{ik} \in \mathbb{C}^{3\times 3}$ is the total line impedance consists of resistance $\boldsymbol{r}_{ik}$ and reactance $\boldsymbol{x}_{ik}$, which is determined by the phase impedance matrix $\boldsymbol{z}_{ik}^{abc} \in \mathbb{C}^{3\times 3}$ in Ω/mile and the length of the line $l(i,k)$ in mile [111]:

$$\boldsymbol{z}_{ik} = l(i,k)\boldsymbol{z}_{ik}^{abc} = \boldsymbol{r}_{ik} + j\boldsymbol{x}_{ik} \tag{3.10}$$

Denote $\odot$ and $\oslash$ the element-wise product and division respectively, the line current $\boldsymbol{I}_{ik}$ can be calculated by:

$$\boldsymbol{I}_{ik} = \boldsymbol{S}_{ik}^{*} \oslash \boldsymbol{V}_{i}^{*} \tag{3.11}$$

where $\boldsymbol{S}_{ik} = \left[P_{ik}^{a} + jQ_{ik}^{a}, P_{ik}^{b} + jQ_{ik}^{b}, P_{ik}^{c} + jQ_{ik}^{c}\right]^{\mathrm{T}} \in \mathbb{C}^{3\times 1}$is the apparent power from bus i to bus k. Substituting (3.11) into (3.9) and multiplying the left side and the right side by their complex conjugate respectively [115], we have:

$$\boldsymbol{V}_{k}\odot\boldsymbol{V}_{k}^{*} = \boldsymbol{V}_{i}\odot\boldsymbol{V}_{i}^{*} - \boldsymbol{z}_{ik}(\boldsymbol{S}_{ik}^{*} \oslash \boldsymbol{V}_{i}^{*})\odot\boldsymbol{V}_{i}^{*} - \boldsymbol{z}_{ik}^{*}(\boldsymbol{S}_{ik} \oslash \boldsymbol{V}_{i})\odot\boldsymbol{V}_{i} + \boldsymbol{c}_{ik}(\boldsymbol{S}_{ik}, \boldsymbol{V}_{i}, \boldsymbol{z}_{ik}) \tag{3.12}$$

where $\boldsymbol{c}_{ik}(\boldsymbol{S}_{ik}, \boldsymbol{V}_{i}, \boldsymbol{z}_{ik})$ is the higher order term that be neglected. The linear unbalanced three-phase power flow can be derived by assuming the phase voltages are nearly balanced [114]:

$$\frac{V_{i}^{a}}{V_{i}^{b}} \approx \frac{V_{i}^{b}}{V_{i}^{c}} \approx \frac{V_{i}^{c}}{V_{i}^{a}} \approx e^{j2\pi/3} \tag{3.13}$$

Note that (6) only holds for three-phase buses. For two-phase buses, only presenting phases are assumed to be nearly balanced. Rearrange (3.12), denote $\boldsymbol{U} = [|V^{a}|^{2}, |V^{b}|^{2}, |V^{c}|^{2}]^{T}$ and neglect $\boldsymbol{c}_{ik}$, we have:

$$\boldsymbol{U}_{\boldsymbol{k}} = \boldsymbol{U}_{\boldsymbol{i}} - \widetilde{\boldsymbol{z}}_{ik}\boldsymbol{S}_{ik}^{*} - \widetilde{\boldsymbol{z}}_{ik}^{*}\boldsymbol{S}_{ik} \tag{3.14}$$

where $\widetilde{\boldsymbol{z}}_{ik} = \boldsymbol{\alpha}\odot\boldsymbol{z}_{ik} \in \mathbb{C}^{3\times 3}$, and $\boldsymbol{\alpha}$ is defined as:

$$\boldsymbol{\alpha} = \begin{bmatrix} 1 & e^{-j2\pi/3} & e^{j2\pi/3} \\ e^{j2\pi/3} & 1 & e^{-j2\pi/3} \\ e^{-j2\pi/3} & e^{j2\pi/3} & 1 \end{bmatrix}$$

Together with the power balance constraints for each bus at each step, we can formulate the linear power flow constraints considering the energization status of each line at each step. For single-phase and two-phase lines, corresponding variables for the missing phase(s) should be set to zero. Considering the power balance for each bus at each step and neglecting the line loss, we have:

$$\boldsymbol{U}_{i,t} - \boldsymbol{U}_{j,t} \leq \widetilde{\boldsymbol{z}}_{ij}\boldsymbol{S}^{*}_{ij,t} + \widetilde{\boldsymbol{z}}^{*}_{ij}\boldsymbol{S}_{ij,t} + M\left(1 - x^{BR}_{ij,t}\right)\boldsymbol{e}^{\phi}_{\boldsymbol{ij}}, \tag{3.15}$$

$$\boldsymbol{U}_{i,t} - \boldsymbol{U}_{j,t} \geq \widetilde{\boldsymbol{z}}_{ij}\boldsymbol{S}^{*}_{ij,t} + \widetilde{\boldsymbol{z}}^{*}_{ij}\boldsymbol{S}_{ij,t} - M\left(1 - x^{BR}_{ij,t}\right)\boldsymbol{e}^{\phi}_{\boldsymbol{ij}},\ (i,j) \in B\backslash\mathcal{V}, t \in \mathcal{T}, \tag{3.16}$$

$$\sum_{h:(h,i)\in B}\boldsymbol{P}^{BR}_{hi,t} + \sum_{g:g=i,g\in\mathcal{G}}\boldsymbol{P}^{\phi}_{g,t} = \sum_{j:(i,j)\in B}\boldsymbol{P}^{BR}_{ij,t} + \sum_{l:l=i,l\in\mathcal{L}}\boldsymbol{P}^{L}_{l,t}, \tag{3.17}$$

$$\sum_{h:(h,i)\in B}\boldsymbol{Q}^{BR}_{hi,t} + \sum_{g:g=i,g\in\mathcal{G}}\boldsymbol{Q}^{\phi}_{g,t} = \sum_{j:(i,j)\in B}\boldsymbol{Q}^{BR}_{ij,t} + \sum_{l:l=i,l\in\mathcal{L}}\boldsymbol{Q}^{L}_{l,t}, \tag{3.18}$$

$$(i,j) \in B, \phi \in \Phi_{\mathrm{ij}}, t \in \mathcal{T} \tag{3.19}$$

where $\boldsymbol{e}^{\phi}_{\boldsymbol{ij}} \in \mathbb{Z}^3_2$ is the vector with binary entries to represent the phases. For example, if a branch (i,j) is a single-phase line (e.g., phase B), then $\boldsymbol{e}^{\phi}_{\boldsymbol{ij}} = [0,1,0]^T$. $\boldsymbol{S}_{ij,t} = \boldsymbol{P}^{BR}_{ij,t} + j\boldsymbol{Q}^{BR}_{ij,t}$ is the vector of three-phase apparent power flowing from bus i to bus j through line (i,j) at step t. $(\boldsymbol{P}^{L}_{l,t} + j\boldsymbol{Q}^{L}_{l,t})$ is the three-phase load demand on node i at step t. Equations (3.15) and (3.16) ensure the constraints are only applied to energized lines except voltage regulators and transformers. M is a big number and should be selected carefully to ensure the constraints are valid only when the line is energized.

3.5.3.2 Load Models

Two load models were developed to accurately model the load demand during the black start process, namely, loads under cold load pickup (CLPU) conditions, and voltage-dependent loads modeled as a composite of constant impedance load, constant current load, and constant power (ZIP) load. In addition, the loads in distribution systems can be wye-connected or delta-connected. Delta-connected ZIP loads introduce nonlinear terms after being converted to wye-connected loads. A method that can convert delta-connected loads into linear wye-connected loads is introduced.

3.5.3.2.1 Load Model Under Cold Load Pick-up Conditions

CLPU refers to the phenomenon that when restoring a load after an extended outage, a much higher demand than the pre-outage level will be resulted initially, because thermostatically controlled loads (e.g., air conditioners, heaters, and refrigerators) will start at the same time [52].

Researchers have proposed various models to estimate the behavior of the loads under CLPU conditions [117, 118]. The performance of different modeling methods is compared in [117]. In this dissertation research, a linear CLPU model is proposed to model the behavior of load demands at different time steps, based on any given CLPU curve. Figure 3.4 shows a typical delayed exponential CLPU curve. The horizon axis represents the time steps, and the vertical axis represents the load demand presenting in the system. The outage occurs at t_0, and the load is restored at t_1. Due to the loss of diversity, the undiversified loading factor at t_1 is S_U. Then the load starts to gain diversity at t_2, and decreases exponentially. The post-outage diversified loading factor is S_D, which is

normally equal to the pre-outage loading level. It should be noted that the restoration time (t_1) for each load is not pre-determined.

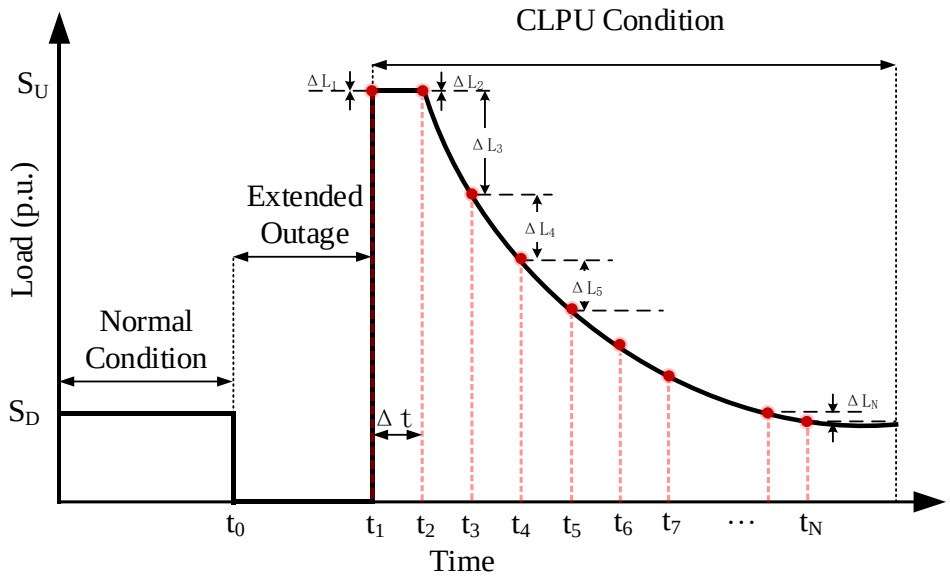

Figure 3.4. The load demand under CLPU conditions

The load demand under CLPU conditions can be formulated as [54]:

$$S_l = \begin{cases} 0, & t < \_T_0 \\ S_U, & T_0 \le t \le T_1 \\ S_D + (S_U - S_D)e^{-\alpha(t-T_1)}, & t > T_1 \end{cases} \tag{3.20}$$

In this dissertation research, we assumed the CLPU curve is equally sampled, and the sampling interval is Δt, which is the interval used for the BSR model. Assuming total N samples are collected from the CLPU curve of load l, denote $L_l(k)$ as the scale factor on the CLPU curve at k_{th} sample, and $\Delta L_l(k)$ as the difference between two scale factors at

k_{th} sample and $(k-1)_{th}$ sample. $\Delta L_l(k)$ can be replaced with $\Delta P_l(k)$, $\Delta Q_l(k)$, and $\Delta S_l(k)$ for formulating P_t^L, $Q_{l,t}^L$, and $S_{l,t}^L$, respectively. $\Delta L_l(k)$ can be calculated as:

$$\Delta L_l(k) = \begin{cases} 0, & k = 1 \\ L_l(k) - L_l(k-1), & 1 < k \leq N \end{cases} \tag{3.21}$$

Note that $\Delta L_l(1)$ is defined as the load difference between S_U and $L_l(1)$, which is 0. Equation (3.21) can be applied to any CLPU curve, and $\Delta L_l(k)$ should be calculated prior to running the BSR algorithm.

For a delayed exponential CLPU curve as shown in Figure 3.4, $L_l(k)$ can be calculated as [18]:

$$L_l(k) = (S^D + (S_l^U - S_l^D)e^{-\alpha_l \cdot C_{l,k}})u(C_{l,k}) + S^U\left(1 - u(C_{l,k})\right), 1 \leq k \leq N, \tag{3.22}$$

$$C_{l,k} = (k-1)\Delta t - D_l, \tag{3.23}$$

$$u(i) = \begin{cases} 1, & i > 0 \\ 0, & i \leq 0 \end{cases}, \tag{3.24}$$

where $C_{l,k}$ is the duration between the time step when load l starts gaining diversity and the k_{th} time step. Then, the three-phase CLPU load can be calculated in an accumulative manner, which could be formulated as:

$$\boldsymbol{P}_{l,t}^L = \boldsymbol{P}_l^L \odot \left(\boldsymbol{S}^U x_{l,t}^L - \sum_{k=1}^{t} \Delta \boldsymbol{P}_l(k) x_{l,t-k+1}^L\right), l \in \mathcal{L}, t \in \mathcal{T}, \tag{3.25}$$

$$\boldsymbol{Q}_{l,t}^L = \boldsymbol{Q}_l^L \odot \left(\boldsymbol{S}^U x_{l,t}^L - \sum_{k=1}^{t} \Delta \boldsymbol{Q}_l(k) x_{l,t-k+1}^L\right), l \in \mathcal{L}, t \in \mathcal{T}, \tag{3.26}$$

where $\boldsymbol{P}_l^L, \boldsymbol{Q}_l^L$ are pre-outage three-phase active and reactive power of load l; $\boldsymbol{S}_l^D, \boldsymbol{S}_l^U$ are vectors representing the diversified loading factors and undiversified loading factors for load l; $\Delta \boldsymbol{P}_l(k)$ and $\Delta \boldsymbol{Q}_l(k)$ are calculated using (3.22) – (3.24) for each phase.

3.5.3.2.2 ZIP Load Model

All the loads are assumed to be voltage dependent loads, which are normally modeled by the composite of constant impedance (Z), constant current (I) and constant power (P and Q). For each phase, the voltage dependent load demand ($P_l + jQ_l$) can be described as [111]:

$$\frac{P_l}{P_0} = a_p^Z \left(\frac{|V|}{|V_0|}\right)^2 + a_p^I \left(\frac{|V|}{|V_0|}\right) + a_p^P \tag{3.27}$$

$$\frac{Q_l}{Q_0} = a_q^Z \left(\frac{|V|}{|V_0|}\right)^2 + a_q^I \left(\frac{|V|}{|V_0|}\right) + a_q^P \tag{3.28}$$

where $P_0 + jQ_0$ is the load demand at the nominal voltage V_0; a_p^Z, a_p^I, a_p^P, a_q^Z, a_q^I, a_q^P are coefficients representing the percentage of constant impedance, current and power of active and reactive power of load l, and should satisfy [111]:

$$a_p^Z + a_p^I + a_p^P = 1, \tag{3.29}$$

$$a_q^Z + a_q^I + a_q^P = 1, \tag{3.30}$$

$$a_p^Z, a_{\mathrm{p}}^I, a_p^P, a_q^Z, a_q^I, a_q^P \in \mathbb{R}_{\geq 0} \tag{3.31}$$

Substituting $U_{l,t} = \left|V_{l,t}\right|^2$ into the above equations while considering the energization status of load at step t, the single-phase load demand at each step can be expressed by two nonlinear functions of $U_{l,t}$ and $x_{l,t}^L$:

$$P_{l,t} = x_{l,t}^{L}\left(\frac{a_p^Z P_0}{|V_0|^2}U_{l,t} + \frac{a_p^I P_0}{|V_0|}\sqrt{U_{l,t}} + a_p^P P_0\right) \tag{3.32}$$

$$Q_{l,\mathrm{t}} = x_{l,t}^{L}\left(\frac{a_q^Z Q_0}{|V_0|^2}U_{l,t} + \frac{a_q^I Q_0}{|V_0|}\sqrt{U_{l,t}} + a_q^P Q_0\right) \tag{3.33}$$

Considering $U_{l,t}$ varies in a small range which is constrained by the voltage magnitude constraint introduced below, the nonlinear term $\sqrt{U_{l,t}}$ can be linearized around $U_{l,t} = 1.0$ based on its Taylor series expansion:

$$\sqrt{U_{l,t}} \approx 0.5 + 0.5U_{l,t} \tag{3.34}$$

The nonlinear term $x_{l,t}^{L}U_l$ can be linearized by introducing an extra variable $y_{l,t} = x_{l,t}^{L}U_{l,t}$ and two extra inequality constraints:

$$V_{min}^2 x_{l,t}^{L} \le y_{l,t} \le V_{max}^2 x_{l,t}^{L} \tag{3.35}$$

$$V_{min}^2\left(1 - x_{l,t}^{L}\right) \le U_{l,t} - y_{l,t} \le V_{max}^2\left(1 - x_{l,t}^{L}\right) \tag{3.36}$$

Substituting (3.34), (3.35), and (3.36) into (3.32) and (3.33), the three-phase wye-connected load at step t can be described as:

$$\boldsymbol{P}_{l,t}^{L} = \left(\frac{a_p^Z}{|V_0|^2}\boldsymbol{P}_0 + 0.5\frac{a_p^I}{|V_0|}\boldsymbol{P}_0\right)\odot\boldsymbol{y}_{l,t} + x_{l,t}^{L}\left(0.5\frac{a_p^I}{|V_0|}\boldsymbol{P}_0 + a_p^P\boldsymbol{P}_0\right) \tag{3.37}$$

$$\boldsymbol{Q}_{l,t}^{L} = \left(\frac{a_q^Z}{|V_0|^2}\boldsymbol{Q}_0 + 0.5\frac{a_q^I}{|V_0|}\boldsymbol{Q}_0\right)\odot\boldsymbol{y}_{l,t} + x_{l,t}^{L}\left(0.5\frac{a_q^I}{|V_0|}\boldsymbol{Q}_0 + a_q^P\boldsymbol{Q}_0\right) \tag{3.38}$$

$$\boldsymbol{0} \le \boldsymbol{y}_{l,t} \le x_{l,t}^{L}\boldsymbol{U}_{max} \tag{3.39}$$

$$\left(1 - x_{l,t}^{L}\right)\boldsymbol{U}^{min} \le \boldsymbol{U}_{l,t} - \boldsymbol{y}_{l,t} \le \left(1 - x_{l,t}^{L}\right)\boldsymbol{U}^{max} \tag{3.40}$$

where $\boldsymbol{y}_{l,t} = x_{l,t}^{L}\left[U_{l,t}^{a}, U_{l,t}^{b}, U_{l,t}^{c}\right]^{T}$. $\boldsymbol{U}^{min}$ and $\boldsymbol{U}^{max}$ are set to $0.95^2\ p.u.$ and $1.05^2\ p.u.$, respectively, for each presenting phase.

3.5.3.2.3 Delta-Connected Load

For delta-connected loads as shown in Figure 3.5, the approximated wye-connected model can be derived by assuming (3.13) still holds. For the approximated load on phase A, we have:

$$S_a^L = V_a I_a^* = V_a\left(\frac{S_{ab}^L}{V_{ab}} - \frac{S_{ca}^L}{V_{ca}}\right) \approx \frac{e^{-j\pi/6}}{\sqrt{3}} S_{ab}^L - \frac{e^{-j5\pi/6}}{\sqrt{3}} S_{ca}^L \tag{3.41}$$

Similarly, we can derive S_b^L and S_c^L and derive the approximated wye-connected load in matrix form:

$$\begin{bmatrix} S_a^L \\ S_b^L \\ S_c^L \end{bmatrix} = \frac{1}{\sqrt{3}} \begin{bmatrix} e^{-\frac{j\pi}{6}} & 0 & -e^{-\frac{j5\pi}{6}} \\ -e^{-\frac{j5\pi}{6}} & e^{-\frac{j\pi}{6}} & 0 \\ 0 & -e^{-\frac{j5\pi}{6}} & -e^{-\frac{j\pi}{6}} \end{bmatrix} \begin{bmatrix} S_{ab}^L \\ S_{bc}^L \\ S_{ca}^L \end{bmatrix} \tag{3.42}$$

Note the same ZIP parameters are applied for $S_{ab}^L, S_{bc}^L, S_{ca}^L$. Single-phase and two-phase loads in both wye-connection and delta connection can be modeled in the similar way by setting the variables associated with the missing phase(s) to zero. Wye-connected and delta-connected capacitor banks are modeled as constant impedance loads and share the same model as ZIP load.

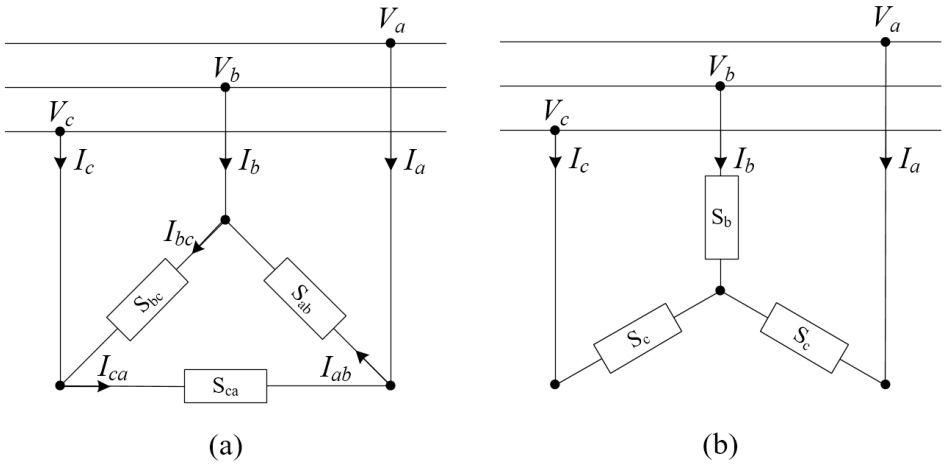

Figure 3.5. The approximated wye-connected model of a delta-connected load. (a) delta-connected load, (b) approximated wye-connected load

3.5.3.3 Voltage Regulator and Transformer Model

A single-phase voltage regulator can be modeled as an ideal transformer connected with an equivalent line representing the leakage impedance, as shown in Figure 3.6 [119]. A three-phase voltage regulator can be modeled by connecting three single-phase voltage regulators. Transformers share the same model as voltage regulators but with fixed ratios. In this dissertation research, all of the regulators were modeled as wye-connected type B regulators [111]. The relationship between the voltage magnitudes on both sides for a three-phase voltage regulator, with i as the primary side and j as the secondary side, can be expressed as:

$$-M\left(1-x_{ij,t}^{BR}\right)\boldsymbol{e}_{\boldsymbol{ij}}^{\boldsymbol{\phi}} \leq \boldsymbol{a}^2 \odot \boldsymbol{U}_j - \boldsymbol{U}_i \leq M\left(1-x_{ij,t}^{BR}\right)\boldsymbol{e}_{\boldsymbol{ij}}^{\boldsymbol{\phi}}, (i,j) \in \mathcal{V}, t \in \mathcal{T}, \quad (3.43)$$

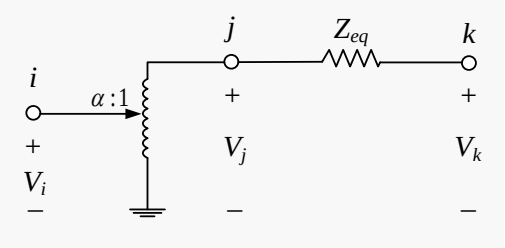

(a)

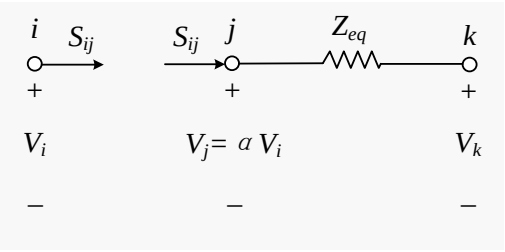

(b)

Figure 3.6. Voltage regulator model. (a): Original voltage regulator model. (b): equivalent model

where $\boldsymbol{a} \in \mathbb{R}^{3\times 1}$ is the vector representing the ratio between secondary winding and primary winding for each phase. *M* is a large number that should be selected carefully. The regulator is assumed to be adjustable from −16 step to +16 step, in order to regulate the voltage from +10% to −10%, with 5/8% per step [111]. Denoting $\boldsymbol{n^{tap}} \in \{-16, -15, \dots, +15, +16\}$ as the tap position for each phase, the ratio is calculated by:

$$\boldsymbol{a} = 1 + 0.00625\boldsymbol{n^{tap}}, \tag{3.44}$$

$$-16 \leq \boldsymbol{n^{tap}} \leq 16. \tag{3.45}$$

Tap position can be either fixed or controllable. For fixed tap positions, voltage regulators and transformers can be modeled by equations (3.43)–(3.45). For variable tap positions, a mixed-integer linear model proposed in [120] can be integrated with the BSR formulation for determining tap positions at each step. Unfortunately, in order to precisely

model the discrete tap variables, the formulation in [120] introduces too many constraints, hence becoming intractable for systems with a large number of voltage regulators. An alternative formulation is proposed in [119, 121, 122] to relax the discrete tap position variables to continuous variables, then the tap position is determined by rounding up to the nearest integer values. This relaxation yields acceptable performance, without introducing over-complicated constraints.

A challenge appears when the tap position is defined as a variable in equation (3.43), in which the term "$\boldsymbol{\alpha}^2 \odot \boldsymbol{U}_j$" becomes nonlinear and needs to be linearized. Denote $\boldsymbol{\beta}_{r,t} \coloneqq \boldsymbol{\alpha}^2$ as the decision variables for regulator $r \in \mathcal{R}$ at time step t. Then $\boldsymbol{\alpha}^2 \odot \boldsymbol{U}_j$ becomes $\boldsymbol{\beta}_{r,t} \odot \boldsymbol{U}_j$. $\boldsymbol{\beta}_{r,t}$ is changing within the range associated with the minimal tap position and the maximum tap position; i.e., between 0.81 and 1.21. Similarly, $\boldsymbol{U}_j$ is maintained between 0.9025 (V_{min}^2) and 1.1025 (V_{max}^2). The narrow ranges for $\boldsymbol{\beta}_{r,t}$ and $\boldsymbol{U}_j$ make the surface of their product flat, which can be approximated by a plane in the three-dimensional space. Then the term $\boldsymbol{\beta}_{r,t} \odot \boldsymbol{U}_j$ can be linearized by a linear function of $\boldsymbol{\beta}_{r,t}$ and $\boldsymbol{U}_j$:

$$\boldsymbol{\beta}_{r,t} \odot \boldsymbol{U}_j \approx \boldsymbol{a} \odot \boldsymbol{\beta}_{r,t} + \boldsymbol{b} \odot \boldsymbol{U}_j + \boldsymbol{c} \tag{3.46}$$

where $\boldsymbol{a}$, $\boldsymbol{b}$, and $\boldsymbol{c} \in \mathbb{R}^{3\times 1}$ are denoted as the coefficients for the linear model. They can be determined by solving the following least square method:

$$\max \quad \left\| \left(\boldsymbol{\beta}_{r,t} \odot \boldsymbol{U}_j\right) - \left(\boldsymbol{a} \odot \boldsymbol{\beta}_{r,t} + \boldsymbol{b} \odot \boldsymbol{U}_j + \boldsymbol{c}\right) \right\| \tag{3.47}$$

$$s.t. \quad \left(1 + 0.00625\boldsymbol{n}_{\boldsymbol{min}}^{\boldsymbol{tap}}\right)^2 \leq \boldsymbol{\beta}_{r,t} \leq \left(1 + 0.00625\boldsymbol{n}_{\boldsymbol{max}}^{\boldsymbol{tap}}\right)^2 \tag{3.48}$$

$$\boldsymbol{V}_{min}^{2} \leq \boldsymbol{U}_{j} \leq \boldsymbol{V}_{max}^{2} \tag{3.49}$$

where $\boldsymbol{n}_{\boldsymbol{min}}^{\boldsymbol{tap}}$ and $\boldsymbol{n}_{\boldsymbol{max}}^{\boldsymbol{tap}}$ are minimum and maximum tap position, respectively. And $\boldsymbol{V}_{min}^{2}$ and $\boldsymbol{V}_{max}^{2}$ are the square of minimum and maximum permissive voltage, respectively.

Then the linearized constraints incorporating voltage regulator variables becomes:

$$-Mx_{ij,t}^{BR} \leq \boldsymbol{\beta}_{r,t} - \boldsymbol{\beta}_{r,0} \leq Mx_{ij,t}^{BR} \tag{3.50}$$

$$-M\left(1 - x_{ij,t}^{BR}\right)\boldsymbol{e}_{\boldsymbol{ij}}^{\boldsymbol{\phi}} \leq \boldsymbol{a} \odot \boldsymbol{\beta}_{r,t} + \boldsymbol{b} \odot \boldsymbol{U}_{j} + \boldsymbol{c} - \boldsymbol{U}_{i} \leq M\left(1 - x_{ij,t}^{BR}\right)\boldsymbol{e}_{\boldsymbol{ij}}^{\boldsymbol{\phi}},$$

$$r \in \mathcal{R}, (i,j) \in \mathcal{V}, t \in \mathcal{T}. \tag{3.51}$$

Constraints (3.48) – (3.51) guarantee the voltage regulators are changing within permissive ratio ranges. Constraint (3.50) requires the tap position should be in the initial position, before the regulator is energized. Additional constraints apply, if we want to constraint the duration between any two consecutive operations. Given $\boldsymbol{n}_{\boldsymbol{min}}^{\boldsymbol{tap}} = [-16, -16, -16]^{T}$, $\boldsymbol{n}_{\boldsymbol{max}}^{\boldsymbol{tap}} = [+16, +16, +16]^{T}$, $\boldsymbol{V}_{min}^{2} = [0.95^{2}, 0.95^{2}, 0.95^{2}]^{T}$, $\boldsymbol{V}_{max}^{2} = [1.05^{2}, 1.05^{2}, 1.05^{2}]^{T}$, the coefficients are: $\boldsymbol{a} = [1,1,1]^{T}$, $\boldsymbol{b} = [1.01,1.01,1.01]^{T}$, $\boldsymbol{c} = [-1.01, -1.01, -1.01]^{T}$.

3.5.3.4 Connectivity Constraints for Components

During a black start process, most components must be energized from a de-energized condition. The binary variables defined for these components (e.g., DGs, loads, lines, and nodes) represent the energization status of each component at each time step. In this subsection, the connectivity of these components is mathematically modeled as a set of equality and inequality constraints. The connectivity constraints describe the physical

connections of each component with the system. For example, as introduced in Section 2, a non-black start DG can only generate power after being started by an external power. Similarly, a load can only be energized when its terminal node is energized.

3.5.3.4.1 Connectivity Constraints for DGs

Different rules representing the physical connections apply to different types of DGs (e.g., black start DGs and non-black start dispatchable DGs). TABLE 3.3 lists the inter-temporal constraints among the bus status at time step t and the DG status at time step $(t-1)$ and t. "—" means this situation is not existing. These rules include:

1) Black start DGs start at the first time step.

2) If a non-black start DG is equipped with a switch, then it can start only when the terminal bus is energized

3) If a non-black start DG is directly connected to the terminal bus, then it will immediately start when the terminal bus is energized.

4) If a DG cannot participate in the restoration, then it should not start.

TABLE 3.3. CONNECTIVITY CONSTRAINTS FOR DGS

Bus Status at t	DG Status at $(t-1)$	Black Start DG	DG with switch	DG without switch
$s_{g,t}^{N}$	$x_{g,t-1}^{G}$	$g \in \mathcal{G}^{S}$	$g \in \mathcal{G} \backslash (\mathcal{G}^{S} \cup \mathcal{G}^{F})$	$g \in \mathcal{G}^{S} \backslash \mathcal{G}^{F}$
0	0	—	0	0
1	0	—	0 or 1	—
0	1	—	—	—
1	1	1	1	1

These rules can be mathematically formulated by the following constraints:

$$x_{g,t}^{G} \le s_{g,t}^{N}, \quad g \in \mathcal{G}\backslash(\mathcal{G}^{S} \cup \mathcal{G}^{F}), t \in \mathcal{T}, \tag{3.52}$$

$$x_{g,t}^{G} - x_{g,t-1}^{G} \ge 0, \ g \in \mathcal{G}, t \in \mathcal{T}, t > 1. \tag{3.53}$$

$$x_{g,t}^{G} = 1, g \in \mathcal{G}^{S}\backslash\mathcal{G}^{F}, t \in \mathcal{T} \tag{3.54}$$

Equation (3.52) ensures a dispatchable DG without black start capability should be able to start only when it connects to an energized node. Equation (3.53) guarantees that once a DG is started, it cannot be tripped in the following steps. Equation (3.54) requires the substation node and the black-start DGs should be started at the first step. The capability of black start DGs to regulator voltage can be formulated as:

$$U_{g,t} = 1.0, \quad g \in \mathcal{G}^{S}\backslash\mathcal{G}^{F}, \ t \in \mathcal{T}. \tag{3.55}$$

3.5.3.4.2 Connectivity Constraints for ESSs

Similarly, the connectivity constraints for ESSs can be formulated as:

$$x_{e,t}^{ESS\_CH} + x_{e,t}^{ESS\_DISCH} \le s_{e,t}^{N} \qquad \text{e} \in E\backslash E^{F}, \ t \in \mathcal{T}. \tag{3.56}$$

Equation (3.56) ensures that an ESS can only charge and discharge power when its terminal node is energized.

3.5.3.4.3 Connectivity Constraints for Loads

As shown in TABLE 3.4, the connectivity constraints for loads include:

1) Loads can only be restored when terminal buses are energized.

2) A switchable load will be restored immediately when the terminal bus is energized.

3) A load should not be shed once being restored.

TABLE 3.4. CONNECTIVITY CONSTRAINTS FOR LOADS

Bus Status	Load Status at $(t-1)$	Switchable Load	Non-switchable Load
$s_{l,t}^N$	$x_{l,t-1}^L$	$x_{l,t}^L,\ l \in \mathcal{L}^S \backslash \mathcal{L}^F$	$x_{l,t}^L, l \in \mathcal{L} \backslash (\mathcal{L}^S \cup \mathcal{L}^F)$
0	0	0	0
1	0	0 or 1	1
0	1	—	—
1	1	1	1

The connectivity constraints can be formulated as:

$$x_{l,t}^L \leq s_{l,t}^N,\ l \in \mathcal{L}^S \backslash \mathcal{L}^F, t \in \mathcal{T}. \tag{3.57}$$

$$x_{l,t}^L = s_{l,t}^N,\ l \in \mathcal{L} \backslash (\mathcal{L}^S \cup \mathcal{L}^F), t \in \mathcal{T}. \tag{3.58}$$

$$x_{l,t}^L - x_{l,t-1}^L \geq 0,\ l \in \mathcal{L}^S, t \in \mathcal{T}, t > 1. \tag{3.59}$$

Equation (3.57) requires that a switchable load can only be energized when it connects to an energized node. Equation (3.58) ensures a non-switchable load will be energized immediately when it connects to an energized node. Equations (3.59) requires that a load is restored, it cannot be tripped again. Furthermore, an optional constraint can be used to ensure that a set of loads (e.g., critical loads) can be restored prior to another set of loads:

$$x_{nl,t}^L \leq x_{cl,t}^L,\ \ cl, nl \in \mathcal{L} \backslash \mathcal{L}^F, t \in \mathcal{T}, \tag{3.60}$$

where the subscript cl represents a particular critical load, and nl represents a particular non-critical load. Equation (3.60) can be used for two or more loads that must be restored at a given sequence. Indeed, we can use (3.60) to require that all the non-critical loads must be restored after all the critical loads are restored. Using (3.60) may generate low-

quality solutions. For example, if restoring a critical load will violate some constraints, it will further prevent all the non-critical loads from being restored.

3.5.3.4.4 Connectivity Constraints for Lines

Transmission lines in the system can be categorized into three types according to the controllability, namely, switchable lines equipped with remotely controllable switches, non-switchable lines that directly connect two terminal buses, and damaged lines that are assumed to be permanently opened before being repaired. Connectivity constraints are defined for lines, as shown in TABLE 3.5, including:

1) A switchable line can only be closed when one of the terminal buses is energized.

2) Closing a non-switchable line will immediately energize the terminal buses.

3) A line cannot be tripped after being energized.

TABLE 3.5. CONNECTIVITY CONSTRAINTS FOR LINES

Branch Status	Bus Status at $(t-1)$		Bus Status at t		Switchable Lines	Non-switchable Lines
$x_{ij,t-1}^{BR}$	$s_{i,t-1}^{N}$	$s_{j,t-1}^{N}$	$s_{i,t}^{N}$	$s_{j,t}^{N}$	$(i,j) \in \mathcal{B}^{S} \backslash \mathcal{B}^{F}$	$(i,j) \in \mathcal{B} \backslash (\mathcal{B}^{S} \cup \mathcal{B}^{F})$
0	0	0	0	0	0	0
0	0	0	0	1	0	—
0	0	0	1	0	0	—
0	0	0	1	1	0	1
0	0	1	0	1	0	—
0	0	1	1	1	0 or 1	1
0	1	0	1	0	0	—
0	1	0	1	1	0 or 1	1
0	1	1	1	1	0	1
1	1	1	1	1	1	1

These rules can be mathematically formulated by the following constraints:

$$x_{ij,t}^{BR} \le s_{i,t}^{N}, \quad (i,j) \in \mathcal{B}^{S} \backslash \mathcal{B}^{F}, t \in \mathcal{T}, \tag{3.61}$$

$$x_{ij,t}^{BR} \le s_{j,t}^{N}, \quad (i,j) \in \mathcal{B}^{S} \backslash \mathcal{B}^{F}, t \in \mathcal{T}, \tag{3.62}$$

$$x_{ij,t}^{BR} = s_{i,t}^{N}, \quad (i,j) \in \mathcal{B} \backslash (\mathcal{B}^{S} \cup \mathcal{B}^{F}), t \in \mathcal{T}, \tag{3.63}$$

$$x_{ij,t}^{BR} = s_{j,t}^{N}, \quad (i,j) \in \mathcal{B} \backslash (\mathcal{B}^{S} \cup \mathcal{B}^{F}), t \in \mathcal{T}, \tag{3.64}$$

$$x_{ij,t}^{BR} - x_{ij,t-1}^{BR} \ge 0, \ (i,j) \in \mathcal{B}^{S} \backslash \mathcal{B}^{F}, t \in \mathcal{T}, t > 1. \tag{3.65}$$

Equations (3.61) and (3.62) require that if a switchable line is energized, both end nodes must be energized. Equations (3.63) and (3.64) guarantee that a non-switchable line will be energized immediately when one of the end nodes is energized. Equation (3.65) implies that a line cannot be tripped after being energized.

3.5.3.5 Initial Condition Constraints

Initial condition constraints describe the energization status of damaged or non-participating components. In addition, since the system is fully de-energized before performing black start restoration, the initial status, which is represented by the energization status at the first step of each component, should be specified. In summary, the aforementioned operating conditions can be described as:

1) All the lines are opened at the first step:

$$x_{ij,t}^{BR} = 0, \ (i,j) \in \mathcal{B}^{S} \backslash \mathcal{B}^{F}, t = 1. \tag{3.66}$$

2) A DG or an ESS that cannot participate in the restoration should keep being de-energized:

$$x_{g,t}^{G} = 0, \quad g \in \mathcal{G}^{F}, t \in \mathcal{T}, \tag{3.67}$$

$$x_{e,t}^{ESS\_C} + x_{e,t}^{ESS\_D} = 0, \ \ e \in \mathcal{E}^{F}, t \in \mathcal{T}. \tag{3.68}$$

3) A load that cannot be energized should keep being de-energized:

$$x_{l,t}^{L} = 0, \ l \in \mathcal{L}^{F}, t \in \mathcal{T} \tag{3.69}$$

4) A disconnected or damaged line that cannot perform reclosing should keep being de-energized:

$$x_{ij,t}^{BR} = 0, \quad (i,j) \in \mathcal{B}^{F}, t \in \mathcal{T} \tag{3.70}$$

5) A damaged node should be kept de-energized:

$$s_{i,t}^{N} = 0, \quad i \in \mathcal{N}^{F}, t \in \mathcal{T} \tag{3.71}$$

3.5.4 System Operational Constraints

To ensure the feasibility of the restoration solutions, various operational constraints must be satisfied throughout the restoration process. IEEE Standard 1547.4-2011 requires that operating microgrids in island mode should be in accordance with ANSI/NEMA C84.1-2006 if part of the system is included in the isolated microgrid [75]. Maintaining the voltage and frequency of the energized system is critical since ANSI/NEMA C84.1-2006 requires DGs to disconnect from the network, if abnormal voltage and frequency conditions are detected. The clearing time for DGs is specified in IEEE Standard 1547.4-2011, as shown in TABLE 3.6 and TABLE 3.7 [75]. It can be observed that once the abnormal voltage or frequency is detected, DGs must be disconnected within a short time duration. Therefore, both voltage and frequency should be well maintained.

TABLE 3.6. INTERCONNECTION SYSTEM RESPONSE TO ABNORMAL VOLTAGES [75]

Voltage range (% of base voltage)	Clearing time (s)
$V < 50$	0.16
$50 \leq V < 88$	2.00
$110 < V < 120$	1.00
$V \geq 120$	0.16

TABLE 3.7. INTERCONNECTION SYSTEM RESPONSE TO ABNORMAL FREQUENCIES [75]

DG Size	Frequency range (Hz)	Clearing time (s)
$\leq 30kW$	>60.5	0.16
	<59.3	0.16
$> 30kW$	>60.5	0.16
	<{59.8 – 57.0} (adjustable)	Adjustable 0.16 to 300
	<57.0	0.16

Also, the thermal constraints on transmission lines and transformers must be considered. The operational constraints can be formulated as:

$$V^{min} \leq |V_{i,t}| \leq V^{max}, \tag{3.72}$$

$$0 \leq |I_{ij,t}| \leq I_{ij}^{max}, \tag{3.73}$$

$$0 \leq |S_{ij,t}| \leq S_{ij}^{max}, \tag{3.74}$$

$$-\Delta f^{max} < \Delta f < \Delta f^{max}, \tag{3.75}$$

where V^{min} and V^{max} are minimum and maximum permissive voltage limit for each phase of any energized nodes. $|V_i|$ is the voltage magnitude of node i, which is energized at step t. I_{ij}^{max} are maximum permissive current flowing through the line between node i and j. $|I_{ij,t}|$ is the current magnitude through the line between node i and j, at step t. S_{ij}^{max} are maximum permissive apparent power flowing through the transformer between node

i and j. $|S_{ij,t}|$ is the apparent power going through the transformer between node i and j, at step t. Δf^{max} is the maximum permissive frequency change during the restoration process. Δf is the frequency derivation from the nominal value (60Hz). Equation (3.72) – (3.75) requires the voltage, line current, transformer capacity, and frequency to be maintained within permissive ranges, so as to avoid tripping DGs and damaging components. The following subsections present the linearized models of transformer and line capacity constraints and voltage magnitude constraint, and a model to approximately limit the amount of step load to avoid excessive frequency drop.

3.5.4.1 Transformer and Line Capacity Constraints

Transformers and transmission lines are allowed to overload at the expense of causing loss of life during emergencies [54]. In this dissertation research, the maximum permissive kVA capacity for a transformer is determined by its rated kVA capacity, and the maximum permissive kVA capacity for a line is determined by its ampacity at rated voltage. For each phase, the loading on the transformers and lines should not exceed the maximum permissive capacity:

$$\left(P_{ij,t}^{BR}\right)^2 + \left(Q_{ij,t}^{BR}\right)^2 \leq \left(S_{ij}^{max}\right)^2 \ (i,j) \in \mathcal{B}, t \in \mathcal{T} \tag{3.76}$$

Note that the above constraint is quadratic. A polygon is used to estimate the quadratic constraints as introduced in [123]. The radius of the polygon S_{ij} is selected as

$$S_{ij} = S_{ij}^{\max} \sqrt{(2\pi/n)/\sin(2\pi/n)}, (i,j) \in \mathcal{B} \tag{3.77}$$

where n is the number of sides of the polygon used for linearization. As shown in Figure 3.7, the estimated area covered most of the original area, plus some extra infeasible sections. However, these small sections, in most cases, are rarely reached. In emerging conditions, some lines can be allowed to be overloaded for a duration of time. Six-side polygon can generate a better estimation than four-side polygon. The original area can be perfected approached using infinite-side polygon. However, more sides used, more constraints will be introduced, hence increase the complexity for solving.

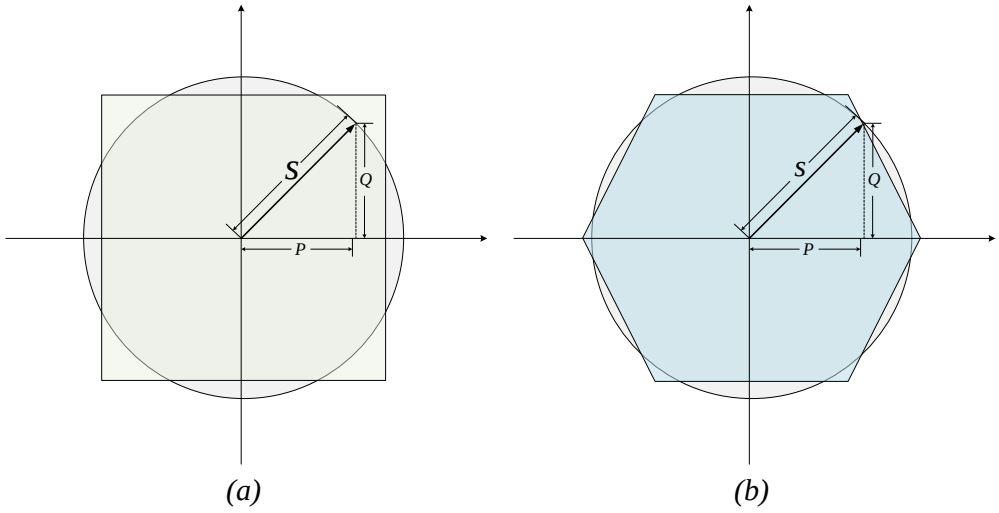

Figure 3.7. Using polygon to estimate the original area. (a): Four-side polygon. (b): Six-side polygon

For each line $(i,j) \in \mathcal{B}$ at each step $t \in \mathcal{T}$, denoting $\boldsymbol{S}_{ij}$ as the vector representing the line kVA capacity of each phase using (3.77), the linear constraints when $n = 6$ can be formulated as:

$$-\sqrt{3}\left(\boldsymbol{P}_{ij,t}^{BR} + \boldsymbol{S}_{ij}\right) \leq \boldsymbol{Q}_{ij,t}^{BR} \leq -\sqrt{3}\left(\boldsymbol{P}_{ij,t}^{BR} - \boldsymbol{S}_{ij}\right), \tag{3.78}$$

$$-\sqrt{3}/2 \cdot \boldsymbol{S}_{ij} \leq \boldsymbol{Q}_{ij,t}^{BR} \leq \sqrt{3}/2 \cdot \boldsymbol{S}_{ij}, \tag{3.79}$$

$$\sqrt{3}\left(\boldsymbol{P}_{ij,t}^{BR} - \boldsymbol{S}_{ij}\right) \leq \boldsymbol{Q}_{ij,t}^{BR} \leq \sqrt{3}\left(\boldsymbol{P}_{ij,t}^{BR} + \boldsymbol{S}_{ij}\right). \tag{3.80}$$

Equations (3.81) and (3.82) ensure the power flowing through each phase is zero if this line is not energized.

$$-M \cdot x_{ij,t}^{BR} \cdot \boldsymbol{e}_{\boldsymbol{ij}}^{\boldsymbol{\phi}} \leq \boldsymbol{P}_{ij,t}^{BR} \leq M \cdot x_{ij,t}^{BR} \cdot \boldsymbol{e}_{\boldsymbol{ij}}^{\boldsymbol{\phi}}, \tag{3.81}$$

$$-M \cdot x_{ij,t}^{BR} \cdot \boldsymbol{e}_{\boldsymbol{ij}}^{\boldsymbol{\phi}} \leq \boldsymbol{Q}_{ij,t}^{BR} \leq M \cdot x_{ij,t}^{BR} \cdot \boldsymbol{e}_{\boldsymbol{ij}}^{\boldsymbol{\phi}}, \quad (i,j) \in \mathcal{B}, t \in \mathcal{T}, \tag{3.82}$$

3.5.4.2 Voltage Limit Constraints

The voltage magnitude of each node should be maintained within the acceptable ranges during the restoration process. Note $\boldsymbol{U}_{i,t}$ is defined as the square of the voltage magnitude in the power flow model. Equation (3.72) can be re-formulated as:

$$s_{i,t}^{N} \cdot (\boldsymbol{V}_i^{\min})^2 \leq \boldsymbol{U}_{i,t} \leq s_{i,t}^{N} \cdot (\boldsymbol{V}_i^{\max})^2, \quad i \in \mathcal{N}, t \in \mathcal{T}, \tag{3.83}$$

where $\boldsymbol{V}_i^{min}$ and $\boldsymbol{V}_i^{max}$ are vectors representing the minimum and maximum voltage magnitudes.

3.5.4.3 Maximum Load Step Constraints

Transient stability is a critical concern for restoring low-inertia microgrids. This is because energizing a group of loads can be seen as a type of disturbances applied to the system. Therefore, changing load demands and renewable outputs may jeopardize the system transient stability. It is known that different types of DERs have different operational requirements. Several operational constraints have been considered in the

MILP formulation, for example, ramp rate constraint, capacity constraint, and DG unbalance current constraint. Since the system dynamic models are difficult to be directly incorporated into the proposed BSR optimization model, the maximum step load constraints are considered in the BSR model to avoid restoring too much load at a single time step. Frequency response rate (FRR) has been defined as the frequency dip subjected to a sudden load pickup [124]. FRRs are developed for typical prime movers and used in the initial state of power system restoration. ΔF is used to specify the change of frequency dip when a sudden load ΔL (defined as the percentage of a generator's rated capacity) is restored. In other work [85, 88, 125], ΔL is set to 5%, which could cause a frequency dip of about 0.5 Hz. Here the FRR factor is set to 5% for all DGs to avoid large frequency deviations. That is, the sudden incremental amount of restored loads at each step should be smaller or equal to the maximum permissive load step change, which is 5% of the total rated capacity of all energized DGs. If multiple black start DGs exist in the system, multiple isolated microgrids will be formed. Then, the incremental loading on each DG at each step should be smaller than the maximum permissive load step:

$$\sum_{\phi\in\{a,b,c\}} \boldsymbol{P}_{g,t}^{\phi} - \sum_{\phi\in\{a,b,c\}} \boldsymbol{P}_{g,t-1}^{\phi} \leq \gamma \cdot P_g^{Cap},\ g \in \mathcal{G}, t \in \mathcal{T}, t > 1, \quad (3.84)$$

where P_g^{Cap} is the rated capacity of DG g. γ is the FRR factor. Note that γ should be carefully approximated for each DG. In this dissertation research, it is assumed that the DGs, transformers, lines, and associated protective relays can withstand the transient inrush current induced by the cold load pickup issues.

3.5.5 DG Operational Constraints

3.5.5.1 DG Current Unbalance Constraints

Three-phase DGs operating under unbalanced conditions should satisfy the current unbalance constraint to avoid overheating [126]. A current unbalance factor (CUF) is defined as the ratio of negative sequence current to positive sequence current at the first harmonic [126]:

$$CUF = \frac{\left|I_2^{(1)}\right|}{\left|I_1^{(1)}\right|} \tag{3.85}$$

$$I_2^{(1)} = (I^a + \alpha^2 I^b + \alpha I^c)/3 \tag{3.86}$$

$$I_1^{(1)} = (I^a + \alpha I^b + \alpha^2 I^c)/3 \tag{3.87}$$

where $\alpha = e^{j2\pi/3}$. Substituting (3.11) into (3.85), (3.86), and (3.87), and assuming (3.13) holds, we have [127]:

$$CUF \approx \frac{\left|S^a+\alpha^2 S^b+\alpha S^c\right|}{\left|S^a+S^b+S^c\right|} = \frac{\left|P^N+jQ^N\right|}{\left|P^P+jQ^P\right|} \tag{3.88}$$

A simple function introduced in [128] is used to approximate (3.88). Let $S_{g,t}^a + \alpha^2 S_{g,t}^b + \alpha S_{g,t}^c = P_{g,t}^N + jQ_{g,t}^N$, $S_{g,t}^a + S_{g,t}^b + S_{g,t}^c = P_{g,t}^P + jQ_{g,t}^P$, we have:

$$\frac{\left|P_{g,t}^N+jQ_{g,t}^N\right|}{\left|P_{g,t}^P+jQ_{g,t}^P\right|} \approx \frac{0.9375\max\left(\left|P_{g,t}^N\right|,\left|Q_{g,t}^N\right|\right)+0.4688\min\left(\left|P_{g,t}^N\right|,\left|Q_{g,t}^N\right|\right)}{0.9375\max\left(\left|P_{g,t}^P\right|,\left|Q_{g,t}^P\right|\right)+0.4688\min\left(\left|P_{g,t}^P\right|,\left|Q_{g,t}^P\right|\right)} \tag{3.89}$$

where:

$$P_{g,t}^N = P_{g,t}^a + \frac{\sqrt{3}}{2}Q_{g,t}^b - 0.5P_{g,t}^b - \frac{\sqrt{3}}{2}Q_{g,t}^c - 0.5P_{g,t}^c \tag{3.90}$$

$$Q_{g,t}^{N} = Q_{g,t}^{a} + \frac{\sqrt{3}}{2}P_{g,t}^{c} - 0.5Q_{g,t}^{b} - \frac{\sqrt{3}}{2}P_{g,t}^{b} - 0.5Q_{g,t}^{c} \tag{3.91}$$

$$P_{g,t}^{P} = P_{g,t}^{a} + P_{g,t}^{b} + P_{g,t}^{c} \tag{3.92}$$

$$Q_{g,t}^{P} = Q_{g,t}^{a} + Q_{g,t}^{b} + Q_{g,t}^{c} \tag{3.93}$$

$$P_{g,t}^{a}, P_{g,t}^{b}, P_{g,t}^{c}, Q_{g,t}^{a}, Q_{g,t}^{b}, Q_{g,t}^{c} \in \mathbb{R} \tag{3.94}$$

Several binary and continuous variables are introduced to linearize the nonlinear terms (e.g., $|P^N|, \max(|P^N|, |Q^N|)$. Define $y_{g,t}^{PN}, y_{g,t}^{QN}, y_{g,t}^{PP}, y_{g,t}^{QP} \in \mathbb{R}^{T \times n_g}$, and $d_{g,t}^{PN1}$, $d_{g,t}^{PN2}, d_{g,t}^{QN1}, d_{g,t}^{QN2}, d_{g,t}^{QP1}$, $d_{g,t}^{QP2} \in \mathbb{Z}_2^{T \times n_g}$, then $\left|P_{g,t}^{N}\right|$, $\left|Q_{g,t}^{N}\right|$, $\left|P_{g,t}^{P}\right|$ and $\left|Q_{g,t}^{P}\right|$ can be linearized by:

$$0 \le y_{g,t}^{PN} - P_{g,t}^{N} \le U_g^{max} d_{g,t}^{PN1}, \tag{3.95}$$

$$0 \le y_{g,t}^{PN} + P_{g,t}^{N} \le U_g^{max} d_{g,t}^{PN2}, \tag{3.96}$$

$$d_{g,t}^{PN1} + d_{g,t}^{PN2} = 1, \tag{3.97}$$

$$0 \le y_{g,t}^{QN} - Q_{g,t}^{N} \le U_g^{max} d_{g,t}^{QN1}, \tag{3.98}$$

$$0 \le y_{g,t}^{QN} + Q_{g,t}^{N} \le U_g^{max} d_{g,t}^{QN2}, \tag{3.99}$$

$$d_{g,t}^{QN1} + d_{g,t}^{QN2} = 1, \tag{3.100}$$

$$y_{g,t}^{PP} = P_{g,t}^{P}, \tag{3.101}$$

$$0 \le y_{g,t}^{QP} - Q_{g,t}^{P} \le U_g^{max} d_{g,t}^{QP1}, \tag{3.102}$$

$$0 \le y_{g,t}^{QP} + Q_{g,t}^{P} \le U_g^{max} d_{g,t}^{QP2}, \tag{3.103}$$

$$d_{g,t}^{QP1} + d_{g,t}^{QP2} = 1, \tag{3.104}$$

$$g \in \mathcal{G}, t \in \mathcal{T}, \tag{3.105}$$

where $U_g^{max} = P_g^{max} + Q_g^{max}$.

Define $y_{g,t}^{Nmax}, y_{g,t}^{Nmin} \in \mathbb{R}^{T \times n_g}$, $d_{g,t}^{Nmax1}$, $d_{g,t}^{Nmax2}$, $d_{g,t}^{Nmin1}$, $d_{g,t}^{Nmin2} \in \mathbb{Z}_2^{T \times n_g}$, then $\max\left(y_{g,t}^{PN}, y_{g,t}^{QN}\right)$ and $\min\left(y_{g,t}^{PN}, y_{g,t}^{QN}\right)$ can be linearized as:

$$y_{g,t}^{Nmax} \geq y_{g,t}^{PN}, y_{g,t}^{Nmax} \geq y_{g,t}^{QN}, \tag{3.106}$$

$$y_{g,t}^{Nmax} \leq y_{g,t}^{PN} + U_g^{Nmax}\left(1 - d_{g,t}^{Nmax1}\right), \tag{3.107}$$

$$y_{g,t}^{Nmax} \leq y_{g,t}^{QN} + U_g^{Nmax}\left(1 - d_{g,t}^{Nmax2}\right), \tag{3.108}$$

$$d_{g,t}^{Nmax1} + d_{g,t}^{Nmax2} = 1, g \in \mathcal{G}, t \in \mathcal{T}. \tag{3.109}$$

$$y_{g,t}^{Nmin} \leq y_{g,t}^{PN}, y_{g,t}^{Nmin} \leq y_{g,t}^{QN}, \tag{3.110}$$

$$y_{g,t}^{Nmin} \geq y_{g,t}^{PN} - U_g^{Nmax}\left(1 - d_{g,t}^{Nmin1}\right), \tag{3.111}$$

$$y_{g,t}^{Nmin} \geq y_{g,t}^{QN} - U_g^{Nmax}\left(1 - d_{g,t}^{Nmin2}\right), \tag{3.112}$$

$$d_{g,t}^{Nmin1} + d_{g,t}^{Nmin2} = 1, g \in \mathcal{G}, t \in \mathcal{T}. \tag{3.113}$$

Similarly, $\max\left(y_{g,t}^{PP}, y_{g,t}^{QP}\right)$ and $\min\left(y_{g,t}^{PP}, y_{g,t}^{QP}\right)$ can be linearized by introducing $y_{g,t}^{Pmax}, y_{g,t}^{Pmin} \in \mathbb{R}^{T \times n_g}$, $d_{g,t}^{Pmax1}$, $d_{g,t}^{Pmax2}$, $d_{g,t}^{Pmin1}$, $d_{g,t}^{Pmin2} \in \mathbb{Z}_2^{T \times n_g}$:

$$y_{g,t}^{Pmax} \geq y_{g,t}^{PP}, y_{g,t}^{Pmax} \geq y_{g,t}^{QP}, \tag{3.114}$$

$$y_{g,t}^{Pmax} \leq y_{g,t}^{PP} + U_g^{Pmax}\left(1 - d_{g,t}^{Pmax1}\right), \tag{3.115}$$

$$y_{g,t}^{Pmax} \le y_{g,t}^{QP} + U_g^{Pmax}\left(1 - d_{g,t}^{Pmax2}\right), \tag{3.116}$$

$$d_{g,t}^{Pmax1} + d_{g,t}^{Pmax2} = 1, g \in \mathcal{G}, t \in \mathcal{T}. \tag{3.117}$$

$$y_{g,t}^{Pmin} \le y_{g,t}^{PP}, y_{g,t}^{Pmin} \le y_{g,t}^{QP}, \tag{3.118}$$

$$y_{g,t}^{Pmin} \ge y_{g,t}^{PP} - U_g^{Pmax}\left(1 - d_{g,t}^{Pmin1}\right), \tag{3.119}$$

$$y_{g,t}^{Pmin} \ge y_{g,t}^{QP} - U_g^{Pmax}\left(1 - d_{g,t}^{Pmin2}\right), \tag{3.120}$$

$$d_{g,t}^{Pmin1} + d_{g,t}^{Pmin2} = 1, g \in \mathcal{G}, t \in \mathcal{T}. \tag{3.121}$$

The DG current unbalance constraints can be described as:

$$0.9375y_{g,t}^{Nmax} + 0.4688y_{g,t}^{Nmin} \le CUF_g\left(0.9375y_{g,t}^{Pmax} + 0.4688y_{g,t}^{Pmin}\right), g \in \mathcal{G}, t \in \mathcal{T} \tag{3.122}$$

where CUF_g is the maximum permissive CUF for DG g. Equations (3.95)–(3.122) guarantee each DG can operate securely under unbalanced conditions.

3.5.5.2 DG Ramp Rate Constraints

The ramp rates of each DG should be within the acceptable range. The constraints involve two consecutive steps for each DG and can be described as:

$$-x_{g,t}^{G} \cdot P_g^{RAMP} \cdot \Delta t \le \sum_{\phi \in \{a,b,c\}} P_{g,t}^{\phi} - \sum_{\phi \in \{a,b,c\}} P_{g,t-1}^{\phi} \le x_{g,t}^{G} \cdot P_g^{RAMP} \cdot \Delta t,$$

$$g \in \mathcal{G}, t \in \mathcal{T}, t > 1, \tag{3.123}$$

where P_g^{RAMP} is the maximum ramp rate for DG g.

3.5.5.3 DG Output Constraints

For each time step, the output active and reactive power of the energized DG should be maintained within their rated capacity:

$$x_{g,t}^{G} \cdot P_g^{min} \leq \sum_{\emptyset} \boldsymbol{P}_{g,t}^{\emptyset} \leq x_{g,t}^{G} \cdot P_g^{\max}, \tag{3.124}$$

$$x_{g,t}^{G} \cdot Q_g^{min} \leq \sum_{\emptyset} \boldsymbol{Q}_{g,t}^{\emptyset} \leq x_{g,t}^{G} \cdot Q_g^{\max}, \; g \in \mathcal{G}, t \in \mathcal{T}, \tag{3.125}$$

where P_g^{min}, P_g^{max}, Q_g^{min} and Q_g^{max} are minimum and maximum values for active and reactive output of DG g. These constraints also force the output of the de-energized DG to zero. For some DGs, like diesel generators, minimal power output should be satisfied to avoid engine failure [96]. In addition, an optional constraint can be added for the dispatchable DG operating at the fixed power factor:

$$\tan(\arccos \varphi_g) \cdot \sum_{\emptyset} \boldsymbol{P}_{g,t}^{\emptyset} - \sum_{\emptyset} \boldsymbol{Q}_{g,t}^{\emptyset} = 0, g \in \mathcal{G} \backslash \mathcal{G}^{S}, t \in \mathcal{T}, \tag{3.126}$$

where φ_g is the fixed power factor for DG g. This constraint does not apply to the substation node or the black start DG.

3.5.6 ESS Operational Constraints

Operating ESS is different from conventional DGs, since ESS can operate either in discharge mode through the DC to AC inverter, or in charge mode to absorb power from the grid. Properly scheduling charging and discharging actions could achieve many benefits such as shifting peak load, compensating renewable power, and service restoration. A set of operational constraints should be considered to properly control an ESS [129]. For single-phase ESS, these constraints can be described as:

$$P_e^{CH\_min} x_{e,t}^{ESS\_CH} \leq P_{e,t}^{ESS\_CH} \leq P_e^{CH\_max} x_{e,t}^{ESS\_CH}, \quad (3.127)$$

$$P_e^{DISCH\_min} x_{e,t}^{ESS\_DISCH} \leq P_{e,t}^{ESS\_DISCH} \leq P_e^{DISCH\_max} x_{e,t}^{ESS\_DISCH}, \quad (3.128)$$

$$Q_e^{CH\_min} x_{e,t}^{ESS\_CH} \leq Q_{e,t}^{ESS\_CH} \leq Q_e^{CH\_max} x_{e,t}^{ESS\_CH}, \quad (3.129)$$

$$Q_e^{DISCH\_min} x_{e,t}^{ESS\_DISCH} \leq Q_{e,t}^{ESS\_DISCH} \leq Q_e^{DISCH\_max} x_{e,t}^{ESS\_DISCH}, \quad (3.130)$$

$$x_{e,t}^{ESS\_CH} + x_{e,t}^{ESS\_DISCH} \leq s_{e,t}^{N} \quad (3.131)$$

$$SOC_{e,t}^{ESS} = SOC_{e,1}^{ESS} + \eta_e^{ESS\_CH} P_{e,t}^{ESS\_CH} \Delta t - \frac{1}{\eta_e^{ESS_{DISCH}}} P_{e,t}^{ESS_{DISCH}} \Delta t, t = 1, \quad (3.132)$$

$$SOC_{e,t}^{ESS} = SOC_{e,t-1}^{ESS} + \eta_e^{ESS\_CH} P_{e,t}^{ESS\_CH} \Delta t - \frac{1}{\eta_e^{ESS_{DISCH}}} P_{e,t}^{ESS_{DISCH}} \Delta t, t \geq 2, \quad (3.133)$$

$$SOC_e^{min} \leq SOC_{e,t}^{ESS} \leq SOC_e^{max}, e \in \mathcal{E} \backslash \mathcal{E}^F, t \in \mathcal{T}, \quad (3.134)$$

where $P_e^{CH\_min}$ and $P_e^{CH\_max}$ are minimum and maximum active charging power for ESS e; $P_e^{DISCH\_min}$ and $P_e^{DISCH\_max}$ are minimum and maximum active discharging power for ESS e; $Q_e^{CH\_min}$ and $Q_e^{CH\_max}$ are minimum and maximum absorbed reactive power for ESS e; $Q_e^{DISCH\_min}$ and $Q_e^{DISCH\_max}$ are minimum and maximum generated reactive power for ESS e; SOC_e^{min} and SOC_e^{max} are minimum and maximum state of charge (SOC) for ESS e; $\eta_e^{ESS\_CH}$ and $\eta_e^{ESS\_DISCH}$ are charging and discharging efficiency for ESS e. The SOC is defined as the energy stored in ESS.

Equations (3.127) and (3.45) limit the active and reactive power when charging and discharging an ESS. Equation (3.46) requires that an ESS can only start to charge or discharge when the connected node is energized. Charging action and discharging action

are mutually exclusive; that is, an ESS cannot charge and discharge at the same time. The residual energy of an ESS is calculated based on (3.47)–(3.48) and maintained within a range as shown in (3.49). Note that there is always some energy loss when charging and discharging an ESS. Self-discharging loss is not considered since the considered time horizon for BSR is relatively short.

3.5.7 Topological Constraints

Topological constraints define a series of rules to describe the inter-temporal relationships among binary decision variables defined for lines and nodes. These rules are critical to ensure that a feasible black start sequence can be generated, and the radial topology for each isolated microgrid is maintained. As shown in the Figure 3.3, a black start sequence is feasible if components can be energized and operated sequentially, while compiling with the operational rules and connectivity constraints. Note that most distribution systems are constructed in weakly meshed topology and operated in radial topology because it is easier to implement fault location, isolation, and protection coordination [111]. However, radially operated distribution systems are no longer radial after introducing a high penetration of DGs that can cause bidirectional power flow [130]. In this dissertation research, we assume that radial distribution systems and microgrids with multiple DGs are operated in tree topology. The tree topology allows bidirectional power flow and maintains radial structure.

In a typical distribution system, some buses may be interconnected by non-switchable lines, and form a “bus block” as shown in Figure 3.8. All the buses can be grouped into multiple bus blocks. Note one bus block contains at least one bus, and all the buses and

lines in a bus block will be energized at one time. Figure 3.8 shows that by replacing each bus block with an equivalent bus, the reduced network will contain switchable lines only. For a reduced network, denote $\mathcal{K} \coloneqq \{1,2,\dots,N_k\}, N_k \leq N_n$ as the set of bus blocks, $\mathcal{C} \coloneqq \{(i,j): i \in \mathcal{K}, j \in \mathcal{K}, i \neq j\}$ as the switchable lines between bus blocks. Note for each $(i,j) \in \mathcal{C}$, its end nodes (i.e., i and j) are actually the buses inside the bus blocks. Since a bus block will be energized as long as one of its inside bus is energized, the energization status of a bus block can be represented by the status of any one of the buses inside.

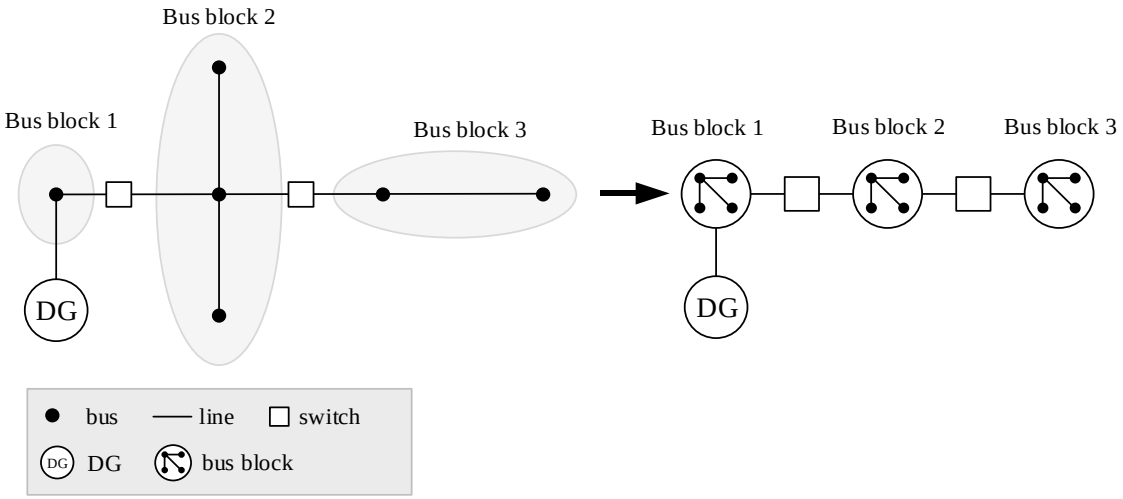

Figure 3.8. The concept of "bus block" which can be formed by a single bus or multiple buses interconnected by non-switchable lines. The reduced network contains the switchable lines only.

The topological constraints can be described as the following four rules:

1) If a bus block is not connected to a black-start DG or a substation, it can be energized by anyone of the lines connected to this bus.

2) If a bus block is de-energized at step $t-1$ and energized at step t, then it must be energized by at most one switchable line at step t.

3) Each switchable line can only be energized when at least one of its end buses is energized at the previous interval.

4) If both end buses of a switchable line are energized, this line cannot be closed, in order to avoid forming a loop.

These rules can be mathematically translated into the following constraints:

$$s_{i,t}^{N} \le \sum_{i:\,(i,j)\in\mathcal{C}} x_{ij,t}^{BR} + \sum_{i:\,(k,i)\in\mathcal{C}} x_{ki,t}^{BR}, i \in \mathcal{K}, t \in \mathcal{T}. \quad (3.135)$$

$$\sum_{i:\,(i,j)\in\mathcal{C}}\left(x_{ij,t}^{BR} - x_{ij,t-1}^{BR}\right) + \sum_{i:\,(k,i)\in\mathcal{C}}\left(x_{ki,t}^{BR} - x_{ki,t-1}^{BR}\right) \le 1 + Ms_{i,t-1}^{N}, i \in \mathcal{K}, t \in \mathcal{T}, t > 1 \quad (3.136)$$

$$x_{(i,j),t}^{BR} \le s_{i,t-1}^{N} + s_{j,t-1}^{N}, \quad (i,j) \in \mathcal{B}^{S}, t \in \mathcal{T}, t > 1. \quad (3.137)$$

$$\left(s_{i,t}^{N} - s_{i,t-1}^{N}\right) + \left(s_{j,t}^{N} - s_{j,t-1}^{N}\right) \ge x_{(i,j),t}^{BR} - x_{(i,j),t-1}^{BR}, \quad (i,j) \in \mathcal{B}^{S}, \mathrm{t} \in \mathcal{T}, t > 1 \quad (3.138)$$

Figure 3.9, in which two isolated microgrids are already developed, demonstrates how the first rule and the second rule work. At step $(t-1)$, both line (i,j) and line (i,k) are de-energized and connected to node i. By requiring that node i can only be energized by at most one line (either (i,j) or (i,k)), the two microgrids are still kept isolated.

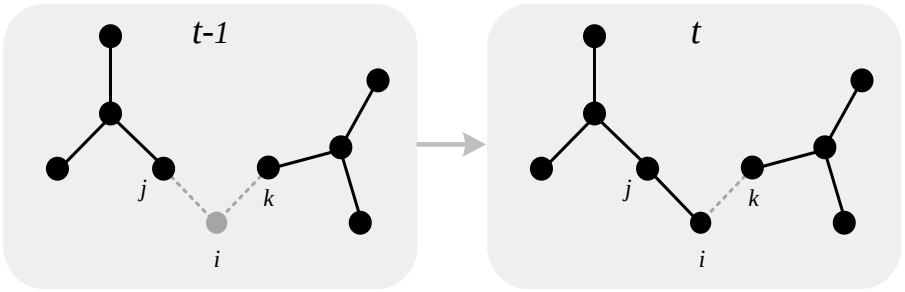

Figure 3.9. An example to show the topological constraints that require a node must be energized by at most one line.

Figure 3.10, in which a single microgrid is already developed, shows how the third rule works. At step $(t-1)$, line (i,j) is de-energized, with node j energized; line (h,k) is also de-energized, but both end buses are de-energized. By requiring that each switchable line can only be energized when at least one of its end buses is energized at the previous interval, only line (i,j) is qualified to be closed at step t. Even if line (h,k) is closed at step t, it cannot be energized, since no energized lines connect to it. Therefore, this rule can ensure that a system can be energized step by step.

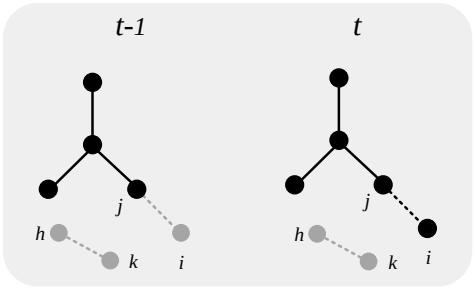

Figure 3.10. An example to show the topological constraint that requires a line must be closed to an energized bus

Figure 3.11 shows how the fourth rule works. At step $(t-1)$, line (i,j) is de-energized. The fourth rule requires that a line cannot be closed if both end buses are previously energized. It can be seen that if line (i,j) is closed, a loop will be formed. This rule ensures a system can be always operated in the tree topology.

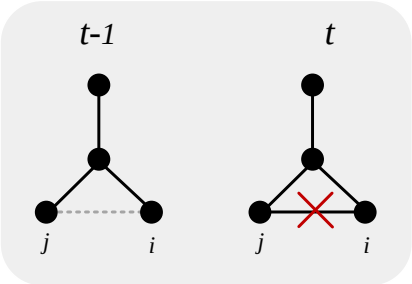

Figure 3.11. An example to show the topological constraints that requires a line cannot be closed if both end buses are previously energized

3.6 BSR Solution Methodology

The MILP model, which is introduced in section 3.5, is the core of the BSR solution methodology. Several commercial solvers can be used for effectively solving the MILP model, such as IBM CPLEX and GUROBI [131, 132]. Given system parameters representing a distribution system or a microgrid, the MILP model can be developed and solved accordingly. Since the BSR problem is formulated as a dynamic optimization problem, decision variables and state variables must be determined at each time step. Various constraints must be satisfied at each time step too. Therefore, the problem size will become intractable when solving large-scale systems over a long horizon [133]. In order to solve the BSR model within acceptable computation time, a rolling-horizon procedure is employed in the BSR solution methodology [134, 135].

In this subsection, the rolling-horizon procedure is introduced first. Then, the implementation framework is introduced. Finally, a flowchart representing the implementation of the solution methodology is presented.

3.6.1 Rolling-Horizon Procedure

Discrete time formulation of the dynamic scheduling optimization problem is effective to solve if the considered time horizon is short. However, as the total number of time steps increases, the MILP model formulated over the considered time horizon becomes too complicated to solve within a reasonable amount of time [136]. Rather than solving a complex problem over the entire considered horizon, the rolling-horizon procedure divides the total scheduled horizon (*H*) into smaller prediction horizons and solve the problem iteratively, so as to reduce the computation time [136]. The rolling-horizon procedure has been used for solving optimization problems in power systems [133, 137]. The schematic of the rolling-horizon procedure with fixed prediction horizon (T) and control horizon (C) over a total scheduled horizon (H) is shown in Figure 3.12 [137]. First, a BSR model is formulated and solved in Iteration 1 during the first prediction horizon $[T_0, T_0 + T]$. After the BSR model is solved, only the control actions during the control horizon $[T_0, T_0 + C]$ is carried out. Then, same procedures are applied for Iteration 2 during $[T_0 + C + 1, T_0 + 2C]$ and Iteration 3 during $[T_0 + 2C + 1, T_0 + 3C]$. The rolling-horizon procedure is iteratively carried out horizon by horizon, until the control actions over the total scheduled horizon (*H*) are generated. The total number of iterations is *K*. To apply the rolling-horizon procedure, the rolling-horizon parameters (e.g., prediction horizon *T*, control horizon *C*, and total scheduled horizon *H*) should be properly selected. In [133], it has been shown that different parameters resulted in different performances in terms of solution optimality and computation time.

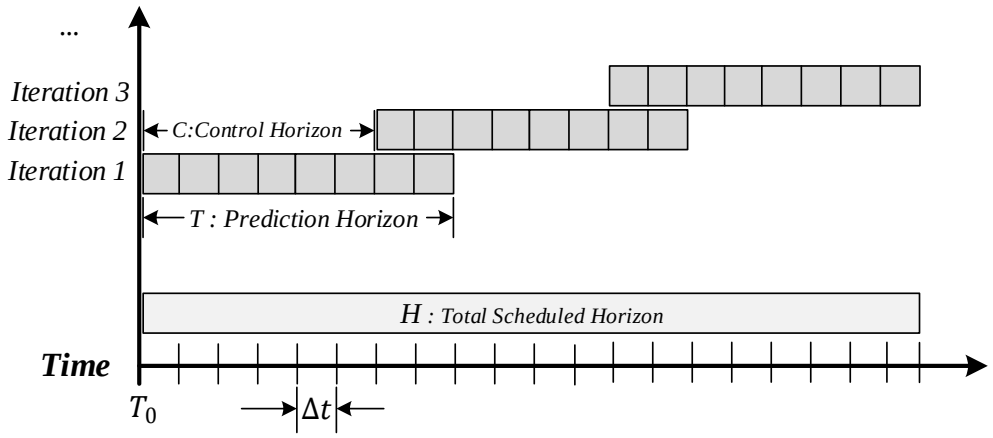

Figure 3.12. The schematic of the rolling-horizon procedure with fixed prediction horizon (*T*) and control horizon (*C*) over a total scheduled horizon (*H*).

For each iteration $K > 1$, the BSR model is formulated over the prediction horizon $[T_0 + KC + 1, T_0 + KC + K]$. The starting time step should be integrated into the initial condition constraints in the BSR model. Specifically, several rules should be followed:

1) Status of DERs, loads and lines, power outputs of DERs at step $T_0 + KC - (C - 1)$ should be the same as the status of the same step in the last iteration $K - 1$.

2) Power outputs of DERs at step $T_0 + KC - (C - 1)$ should be the same the power outputs of the same step in the last iteration $K - 1$.

3) CLPU parameters should be updated to consider the duration of each load has been restored.

These rules can be mathematically formulated as the following equations:

$$x^{G}_{g,T_0+(K-1)C+1} = x^{G}_{g,T_0+JC+1}, J = K-1, K > 1, g \in \mathcal{G} \quad (3.139)$$

$$x^{BR}_{ij,T_0+(K-1)C+1} = x^{BR}_{ij,T_0+JC+1}, J = K-1, K > 1, (i,j) \in \mathcal{B} \quad (3.140)$$

$$x^{L}_{l,T_0+(K-1)C+1} = x^{L}_{l,T_0+JC+1}, J = K-1, K > 1, l \in \mathcal{L} \quad (3.141)$$

$$x_{e,T_0+(K-1)C+1}^{ESS\_CH} = x_{e,T_0+JC+1}^{ESS\_CH}, J = K-1, K > 1, e \in \mathcal{E} \quad (3.142)$$

$$x_{e,T_0+(K-1)C+1}^{ESS\_DISCH} = x_{e,T_0+JC+1}^{ESS\_DISCH}, J = K-1, K > 1, e \in \mathcal{E} \quad (3.143)$$

$$s_{i,T_0+(K-1)C+1}^{N} = s_{i,T_0+JC+1}^{N}, J = K-1, K > 1, i \in \mathcal{N} \quad (3.144)$$

$$\boldsymbol{P}_{g,T_0+(K-1)C+1}^{\phi} = \boldsymbol{P}_{g,T_0+JC+1}^{\phi}, J = K-1, K > 1, \phi \in \{A,B,C\},\ g \in \mathcal{G} \quad (3.145)$$

$$\boldsymbol{Q}_{g,T_0+(K-1)C+1}^{\phi} = \boldsymbol{Q}_{g,T_0+JC+1}^{\phi}, J = K-1, K > 1, \phi \in \{A,B,C\},\ g \in \mathcal{G} \quad (3.146)$$

$$\boldsymbol{P}_{l,T_0+(K-1)C+1}^{L} = \boldsymbol{P}_{l,T_0+JC+1}^{L}, J = K-1, K > 1, l \in \mathcal{L} \quad (3.147)$$

$$\boldsymbol{Q}_{l,T_0+(K-1)C+1}^{L} = \boldsymbol{Q}_{l,T_0+JC+1}^{L}, J = K-1, K > 1,\ l \in \mathcal{L} \quad (3.148)$$

$$P_{e,T_0+(K-1)C+1}^{ESS\_CH} = P_{e,T_0+JC+1}^{ESS\_CH}, J = K-1, K > 1, e \in \mathcal{E} \quad (3.149)$$

$$Q_{e,T_0+(K-1)C+1}^{ESS\_CH} = Q_{e,T_0+JC+1}^{ESS\_CH}, J = K-1, K > 1, e \in \mathcal{E} \quad (3.150)$$

$$P_{e,T_0+(K-1)C+1}^{ESS\_DISCH} = P_{e,T_0+JC+1}^{ESS\_DISCH}, J = K-1, K > 1, e \in \mathcal{E} \quad (3.151)$$

$$Q_{e,T_0+(K-1)C+1}^{ESS\_DISCH} = Q_{e,T_0+JC+1}^{ESS\_DISCH}, J = K-1, K > 1, e \in \mathcal{E} \quad (3.152)$$

$$SOC_{e,T_0+(K-1)C+1}^{ESS\_DISCH} = SOC_{e,T_0+JC+1}^{ESS\_DISCH}, J = K-1, K > 1, e \in \mathcal{E} \quad (3.153)$$

If the loads are under CLPU conditions, $\Delta L_l(k)$ in (3.21) should be updated using (3.22)-(3.24). The duration of a load which has been restored can be formulated as:

$$\sum_{t=T_0}^{T_0+(K-1)C+1} x_{l,t}^{L}, K > 1, l \in \mathcal{L} \quad (3.154)$$

3.6.2 Implementation Framework

The implementation framework of the BSR solution methodology is presented in Figure 3.13 with each procedure marked by a step number. The architecture of the implementation framework consists of four software tools, namely, Microsoft EXCEL, MATLAB [138], YALMIP Toolbox [139], and IBM CPLEX [131].

System model information and measurement data is stored in Microsoft EXCEL files, which can be conveniently accessed from a MATLAB procedure (steps 1 to 5). In MATLAB, the MILP model is developed in YALMIP (steps 6-14), which is a free MATLAB toolbox for rapid prototyping of optimization problems [139]. The MILP model developed in YALMIP is solved by the IBM CLPLEX MILP Solver (step 15). The MILP solution is then returned to the MATLAB procedure for processing (step 17). Next, the procedures will be discussed in detail.

First of all, all the data is gathered and processed in a MATLAB procedure in steps 1-5. Specifically, the load model parameters (such as original load demand $\boldsymbol{P}_{l,t_0}^{\phi} + j\boldsymbol{Q}_{l,t_0}^{\phi}$, load locations, load type, load status, type of load connection, weight coefficients β_l^L, and CLPU parameters S_l^U, S_l^D, α_l, D_l) at step 1 and time-varying load data at step 4 were processed and organized in the MALAB procedure. System model (step 2) contains parameters for node, line, and transformer, respectively. The system parameters include node number and status (damaged or not damaged). A line object contains the information on line end nodes, kVA capacity S_{ij}^{max}, and status (switchable, non-switchable, or damaged). A transformer object contains similar information as a line object, plus the tap limits $\boldsymbol{n}_{ij}^{tap\_min}$ and $\boldsymbol{n}_{ij}^{tap\_max}$.

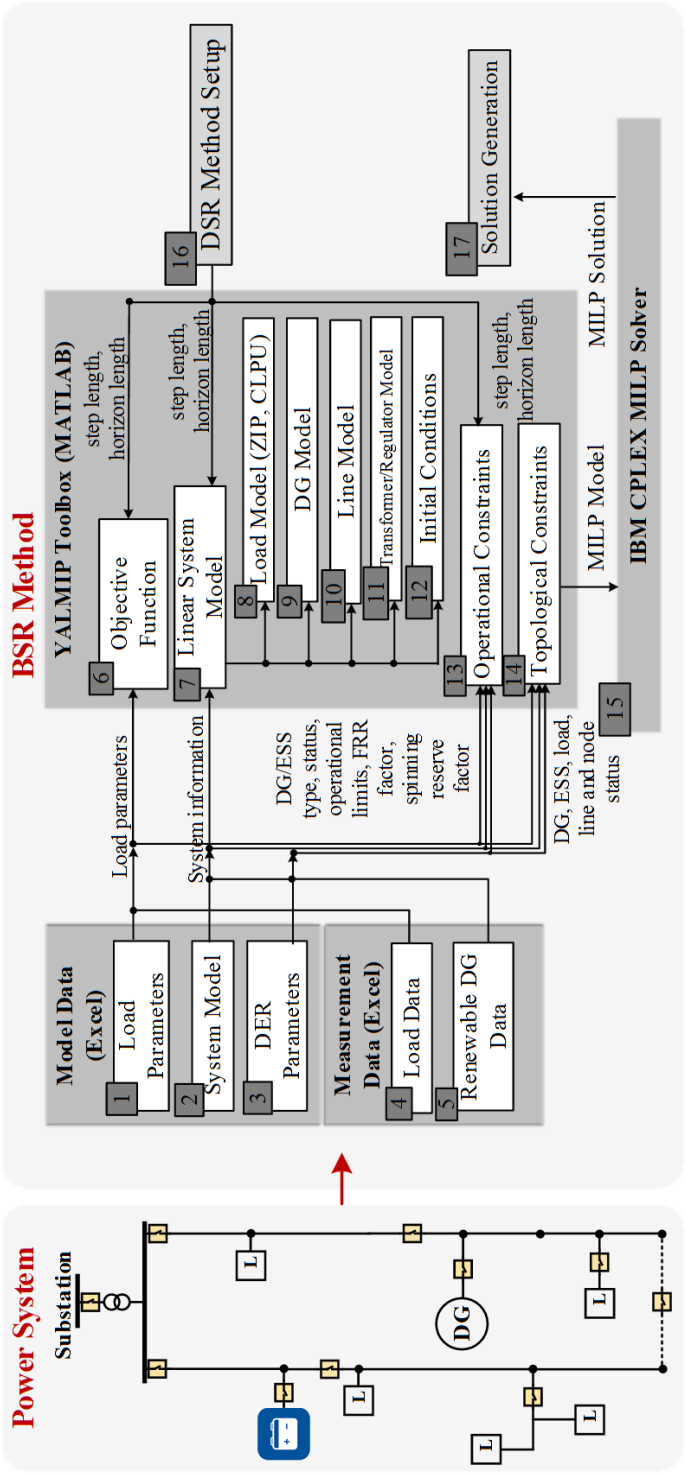

Figure 3.13. Implementation framework for the BSR methodology

DER parameters include parameters for DGs and ESS (step 3) and time-varying renewable predicted data (step 5) are processed and organized in MATLAB. Specifically, DG type (black start DG, dispatchable DG, or renewable DG), location, status, and operational parameters (P_g^{CAP}, P_g^{max}, P_g^{min}, Q_g^{max}, Q_g^{min}, $Ramp_g$, FRR factor, and CUI factor) were incorporated into the MILP model. For each ESS, rated capacity $E_e^{ESS_R}$, initial SOC ρ_e^{ini}, minimum SOC ρ_e^{min}, maximum SOC ρ_e^{max}, charging efficiency η_e^C, discharging efficiency η_e^D, maximum charging and discharging limits $P_e^{C\_max}$, $Q_e^{C\_max}$, $P_e^{D\_max}$, $Q_e^{D\_max}$, minimum charging and discharging limits $P_e^{C\_min}$, $Q_e^{C\_min}$, $P_e^{D\_min}$, $Q_e^{D\_min}$ were incorporated into the MILP model.

Next, the MILP model is formulated in the YALMIP Toolbox [139]. YALMIP allows users to use simple MATLAB languages to formulate the optimization problems, which can be automatically translated into models that can be recognized and solved by various off-the-shelf solvers [139]. At step 16, the rolling-horizon parameters (e.g., prediction horizon T, control horizon C, and total scheduled horizon H) and decision time step Δt are specified. At step 6, the objective function (3.7) is formulated using the load weight coefficients β_l^L from step 1, and horizon length T and decision time step Δt from step 16. From step 7 to step 12, system model introduced in section 3.5.3 is formulated. At step 13, the system operational constraints introduced in section 3.5.4, and the DG and ESS operational constraints introduced in section 3.5.5 and 3.5.6 are formulated. At step 14, the topological constraints introduced in section 3.5.7 are formulated. Next, the MILP model formulated in YALMIP is sent to IBM CPLEX MILP solver at step 15. The solution generated by the CPLEX solver is returned to MATLAB for processing at step 17. The

variables (e.g., objective values, control sequences, power flow results) determined in the solution are organized. The rolling-horizon procedure is implemented at step 16.

The flowchart for implementing the BSR solution methodology is shown in Figure 3.14. The numbers on each procedure block in Figure 3.14 represent the steps in Figure 3.13 needed to implement this particular procedure.

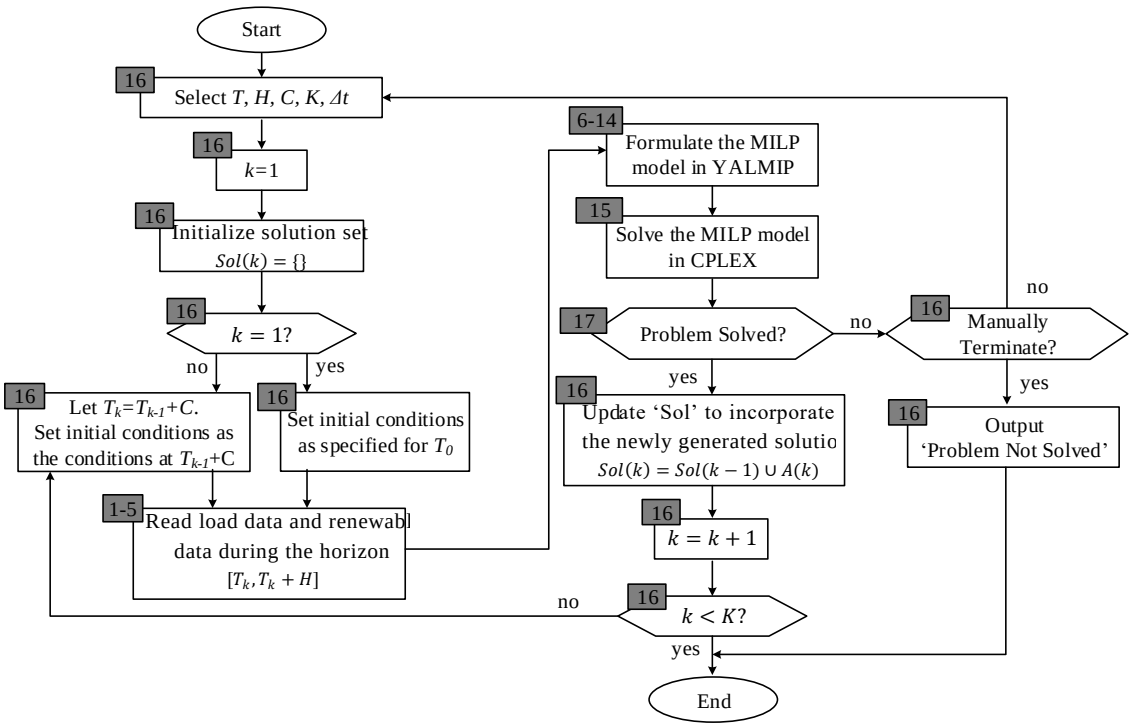

Figure 3.14. Flowchart for implementing the BSR solution methodology. The BSR method is assumed to be initialized at T_0, with a fixed horizon length H, a control horizon C, and a maximum iteration number K.

The BSR method is assumed to be initialized at T_0, with a fixed horizon length *H*, a prediction horizon *T*, a control horizon *C*, and a maximum iteration number *K*. These rolling-horizon parameters are specified in step 16 in Figure 3.13. Next, if the rolling-horizon procedure is enabled, a structure object $Sol\{\}$ in MATLAB will be created at step

16 to store all the control actions over the scheduled horizon. Then, the initial condition constraints for the first iteration should be the starting time of T, which is T_0. Otherwise, if it is not the first iteration, the starting time for the current horizon is set to $T_0 + kC$. The initial condition constraints should be identical with the decision variables determined in the previous iteration. Next, steps 1 – 7 are carried out to read the load profile and renewable DG output profile for the current horizon and incorporated the profiles into the BSR model through steps 6 – 14. At each iteration, after solving the problem at step 15, $Sol\{\}$ should be updated to incorporate the solution for the current horizon at step 16. The iteration will stop when either the maximum iteration K is achieved, or the MILP solver cannot solve the problem.

3.7 Section Summary

In this section, the BSR problem formulation and solution methodology was presented. The BSR problem was formulated as a dynamic optimization problem. Then, the state variables and decision variables defined in the BSR problem were introduced. The objective functions and constraints that should be considered during the black start process were summarized. Next, the MILP model, which formulated the objective function and all the constraints in linear form, was presented in detail. Specifically, the three-phase unbalanced system model, DG and ESS models, and associated operational constraints were introduced. The MILP model can be effectively solved by off-the-shelf solvers. However, the problem size may become intractable for large-scale systems. The rolling-horizon procedure was introduced as a strategy to reduce the computation time by dividing the original schedule horizon into multiple smaller horizons. Finally, the implementation

framework of the BSR methodology are presented. The architecture and tools used for implementing data processing, model formulating, and problem solving were introduced.

4 CASE STUDIES AND PERFORMANCE ANALYSIS

In this section, case studies and performance analysis were performed to study the proposed BSR method. The results are presented in this section. First, the simulated test systems, renewable DG output and load profiles, and simulation software setups are introduced. Next, six case studies are presented to demonstrate how the proposed BSR method works. Then, a set of extensive studies conducted for evaluating the performance of the proposed BSR method are discussed.

4.1 Test Systems

4.1.1 Three-Phase Balanced Test Systems

In this subsection, two three-phase balanced test systems used for case studies and performance analysis are introduced, namely, balanced modified IEEE 13 node system and balanced modified IEEE 123 node system. Both test systems were adapted from the original IEEE 13 node test feeder and the original IEEE 123 node test feeder. The data for the studied test systems can be found in [140].

4.1.1.1 Balanced Modified IEEE 13 Node System

The original IEEE 13 node system is a small radial system operated at 4.16 kV, and it has been used in many papers to study various distribution system applications [140]. The original test system was modified by assuming all the lines and loads are balanced. Since there is no DGs in the original system, three DGs and an ESS were added to the system to illustrate how the proposed BSR method coordinates multiple DGs and ESS. In addition,

three additional switchable lines were added to the system. Note the locations and parameters of DGs, ESS, and additional lines should be properly determined during the planning stage. In this dissertation research, their locations and parameters are assumed to be known.

The single-line diagram of the balanced modified IEEE 13 node radial test system is shown in Figure 4.1. The DGs are connected to Node 650, 646, and 680. The parameters of the DGs are shown in TABLE 4.1. The status indicates the controllability of each DG, with "1" representing the black start DGs that can be started at step $t = 1$, "1/0" representing the non-black start DGs that can be started once the control command is issued, and "0" representing the DG is not available to participate in the service restoration. A storage battery is connected to Node 632 through bidirectional AC/DC converter. Its parameters are shown in TABLE 4.2.

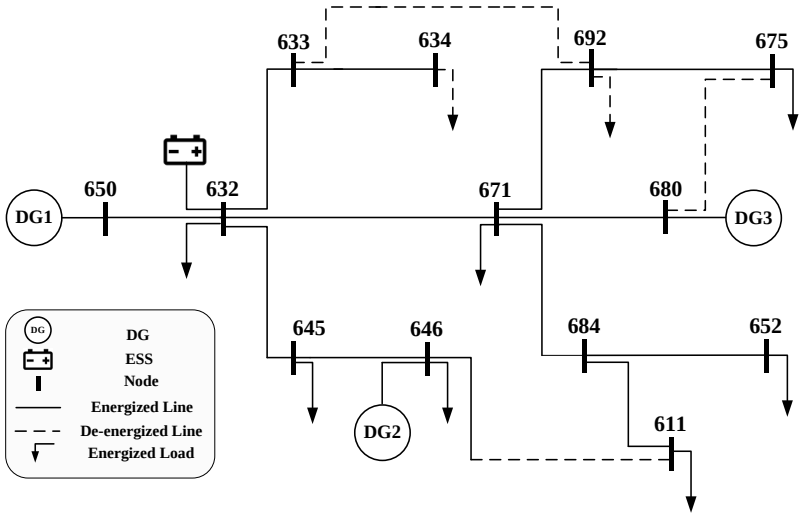

Figure 4.1. Single-line diagram of balanced modified IEEE 13 node test system

TABLE 4.1. DG PARAMETERS OF MODIFIED IEEE 13 NODE TEST FEEDER

Parameter	DG1	DG2	DG3
Node position	650	646	680
Power factor	N/A	0.8	0.8
FRR	5%	5%	5%
P_g^{max} (kW)	10000	500	1000
P_g^{min} (kW)	0	50	100
Q_g^{max} (kVar)	8000	500	1000
Q_g^{min} (kVar)	-8000	-400	-800
P_g^{RAMP} (kW/min)	1000	500	300
Status	1	1/0	1/0

TABLE 4.2. ESS PARAMETERS OF MODIFIED IEEE 13 NODE TEST FEEDER

Parameter	ESS
Node position	632
$E_e^{ESS\_R}$	20 kWh
ρ_e^{min}	10 %
ρ_e^{max}	100 %
η_e^C	0.90
η_e^D	0.90
$P_e^{C\_min}/P_e^{C\_max}$	100/500 kW
$Q_e^{C\_min}/Q_e^{C\_max}$	0/200 kVar
$P_e^{D\_min}/P_e^{D\_max}$	200/500 kW
$Q_e^{D\_min}/Q_e^{D\_max}$	0/200 kVar

The line parameters are shown in TABLE 4.3. The "status" of a line indicates if this line is switchable. For example, "1/0" represents the line can be remotely switched, "1" represents the line is directly connected to two end nodes, and "0" represents the line is disconnected and cannot be closed. The maximum line kVA capacity was determined by its ampacity at rated voltage. For example, if the ampacity of a line is 625A, then the line's kVA capacity at 4.16 kV is $625\times(4160/\sqrt{3}) = 1500\,kVA$. The line ampacity information can be found in [141]. The line impedances were modified by assuming the three-phase lines are perfectly transposed. For three-phase lines, the off-diagonal terms in the line impedance matrix were ignored, and the diagonal terms were equal to the average

value of original diagonal values. For single-phase and two-phase lines, the missing phase(s) were added with the impedance being equal to the other phase(s). The voltage regulator between Node 649 and Node 650 were removed from the system. Node 650 is assumed to be the slack bus. The voltage at Node 650 is regulated at 1.05 p.u. The transformer XFM-1 between Node 633 and Node 634 was replaced by a line, with the kVA capacity being equal to the kVA capacity of XFM-1, and the impedance being equal to the winding impedance of XFM-1. The line impedance for different configurations are summarized in TABLE 4.4.

TABLE 4.3. LINE PARAMETERS OF MODIFIED IEEE 13 NODE TEST FEEDER

Line No.	From Node	To Node	Length (ft)	Ampacity (A)	Capacity (kVA)	Config.	Status
1	650	632	2000	730	1753.3	601	1/0
2	632	633	500	340	816.6	602	1/0
3	633	634	2000	208	500	XFM-1	1/0
4	632	645	500	230	552.4	603	1/0
5	645	646	300	230	552.4	603	1/0
6	632	671	2000	730	1753.3	601	1/0
7	671	692	10	416	1000	Switch	1/0
8	692	675	500	329	790.2	606	1/0
9	671	684	300	230	552.4	604	1/0
10	684	611	300	230	552.4	605	1
11	684	652	800	310	744.6	607	1
12	671	680	1000	730	1753.3	601	1/0
13	633	692	2000	340	816.6	602	1/0
14	646	611	2000	230	552.4	603	1/0
15	675	680	1500	730	1753.3	601	1/0

TABLE 4.4. LINE IMPEDANCE IN MODIFIED IEEE 13 NODE TEST FEEDER

Configuration No.	Impedance in ohms per mile
601	0.3418+j1.0335
602	0.7479+j1.1970
603	1.3266+j1.3520
604	1.3266+j1.3520
605	1.3292+j1.3475
606	0.7952+j0.4322
607	1.3425+j0.5124
XFM-1	1.0051+j1.8274
Switch	0.0001+j0.0001

The load parameters are summarized in TABLE 4.5. All the loads are three-phase balanced spot loads. The load demand was determined as the average value of the total demand of presenting phase(s). The CLPU coefficients S_l^U, S_L^D, D_l and α_l for CLPU load modeling were generated using uniform distribution with the ranges being [1.8, 3.0], [1.0, 1.3], [1, 4] and [0.5, 1.5], respectively. Weight coefficients should be determined by system operators to guarantee the load priorities, based on both economic and societal considerations. Since the original test feeder is lacking the load priority information, the weight coefficients were assumed to be 1.0 for all loads.

TABLE 4.5. SPOT LOAD PARAMETERS OF MODIFIED IEEE 13 NODE TEST FEEDER

Load Name	P (kW)	Q kVar)	Weight	S_l^U/S_l^D	D_l(min)	α_l	Status
L632	33.3	19.3	1	2.0/1.2	2.2	0.7	1/0
L634	133.3	96.7	1	1.8/1.1	2.3	0.8	1/0
L645	56.7	41.7	1	2.4/1.1	1.1	1.0	1/0
L646	76.7	44	1	2.5/1.1	3.6	0.7	1/0
L671	218.3	106	1	2.3/1.0	2.7	1.3	1/0
L692	56.7	50.3	1	2.7/1.0	1.2	0.6	1/0
L675	147.6	87.3	1	3.4/1.3	2.7	0.7	1/0
L611	56.7	26.7	1	2.1/1.3	2.1	0.6	1/0
L652	42.7	28.7	1	3.0/1.1	2.0	0.9	1/0

The power flow for the balanced modified IEEE 13 node radial test system is solved in OpenDSS, which is an open-source AC power flow simulator developed by The Electric Power Research Institute (EPRI) [142]. The DGs and ESS are assumed to be disconnected. Thus, all the loads are supplied by the substation node. The node voltages and line currents are shown in TABLE 4.6 and TABLE 4.7. It can be observed that the voltage magnitude of each node is between 0.95 p.u. and 1.05 p.u. The current is below the line ampacity.

TABLE 4.6. POWER FLOW FOR MODIFIED 13 NODE SYSTEM: VOLTAGE MAGNITUDE AND ANGLE

Node	Base kV (line to line)	Magnitude (p.u.)	Angle (degree)
650	4160	1.05000	0
632	4160	0.99421	-2.5
633	4160	0.99055	-2.5
634	4160	0.96946	-3.1
645	4160	0.98935	-2.5
646	4160	0.98774	-2.5
671	4160	0.96038	-4.2
692	4160	0.96038	-4.2
675	4160	0.95772	-4.2
684	4160	0.95825	-4.2
611	4160	0.95711	-4.2
652	4160	0.95628	-4.2
680	4160	0.96038	-4.2

TABLE 4.7. POWER FLOW FOR MODIFIED 13 NODE SYSTEM: LINE CURRENT MAGNITUDE AND ANGLE

Line	Ampacity (A)	Current (A)	Angle (degree)
650-632	730	414.645	-35.02
632-633	340	70.7262	-39.06
633-634	208	70.7264	-39.06
632-645	230	66.7549	-35.25
645-646	230	37.2598	-32.4
632-671	730	261.185	-33.99
671-692	416	107.016	-38.14
692-675	329	74.58	-34.78
671-684	230	49.4822	-33.34
684-611	230	27.2428	-29.45
684-652	310	22.3792	-38.09
671-680	730	0.00056	85.82

4.1.1.2 Balanced Modified IEEE 123 Node System

The balanced modified IEEE 123 node test system was modified based on the original IEEE 123 node system, which is a three-phase unbalanced system operated at 4.16 kV. The original system data is available in [140]. The original test system was modified using a similar method as used for the IEEE 13 node test system. The single-line diagram of the balanced modified IEEE 123 node test system is shown in Figure 4.2. The detailed system data for DGs, lines, and loads can be found in APPENDIX A.

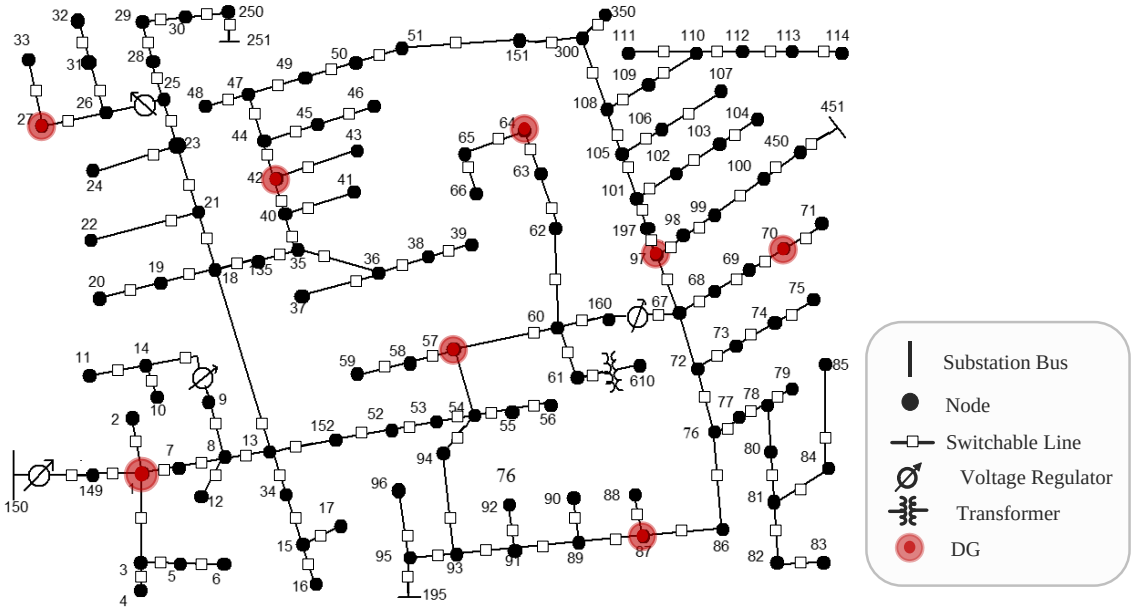

Figure 4.2. Single-line diagram of modified IEEE 123 node test system

4.1.2 Three-Phase Unbalanced IEEE 123 Node System

Three-phase unbalanced IEEE 123 node system used for case studies and performance analysis was modified based on the original IEEE 123 node test feeder. A set of switches and DGs were added to the system. All the original lines, nodes, transformers, regulators, capacitor banks, and unbalanced loads were kept. The single-line diagram is shown in Figure 4.3, in which buses are represented by dots, and the substation bus (node 150) is represented by a bar. Three-phase, two-phase, and single-phase lines are represented by black, yellow, and green wires, respectively. There are a total of 46 switchable lines and 4 voltage regulators in the system. A line is switchable by installing a switch, which is represented by a square on the line. All the component parameters can be found in the APPENDIX B.

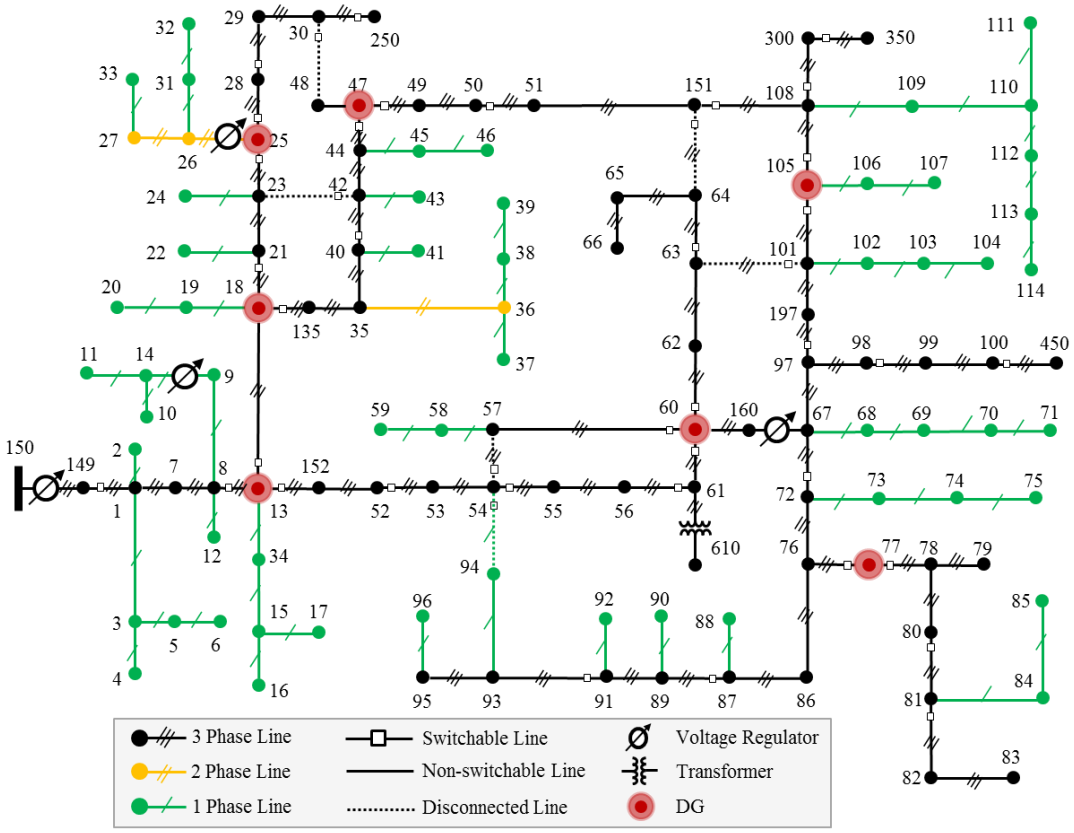

Figure 4.3. Single-line diagram of unbalanced modified IEEE 123 Node Test System

4.1.3 Renewable Profiles and Load Profiles

In order to study the performance of the proposed BSR method when renewable DERs and time-changing loads are considered, a set of renewable DG output profiles and load profiles were developed. In this dissertation research, residential rooftop photovoltaics (PV), which are most commonly installed in residential and commercial areas, were considered in studies. The actual time-varying load demand of residential, commercial and industrial customers, together with a certain penetration of ESS, was considered too.

The data provided by the Pecan Street project database was used for generating the residential load profiles and PV profiles [143]. The Pecan Street project database is the world's largest energy data resource [143]. This subsection introduces how the data retrieved from the Pecan Street project database and several other databases was used to generate PV profiles and load profiles.

4.1.3.1 PV Profiles

The PV profiles used in this dissertation research were retrieved from the Pecan Street project database. The one-minute resolution PV profiles for three residential homes on June 1st 2016 are shown in Figure 4.4. The profiles indicate that it was a cloudy day, because the clouds affect the radiation on the PV panels and make the power output change significantly throughout the day. In this dissertation research, the PV penetration is defined as the ratio of the energy generated by PV over the energy consumed by loads for 24 hours [144]:

$$\gamma^{PV} = \frac{\int_{t=1}^{24hr} P^{PV}(t)dt}{\int_{t=1}^{24hr} P^{LOAD}(t)dt} \times 100\% \tag{4.1}$$

where $P^{PV}(t)$ is the power output of PV at time t, $P^{LOAD}(t)$ is the load demand at time t, γ^{PV} is the penetration of PV.

By grouping multiple PV profiles, an aggregated PV profile was generated to approximate the required penetration for study purposes. For example, an aggregated load consumes 12kWh a day, and the required PV penetration is 20%. Then an aggregated PV profile with around 2.4 kWh of average energy consumption is generated. As shown in Figure 4.5, the PV profiles of house No. 99, 123, and 174 are grouped. By generating

different PV profiles, we can perform case studies and performance analysis with different PV penetrations.

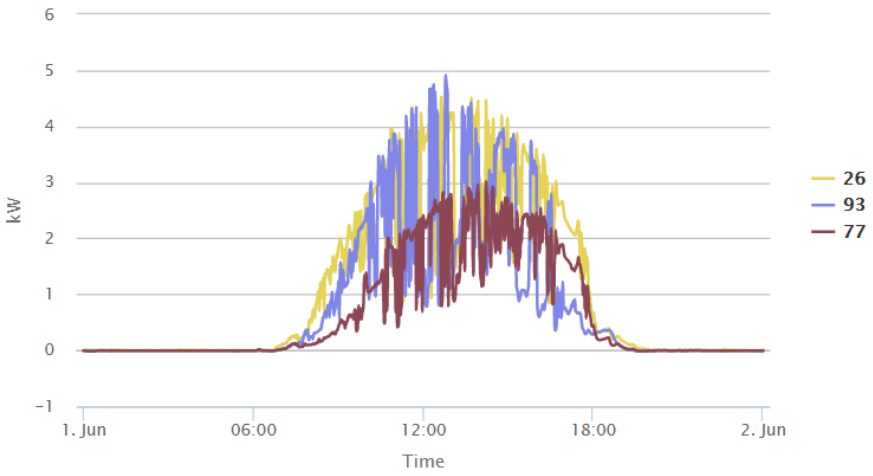

Figure 4.4. One-minute resolution PV profiles for three residential homes on June 1st 2016

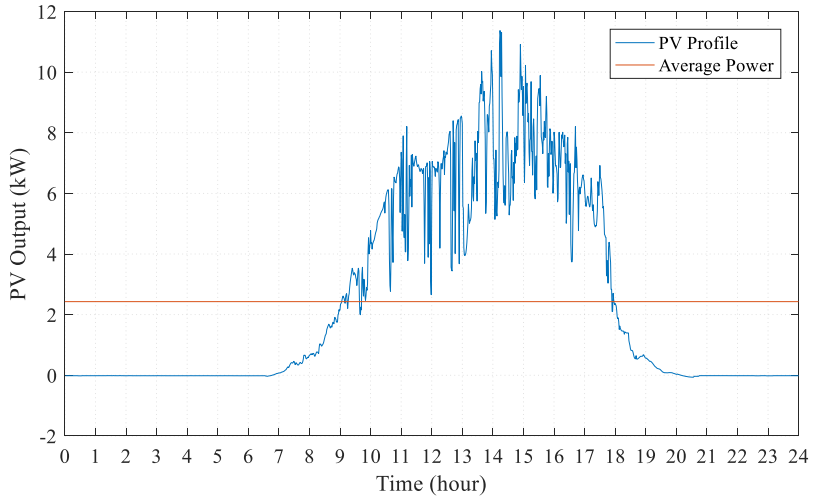

Figure 4.5. Grouping PV profiles of three houses (No. 99, 123, and 174) to achieve the required penetration (20%) for an aggregated load (12kW)

4.1.3.2 Load Profiles

It is known that in distribution systems, different types of loads exist, for example, residential loads, commercial loads, and industrial loads. Normally, residential loads are single-phase and connect to transformers. Commercial and industrial loads are two-phase or three-phase. In this dissertation research, the load profiles were retrieved from different databases.

Single-phase load profiles were generated using residential load data retrieved from the Pecan Street project database. Figure 4.6 shows the residential load profiles of 3 houses on June 1st 2016. Each house has a significantly different load profile. Aggregated residential load profiles for 10 houses, 50 houses, and 80 houses are shown in Figure 4.7. It can be seen that the aggregated load profiles are much smoother than a single house load. Two-phase and three-phase load profiles were generated using commercial and industrial load data. Commercial and industrial load data was retrieved from a database provided by Market Analysis and Information System (MAISY, http://www.maisy.com/demos.htm). More data can be found at OpenEI (http://en.openei.org/wiki/Main_Page) and Buildings Datasets (https://trynthink.github.io/buildingsdatasets/). A sample industrial load profile with the resolution of 15 minute per sample is shown in Figure 4.8.

By aggregating different load profiles, a set of load profiles were generated and used for case studies and performance analysis. A certain penetration of ESS is assumed to be installed for each aggregated load. Similarly, the ESS penetration is defined as the ratio of

the energy stored in an ESS (e.g., rated capacity) over the energy consumed by loads for 24 hours:

$$\gamma^{ESS} = \frac{E^{RATED}}{\int_{t=1}^{24hr} P^{LOAD}(t)dt} \times 100\% \quad (4.2)$$

where E^{RATED} is the rated capacity of ESS, $P^{LOAD}(t)$ is the load demand at time t, γ^{ESS} is the penetration of ESS.

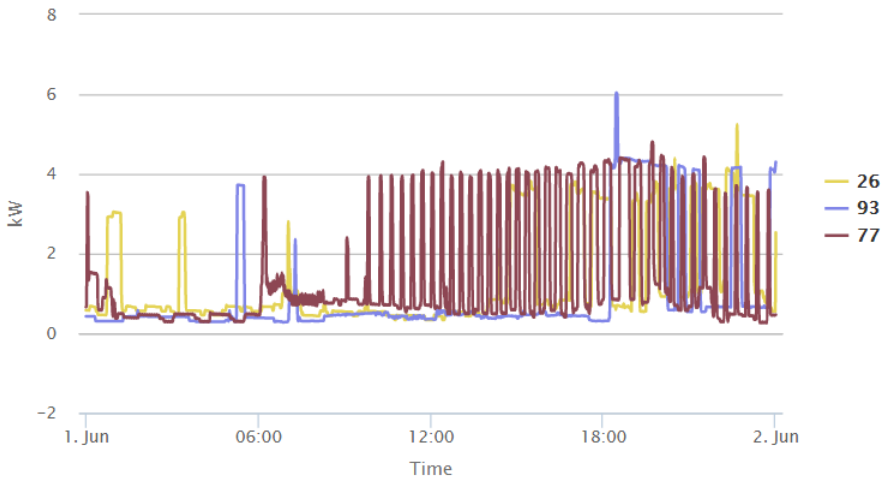

Figure 4.6. Residential load profiles of three houses (No. 25, 93, and 77) on June 1st 2016 [143]

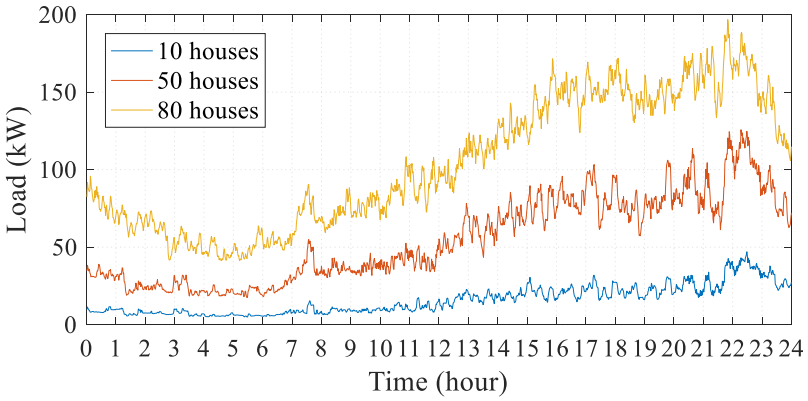

Figure 4.7. Aggregated residential load profiles for 10 houses, 50 houses, and 80 houses [143]

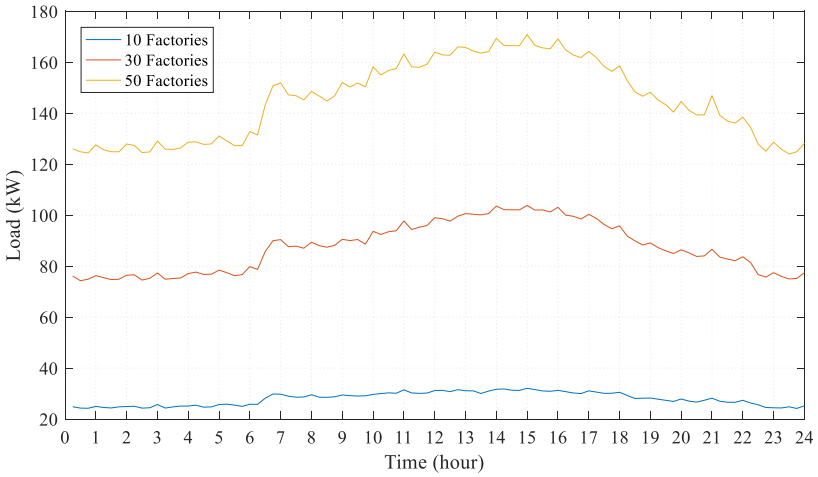

Figure 4.8. Aggregated industrial load profiles for 10 factories, 50 factories, and 80 factories [143]

4.2 Simulation Software Setup

The proposed BSR method incorporates both steady-state constraints (e.g., voltage magnitude limit, line apparent power limit) to ensure the steady-state operation security, and frequency response rate constraint to ensure the dynamic security. The linear models used in the MILP model will significantly reduce the computation efforts, but inevitably introduce approximation errors. The simulation software setups used for verifying the voltage magnitude constraints, line power constraints and frequency constraints are introduced in APPENDIX C.

4.3 Case Studies

In this subsection, six case studies are presented to show how the BSR method works. TABLE 4.8 lists the test system and load model used in each case. In Case I, the capability of the BSR method to coordinate multiple DGs and ESS will be shown. In Case II, different restoration sequences were generated by the BSR method in response to different

initial conditions. In Case III, the BSR method was applied to the unbalanced IEEE 123 node test system with multiple black start DGs. Multiple microgrids were formed. In Case IV, it will be shown that the rolling-horizon procedure can be used for large-scale systems to achieve sub-optimal yet feasible solutions within reasonable time. In Case V, the restoration solutions are compared using three scenarios with different penetrations of PV and ESS. In Case VI, the linear power flow models for both balanced and unbalanced modified IEEE 123 node test systems are validated against OpenDSS.

TABLE 4.8. CASE STUDIES: TEST SYSTEM, LOAD MODEL, AND PURPOSE OF STUDY

Case No.	Test System	Load Model	Purpose of Study
I	Balanced 13 Node	CLPU	Show how to generate the sequence, and coordinate multiple DGs, ESS, and switches
II	Balanced 13 Node	CLPU	Show how to cope with different initial conditions
III	Unbalanced 123 Node	ZIP CLPU	Show the capability of solving unbalanced three-phase systems and form multiple microgrids
IV	Balanced 123 Node	CLPU	Show how the rolling-horizon procedure works
V	Unbalanced 123 Node	CLPU	Show how the renewable DGs and ESS work
VI	Balanced/Unbalanced 123 Node	CLPU ZIP	Validate the linear power flow results (voltage and line power) against OpenDSS results

4.3.1 Case I: Coordinating Multiple DGs and ESS

In Case I, the capability of the proposed BSR method to coordinate multiple DGs and ESS during the restoration process is studied. The purpose of the study is to show how the BSR method coordinates DGs dispatching operations, ESS charging/discharging operations, and line switching operations over multiple time steps. Case I was performed on the balanced modified IEEE 13 node test system. The system parameters for DGs, ESS, lines, and loads can be found in section 4.1.1.1. The initial SOC of the ESS was 83.3%.

The single-line diagram of the test system is shown in Figure 4.9. In Case I, it is assumed that the system was totally de-energized due to a blackout caused by extreme weather events. In addition, line 671-692, line 671-684 and L652 are assumed to be damaged, thus they cannot participate in the restoration. All loads were under CLPU conditions, and the associated CLPU parameters are listed in TABLE 4.5. Rolling-horizon procedure was disabled. The studied time horizon was 10 minutes, with the discrete time step fixed at 1 minute. Note the discrete time step should be determined based on many factors, such as the ramp rates of DGs, control delay for operating switches, and transient responses when restoring loads. In Case I, it is assumed that the decision time step is 1 minute, within which control actions can be performed and transient response has damped out.

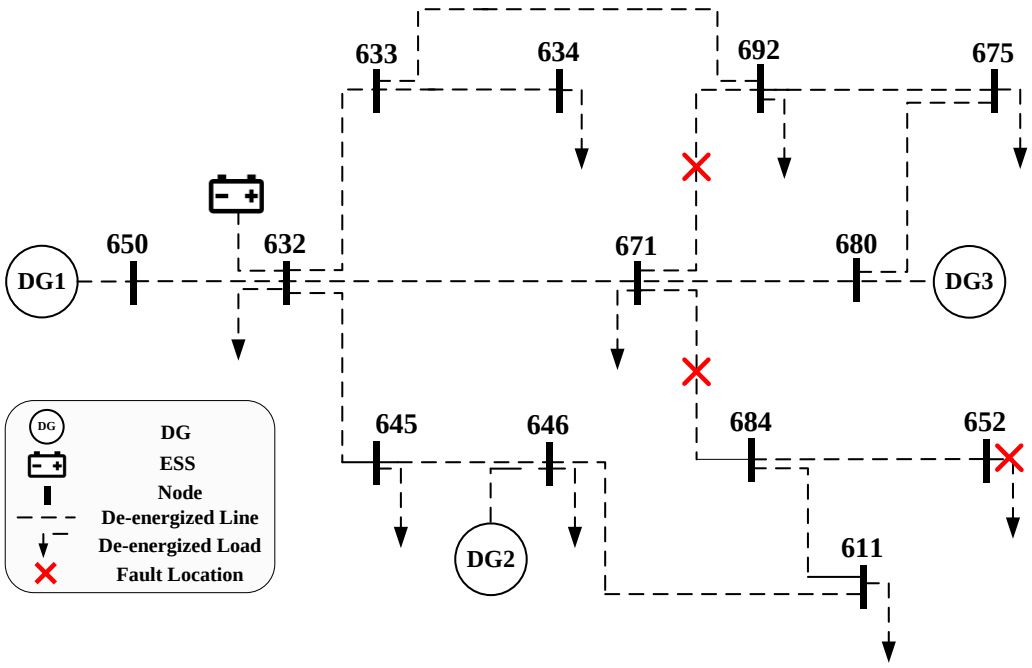

Figure 4.9. Single-line diagram of the balanced modified IEEE 13 node test system used for Case I

In Case I, the restoration solutions for two scenarios are compared to show how the BSR method works. In Scenario I.1, only DG1 connected to the substation node (Node 650) was used for service restoration. In Scenario I.2, three DGs (DG1 on Node 650, DG2 on Node 646, and DG3 on Node 680) and an ESS on Node 632 was considered. The objective function for both scenarios was to maximize the total amount of restored energy over the horizon. The following constraints were simplified to single-phase constraints:

1) Power flow constraints for balanced systems (3.15)-(3.20)
2) CLPU load model constraints (3.25)-(3.26)
3) System operational constraints (3.52)-(3.71)
4) DG operational constraints (3.123)-(3.126)
5) ESS operational constraints (3.127)-(3.134)
6) Topological constraints (3.135)-(3.138)

The restoration solutions for both scenarios in Case I were generated using the implementation framework introduced in section 3.6. The BSR model was formulated based on the DG and ESS parameters, load parameters, and network parameters listed in section 4.1.1.1. Since the system was totally de-energized at the beginning and four components were kept disconnected, the initial condition constraints were updated:

$$x_{ij,t}^{BR} = 0, \quad \forall\, (i,j) \in \mathcal{B}, \;\; t = 1, \tag{4.3}$$

$$x_{671-692,t}^{BR} = 0, \;\; x_{671-684,t}^{BR} = 0, \;\; x_{652,t}^{L} = 0, \quad t = \{1,2,3, \dots 10\}. \tag{4.4}$$

Since DG2, DG3, and ESS were not considered in Scenario I.1, three additional constraints were added to the initial condition constraints for Scenario I.1 to disable DG2, DG3, and ESS:

$$x_{646,t}^{G} = 0, \quad x_{680,t}^{G} = 0, \quad x_{632,t}^{ESS\_CH} + x_{632,t}^{ESS\_DISCH} = 0, \ t = \{1,2,3, \dots 10\}. \quad (4.5)$$

It is assumed that the voltage magnitude on N650 was maintained to be 1.05 p.u.:

$$U_{650,t}^{2} = 1.05^{2}, \ t = \{1,2,3, \dots 10\}. \quad (4.6)$$

The restoration solutions are represented by the decision variables defined in the BSR model such as $x_{ij,t}^{BR}$, $P_{ij,t}^{BR}$, $Q_{ij,t}^{BR}$, $x_{l,t}^{L}$, $P_{l,t}^{L}$, $Q_{l,t}^{L}$, $x_{g,t}^{G}$, $P_{g,t}^{G}$, $Q_{g,t}^{G}$, $x_{e,t}^{ESS\_CH}$, $x_{e,t}^{ESS\_DISCH}$, $P_{e,t}^{ESS\_CH}$, $P_{e,t}^{ESS\_\mathrm{DISCH}}$, $Q_{e,t}^{ESS\_CH}$, and $Q_{e,t}^{ESS\_\mathrm{DISCH}}$. The restoration sequences can be generated based on the values of decision variables. The load demand restored at each time step for Scenario I.1 and Scenario I.2 is shown in Figure 4.10. In Scenario I.1, 73.23 kWh energy was restored. In Scenario 2, 146.01 kWh energy was restored.

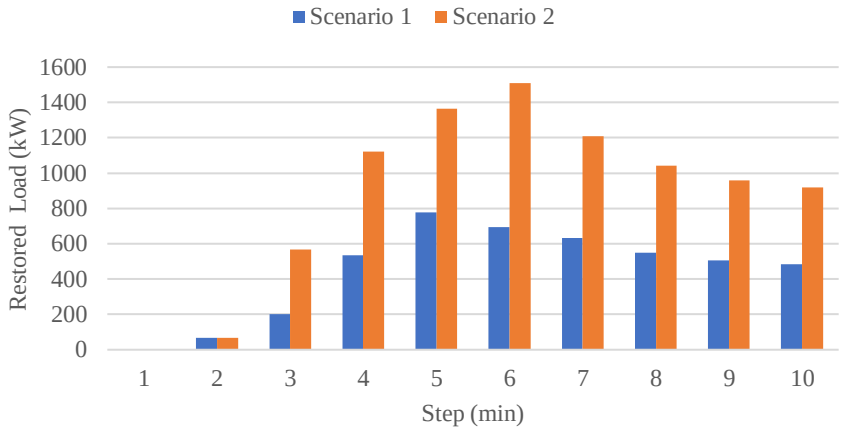

Figure 4.10. Load demand restored at each time step for Scenario I.1 and I.2.

4.3.1.1 Restoration Solution for Scenario I.1

The system diagrams representing the energized systems after implementing the control sequences are shown in Figure 4.11. For each step, the newly energized components are shown in black, and the previously-energized components are shown in grey. It can be seen that six loads (L632, L645, L634, L692, L646, and L611) were restored by the end of the horizon. Next, it will be shown how the BSR method makes decisions on how to optimally restore the loads based on the constraints defined in the BSR model.

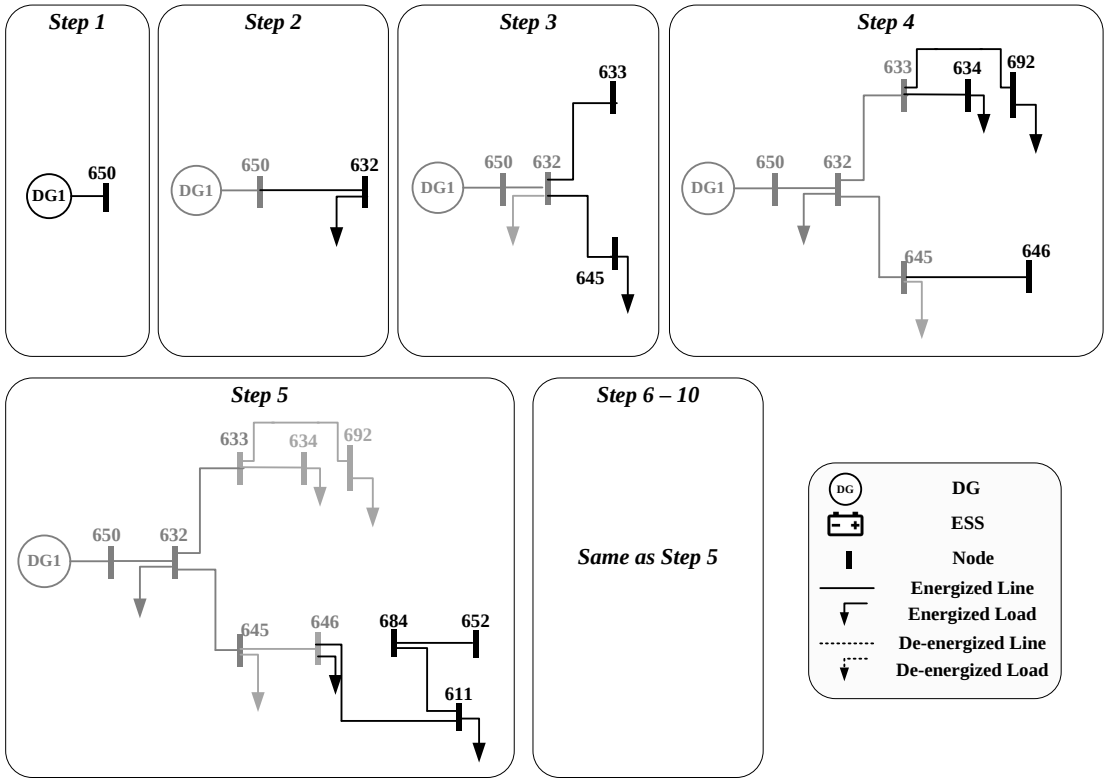

Figure 4.11. System diagrams at each time step in Case I Scenario I.1

In Scenario I.1, the system diagram at Step 1 is shown in Figure 4.12 based on the solution values listed in TABLE 4.9. All lines were de-energized at Step 1. This is because the system was fully de-energized at Step 1 (see equation (4.3)). DG1 was started at Step 1, as required by equation (3.54) in the connectivity constraints. Since no loads were restored at Step 1, power balance constraints formulated by equations (3.17)-(3.18) ensured that DG1 was in idle state. Equation (3.52) ensured the node connected to a black start DG should be energized from Step 1; i.e., $s^N_{650,t} = 1$. The voltage regulated on N650 by DG1 was 1.05 p.u., as required by equation (3.55) in the initial condition constraints. At Step 1, N650 was energized ($s^N_{650,1} = 1$) and N632 was de-energized ($s^N_{632,1} = 0$). Line 650-632 must be de-energized ($x^{BR}_{650-632,1} = 0$) as required by equations (3.61)-(3.64), which ensured that if a line is energized, both its end nodes must be energized. The total load restored was 0 kW at Step 1. So the restored energy at Step 1 was 0 kWh.

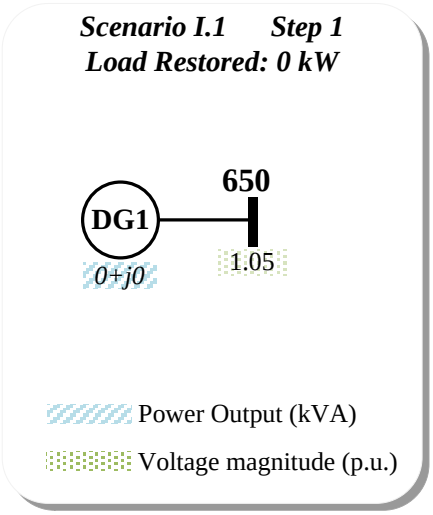

Figure 4.12. System diagram at Step 1 in Scenario I.1

TABLE 4.9. VALUES OF DECISION VARIABLES AT STEP 1 FOR SCENARIO I.1

Binary Variables		Continuous Variables	
Variables	Energized Components	Variables	Values
$x_{ij,t}^{BR}$	None	$P_{ij,t}^{BR} + jQ_{ij,t}^{BR}$ (kVA)	None
$x_{l,t}^{L}$	None	$P_{l,t}^{L} + jQ_{l,t}^{L}$ (kVA)	None
$x_{g,t}^{G}$	DG1	$P_{g,t}^{G} + jQ_{g,t}^{G}$ (kVA)	DG1: 0+j0
$s_{i,t}^{N}$	N650	$V_{i,t}$ (p.u.)	N650: 1.05

The system diagram at Step 2 is shown in Figure 4.13 based on the solution values listed in TABLE 4.10. The apparent power flows through each energized line is represented as a percentage of the line's kVA capacity. The voltage magnitude of each energized node is represented as the per unit value. The system at Step 2 was developed by closing line 650-632 and restoring L632, based on the system energized at Step 1. As shown in Figure 4.13, L632 was restored immediately when line 650-632 was closed. At Step 2, N650 was energized ($s_{650,1}^{N} = 1$) and N632 was de-energized ($s_{632,1}^{N} = 0$). Line 650-632 was closed since the constraints (3.137)-(3.138) ensured that closing a line will always energize a previously de-energized node. Note that closing line 650-632 should also satisfy the line kVA capacity constraint and voltage magnitude constraint.

TABLE 4.10. VALUES OF DECISION VARIABLES AT STEP 2 FOR SCENARIO I.1

Binary Variables		Continuous Variables	
Variables	Energized Components	Variables	Values
$x_{ij,t}^{BR}$	650-632	$P_{ij,t}^{BR} + jQ_{ij,t}^{BR}$ (kVA)	650-632: 66.6+j38.6
$x_{l,t}^{L}$	L632	$P_{l,t}^{L} + jQ_{l,t}^{L}$ (kVA)	L632: 66.6+j38.6
$x_{g,t}^{G}$	DG1	$P_{g,t}^{G} + jQ_{g,t}^{G}$ (kVA)	DG1: 66.6+j38.6
$s_{i,t}^{N}$	N650, N632	$V_{i,t}$ (p.u.)	N650: 1.05 N632: 1.046

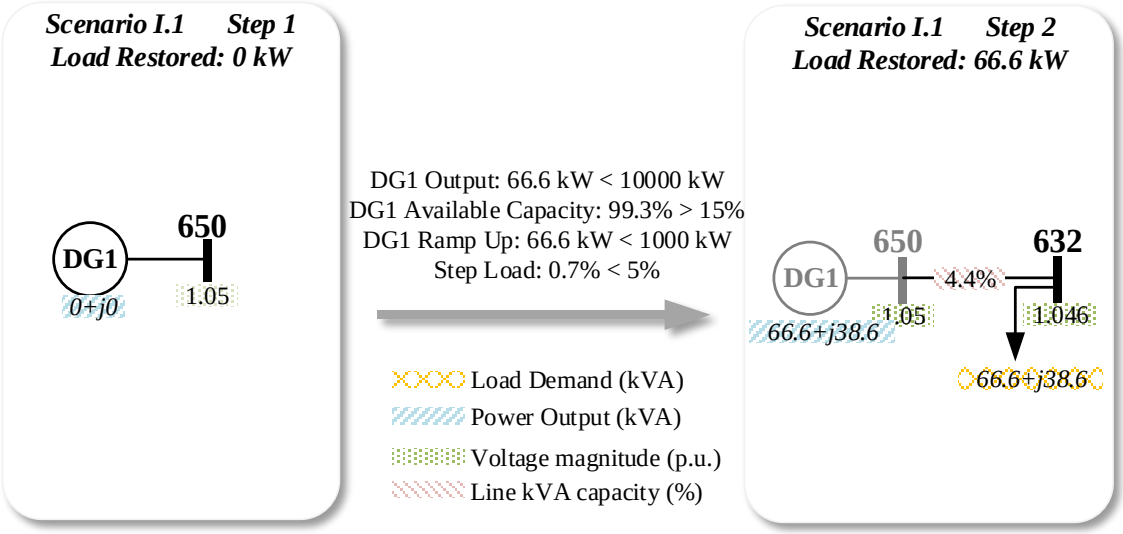

Figure 4.13. System diagrams at Step 1 and Step 2 in Scenario I.1.

Assuming $x^{BR}_{650-632,2} = 1$, $x^{L}_{632,2} = 1$, the linear power flow equations for the system diagram at Step 2 can be formulated as follows.

Power balance based on equations (3.17)-(3.18):

$$P^{G}_{650,2} = P^{BR}_{650-632,2}, Q^{G}_{650,2} = Q^{BR}_{650-632,2} \tag{4.7}$$

$$P^{BR}_{650-632,2} = P^{L}_{632,2}, Q^{BR}_{650-632,2} = Q^{L}_{632,2} \tag{4.8}$$

Voltage difference based on equations (3.15)-(3.16):

$$U_{650,2} - U_{632,2} = 2\left(r_{650-632}P^{BR}_{650-632,2} + x_{650-632}Q^{BR}_{650-632}\right) \tag{4.9}$$

Since $P^{L}_{632,2} + jQ^{L}_{632,2} = 66 + \text{j}38.6$, $U_{650,2} = 1.05^2$, the power flow can be easily solved:

$$P^{BR}_{650-632,2} + jQ^{BR}_{650-632,2} = 66.6 + \text{j}38.6 \tag{4.10}$$

$$P^{G}_{650,2} + jQ^{G}_{650,2} = 66.6 + \text{j}38.6 \tag{4.11}$$

$$V_{650,2} = 1.05, V_{632,2} = 1.046 \quad (4.12)$$

Note the linear power flow equations are integrated in the BSR model, instead of being solved separately. Therefore, as long as a solution can be generated by the BSR method, all the variables associated with power flow equations can be determined, and various constraints can be satisfied. DG related operational constraints (e.g., output capacity, spinning reserving, ramp rate, and maximum step load constraints) must be satisfied in order to restore more loads. These constraint values are shown in Figure 4.13. At last, the load demand used for L632 were determined by CLPU equations (3.20)-(3.26). Given the CLPU parameters determined for L632, L_{632} in equation (3.22) was calculated as:

$$L_{632} = \begin{Bmatrix} 66.6 + j38.6, 66.6 + j38.6, 53.19 + j30.83, 46.53 + j26.97, 43.22 + j25.05, \\ 41.58 + j24.10, 40.76 + j23.63, 40.35 + j23.39, 40.16 + j23.27, \dots \end{Bmatrix} \quad (4.13)$$

Δl_{632} was calculated in equation (3.21) and used for formulating the CLPU model:

$$L_{632} = \begin{Bmatrix} 0 + j0, 0 + j0, -13.41 - j7.77, -6.66 - j3.86, -3.31 - j1.92, \\ -1.64 + j - 0.95, -0.82 - j0.47, -0.40 - j0.23, -0.2 - j0.12, \dots \end{Bmatrix} \quad (4.14)$$

Then $P_{632,2}^{L} + jQ_{632,2}^{L}$ can be integrated into the BSR model using equations (3.25)-(3.26). A load must be kept energized after being restored. Therefore, once a load is restored, its demand profile during the following steps can be known. The load demand of L632 (vertical axis) at each step (horizontal axis) is shown in Figure 4.14. It is important to know that restoring L632 at Step 2 was determined by solving the BSR model. It is not possible to directly use the values in Figure 4.14 in the BSR model. Instead, $P_{632,2}^{L}$ and $Q_{632,2}^{L}$ should be formulated as variables and their values will be known after the BSR

model is solved. The total amount of load demand restored at Step 2 was 66.6 kW. Since the interval was 1 minute, the restored energy at Step 2 is 1.11 kWh.

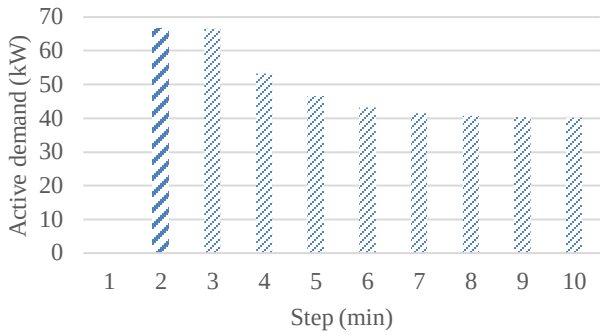

Figure 4.14. Load profile of L632 in Scenario I.1. L632 was restored at Step 2 and will change during the following steps under CLPU conditions The load profile was determined by the CLPU parameters.

The system diagram at Step 3 is shown in Figure 4.15 based on the solution values listed in TABLE 4.11. Similarly, line 632-633 and line 632-645 were closed to a previously energized node N632 to energize N633 and N645, respectively. L645 was restored when N645 was energized, as required by equation (3.58). Note that the demand of L671 on N671 (502.1 kW) is much larger than L645 (136.1 kW), restoring L671 by closing line 632-671 at Step 3 may restore more load demand. However, line 632-671 was not energized at Step 3, because restoring L671 could violate the maximum step load constraints. At Step 3, the maximum permissive step load, according to equation (3.84), can be calculated as: $P_{DG1}^{max} \times 5\% = 500\ kW$, which was smaller than the step load demand (502.1 kW) if restoring L671. In Scenario I.2, it will be shown that by energizing ESS, the maximum permissive step load will become larger, and allow to safely restore L671. The

voltage magnitudes and line powers were maintained within the permissive ranges, as shown in Figure 4.15. Again, the values of voltage magnitudes and line powers were known when the BSR model was solved, since the power flow equations were formulated as a part of the optimization problem. Operational constraints defined for DGs (e.g., output capacity, spinning reserving, ramp rate, and maximum step load constraints) were satisfied at Step 3. The load demands used for L632 and L645 at Step 3 were determined by CLPU equations (3.20)-(3.26), as shown in Figure 4.16. Note that the demands for L532 and L645 will decrease in the following steps. Each demand profile was calculated using the CLPU parameters specified for each load. The amount of restored load at Step 3 was 202.68 kW.

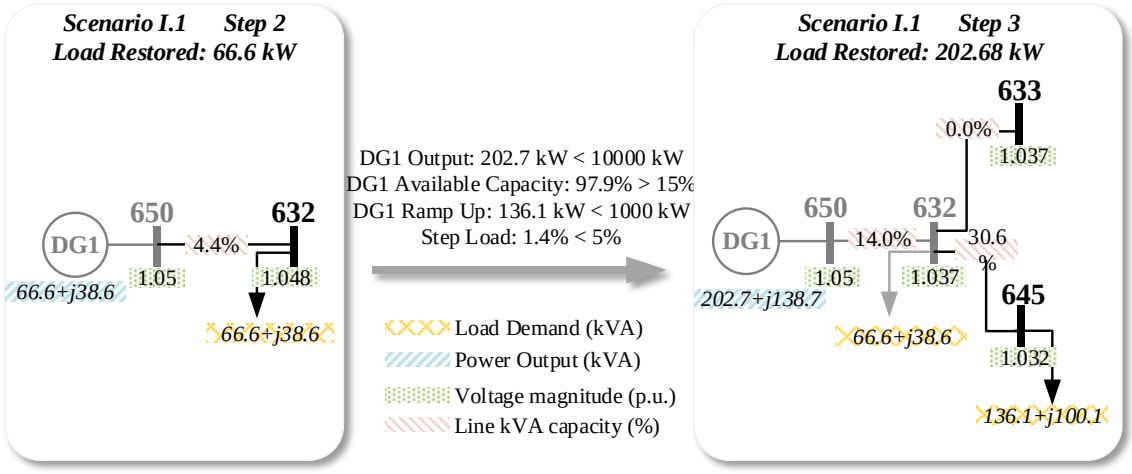

Figure 4.15. System diagrams at Step 2 and Step 3 in Scenario I.1.

TABLE 4.11. VALUES OF DECISION VARIABLES AT STEP 3 FOR SCENARIO I.1

Binary Variables		Continuous Variables	
Variables	Energized Components	Variables	Values
$x_{ij,t}^{BR}$	650-632, 632-633, 632-645	$P_{ij,t}^{BR} + jQ_{ij,t}^{BR}$ (kVA)	650-632: 202.68+j138.68 632-633: 0+j0 632-645: 136.08+j100.08
$x_{l,t}^{L}$	L632, L645	$P_{l,t}^{L} + jQ_{l,t}^{L}$ (kVA)	L632: 66.6+j38.6 L645: 136.08+j100.08
$x_{g,t}^{G}$	DG1	$P_{g,t}^{G} + jQ_{g,t}^{G}$ (kVA)	DG1: 202.68+j138.68
$s_{i,t}^{N}$	N650, N632, N633, N645	$V_{i,t}$ (p.u.)	N650: 1.05 N632:1.037 N633:1.037 N645: 1.032

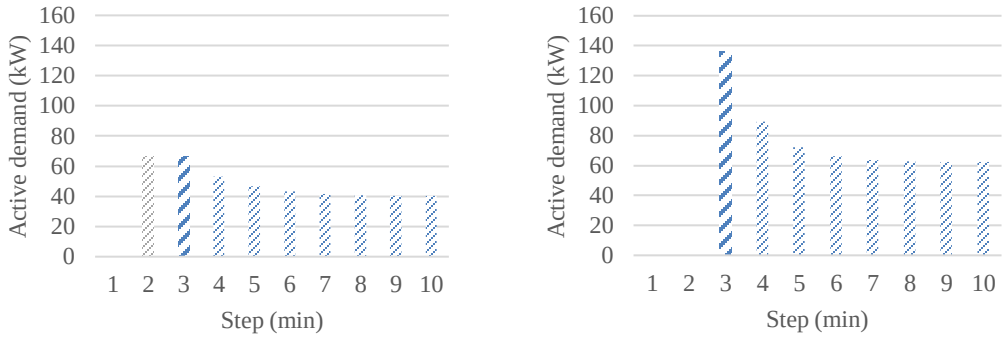

(a) (b)

Figure 4.16. Load profile of L632 and L645 in Scenario I.1. L632 was restored at Step 2, L645 was restored at Step 3. They will change during the following steps under CLPU conditions. (a): L632; (b): L645

The system diagram at Step 4 is shown in Figure 4.17 based on the solution values listed in TABLE 4.12. N634, N692, and N646 were energized at Step 4. It can be found that restoring all the three loads will cause a 584.3 kW step load and violate the maximum step load constraints. Restoring L634 and L692 will cause a 392.5 kW step load, which is smaller than the step load of 431.2 kW caused by restoring L634 and L646. However, L634 and L692 were restored, L646 was not restored. It seems like the solution generated

by the BSR method made a suboptimal choice at this step, because less load demand was restored at this step. However, more energy can be restored over the horizon if restoring L692 instead of L646 at Step 3. Figure 4.18 compares the values of the objective function when L692 was restored as Step 4, or when L646 was restored at Step 4. This was done by adding an additional constraint into the initial condition constraints: $x_{646,4}^{L} = 1$. It can be observed that the original solution restored more energy. Indeed, since the objective function was to maximize the total amount of restored energy over the horizon, the most intuitive strategy is to restore as much load demand as possible at each step. However, the BSR method can make decisions on when to restore each load over multiple time steps to generate unintuitive yet optimal solutions.

TABLE 4.12. VALUES OF DECISION VARIABLES AT STEP 4 FOR SCENARIO I.1

Binary Variables		Continuous Variables	
Variables	Energized Components	Variables	Values
$x_{ij,t}^{BR}$	650-632,632-633,633-634, 632-645, 645-646, 633-692	$P_{ij,t}^{BR} + jQ_{ij,t}^{BR}$ (kVA)	650-632: 535.71+j406.51 632-633: 393.03+j309.87 633-634:239.94+j174.06 632-645: 89.49+j65.81 645-646:0+j0 633-692: 153.09+j135.81
$x_{l,t}^{L}$	L632, L645, L634, L692	$P_{l,t}^{L} + jQ_{l,t}^{L}$ (kVA)	L632: 53.18+j30.83 L645: 89.49+j65.81 L634:239.94+j174.06 L692:153.09+j135.81
$x_{g,t}^{G}$	DG1	$P_{g,t}^{G} + jQ_{g,t}^{G}$ (kVA)	DG1: 535.71+j406.51
$s_{i,t}^{N}$	N650, N632, N633, N634, N645, N646, N692	$V_{i,t}$ (p.u.)	N650: 1.05 N632:1.012 N633:1.001 N634: 0.963 N645: 1.008 N646:1.008 N692:1.001

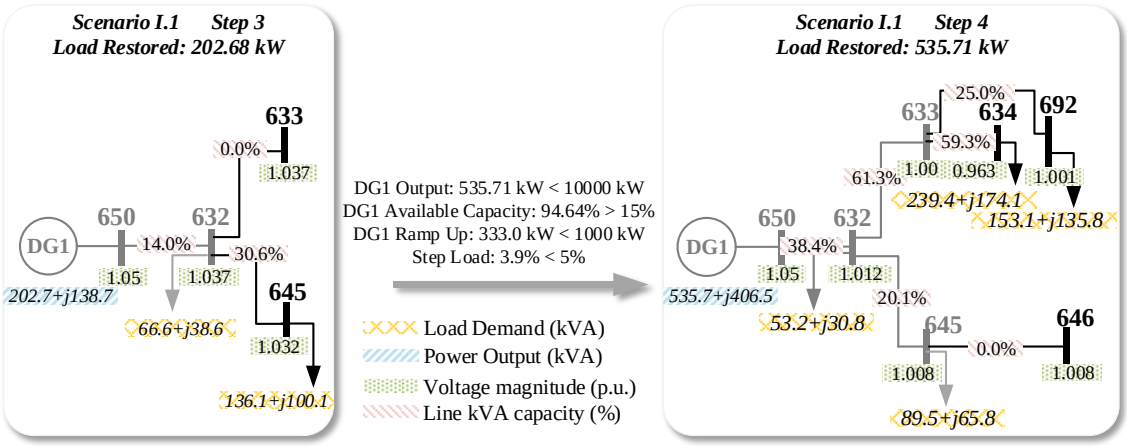

Figure 4.17. System diagrams at Step 3 and Step 4 in Scenario I.1

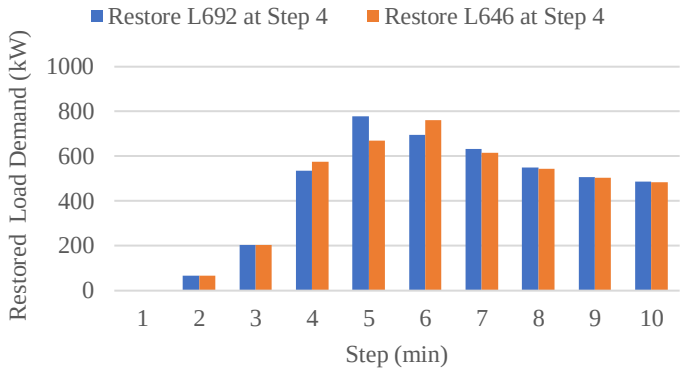

Figure 4.18. Load demand restored at each step for different loads (L692 vs L646) restored at Step 4

The system diagram at Step 5 is shown in Figure 4.19 based on the solution values listed in TABLE 4.13. In Step 5, L646 was restored. Note N646 was energized at Step 4. It has been shown that doing so can restore more energy over the entire horizon than restoring L646 at Step 4. At Step 5, line 646-611 was closed to energize N611. Note line 611-684 and line 684-652 were energized as well. This is because both lines are non-

switchable lines, and constraints (3.63)-(3.64) require that a non-switchable line must be energized immediately as long as one of its end nodes is energized.

TABLE 4.13. VALUES OF DECISION VARIABLES AT STEP 5 FOR SCENARIO I.1

Binary Variables		Continuous Variables	
Variables	Energized Components	Variables	Values
$x_{ij,t}^{BR}$	650-632,632-633,633-634, 632-645, 645-646, 633-692, 646-611, 611-684, 684-652	$P_{ij,t}^{BR} + jQ_{ij,t}^{BR}$ (kVA)	650-632: 779.24+j517.53 632-633: 349.54+j271.29 633-634:239.94+j174.06 632-645: 383.17+j219.28 645-646: 310.82+j166.07 633-692: 109.6+j97.23 646-611:119.07+j56.07 611-684:0+j0 684-652:0+j0
$x_{l,t}^{L}$	L632, L645, L634, L692	$P_{l,t}^{L} + jQ_{l,t}^{L}$ (kVA)	L632: 46.53+j26.97 L645: 72.35+j53.21 L634 :239.94+j174.06 L692: 109.6+j97.23 L646:191.75+j110 L611:119.07+j56.07
$x_{g,t}^{G}$	DG1	$P_{g,t}^{G} + jQ_{g,t}^{G}$ (kVA)	DG1:779.24+j517.53
$s_{i,t}^{N}$	N650, N632, N633, N634, N645, N646, N692, N611, N684, N652	$V_{i,t}$ (p.u.)	N650: 1.05 N632:0.999 N633:0.989 N634: 0.951 N645: 0.985 N646:0.979 N692:0.989 N611:0.979 N684:0.979 N652:0.979

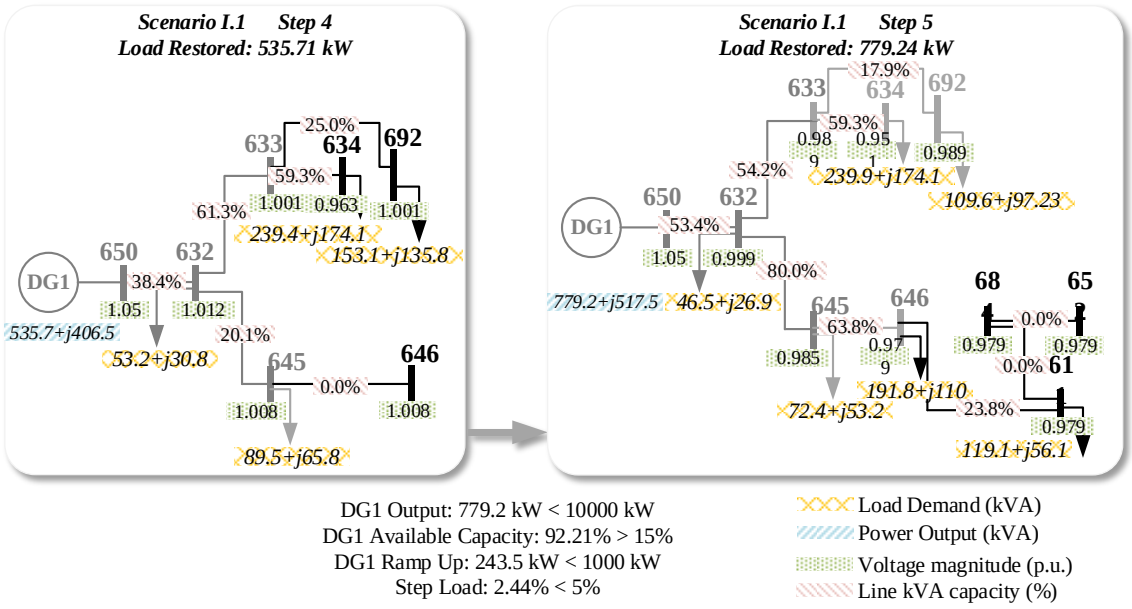

Figure 4.19. System diagrams at Step 4 and Step 5 in Scenario I.1

In Scenario I.1, no loads were restored after Step 5. All the energized loads decreased by following their CLPU profiles. All load profiles at each step are shown in Figure 4.20. The load profile for each load is presented as a cluster on the horizontal axis. Within each cluster, the load demand at each step is shown. In Scenario I.1, six loads were restored by Step 10. Loads were scheduled to be restored at different steps, and presented changing load demand under CLPU conditions. The node voltages at each step for Scenario I.1 are illustrated in Figure 4.21. The voltage profile at each node is presented as a cluster on the horizontal axis. Within each cluster, the voltage magnitude at each step is shown. The node voltage of each node was maintained between 0.95 and 1.05 p.u. In addition, voltage at each node increased starting from Step 5, because no more loads were restored and all restored loads were decreased under CLPU conditions.

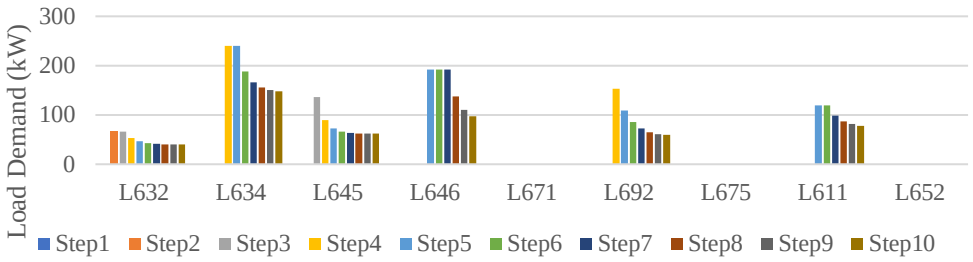

Figure 4.20. Active power load profiles for each load at each step in Scenario I.1. Loads were scheduled to be restored at different steps, and presented changing load demand under CLPU conditions

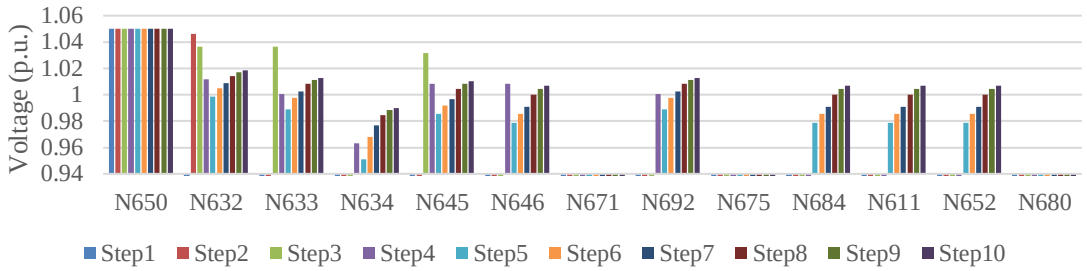

Figure 4.21. Node voltage at each step during restoration in Scenario I.1. Voltage at each node increased starting from Step 5, because no more loads were restored and all restored loads were decreased under CLPU conditions

4.3.1.2 Restoration Solution for Scenario I.2

The system diagrams representing the energized systems after implementing the control sequences are shown in Figure 4.22. For each step, the newly energized components are shown in black, and the previously-energized components are shown in grey. It can be seen that all loads except L652 were restored. Non-black start DGs and ESS were started at different steps. Next, it will be shown how the BSR method can coordinate DGs, ESS, and switches at each step and across multiple steps.

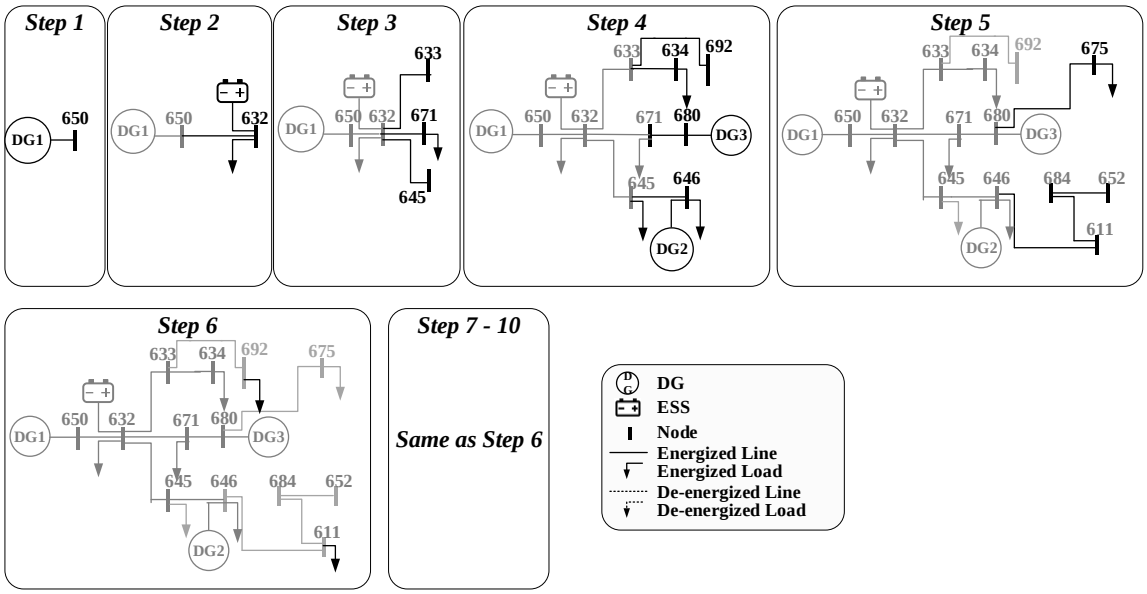

Figure 4.22. System diagrams at each time step in Case I Scenario I.2

The system diagram at Step 1 in Scenario I.2 is the same as in Scenario I.1. The system diagram at Step 2 is shown in Figure 4.23, based on the values of the variables listed in TABLE 4.14. In Scenario I.2, similar constraints that have been introduced for Scenario I.1 were still applied. Therefore, the system operations specified for Scenario I.2 were formulated into the initial condition constraints. Hence, only DG1 was started at Step1 and N650 was energized. At Step 2, ESS on N632 was started. Note the ESS is assumed to be a non-black start unit, thus it is constrained by equation (3.56) that requires an ESS can only charge and discharge power when its terminal node is energized. Equation (3.56) also ensured the ESS can only be charged or discharged for during a single step. It can be seen that the ESS was in charging state at Step 2, and the SOC of the ESS by Step 2 was 93.3%. The power flow results for the system diagram at Step 2 indicate that the voltage on each energized node and the line power for each energized line were kept within the

permissive ranges. The total restored load at Step 2 was 66.6 kW. Note the ESS charging power was not counted as the restored load.

TABLE 4.14. VALUES OF DECISION VARIABLES AT STEP 2 FOR SCENARIO I.2

Binary Variables		Continuous Variables	
Variables	Energized Components	Variables	Values
$x_{ij,t}^{BR}$	650-632	$P_{ij,t}^{BR} + jQ_{ij,t}^{BR}$ (kVA)	650-632:166.6+j38.6
$x_{l,t}^{L}$	L632	$P_{l,t}^{L} + jQ_{l,t}^{L}$ (kVA)	L632: 66.6+j38.6
$x_{g,t}^{G}$	DG1	$P_{g,t}^{G} + jQ_{g,t}^{G}$ (kVA)	DG1: 166.6+j38.6
$x_{e,t}^{ESS\_CH}$	ESS on 632	$P_{e,t}^{ESS\_CH} + jQ_{e,t}^{ESS\_CH}$ (kVA)	ESS: 100+j0
$x_{e,t}^{ESS\_DISCH}$	None	$P_{e,t}^{ESS\_DISCH} + jQ_{e,t}^{ESS\_DISCH}$ (kVA)	ESS: 0+j0
		$SOC_{e,t}$	ESS: 90.8%
$s_{i,t}^{N}$	N650, N632	$V_{i,t}$ (p.u.)	N650: 1.05 N632: 1.044

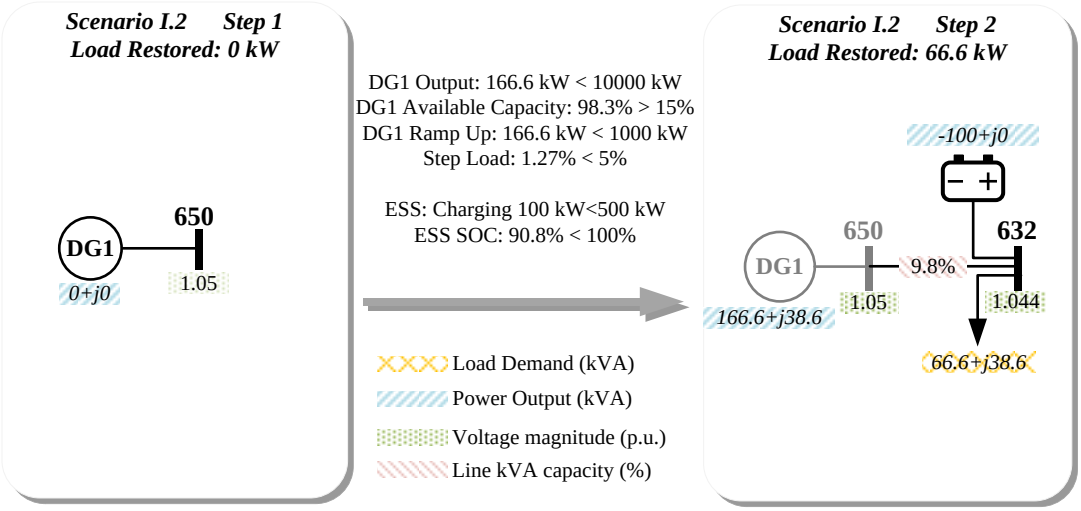

Figure 4.23. System diagrams at Step 1 and Step 2 in Scenario I.2

The system diagram at Step 3 is shown in Figure 4.24, based on the values of the variables listed in TABLE 4.15. Different from Scenario I.1, L671 was restored. The load demand of L671 was 502.1 kW under CLPU conditions. Since the ESS was in discharging state, according to equation (3.84), the maximum permissive step load at Step 3 was 525 kW. Therefore, L671 can be restored without causing excessive frequency drop. L645 was not restored together with L671, otherwise the maximum step load constraints may be violated. Note DG1 and ESS shared the load demand at this step. Therefore, the power went through line 650-532 (26.5% of the line's kVA capacity) was smaller than line 632-671 (31.8% of the line's kVA capacity). Power flow equations and associated operational constraints ensured voltage magnitudes and line powers were maintained within the specified ranges.

TABLE 4.15. VALUES OF DECISION VARIABLES AT STEP 3 FOR SCENARIO I.2

Binary Variables		Continuous Variables	
Variables	Energized Components	Variables	Values
$x_{ij,t}^{BR}$	650-632, 632_633, 632-645, 632-671	$P_{ij,t}^{BR} + jQ_{ij,t}^{BR}$ (kVA)	650-632:368.7+j282.4 632-633:0+j0 632-645:0+j0 632-671:502.1+j243.8
$x_{l,t}^{L}$	L632, L671	$P_{l,t}^{L} + jQ_{l,t}^{L}$ (kVA)	L632: 66.6+j38.6 L671: 502.1+j243.8
$x_{g,t}^{G}$	DG1	$P_{g,t}^{G} + jQ_{g,t}^{G}$ (kVA)	DG1: 368.7+j282.4
$x_{e,t}^{ESS\_CH}$	None	$P_{e,t}^{ESS\_CH} + jQ_{e,t}^{ESS\_CH}$ (kVA)	ESS: 0+j0
$x_{e,t}^{ESS\_DISCH}$	ESS on 632	$P_{e,t}^{ESS\_DISCH} + jQ_{e,t}^{ESS\_DISCH}$ (kVA)	ESS:200+j0
		$SOC_{e,t}$	ESS: 72.3%
$s_{i,t}^{N}$	N650, N632, N633, N645, N671	$V_{i,t}$ (p.u.)	N650: 1.05 N632: 1.024 N633:1.024 N645:1.024 N671:0.996

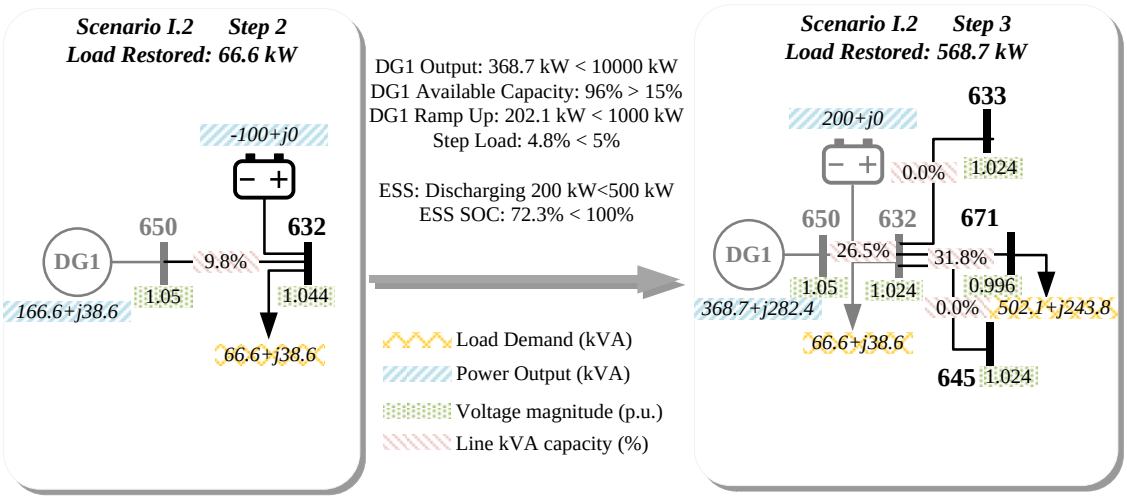

Figure 4.24. System diagrams at Step 2 and Step 3 in Scenario I.2

The system diagram at Step 4 is shown in Figure 4.25, based on the values of the variables listed in TABLE 4.16. At Step 4, both DG2 on N646 and DG3 on N680 were started to share the load demand and increase the maximum permissive step load, which was 600 kW at Step 4. L645, L646, and L634 were restored. L692 was not restored to avoid violating the maximum step load constraint. All the DGs and ESS were dispatched to share the load demand and ensure all the operational constraints were satisfied. For example, DG3 outputted *300+j225 kVA*, which was transmitted through line 671-680. Then, L671 was fed by the power transmitted from line 632-671 and line 671-680. DG2 on N646 outputted *439.1+j329.3* kVA, which was sufficient for support the local load L646 and the load L645. The remaining power (111.2+j119.2 kVA) was transmitted through line 632-645 to support other loads. In addition, the voltage magnitudes on each node were boosted, since DG2 and DG3 outputted reactive power locally.

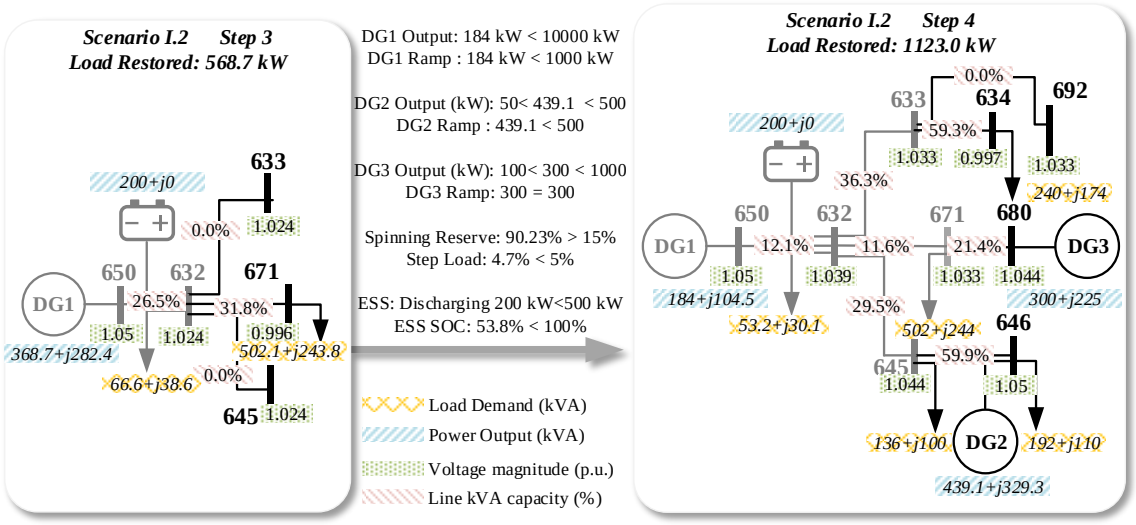

Figure 4.25. System diagrams at Step 3 and Step 4 in Scenario I.2

TABLE 4.16. VALUES OF DECISION VARIABLES AT STEP 4 FOR SCENARIO I.2

Binary Variables		Continuous Variables	
Variables	Energized Components	Variables	Values
$x_{ij,t}^{BR}$	650-632, 632_633, 632-645, 632-671, 633-634, 645-646, 671-680, 633-692	$P_{ij,t}^{BR} + jQ_{ij,t}^{BR}$ (kVA)	650-632:184+j104.5 632-633: 239.9+j174.1 632-645: 111.2+j119.2 632-671:202.1+j18.8 633-634:239.9+j174.1 645-646:247.3+j219.3 671-680:300+j225 633-692:0+j0
$x_{l,t}^{L}$	L632, L671, L634, L645, L646	$P_{l,t}^{L} + jQ_{l,t}^{L}$ (kVA)	L632: 53.2+j30.8 L671: 502.1+j243.8 L634: 239.9+j174.1 L645: 136.1+j100.1 L646: 191.8+j110
$x_{g,t}^{G}$	DG1, DG2, DG3	$P_{g,t}^{G} + jQ_{g,t}^{G}$ (kVA)	DG1: 184+j104.5 DG2: 439.1+j329.3 DG3: 300+j225
$x_{e,t}^{ESS\_CH}$	None	$P_{e,t}^{ESS\_CH} + jQ_{e,t}^{ESS\_CH}$ (kVA)	ESS: 0+j0
$x_{e,t}^{ESS\_DISCH}$	ESS on 632	$P_{e,t}^{ESS\_DISCH} + jQ_{e,t}^{ESS\_DISCH}$ (kVA)	ESS:200+j0
		$SOC_{e,t}$	ESS: 53.8%
$s_{i,t}^{N}$	N650, N632, N633, N645, N671, N634, N646, N692, N680	$V_{i,t}$ (p.u.)	N650: 1.05 N632: 1.039 N633:1.033 N645:1.044 N671:1.033 N634:0.997 N646:1.05 N692:1.033 N680:1.044

The system diagram at Step 5 is shown in Figure 4.26, based on the values of the variables listed in TABLE 4.17. N675, N611, N684, and N652 were energized. Again, the maximum step load constraint prevented L675, L692, and L611 from being restored at the same step. L675 was restored, whereas L692 and L611 were restored at the next step. At Step 5, all the DGs and ESS continued coordinating to share the load demand. Note the load profiles for each restored load were changing at each step based on their particular CLPU parameters. It can be observed that the load demands of L632, L671, L645 at Step 5 were smaller than the load demands at Step 4. Load demands for L634 and L646 were the same as at Step 4, because they were still gaining diversity. Note the constraints (3.138) do not allow a line to be closed if both of its end nodes are energized in previous steps, in order to maintain the tree topology of each isolated microgrid and avoid forming loops. At Step 6, on more lines were energized. Only L692 and L611 were restored. Again, the load demands for each restored load were changing during the following steps, and DGs and ESS were coordinated at each step to make sure all the constraints were satisfied.

All the load profiles at each step are shown in Figure 4.27. The load profile for each load is presented as a cluster on the horizontal axis. With each cluster, the load demand at each step is shown. A total of 8 loads were restored, except L652, which is assumed to be disconnected. The Node voltages at each step for Scenario I.2 are illustrated in Figure 4.28. The voltage profile at each node is presented as a cluster on the horizontal axis. Within each cluster, the voltage magnitude at each step is shown.

TABLE 4.17. VALUES OF DECISION VARIABLES AT STEP 5 FOR SCENARIO I.2

Binary Variables		Continuous Variables	
Variables	Energized Components	Variables	Values
$x_{ij,t}^{BR}$	650-632, 632_633, 632-645, 632-671, 633-634, 645-646, 671-680, 633-692, 684-611, 684-652, 646-611, 675-680	$P_{ij,t}^{BR} + jQ_{ij,t}^{BR}$ (kVA)	650-632:828.4+j564.6 632-633: 239.9+j174.1 632-645: 231.2+j138.2 632-671:510.7+j225.3 633-634:239.9+j174.1 645-646:141.8+j72.5 671-680:215.1+j81.7 633-692:0+j0 684-611:0+j0 684-652:0+j0 646-611:0+j0 675-680:501.8+j296.8
$x_{l,t}^{L}$	L632, L671, L634, L645, L646, L675	$P_{l,t}^{L} + jQ_{l,t}^{L}$ (kVA)	L632: 46.5+j27.0 L671: 295.6+j143.6 L634: 239.4+j174.1 L645: 89.5+j65.8 L646: 191.8+j110 L675: 501.8+j296.8
$x_{g,t}^{G}$	DG1, DG2, DG3	$P_{g,t}^{G} + jQ_{g,t}^{G}$ (kVA)	DG1: 828.4+j564.6 DG2: 50+j37.5 DG3: 286.8+j215.1
$x_{e,t}^{ESS\_CH}$	None	$P_{e,t}^{ESS\_CH} + jQ_{e,t}^{ESS\_CH}$ (kVA)	ESS: 0+j0
$x_{e,t}^{ESS\_DISCH}$	ESS on 632	$P_{e,t}^{ESS\_DISCH} + jQ_{e,t}^{ESS\_DISCH}$ (kVA)	ESS:200+j0
		$SOC_{e,t}$	ESS: 35.3%
$s_{i,t}^{N}$	N650, N632, N633, N645, N671, N634, N646, N692, N680, N675, N684, N611, N652	$V_{i,t}$ (p.u.)	N650: 1.05 N632: 0.994 N633:0.988 N645:0.986 N671:0.967 N634:0.95 N646:0.983 N692:0.988 N680:0.962 N675:0.962 N684:0.983 N611:0.983 N652:0.983

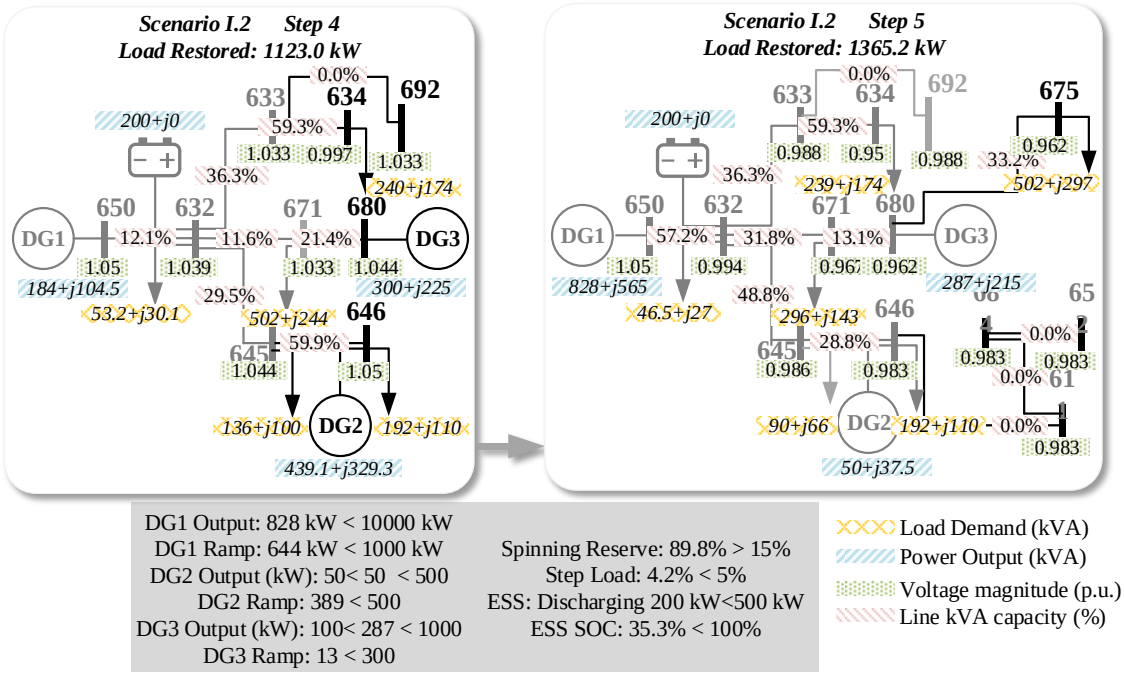

Figure 4.26. System diagrams at Step 4 and Step 5 in Scenario I.2

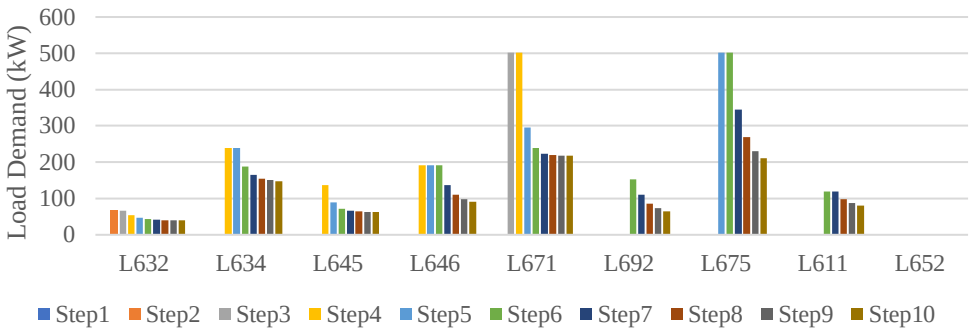

Figure 4.27. Active power load profiles for each load at each step in Scenario I.2. Loads were scheduled to be restored at different steps, and presented changing load demand under CLPU conditions.

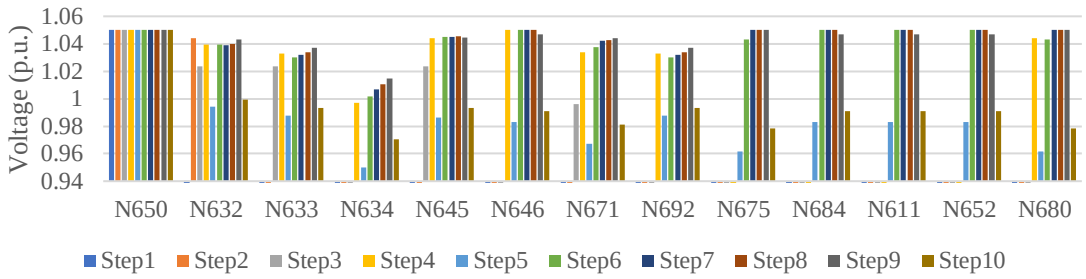

Figure 4.28. Node voltage at each step during restoration in Scenario I.2

The SOC of the ESS on N632 in Scenario I.2 is shown in Figure 4.29. It can be seen that the ESS charged at Step 2 to increase SOC, then discharged from Step 3 to Step 6 in order to facilitate the restoration. The ESS stopped discharging by Step 6, because the SOC at Step 6 was 10%, which is the lower SOC limit. Therefore, the ESS charged again to absorb energy from the grid at Step 7 and Step 8. Note the charging and discharging actions were coordinated with other control actions for DGs, loads, and switches.

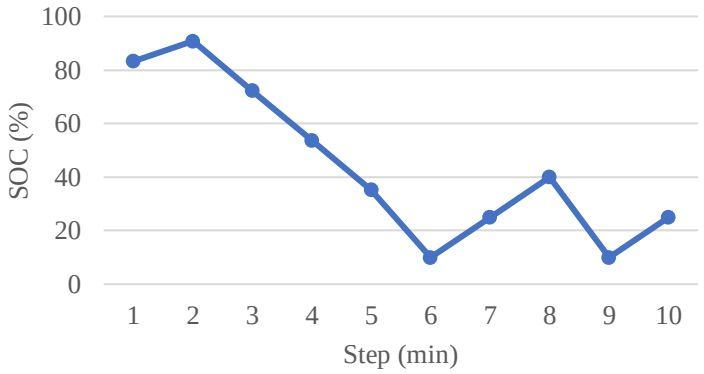

Figure 4.29. SOC of the ESS on N632 in Scenario I.2.

In summary, in Case I, the restoration solutions for restoring loads for two scenarios in a small three-phase balanced test system were discussed. Specifically, in Scenario I.1, how the system is energized at each step is explained based on the solution values and equations defined in the BSR model. In Scenario I.2, the capability of the BSR method to coordinate dispatchable DGs, ESS, loads and switches for service restoration is illustrated. The proposed BSR method can generate a sequence of control actions that optimally coordinate various controllable components to achieve an optimal restoration solution. Meanwhile, the control sequence ensures that various operational constraints are satisfied during the restoration process. In some cases, a load may be scheduled to be restored several steps later even if its terminal node is energized already, so as to maximize the overall restored energy.

4.3.2 Case II: Different Initial Conditions

In Case II, restoration sequences were generated by the BSR method in response to different initial conditions, such as fault components, DG locations, and line configurations. The test system used in Case II was the balanced modified IEEE 13 node test system. The system parameters for DGs, lines, and loads can be found in section 4.1.1.1. ESS was not considered. The scenarios studied in Case II are summarized in TABLE 4.18. In Scenario II.1, all the components were assumed to be switchable. In Scenario II.2, four lines were assumed to be directly interconnected. In Scenario II.3, four lines were assumed to be damaged and disconnected, so they cannot participate in the restoration. In Scenario II.4, a node was assumed to be damaged (e.g., a power pole is blown down, or a substation is flooded). All the lines connected to the damaged nodes

should be disconnected, until the damaged components are repaired. In Scenario II.5, partial system was assumed to be energized before initiating the service restoration. In Scenario II.6, the black start DG originally located on N650 was relocated to N671. The studied time horizon was 10 minutes, with the discrete time step fixed at 1 minute. In all the scenarios except Scenario II.5, the system was assumed to be totally de-energized due to a blackout caused by extreme weather events. All loads were assumed to be switchable and under CLPU conditions. The rolling-horizon procedure was disabled. The objective function and the constraints in the BSR model were the same as in Scenario I.2 of Case I.

TABLE 4.18. SCENARIOS STUDIED IN CASE II

Scenario No.	Description
II.1	No failed components, all lines are switchable.
II.2	Lines 671-692, 692-675, 671-684, 684-611 are directly connected to their end nodes.
II.3	Lines 671-692, 692-675, 671-684, 684-611 are damaged and disconnected. These lines cannot be energized during the restoration process.
II.4	Node 671 is damaged and isolated. Any lines connected to Node 671 (671-632, 671-692, 671-680, and 671-684) should be disconnected.
II.5	Partial system (Lines 650-532, 632-633, 632-671, 632-645) is energized before initiating the service restoration.
II.6	Black start DG is allocated on N671.

4.3.2.1 Scenario II.1: All the Lines Were Switchable

The single-line system diagrams at each step are shown in Figure 4.30. At each step, newly energized components are colored in black, and components energized during previous steps are colored in gray. It can be observed that all the 13 nodes were energized within 5 steps. However, to avoid violating the constraints defined in the BSR model, some switchable loads were scheduled to be restored at different steps. At Step 1, only the

black start DG on N650 was started. N632 was energized at Step 2 by closing line 650-632. L632 was restored when N632 was energized. At Step 4, only three loads (L632, L645, and L671) were restored. L634 and L692 were scheduled to be restored at Step 5. At Step 5, although all the nodes were energized, L646, L611, and L652 were not restored, since the maximum step load constraints prevented them from being restored all together. In addition, the tree topology was maintained at each step. DG active and reactive power outputs and load demands at each step are summarized in TABLE 4.19 and TABLE 4.20. Zero values represent DGs and loads were in de-energized status. At each step, both active and reactive load demand were balanced by black start DGs and dispatchable DGs. For each load, the load demand decreased after being restored according to its CLPU parameters. Node voltages and apparent line powers are summarized in TABLE 4.21 and TABLE 4.22. Zeros values represent a node or a line was de-energized. Both voltages and line apparent powers were maintained within the operating limits.

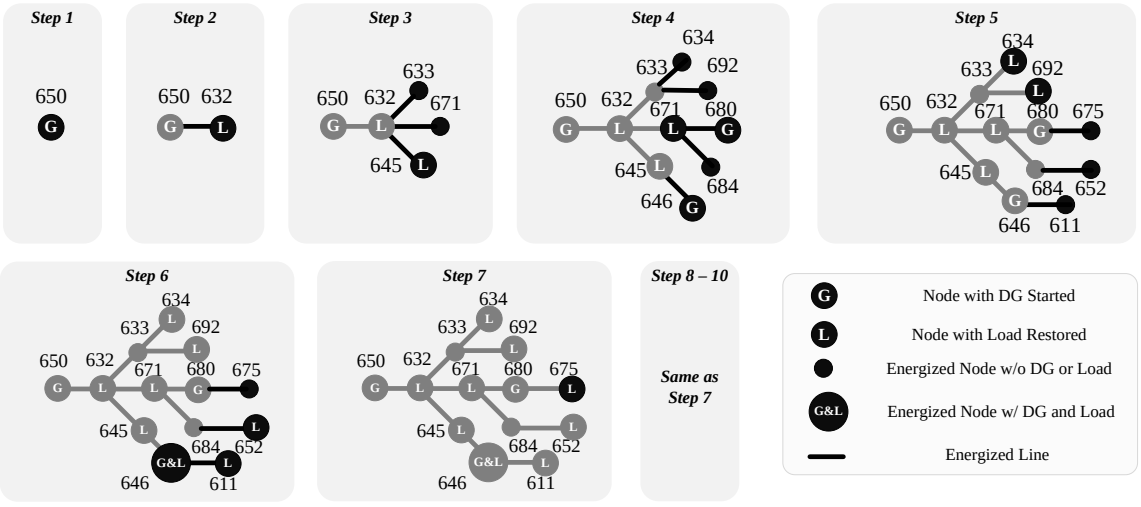

Figure 4.30. Restoration sequence for Scenario II.1

TABLE 4.19. ACTIVE DG OUTPUTS AND LOAD DEMANDS IN KW IN SCENARIO II.1

Step	$P_{g,t}^{G}$ (kW)			$P_{g,t}^{L}$ (kW)								
	DG650	DG646	DG680	L632	L634	L645	L646	L671	L692	L675	L611	L652
1	0.0	0.0	0.0	0.0	0.0	0.0	0.0	0.0	0.0	0.0	0.0	0.0
2	200.0	0.0	0.0	200.0	0.0	0.0	0.0	0.0	0.0	0.0	0.0	0.0
3	680.0	0.0	0.0	200.0	0.0	480.0	0.0	0.0	0.0	0.0	0.0	0.0
4	665.4	200.0	300.0	159.7	0.0	315.6	0.0	690.0	0.0	0.0	0.0	0.0
5	1304.9	400.0	100.0	139.7	180.0	255.2	0.0	690.0	540.0	0.0	0.0	0.0
6	1649.5	600.0	126.2	129.8	180.0	232.9	500.0	406.3	386.6	0.0	420.0	120.0
7	1649.5	800.0	393.0	124.9	141.5	224.8	500.0	329.0	302.4	680.0	420.0	120.0
8	1534.7	757.6	342.7	122.4	124.1	221.8	500.0	307.9	256.2	680.0	347.8	74.9
9	1525.9	557.6	100.0	121.2	116.4	220.6	359.0	302.2	230.8	468.6	308.2	56.6
10	1501.7	357.6	100.0	120.6	112.9	220.2	289.0	300.6	216.9	363.6	286.4	49.1

TABLE 4.20. REACTIVE DG OUTPUTS AND LOAD DEMANDS IN KVAR IN SCENARIO II.1

Step	$Q_{g,t}^{G}$ (kVar)			$Q_{g,t}^{L}$ (kVar)								
	DG650	DG646	DG680	L632	L634	L645	L646	L671	L692	L675	L611	L652
1	0.0	0.0	0.0	0.0	0.0	0.0	0.0	0.0	0.0	0.0	0.0	0.0
2	80.0	0.0	0.0	80.0	0.0	0.0	0.0	0.0	0.0	0.0	0.0	0.0
3	320.0	0.0	0.0	80.0	0.0	240.0	0.0	0.0	0.0	0.0	0.0	0.0
4	0.0	500.0	135.7	63.9	0.0	157.8	0.0	414.0	0.0	0.0	0.0	0.0
5	574.5	500.0	0.0	55.9	72.0	127.6	0.0	414.0	405.0	0.0	0.0	0.0
6	866.1	500.0	0.0	51.9	72.0	116.5	250.0	243.8	289.9	0.0	252.0	90.0
7	810.2	500.0	60.9	49.9	56.6	112.4	250.0	197.4	226.8	136.0	252.0	90.0
8	0.0	500.0	737.2	49.0	49.7	110.9	250.0	184.7	192.2	136.0	208.7	56.2
9	0.0	500.0	560.3	48.5	46.5	110.3	179.5	181.3	173.1	93.7	184.9	42.4
10	0.0	500.0	472.5	48.2	45.1	110.1	144.5	180.4	162.7	72.7	171.9	36.8

TABLE 4.21. NODE VOLTAGE IN PER UNIT IN SCENARIO II.1

Step	$V_{i,t}$ (p.u.)												
	N650	N632	N633	N634	N645	N646	N671	N692	N675	N684	N611	N652	N680
1	1.05	0.00	0.00	0.00	0.00	0.00	0.00	0.00	0.00	0.00	0.00	0.00	0.00
2	1.05	1.04	0.00	0.00	0.00	0.00	0.00	0.00	0.00	0.00	0.00	0.00	0.00
3	1.05	1.03	0.00	0.00	1.02	0.00	1.03	0.00	0.00	0.00	0.00	0.00	0.00
4	1.05	1.04	1.04	0.00	1.05	1.05	1.02	0.00	0.00	1.02	0.00	0.00	1.03
5	1.05	1.01	1.01	1.01	1.02	1.02	0.96	0.96	0.96	0.96	1.02	0.96	0.96
6	1.05	0.99	0.99	0.99	0.99	0.99	0.95	0.95	0.96	0.95	0.99	0.95	0.96
7	1.05	0.99	0.99	0.99	0.99	0.99	0.95	0.95	0.95	0.95	0.99	0.95	0.95
8	1.05	1.03	1.03	1.03	1.03	1.03	1.03	1.03	1.04	1.03	1.03	1.03	1.04
9	1.05	1.03	1.03	1.03	1.03	1.03	1.03	1.03	1.04	1.03	1.03	1.03	1.04
10	1.05	1.03	1.03	1.03	1.03	1.03	1.02	1.02	1.03	1.02	1.03	1.02	1.03

TABLE 4.22. APPARENT LINE POWER IN KVA IN SCENARIO II.1

Line	$S_{ij,t}^{BR}$ (kVA)									
	Step 1	Step 2	Step 3	Step 4	Step 5	Step 6	Step 7	Step 8	Step 9	Step 10
650_632	0.0	215.4	751.5	665.4	988.9	1421.3	1432.8	1474.3	1383.6	1649.5
632_633	0.0	0.0	0.0	0.0	193.9	193.9	152.3	133.7	125.3	121.5
633_634	0.0	0.0	0.0	0.0	193.9	193.9	152.3	133.7	125.3	121.5
632_645	0.0	0.0	536.7	361.2	399.6	565.5	363.2	474.7	488.5	590.4
645_646	0.0	0.0	0.0	538.5	640.3	320.0	120.0	251.2	299.7	409.1
632_671	0.0	0.0	0.0	479.1	1033.3	677.4	820.3	776.6	661.8	830.4
671_692	0.0	0.0	0.0	0.0	675.0	483.2	378.0	320.3	288.6	271.2
692_675	0.0	0.0	0.0	0.0	0.0	0.0	0.0	0.0	0.0	0.0
671_684	0.0	0.0	0.0	0.0	0.0	150.0	150.0	93.6	70.7	61.4
684_611	0.0	0.0	0.0	0.0	0.0	0.0	0.0	0.0	0.0	0.0
684_652	0.0	0.0	0.0	0.0	0.0	150.0	150.0	93.6	70.7	61.4
671_680	0.0	0.0	0.0	329.3	600.0	648.7	195.8	612.9	471.6	478.8
633_692	0.0	0.0	0.0	0.0	0.0	0.0	0.0	0.0	0.0	0.0
646_611	0.0	0.0	0.0	0.0	0.0	489.8	489.8	405.6	359.4	334.1
675_680	0.0	0.0	0.0	0.0	0.0	0.0	693.5	693.5	477.8	370.8

4.3.2.2 Scenario II.2: Four Lines Were Directly Connected

In Scenario II.2, four lines (671-692, 692-675, 671-684, 684-611) were assumed to be directly connected to their end nodes. Therefore, equations (3.63)-(3.64) defined in the connectivity constraints should be used:

$$x_{671-692,t}^{BR} = s_{671,t}^{N} = s_{692,t}^{N}, \ \ t \in \{1,2,3,\dots 10\} \tag{4.15}$$

$$x_{675-692,t}^{BR} = s_{675,t}^{N} = s_{692,t}^{N}, \ \ t \in \{1,2,3,\dots 10\} \tag{4.16}$$

$$x_{671-684,t}^{BR} = s_{671,t}^{N} = s_{684,t}^{N}, \ \ t \in \{1,2,3,\dots 10\} \tag{4.17}$$

$$x_{611-684,t}^{BR} = s_{611,t}^{N} = s_{684,t}^{N}, \ \ t \in \{1,2,3,\dots 10\} \tag{4.18}$$

Since the four lines are interconnected, as long as one of the five nodes is energized, all the other four nodes will be energized immediately. The restoration sequence generated by the BSR method is shown in Figure 4.31. DG active and reactive power outputs and

load demands at each step are summarized in TABLE 4.23 and TABLE 4.24. Zero values represent DGs and loads were in de-energized status. Node voltages and apparent line powers are summarized in TABLE 4.25 and TABLE 4.26. Zeros values represent a node or a line was de-energized. Similar to the sequence for Scenario II.1, L632 was restored at Step 2. However, L645 was not restored at Step 3. Instead, L611 on N611 was restored. At Step 3, N671 was energized by closing line 632-671. Since lines 671-692, 671-684, 684-611 and 692-675 were directly connected, energizing N671 immediately energized N692, N675, N684, and N611. Since restoring all the loads on the energized nodes may violate some constraints, DG2 on N646 and DG3 on N680 were started to share the load demand during the following steps. All the nodes were energized within 4 steps, which is faster than in Scenario II.1. This is because energizing N671 by closing 632-671 will immediately energize all the interconnected nodes. Whereas in Scenario II.1, it will take extra steps to close the switches one by one.

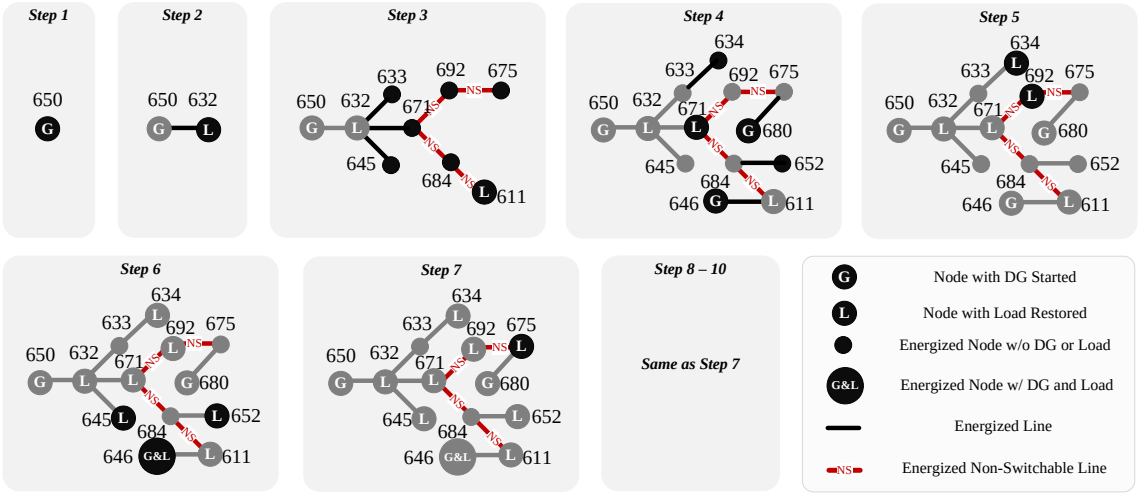

Figure 4.31. Restoration sequence for Scenario II.2

TABLE 4.23. ACTIVE DG OUTPUTS AND LOAD DEMANDS IN KW IN SCENARIO II.2

Step	DG650	DG646	DG680	L632	L634	L645	L646	L671	L692	L675	L611	L652
1	0.0	0.0	0.0	0.0	0.0	0.0	0.0	0.0	0.0	0.0	0.0	0.0
2	200.0	0.0	0.0	200.0	0.0	0.0	0.0	0.0	0.0	0.0	0.0	0.0
3	620.0	0.0	0.0	200.0	0.0	0.0	0.0	0.0	0.0	0.0	420.0	0.0
4	769.7	200.0	300.0	159.7	0.0	0.0	0.0	690.0	0.0	0.0	420.0	0.0
5	897.5	400.0	600.0	139.7	180.0	0.0	0.0	690.0	540.0	0.0	347.8	0.0
6	1471.0	600.0	439.9	129.8	180.0	480.0	500.0	406.3	386.6	0.0	308.2	120.0
7	1649.5	760.4	389.9	124.9	141.5	315.6	500.0	329.0	302.4	680.0	286.4	120.0
8	1649.5	560.4	385.4	122.4	124.1	255.2	500.0	307.9	256.2	680.0	274.5	74.9
9	709.8	760.4	685.4	121.2	116.4	232.9	359.0	302.2	230.8	468.6	268.0	56.6
10	387.1	800.0	754.7	120.6	112.9	224.8	289.0	300.6	216.9	363.6	264.4	49.1

TABLE 4.24. REACTIVE DG OUTPUTS AND LOAD DEMANDS IN KVAR IN SCENARIO II.2

Step	$Q_{g,t}^{G}$ (kVar)			$Q_{g,t}^{L}$ (kVar)								
	DG650	DG646	DG680	L632	L634	L645	L646	L671	L692	L675	L611	L652
1	0.0	0.0	0.0	0.0	0.0	0.0	0.0	0.0	0.0	0.0	0.0	0.0
2	80.0	0.0	0.0	80.0	0.0	0.0	0.0	0.0	0.0	0.0	0.0	0.0
3	332.0	0.0	0.0	80.0	0.0	0.0	0.0	0.0	0.0	0.0	252.0	0.0
4	229.9	500.0	0.0	63.9	0.0	0.0	0.0	414.0	0.0	0.0	252.0	0.0
5	171.1	500.0	484.5	55.9	72.0	0.0	0.0	414.0	405.0	0.0	208.7	0.0
6	309.1	351.6	761.9	51.9	72.0	240.0	250.0	243.8	289.9	0.0	184.9	90.0
7	0.0	476.1	860.3	49.9	56.6	157.8	250.0	197.4	226.8	136.0	171.9	90.0
8	0.0	312.1	897.9	49.0	49.7	127.6	250.0	184.7	192.2	136.0	164.7	56.2
9	0.0	500.0	542.4	48.5	46.5	116.5	179.5	181.3	173.1	93.7	160.8	42.4
10	0.0	364.1	597.4	48.2	45.1	112.4	144.5	180.4	162.7	72.7	158.6	36.8

TABLE 4.25. NODE VOLTAGE IN PER UNIT IN SCENARIO II.2

Step	$V_{i,t}$ (p.u.)												
	N650	N632	N633	N634	N645	N646	N671	N692	N675	N684	N611	N652	N680
1	1.05	0.00	0.00	0.00	0.00	0.00	0.00	0.00	0.00	0.00	0.00	0.00	0.00
2	1.05	1.04	0.00	0.00	0.00	0.00	0.00	0.00	0.00	0.00	0.00	0.00	0.00
3	1.05	1.03	1.03	0.00	1.03	0.00	1.01	1.01	1.01	1.00	1.00	0.00	0.00
4	1.05	1.03	1.03	1.03	1.04	1.04	0.98	0.98	0.98	0.98	0.98	0.98	0.98
5	1.05	1.03	1.03	1.03	1.04	1.04	0.99	0.99	1.00	0.99	0.98	0.99	1.00
6	1.05	1.02	1.01	1.01	1.01	1.01	1.00	1.00	1.01	1.00	1.00	1.00	1.01
7	1.05	1.03	1.03	1.03	1.03	1.03	1.01	1.01	1.02	1.01	1.01	1.01	1.02
8	1.05	1.03	1.03	1.03	1.03	1.03	1.02	1.02	1.03	1.02	1.02	1.02	1.03
9	1.05	1.04	1.04	1.04	1.04	1.05	1.03	1.03	1.03	1.03	1.02	1.02	1.03
10	1.05	1.05	1.04	1.04	1.05	1.05	1.04	1.04	1.05	1.04	1.04	1.04	1.05

TABLE 4.26. APPARENT LINE POWER IN KVA IN SCENARIO II.2

Line	$S_{ij,t}^{BR}$ (kVA)									
	Step 1	Step 2	Step 3	Step 4	Step 5	Step 6	Step 7	Step 8	Step 9	Step 10
650_632	0.0	215.4	703.3	803.3	913.7	1503.1	1649.5	1649.5	709.8	387.1
632_633	0.0	0.0	0.0	0.0	193.9	193.9	152.3	133.7	125.3	121.5
633_634	0.0	0.0	0.0	0.0	193.9	193.9	152.3	133.7	125.3	121.5
632_645	0.0	0.0	0.0	538.5	640.3	404.4	87.8	205.5	264.5	305.6
645_646	0.0	0.0	0.0	538.5	640.3	142.6	344.8	86.6	513.6	556.1
632_671	0.0	0.0	489.8	1048.6	1118.6	782.6	1328.4	1219.2	649.9	440.1
671_692	0.0	0.0	0.0	300.0	99.6	474.9	773.7	792.4	275.9	401.7
692_675	0.0	0.0	0.0	300.0	771.2	879.7	780.3	816.8	498.3	654.5
671_684	0.0	0.0	489.8	489.8	405.6	508.8	483.5	413.4	382.9	369.4
684_611	0.0	0.0	489.8	489.8	405.6	359.4	334.1	320.1	312.5	308.3
684_652	0.0	0.0	0.0	0.0	0.0	150.0	150.0	93.6	70.7	61.4
671_680	0.0	0.0	0.0	0.0	0.0	0.0	0.0	0.0	0.0	0.0
633_692	0.0	0.0	0.0	0.0	0.0	0.0	0.0	0.0	0.0	0.0
646_611	0.0	0.0	0.0	0.0	0.0	0.0	0.0	0.0	0.0	0.0
675_680	0.0	0.0	0.0	300.0	771.2	879.7	944.6	977.1	874.0	962.6

4.3.2.3 Scenario II.3: Four Lines Were Disconnected

In Scenario II.3, four lines (671-692, 692-675, 671-684, and 684-611) were assumed to be damaged (e.g., by fallen trees) and disconnected. Four constraints should be added to the initial condition constraints:

$$x_{671-692,t}^{BR} = 0, x_{675-692,t}^{BR} = 0, x_{671-684,t}^{BR} = 0, x_{611-684,t}^{BR} = 0, t \in \{1,2,3, \dots 10\} \quad (4.19)$$

The restoration sequence generated by the BSR method is shown in Figure 4.32. DG active and reactive power outputs and load demands at each step are summarized in TABLE 4.27 and TABLE 4.28. Zero values represent DGs and loads were in de-energized status. Node voltages and apparent line powers are summarized in TABLE 4.29 and TABLE 4.30. Zeros values represent a node or a line was de-energized. It can be seen that the restoration sequence for lines and loads was different from the sequence generated for Scenario II.1. Since the faulty lines were disconnected, alternative energization paths were figured out by the BSR method. For example, line 611-684 was energized at Step 4 in

Scenario II.1, but was damaged in Scenario II.3. Therefore, line 646-611 was closed to energize N611 at Step 5. Note that N684 was isolated by the faulty lines (671-684, 6611-684). Thus, N684 was kept de-energized. Similarly, N652 was also isolated, since N684 was de-energized and 684-652 was the only line that connected N652 to the system. However, there is no need to explicitly add $s^{N}_{684,t} = 0$ and $s^{N}_{652,t} = 0$ to the BSR model, because the initial condition constraints in the BSR model can automatically guarantee N652 and N684 were de-energized throughout the restoration process.

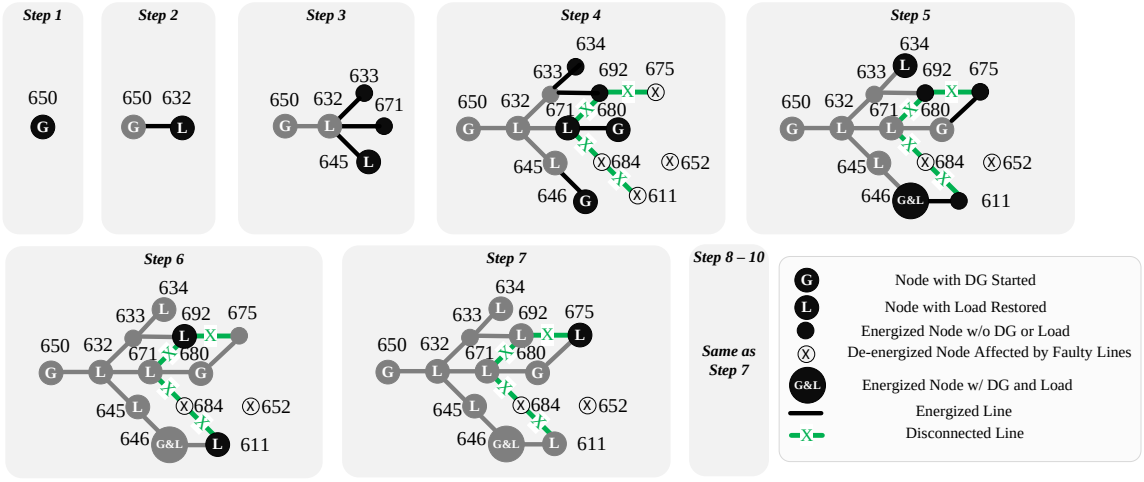

Figure 4.32. Restoration sequence for Scenario II.3

TABLE 4.27. ACTIVE DG OUTPUTS AND LOAD DEMANDS IN KW IN SCENARIO II.3

Step	DG650	DG646	DG680	L632	L634	L645	L646	L671	L692	L675	L611	L652
1	0.0	0.0	0.0	0.0	0.0	0.0	0.0	0.0	0.0	0.0	0.0	0.0
2	200.0	0.0	0.0	200.0	0.0	0.0	0.0	0.0	0.0	0.0	0.0	0.0
3	680.0	0.0	0.0	200.0	0.0	480.0	0.0	0.0	0.0	0.0	0.0	0.0
4	665.4	200.0	300.0	159.7	0.0	315.6	0.0	690.0	0.0	0.0	0.0	0.0
5	764.9	400.0	600.0	139.7	180.0	255.2	500.0	690.0	0.0	0.0	0.0	0.0
6	909.0	600.0	900.0	129.8	180.0	232.9	500.0	406.3	540.0	0.0	420.0	0.0
7	1490.6	716.0	600.0	124.9	141.5	224.8	500.0	329.0	386.6	680.0	420.0	0.0
8	1649.5	516.0	300.0	122.4	124.1	221.8	359.0	307.9	302.4	680.0	347.8	0.0
9	1649.5	332.9	100.0	121.2	116.4	220.6	289.0	302.2	256.2	468.6	308.2	0.0
10	1649.5	140.0	100.0	120.6	112.9	220.2	254.3	300.6	230.8	363.6	286.4	0.0

TABLE 4.28. REACTIVE DG OUTPUTS AND LOAD DEMANDS IN KVAR IN SCENARIO II.3

Step	$Q^G_{a,t}$ (kVar)			$Q^L_{a,t}$ (kVar)								
	DG650	DG646	DG680	L632	L634	L645	L646	L671	L692	L675	L611	L652
1	0.0	0.0	0.0	0.0	0.0	0.0	0.0	0.0	0.0	0.0	0.0	0.0
2	80.0	0.0	0.0	80.0	0.0	0.0	0.0	0.0	0.0	0.0	0.0	0.0
3	320.0	0.0	0.0	80.0	0.0	240.0	0.0	0.0	0.0	0.0	0.0	0.0
4	0.0	500.0	135.7	63.9	0.0	157.8	0.0	414.0	0.0	0.0	0.0	0.0
5	30.6	500.0	388.9	55.9	72.0	127.6	250.0	414.0	0.0	0.0	0.0	0.0
6	440.7	500.0	450.5	51.9	72.0	116.5	250.0	243.8	405.0	0.0	252.0	0.0
7	275.1	500.0	569.2	49.9	56.6	112.4	250.0	197.4	289.9	136.0	252.0	0.0
8	0.0	500.0	645.2	49.0	49.7	110.9	179.5	184.7	226.8	136.0	208.7	0.0
9	0.0	500.0	501.9	48.5	46.5	110.3	144.5	181.3	192.2	93.7	184.9	0.0
10	0.0	500.0	428.7	48.2	45.1	110.1	127.1	180.4	173.1	72.7	171.9	0.0

TABLE 4.29. NODE VOLTAGE IN PER UNIT IN SCENARIO II.3

Step	$V_{i,t}$ (p.u.)												
	N650	N632	N633	N634	N645	N646	N671	N692	N675	N684	N611	N652	N680
1	1.05	0.00	0.00	0.00	0.00	0.00	0.00	0.00	0.00	0.00	0.00	0.00	0.00
2	1.05	1.04	0.00	0.00	0.00	0.00	0.00	0.00	0.00	0.00	0.00	0.00	0.00
3	1.05	1.03	1.03	0.00	1.02	0.00	1.03	0.00	0.00	0.00	0.00	0.00	0.00
4	1.05	1.04	1.04	1.04	1.05	1.05	1.02	0.00	0.00	0.00	0.00	0.00	1.03
5	1.05	1.04	1.04	1.04	1.04	1.04	1.04	0.00	1.05	0.00	1.04	0.00	1.05
6	1.05	1.02	1.01	1.01	1.01	1.01	1.03	1.01	1.05	0.00	1.01	0.00	1.05
7	1.05	1.02	1.01	1.01	1.01	1.01	1.02	1.01	1.03	0.00	1.01	0.00	1.03
8	1.05	1.03	1.02	1.02	1.03	1.03	1.04	1.02	1.05	0.00	1.03	0.00	1.05
9	1.05	1.03	1.02	1.02	1.03	1.03	1.03	1.02	1.04	0.00	1.03	0.00	1.04
10	1.05	1.03	1.03	1.02	1.03	1.03	1.03	1.03	1.04	0.00	1.03	0.00	1.04

TABLE 4.30. APPARENT LINE POWER IN KVA IN SCENARIO II.3

Line	$S^{BR}_{ij,t}$ (kVA)									
	Step 1	Step 2	Step 3	Step 4	Step 5	Step 6	Step 7	Step 8	Step 9	Step 10
650_632	0.0	215.4	751.5	665.4	765.5	1010.2	1515.8	1649.5	1649.5	1649.5
632_633	0.0	0.0	0.0	0.0	193.9	863.7	631.6	508.3	442.5	407.2
633_634	0.0	0.0	0.0	0.0	193.9	193.9	152.3	133.7	125.3	121.5
632_645	0.0	0.0	536.7	361.2	375.7	565.5	443.8	412.6	488.7	627.6
645_646	0.0	0.0	0.0	538.5	269.3	320.0	204.0	221.2	314.6	448.3
632_671	0.0	0.0	0.0	479.1	93.4	535.2	472.1	760.6	708.1	590.9
671_692	0.0	0.0	0.0	0.0	0.0	0.0	0.0	0.0	0.0	0.0
692_675	0.0	0.0	0.0	0.0	0.0	0.0	0.0	0.0	0.0	0.0
671_684	0.0	0.0	0.0	0.0	0.0	0.0	0.0	0.0	0.0	0.0
684_611	0.0	0.0	0.0	0.0	0.0	0.0	0.0	0.0	0.0	0.0
684_652	0.0	0.0	0.0	0.0	0.0	0.0	0.0	0.0	0.0	0.0
671_680	0.0	0.0	0.0	329.3	715.0	1006.5	440.5	635.4	550.0	442.9
633_692	0.0	0.0	0.0	0.0	0.0	675.0	483.2	378.0	320.3	288.6
646_611	0.0	0.0	0.0	0.0	0.0	489.8	489.8	405.6	359.4	334.1
675_680	0.0	0.0	0.0	0.0	0.0	0.0	693.5	693.5	477.8	370.8

4.3.2.4 Scenario II.4: A Node Was Damaged

In Scenario II.4, N671 was assumed to be damaged. Thus, all the lines connected to N671 should be disconnected in order to isolate N671. In addition, the load on N671 cannot be restored during the restoration process. However, there is no need to formulate initial condition constraints for each affected line and load. Only one initial condition constraint reflecting the failure status of node N671 is required:

$$s^{N}_{671,t} = 0, \quad t \in \{1,2,3, \dots 10\} \tag{4.20}$$

The restoration sequence generated by the BSR method is shown in Figure 4.33. DG active and reactive power outputs and load demands at each step are summarized in TABLE 4.31 and TABLE 4.32. Zero values represent DGs and loads were in de-energized status. Node voltages and apparent line powers are summarized in TABLE 4.33 and TABLE 4.34. Zeros values represent a node or a line was de-energized. It can be observed that N671 was isolated throughout the restoration process. In previous scenarios, line 632-671 were always closed at Step3. However, in this case, since N671 was isolated, line 632-671 was always opened. Alternative energization paths were found by the BSR method to bypass N671.

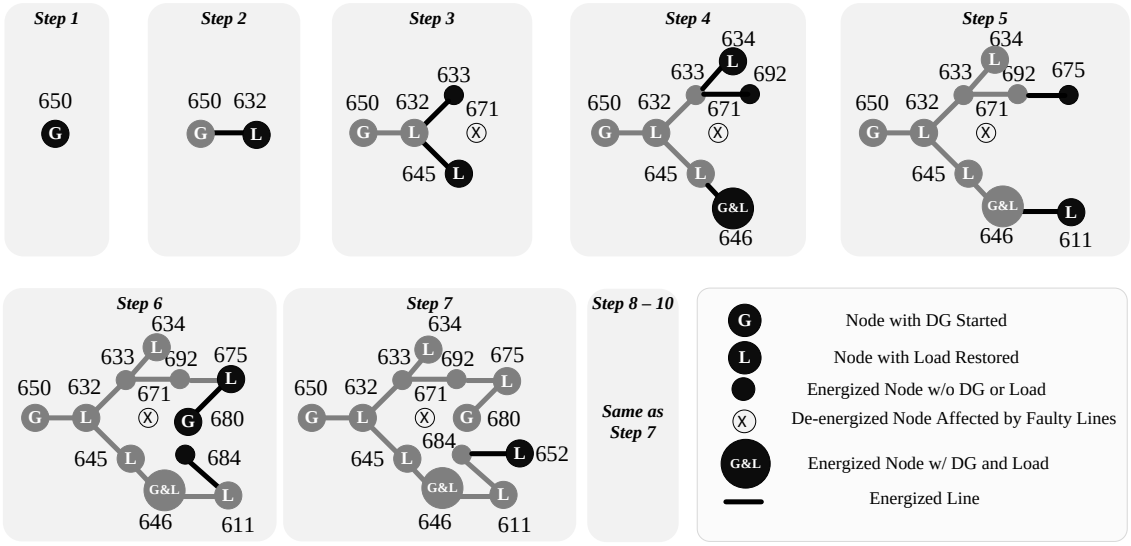

Figure 4.33. Restoration sequence for Scenario II.4

TABLE 4.31. ACTIVE DG OUTPUTS AND LOAD DEMANDS IN KW IN SCENARIO II.4

Step	DG650	DG646	DG680	L632	L634	L645	L646	L671	L692	L675	L611	L652
1	0.0	0.0	0.0	0.0	0.0	0.0	0.0	0.0	0.0	0.0	0.0	0.0
2	200.0	0.0	0.0	200.0	0.0	0.0	0.0	0.0	0.0	0.0	0.0	0.0
3	680.0	0.0	0.0	200.0	0.0	480.0	0.0	0.0	0.0	0.0	0.0	0.0
4	955.4	200.0	0.0	159.7	180.0	315.6	500.0	0.0	0.0	0.0	0.0	0.0
5	1214.9	400.0	0.0	139.7	180.0	255.2	500.0	0.0	0.0	0.0	420.0	120.0
6	1387.9	600.0	236.3	129.8	141.5	232.9	500.0	0.0	0.0	680.0	420.0	120.0
7	1497.3	800.0	178.3	124.9	124.1	224.8	359.0	0.0	540.0	680.0	347.8	74.9
8	1069.5	800.0	100.0	122.4	116.4	221.8	289.0	0.0	386.6	468.6	308.2	56.6
9	810.5	800.0	100.0	121.2	112.9	220.6	254.3	0.0	302.4	363.6	286.4	49.1
10	677.4	800.0	100.0	120.6	111.3	220.2	237.0	0.0	256.2	311.4	274.5	46.1

TABLE 4.32. REACTIVE DG OUTPUTS AND LOAD DEMANDS IN KVAR IN SCENARIO II.4

Step	$Q_{g,t}^{G}$ (kVar)			$Q_{g,t}^{L}$ (kVar)								
	DG650	DG646	DG680	L632	L634	L645	L646	L671	L692	L675	L611	L652
1	0.0	0.0	0.0	0.0	0.0	0.0	0.0	0.0	0.0	0.0	0.0	0.0
2	80.0	0.0	0.0	80.0	0.0	0.0	0.0	0.0	0.0	0.0	0.0	0.0
3	320.0	0.0	0.0	80.0	0.0	240.0	0.0	0.0	0.0	0.0	0.0	0.0
4	43.7	500.0	0.0	63.9	72.0	157.8	250.0	0.0	0.0	0.0	0.0	0.0
5	347.5	500.0	0.0	55.9	72.0	127.6	250.0	0.0	0.0	0.0	252.0	90.0
6	453.0	500.0	0.0	51.9	56.6	116.5	250.0	0.0	0.0	136.0	252.0	90.0
7	263.6	0.0	933.7	49.9	49.7	112.4	179.5	0.0	405.0	136.0	208.7	56.2
8	461.9	500.0	0.0	49.0	46.5	110.9	144.5	0.0	289.9	93.7	184.9	42.4
9	339.3	500.0	0.0	48.5	45.1	110.3	127.1	0.0	226.8	72.7	171.9	36.8
10	775.1	0.0	0.0	48.2	44.5	110.1	118.5	0.0	192.2	62.3	164.7	34.6

TABLE 4.33. NODE VOLTAGE IN PER UNIT IN SCENARIO II.4

Step	$V_{i,t}$ (p.u.)												
	N650	N632	N633	N634	N645	N646	N671	N692	N675	N684	N611	N652	N680
1	1.05	0.00	0.00	0.00	0.00	0.00	0.00	0.00	0.00	0.00	0.00	0.00	0.00
2	1.05	1.04	0.00	0.00	0.00	0.00	0.00	0.00	0.00	0.00	0.00	0.00	0.00
3	1.05	1.03	1.03	0.00	1.02	0.00	1.03	0.00	0.00	0.00	0.00	0.00	0.00
4	1.05	1.04	1.03	1.03	1.03	1.04	1.04	0.00	0.00	1.04	0.00	0.00	1.04
5	1.05	1.02	1.02	1.01	1.02	1.02	0.99	0.00	0.00	0.99	0.99	0.99	0.99
6	1.05	1.01	1.01	1.01	1.01	1.01	0.97	1.01	0.96	0.97	0.96	0.96	0.96
7	1.05	1.02	1.01	1.01	1.01	1.01	1.03	1.01	1.05	1.03	1.03	1.03	1.05
8	1.05	1.01	1.01	1.01	1.02	1.02	0.99	1.01	0.98	0.98	0.98	0.98	0.98
9	1.05	1.02	1.02	1.02	1.03	1.03	1.00	1.02	1.00	1.00	1.00	1.00	1.00
10	1.05	1.00	1.00	1.00	1.00	1.00	0.98	1.00	0.98	0.98	0.98	0.98	0.98

TABLE 4.34. APPARENT LINE POWER IN KVA IN SCENARIO II.4

Line	$S_{ij,t}^{BR}$ (kVA)									
	Step 1	Step 2	Step 3	Step 4	Step 5	Step 6	Step 7	Step 8	Step 9	Step 10
650_632	0.0	215.4	751.5	956.4	1263.6	1460.0	1520.3	1165.0	878.7	1029.4
632_633	0.0	0.0	0.0	193.9	193.9	152.3	804.8	605.1	496.4	437.1
633_634	0.0	0.0	0.0	193.9	193.9	152.3	133.7	125.3	121.5	119.9
632_645	0.0	0.0	536.7	622.5	375.7	188.4	363.2	378.8	417.8	412.0
645_646	0.0	0.0	0.0	390.5	269.3	269.3	476.1	622.4	660.9	575.3
632_671	0.0	0.0	0.0	0.0	639.2	1093.7	1067.0	800.5	661.9	592.8
671_692	0.0	0.0	0.0	0.0	0.0	0.0	0.0	0.0	0.0	0.0
692_675	0.0	0.0	0.0	0.0	0.0	0.0	0.0	0.0	0.0	0.0
671_684	0.0	0.0	0.0	0.0	639.2	639.2	498.8	429.8	395.2	377.5
684_611	0.0	0.0	0.0	0.0	489.8	489.8	405.6	359.4	334.1	320.1
684_652	0.0	0.0	0.0	0.0	150.0	150.0	93.6	70.7	61.4	57.6
671_680	0.0	0.0	0.0	0.0	0.0	464.1	942.4	380.3	273.4	220.4
633_692	0.0	0.0	0.0	0.0	0.0	0.0	675.0	483.2	378.0	320.3
646_611	0.0	0.0	0.0	0.0	0.0	0.0	0.0	0.0	0.0	0.0
675_680	0.0	0.0	0.0	0.0	0.0	693.5	693.5	477.8	370.8	317.6

4.3.2.5 Scenario II.5: Partial System Was Energized

In Scenario II.5, four lines (650-632, 632-633, 632-671, 632-645), DG1, and two loads (L645, L671) were assumed to be energized before initiating the restoration process. The initial condition constraints can be formulated as:

$$x_{650,1}^{G} = 1 \tag{4.21}$$

$$x_{650-632,1}^{BR} = 1, x_{632-633,1}^{BR} = 1, x_{632-671,1}^{BR} = 1, x_{632-645,1}^{BR} = 1 \tag{4.22}$$

$$x_{645,1}^{L} = 1, x_{671,1}^{L} = 1 \tag{4.23}$$

The generated restoration sequence is shown in Figure 4.34. DG active and reactive power outputs and load demands at each step are summarized in TABLE 4.35 and TABLE 4.36. Zero values represent DGs and loads were in de-energized status. Node voltages and apparent line powers are summarized in TABLE 4.37 and TABLE 4.38. Zeros values represent a node or a line was de-energized. The sequence for lines was similar to the sequence from Step 3 to Step 5 shown in Figure 4.30 for Scenario II.1. However, the sequence for loads was different, because L645 and L671 were restored before initiating the restoration process, so they were not affected by the CLPU issues. All the loads were restored by Step 4. This case study demonstrates that the BSR method can be applied for both totally de-energized systems and partially energized systems.

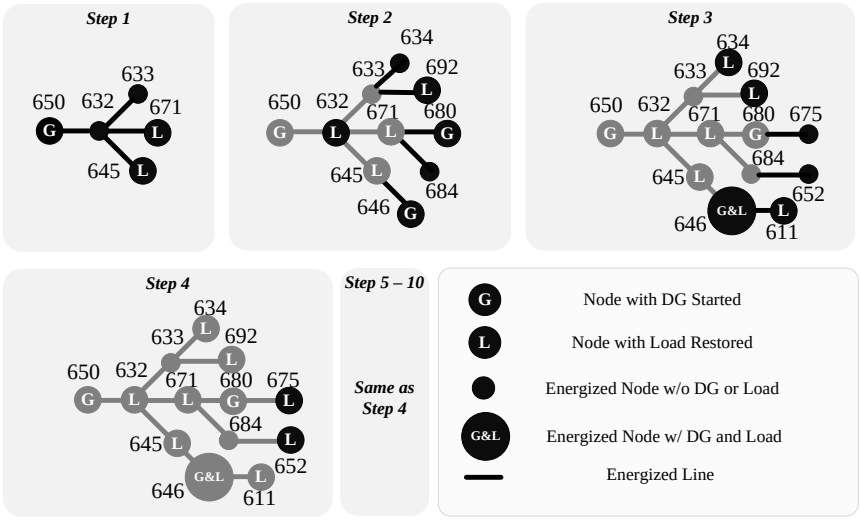

Figure 4.34. Restoration sequence for Scenario II.5

TABLE 4.35. ACTIVE DG OUTPUTS AND LOAD DEMANDS IN KW IN SCENARIO II.5

Step	DG650	DG646	DG680	L632	L634	L645	L646	L671	L692	L675	L611	L652
1	1170.0	0.0	0.0	0.0	0.0	480.0	0.0	690.0	0.0	0.0	0.0	0.0
2	1245.6	200.0	300.0	200.0	0.0	315.6	0.0	690.0	540.0	0.0	0.0	0.0
3	1563.7	400.0	384.4	200.0	180.0	255.2	500.0	406.3	386.6	0.0	420.0	0.0
4	1639.6	600.0	684.4	159.7	180.0	232.9	500.0	329.0	302.4	680.0	420.0	120.0
5	1533.4	800.0	384.4	139.7	141.5	224.8	500.0	307.9	256.2	680.0	347.8	120.0
6	1519.4	600.0	100.0	129.8	124.1	221.8	359.0	302.2	230.8	468.6	308.2	74.9
7	1475.0	400.0	100.0	124.9	116.4	220.6	289.0	300.6	216.9	363.6	286.4	56.6
8	1554.3	200.0	100.0	122.4	112.9	220.2	254.3	300.2	209.3	311.4	274.5	49.1
9	1414.0	50.0	330.3	121.2	111.3	220.1	237.0	300.0	205.1	285.5	268.0	46.1
10	1421.0	243.3	100.0	120.6	110.6	220.0	228.5	300.0	202.8	272.7	264.4	44.8

TABLE 4.36. REACTIVE DG OUTPUTS AND LOAD DEMANDS IN KVAR IN SCENARIO II.5

Step	$Q_{g,t}^{G}$ (kVar)			$Q_{g,t}^{L}$ (kVar)								
	DG650	DG646	DG680	L632	L634	L645	L646	L671	L692	L675	L611	L652
1	654.0	0.0	0.0	0.0	0.0	240.0	0.0	414.0	0.0	0.0	0.0	0.0
2	0.0	500.0	556.8	80.0	0.0	157.8	0.0	414.0	405.0	0.0	0.0	0.0
3	97.7	500.0	717.6	80.0	72.0	127.6	250.0	243.8	289.9	0.0	252.0	0.0
4	17.0	500.0	887.5	63.9	72.0	116.5	250.0	197.4	226.8	136.0	252.0	90.0
5	201.0	500.0	585.5	55.9	56.6	112.4	250.0	184.7	192.2	136.0	208.7	90.0
6	0.0	500.0	581.2	51.9	49.7	110.9	179.5	181.3	173.1	93.7	184.9	56.2
7	302.2	500.0	179.2	49.9	46.5	110.3	144.5	180.4	162.7	72.7	171.9	42.4
8	164.8	500.0	267.4	49.0	45.1	110.1	127.1	180.1	157.0	62.3	164.7	36.8
9	407.8	500.0	0.0	48.5	44.5	110.0	118.5	180.0	153.8	57.1	160.8	34.6
10	395.6	500.0	0.0	48.2	44.2	110.0	114.2	180.0	152.1	54.5	158.6	33.6

TABLE 4.37. NODE VOLTAGE IN PER UNIT IN SCENARIO II.5

Step	$V_{i,t}$ (p.u.)												
	N650	N632	N633	N634	N645	N646	N671	N692	N675	N684	N611	N652	N680
1	1.05	1.00	1.00	0.00	1.00	0.00	0.97	0.00	0.00	0.00	0.00	0.00	0.00
2	1.05	1.03	1.03	1.03	1.04	1.04	1.01	1.01	0.00	0.00	0.00	0.00	1.03
3	1.05	1.03	1.02	1.02	1.02	1.02	1.03	1.03	1.05	1.03	1.02	0.00	1.05
4	1.05	1.03	1.03	1.03	1.03	1.02	1.03	1.03	1.05	1.03	1.02	1.03	1.05
5	1.05	1.02	1.02	1.02	1.02	1.02	1.01	1.01	1.02	1.01	1.02	1.00	1.02
6	1.05	1.03	1.03	1.03	1.03	1.03	1.02	1.02	1.03	1.02	1.03	1.02	1.03
7	1.05	1.02	1.01	1.01	1.02	1.02	0.99	0.99	0.99	0.99	1.02	0.99	0.99
8	1.05	1.02	1.02	1.02	1.02	1.02	1.00	1.00	1.01	1.00	1.02	1.00	1.01
9	1.05	1.01	1.01	1.01	1.01	1.01	0.98	0.98	0.98	0.98	1.01	0.98	0.98
10	1.05	1.01	1.01	1.01	1.01	1.01	0.98	0.98	0.98	0.98	1.01	0.98	0.98

TABLE 4.38. APPARENT LINE POWER IN KVA IN SCENARIO II.5

Line	$S_{ij,t}^{BR}$ (kVA)									
	Step 1	Step 2	Step 3	Step 4	Step 5	Step 6	Step 7	Step 8	Step 9	Step 10
650_632	1340.4	1245.6	1566.7	1639.7	1546.5	1519.4	1505.6	1563.0	1471.6	1475.1
632_633	0.0	0.0	193.9	193.9	152.3	133.7	125.3	121.5	119.9	119.1
633_634	0.0	0.0	193.9	193.9	152.3	133.7	125.3	121.5	119.9	119.1
632_645	536.7	361.2	785.9	565.5	281.7	290.0	402.9	557.7	684.1	483.9
645_646	0.0	538.5	520.0	320.0	63.2	151.3	254.0	389.1	505.7	337.4
632_671	804.7	966.2	448.0	783.8	979.8	979.5	882.9	788.3	661.5	834.0
671_692	0.0	675.0	483.2	378.0	320.3	288.6	271.2	261.6	256.4	253.5
692_675	0.0	0.0	0.0	0.0	0.0	0.0	0.0	0.0	0.0	0.0
671_684	0.0	0.0	0.0	150.0	150.0	93.6	70.7	61.4	57.6	56.1
684_611	0.0	0.0	0.0	0.0	0.0	0.0	0.0	0.0	0.0	0.0
684_652	0.0	0.0	0.0	150.0	150.0	93.6	70.7	61.4	57.6	56.1
671_680	0.0	632.5	814.1	751.5	538.0	611.1	284.3	294.6	72.6	181.1
633_692	0.0	0.0	0.0	0.0	0.0	0.0	0.0	0.0	0.0	0.0
646_611	0.0	0.0	489.8	489.8	405.6	359.4	334.1	320.1	312.5	308.3
675_680	0.0	0.0	0.0	693.5	693.5	477.8	370.8	317.6	291.2	278.1

4.3.2.6 Scenario II.6: Black Start DG is Located at Node N671

In Scenario II.6, the black start DG originally located at N650 was changed to N671. Locating the black start DG on N671 will potentially shorten the number of steps needed for restoring loads. For example, if the black start DG is on N650, it will take at least three steps to energize N692; e.g., closing line 650-632, 632-671 and 671-692 sequentially. If the black start DG is on N671, it will take at least one step to energize N692; e.g., close line 671-692. The restoration sequence is shown in Figure 4.35. It can be seen that the black start DG and the local load L671 were energized at Step 1. All the loads were energized by Step 5. Meanwhile, DG2 and DG3 were dispatched to share the load demand. DG active and reactive power outputs and load demands at each step are summarized in TABLE 4.39 and TABLE 4.40. Zero values represent DGs and loads were in de-energized status. Node voltages and apparent line powers are summarized in TABLE 4.41 and TABLE 4.42. Zeros values represent a node or a line was de-energized.

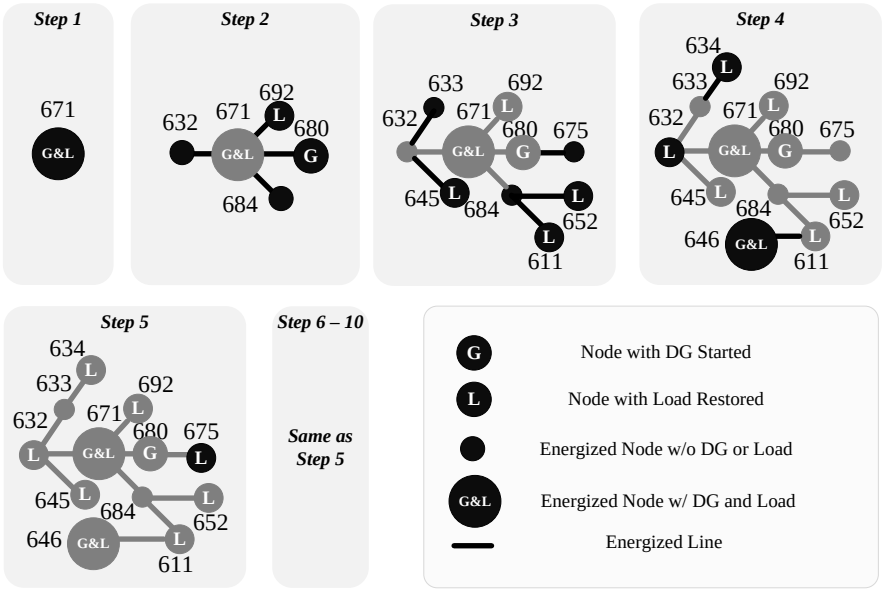

Figure 4.35. Restoration sequence for Scenario II.6

TABLE 4.39. ACTIVE DG OUTPUTS AND LOAD DEMANDS IN KW IN SCENARIO II.6

Step	DG650	DG646	DG680	L632	L634	L645	L646	L671	L692	L675	L611	L652
1	690.0	0.0	0.0	0.0	0.0	0.0	0.0	690.0	0.0	0.0	0.0	0.0
2	930.0	0.0	300.0	0.0	0.0	0.0	0.0	690.0	540.0	0.0	0.0	0.0
3	1712.9	0.0	100.0	0.0	0.0	480.0	0.0	406.3	386.6	0.0	420.0	120.0
4	2067.0	200.0	100.0	200.0	180.0	315.6	500.0	329.0	302.4	0.0	420.0	120.0
5	2539.8	162.2	100.0	200.0	180.0	255.2	500.0	307.9	256.2	680.0	347.8	74.9
6	2461.9	50.0	100.0	159.7	141.5	232.9	500.0	302.2	230.8	680.0	308.2	56.6
7	2019.3	50.0	100.0	139.7	124.1	224.8	359.0	300.6	216.9	468.6	286.4	49.1
8	1800.6	50.0	100.0	129.8	116.4	221.8	289.0	300.2	209.3	363.6	274.5	46.1
9	1692.0	50.0	100.0	124.9	112.9	220.6	254.3	300.0	205.1	311.4	268.0	44.8
10	1638.0	50.0	100.0	122.4	111.3	220.2	237.0	300.0	202.8	285.5	264.4	44.3

TABLE 4.40. REACTIVE DG OUTPUTS AND LOAD DEMANDS IN KVAR IN SCENARIO II.6

Step	$Q^G_{g,t}$ (kVar)			$Q^L_{g,t}$ (kVar)								
	DG650	DG646	DG680	L632	L634	L645	L646	L671	L692	L675	L611	L652
1	414.0	0.0	0.0	0.0	0.0	0.0	0.0	414.0	0.0	0.0	0.0	0.0
2	494.0	0.0	0.0	80.0	0.0	0.0	0.0	414.0	0.0	0.0	0.0	0.0
3	549.8	0.0	0.0	80.0	0.0	0.0	0.0	243.8	0.0	136.0	0.0	90.0
4	603.3	0.0	206.0	63.9	72.0	0.0	250.0	197.4	0.0	136.0	0.0	90.0
5	704.5	500.0	0.0	55.9	72.0	240.0	250.0	184.7	0.0	93.7	252.0	56.2
6	969.8	500.0	0.0	51.9	56.6	157.8	250.0	181.3	405.0	72.7	252.0	42.4
7	1184.8	0.0	0.0	49.9	49.7	127.6	179.5	180.4	289.9	62.3	208.7	36.8
8	1040.0	0.0	0.0	49.0	46.5	116.5	144.5	180.1	226.8	57.1	184.9	34.6
9	965.4	0.0	0.0	48.5	45.1	112.4	127.1	180.0	192.2	54.5	171.9	33.6
10	555.7	370.8	0.0	48.2	44.5	110.9	118.5	180.0	173.1	53.3	164.7	33.3

TABLE 4.41. NODE VOLTAGE IN PER UNIT IN SCENARIO II.6

Step	$V_{i,t}$ (p.u.)												
	N650	N632	N633	N634	N645	N646	N671	N692	N675	N684	N611	N652	N680
1	0.00	0.00	0.00	0.00	0.00	0.00	1.05	0.00	0.00	0.00	0.00	0.00	0.00
2	0.00	1.04	0.00	0.00	0.00	0.00	1.05	0.00	0.00	1.05	0.00	0.00	1.05
3	0.00	1.04	1.04	0.00	0.00	0.00	1.05	0.00	1.04	1.05	1.05	1.05	1.04
4	0.00	1.04	1.04	1.04	0.00	1.04	1.05	0.00	1.05	1.05	1.04	1.04	1.05
5	0.00	1.02	1.02	1.02	1.02	1.05	1.05	0.00	1.05	1.05	1.05	1.05	1.05
6	0.00	1.00	0.99	0.99	1.00	1.05	1.05	0.99	1.05	1.05	1.05	1.05	1.05
7	0.00	1.01	1.01	1.01	1.01	1.04	1.05	1.01	1.05	1.05	1.04	1.05	1.05
8	0.00	1.02	1.01	1.01	1.02	1.04	1.05	1.01	1.05	1.05	1.04	1.05	1.05
9	0.00	1.02	1.02	1.02	1.02	1.04	1.05	1.02	1.05	1.05	1.04	1.05	1.05
10	0.00	1.02	1.02	1.02	1.02	1.05	1.05	1.02	1.05	1.05	1.05	1.05	1.05

TABLE 4.42. APPARENT LINE POWER IN KVA IN SCENARIO II.6

Line	$S_{ij,t}^{BR}$ (kVA)									
	Step 1	Step 2	Step 3	Step 4	Step 5	Step 6	Step 7	Step 8	Step 9	Step 10
650_632	0.0	0.0	0.0	0.0	0.0	0.0	0.0	0.0	0.0	0.0
632_633	0.0	0.0	0.0	193.9	193.9	823.1	613.3	500.1	438.8	405.5
633_634	0.0	0.0	0.0	193.9	193.9	152.3	133.7	125.3	121.5	119.9
632_645	0.0	0.0	0.0	0.0	536.7	352.9	285.3	260.4	251.3	247.9
645_646	0.0	0.0	0.0	0.0	0.0	0.0	0.0	0.0	0.0	0.0
632_671	0.0	215.4	215.4	365.9	880.3	1311.7	1030.0	889.8	818.4	781.3
671_692	0.0	0.0	0.0	0.0	0.0	0.0	0.0	0.0	0.0	0.0
692_675	0.0	0.0	0.0	0.0	0.0	0.0	0.0	0.0	0.0	0.0
671_684	0.0	0.0	150.0	540.4	597.7	379.2	554.4	535.9	630.5	310.7
684_611	0.0	0.0	0.0	390.5	520.0	320.0	494.8	478.6	574.7	275.8
684_652	0.0	0.0	150.0	150.0	93.6	70.7	61.4	57.6	56.1	55.4
671_680	0.0	0.0	595.7	288.6	380.3	273.4	220.4	194.1	181.1	143.9
633_692	0.0	0.0	0.0	0.0	0.0	675.0	483.2	378.0	320.3	288.6
646_611	0.0	0.0	0.0	390.5	269.3	269.3	184.1	149.7	240.6	252.6
675_680	0.0	0.0	693.5	693.5	477.8	370.8	317.6	291.2	278.1	271.6

In summary, six scenarios are studied in Case II to show how the proposed BSR method can generate restoration solutions according to different initial conditions. For each scenario, the specified operating condition can be formulated in the initial condition constraints of the BSR model, which in turn can generate corresponding solutions.

4.3.3 Case III: Unbalanced Three-Phase System

In Case III, the capability of the BSR method to restore three-phase unbalanced systems with multiple black start DGs is shown. The test system was the unbalanced modified IEEE 123 node test system introduced in section 4.1.2. The system parameters can be found in APPENDIX B.

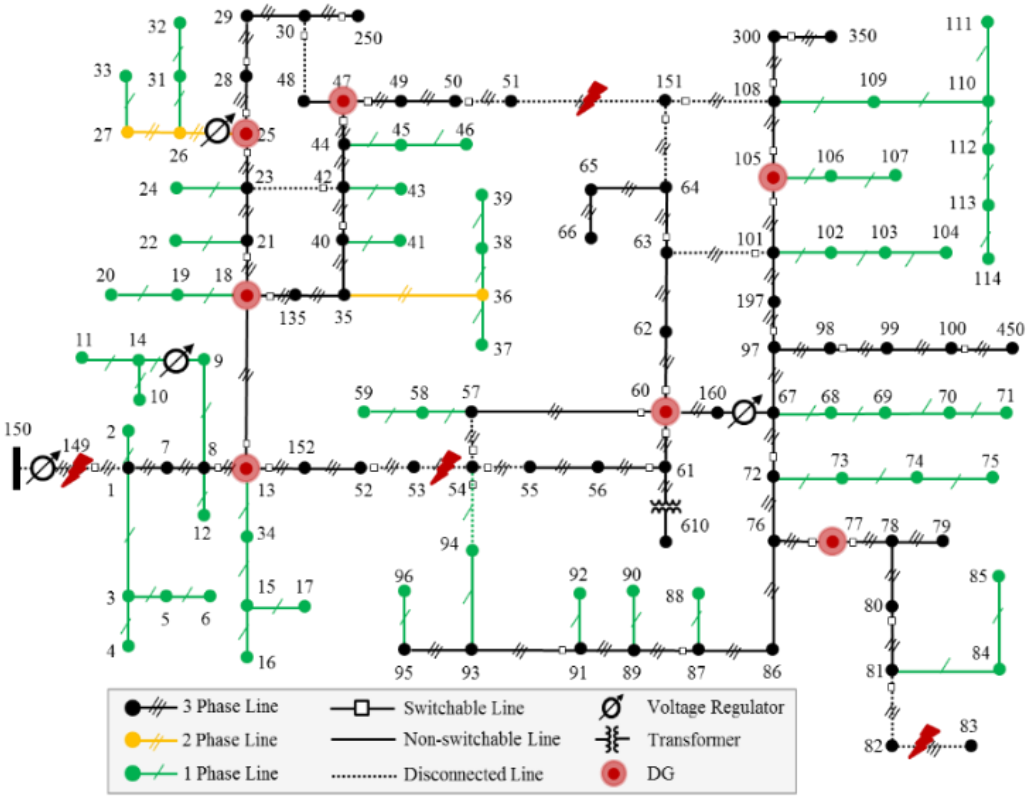

Figure 4.36. Unbalanced modified 123 node test system studied in Case III

Two scenarios with two types of load models were studied in Case III. In Scenario III.1, all the system loads were modeled as ZIP loads. In Scenario III.2, all the system loads were modeled as constant power load under CLPU conditions. In addition, the

practical load profiles introduced in 4.1.3.2 were used in Scenario III.2. For both scenarios, four permanent faults were applied to the system, as shown in Figure 4.36. Dashed lines indicate that these lines were opened in order to maintain the tree topology or isolate the faulty areas. Tripped lines are opened until the faulty areas are cleared. The tap positions of the voltage regulators were assumed to be fixed. Renewable DGs and ESSs were not considered. DG25 was disabled. The system was assumed to be fully de-energized. The weight factor for each load was assumed to be 1.

The horizon used in the BSR model was set to 7 minutes for Scenario III.1, and 12 minutes for Scenario III.2. The decision time step was set to 1 minute. The rolling-horizon procedure was disabled.

4.3.3.1 Scenario III.1: Unbalanced System with ZIP Load

The control sequences for switchable lines, DGs, and loads are listed in TABLE 4.43. A load was represented by the letter "L" followed by the node number. Since both switchable loads and non-switchable loads were considered, a subscript was used to distinguish them. The subscript "1" indicates that the load is directly connected to the bus, "1/0" indicates that the load can be remotely switched on or off, and "0" indicates that the load cannot be restored. Switchable lines were named by the letter "S" with the superscript and the subscript as the "from bus" and "to bus", respectively. Each isolated microgrid was denoted by a bracket $\{\blacksquare\}^{\text{No.}}$. 'No.' represents the index of each formed microgrid. The components in the same microgrid are placed in the same bracket. At Step 1, 3 single-phase loads ($L_{1/0}16$, $L_{1/0}17$, and $L_{1/0}34$) were restored by DG1. This is because DG1 is inverter-based, hence it can operate at 100% CUF. By Step 7, four loads were not restored,

because they were isolated due to the faults. The total amount of restored load demand at each step is listed in Figure 4.37. The total area of all the bars was the total restored energy over the horizon.

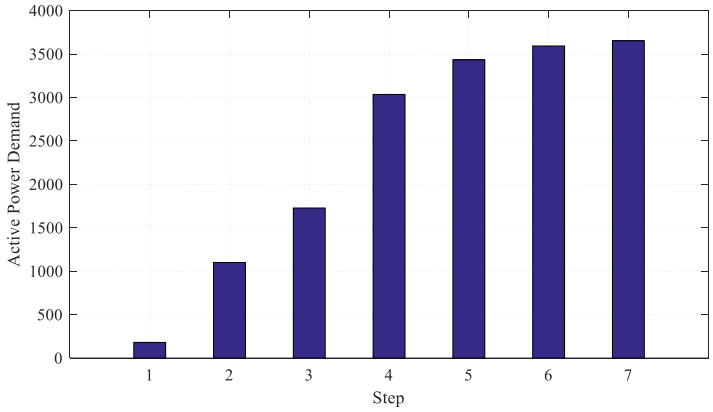

Figure 4.37. Scenario III.1: Total restored load using ZIP load model

TABLE 4.43. SCENARIO III.1: SWITCHABLE LINES AND LOADS ENERGIZED AT EACH STEP

Step	Energized Switchable Lines $x_{ij,t}^{BR}=1$	Restored Loads and DGs $x_{g,t}^{G}=1, x_{l,t}^{L}=1$
1	None	**{**DG13, $L_{1/0}$16, $L_{1/0}$17, $L_{1/0}$34**}^{1}**, **{**DG18**}^{2}**, **{**DG66**}^{3}**, **{**DG105, $L_{1/0}$106, $L_{1/0}$107**}^{4}**
2	**{**S_{13}^{8}, S_{152}^{13}**}^{1}**, **{**$S_{21}^{18}, S_{135}^{18}$**}^{2}**, **{**$S_{60}^{57}, S_{61}^{60}, S_{62}^{60}$**}^{3}**, **{**$S_{105}^{101}, S_{108}^{105}$**}^{4}**	**{**$L_1$1, $L_1$2, $L_1$4, $L_1$5,$L_1$6,$L_1$7,$L_1$9,$L_1$12,$L_1$52**}^{1}**, **{**$L_{1/0}$19, $L_1$22, $L_1$24, $L_1$35, $L_1$37,$L_1$38, $L_1$39,$L_1$41**}^{2}**, **{**$L_1$58, $L_1$59, $L_{1/0}$60, $L_1$62, $L_1$63**}^{3}**, **{**$L_1$102, $L_1$103, $L_1$104, $L_1$109, $L_1$111, $L_1$112, $L_1$113, $L_1$114**}^{4}**
3	**{**S_{14}^{9}**}^{1}**, **{**S_{25}^{23}, S_{42}^{40}**}^{2}**, **{**S_{64}^{63}, S_{61}^{56}**}^{3}**, **{**S_{197}^{97}**}^{4}**	**{**$L_1$10, $L_1$11**}^{1}**, **{**$L_1$43, $L_1$45**}^{2}**, **{**$L_{1/0}$55, $L_{1/0}$56, $L_1$64, $L_1$65, $L_1$66, $L_1$68, $L_1$69 **}^{3}**, **{**$L_1$70, $L_1$71, $L_1$98**}^{4}**
4	**{**$S_{26}^{25}, S_{28}^{25}, S_{47}^{44}$**}^{2}**, **{**$S_{72}^{67}, S_{99}^{98}$**}^{4}**	**{**DG25,DG47,$L_{1/0}$20,$L_1$28,$L_1$31,$L_1$32,$L_1$33,$L_{1/0}$42,$L_{1/0}$46 ,$L_1$47,$L_1$48**}^{2}**, **{**$L_1$73,$L_1$74, $L_1$75,$L_1$76,$L_1$86, $L_1$87, $L_1$88, $L_1$99, $L_1$100**}^{4}**
5	**{**S_{29}^{28}, S_{49}^{47}**}^{2}**, **{**S_{77}^{76}, S_{89}^{87}**}^{4}**	**{**$L_1$29, $L_1$30, $L_1$49, $L_1$50**}^{2}**, **{**DG77, $L_1$77, $L_1$90, $L_1$92, $C_{1/0}$90, $C_{1/0}$92**}^{4}**
6	**{**S_{78}^{77}, S_{93}^{91}**}^{4}**	**{**$L_1$79,$L_1$80,$L_1$94,$L_1$95,$L_1$96,$C_{1/0}$88**}^{4}**
7	**{**S_{81}^{80},**}^{4}**	**{**$L_1$84, $L_1$85**}^{4}**
Loads Not Restored:		$L_0$51, $L_0$53, $L_0$82, $L_0$83

The values of decision variables, $x_{ij,t}^{BR}$, $x_{g,t}^{G}$, and $x_{l,t}^{L}$ could be determined from TABLE 4.43. In addition, DG three-phase power outputs for scenario III.1 are summarized in TABLE 4.44, TABLE 4.45, and TABLE 4.46.

TABLE 4.44. SCENARIO III.1: DG POWER OUTPUT ON PHASE A

Step	$P_{g,t}^{A}\ (kW) + jQ_{g,t}^{A}(kVar)$						
	DG13	DG18	DG25	DG47	DG60	DG77	DG105
1	0	0	0	0	20+j10	0	0
2	140+j70	106+j38	0	0	60+j30	0	139+j70
3	199+j99	126+j40	0	0	105+j77	0	299+j150
4	199+j99	282+j0	42+j0	67+j203	125+j87	0	435+j224
5	199+j99	253+j0	80+j0	133+j249	125+j87	129+j224	306+j0
6	199+j99	266+j0	134+j0	67+j248	125+j87	516+j265	0
7	199+j99	336+j0	80+j0	50+j248	125+j87	516+j265	0

TABLE 4.45. SCENARIO III.1: DG POWER OUTPUT ON PHASE B

Step	$P_{g,t}^{B}\ (kW) + jQ_{g,t}^{B}(kVar)$						
	DG13	DG18	DG25	DG47	DG60	DG77	DG105
1	0.0	0	0	0	0	0	80+j40
2	40+j20	94+j61	0	0	40+j20	0	80+j40
3	40+j20	134+j81	0	0	149+j80	0	80+j40
4	40+j20	131+j0	42+j0	67+j157	169+j90	0	258+j165
5	40+j20	96+j0	80+j0	133+j207	169+j90	0+j155	339+j0
6	40+j20	109+j0	134+j0	67+j207	169+j90	113+j195	305+j0
7	40+j20	179+j0	80+j0	50+j207	169+j90	253+j195	165+j0

TABLE 4.46. SCENARIO III.1: DG POWER OUTPUT ON PHASE C

Step	$P_{g,t}^{C}\ (kW) + jQ_{g,t}^{C}(kVar)$						
	DG13	DG18	DG25	DG47	DG60	DG77	DG105
1	100.0+j50	0	0	0	0	0	0
2	199+j100	60+j30	0	0	40+j20	0	100+j50
3	199+j100	60+j30	0	0	174+j82	0	100+j50
4	199+j100	96+j0	42+j0	67+j125	174+j82	0	328+j179
5	199+j100	107+j0	80+j0	133+j185	174+j82	371+j200	0
6	199+j100	120+j0	134+j0	67+j185	174+j82	371+j201	0
7	199+j100	190+j0	80+j0	50+j185	174+j82	431+j230	0

The black start sequence specified in TABLE 4.43 is shown in Figure 4.38. Different from Case I, there were four microgrids developed starting from the first step. In addition, each microgrid was isolated from other three microgrids at each step and operated in the tree topology. The system was eventually partitioned into four isolated microgrids as shown in Figure 4.39, since there were four black start DGs in the system, and constraint (4.63) requires that a black start DG should be started at the first step. Within each microgrid, all the loads were balanced by the local DGs within the same microgrid. This was guaranteed by the power balance constraints. In addition, for each microgrid, the tree topology was maintained. There were 3 DGs in microgrid No2, and two DGs in microgrid No.4. All the DGs within a microgrid were coordinated during the restoration process. For example, in microgrid No.2, DG18 on N18 is the black start DG, so it started at Step 1. DG25 and DG47 are non-black start DGs, and they were started at Step 4 (see TABLE 4.43) and dispatched to coordinate with DG18.

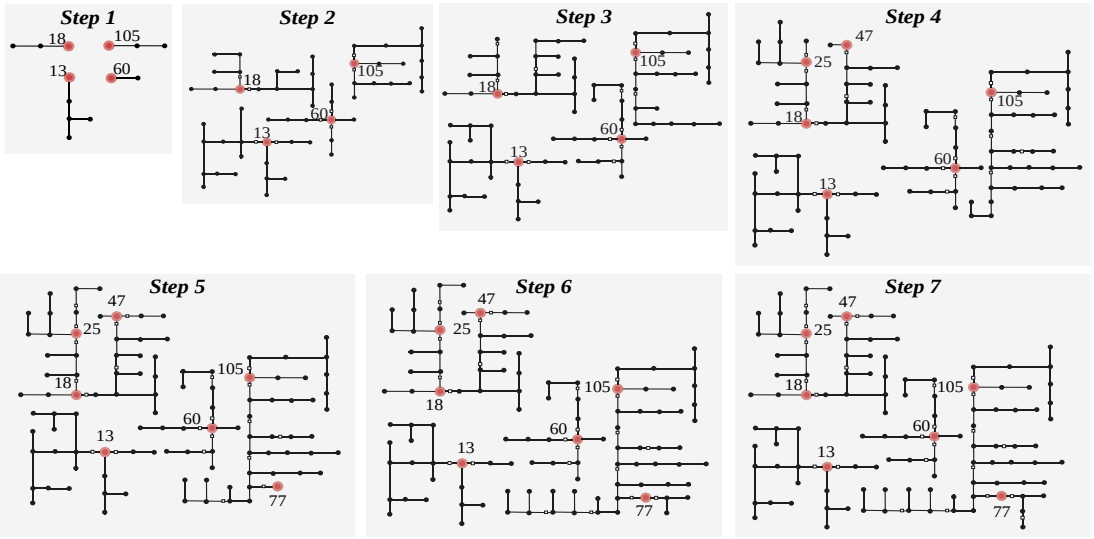

Figure 4.38. System topologies specified in the black start sequence at each time step for Scenario III.1

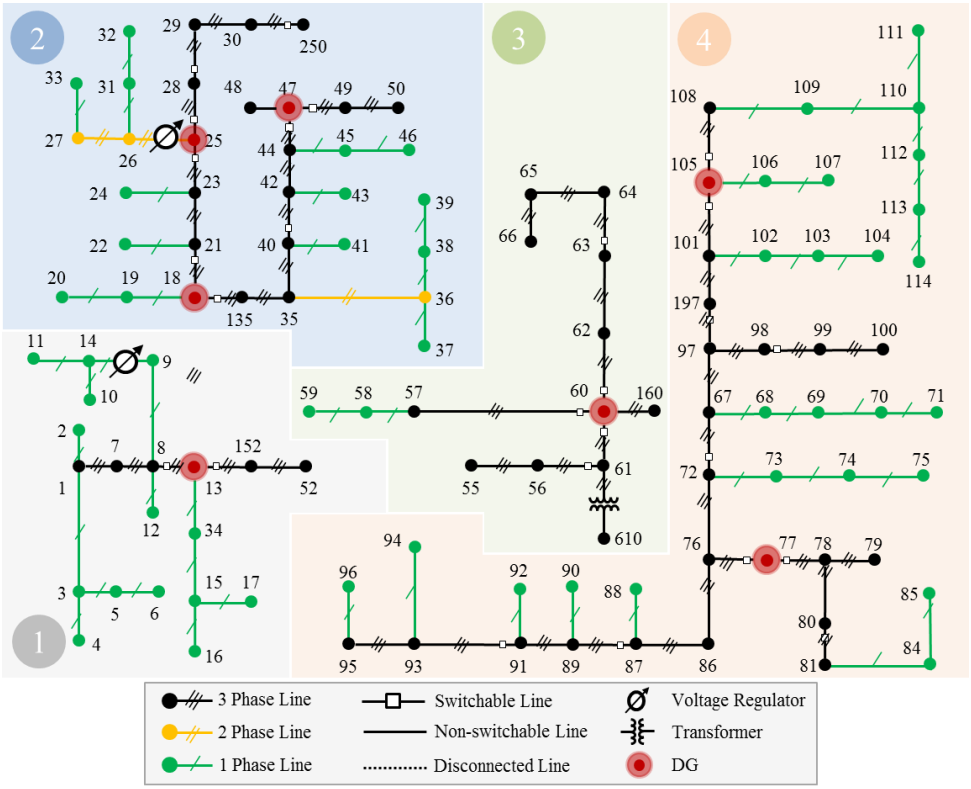

Figure 4.39. Scenario III.1: Energized system at the last step. De-energized components are removed from the original diagram.

As an example, Figure 4.40 illustrates how microgrid No.2 was developed step-by-step by performing the restoration sequence listed in TABLE 4.43. It can be seen that the black start DG18 was started at Step 1 and two lines 18-19 and 19-20 were energized because they were directly connected to DG18. However, the switchable loads L19 and L20 were not restored. This is because the current unbalance index (CUI) for DG18 is 20%. Since 18-19 and 19-20 are single-phase lines on phase A, restoring L19 and L20 can make the CUI 100%, which may be harmful for DG18. At Step 2, two switchable lines 18-21 and 18-135 were energized. All the non-switchable lines that directly connected to them were energized as well. Note that lines 18-19, 19-20, 36-37 are single-phase lines on

phase A; 21-22 36-38, 38-39 are single-phase lines on phase B; 23-24, 40-41 are single-phase lines on phase C. Therefore, loads on different phases were restored at the same step, resulting in a nearly balanced aggregated load. The load demand on phase A was *40+j20* kVA, on phase B was *39.86+j19.92* kVA, on phase C was *40+j20* kVA. The CUI for DG18 at Step 2 was 0.0012. At Step 3, L43 and L45 were restored. However, L46 was not restored even if node N46 was energized, because the CUI for DG18 at Step 3 was 19.9%, which almost hit the limit (20%). Restoring L46 at Step 3 will make the system become more unbalanced. At Step 4, DG25 and DG47 were started to coordinate with DG48 during the following steps.

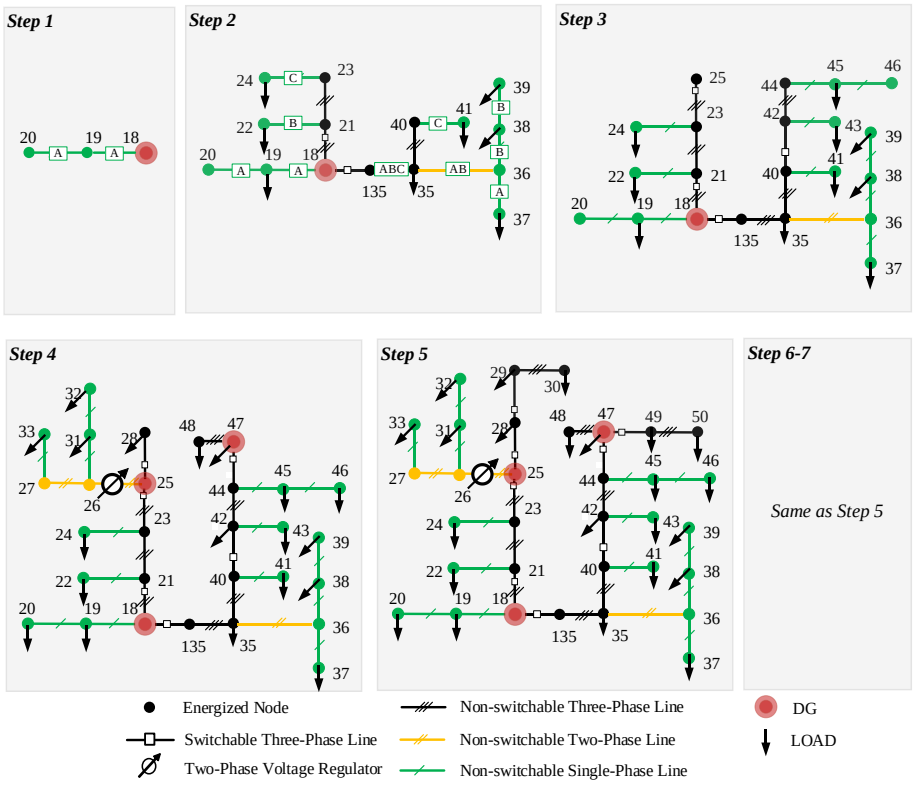

Figure 4.40. Scenario III.1: Restoration sequence showing how microgrid No.2was developed step-by-step. The presenting phase(s) for each line is marked for Step 1 and Step 2

The three-phase active power output of DG18, DG25 and DG47 are shown Figure 4.41. It can be seen that starting from Step 2, DG18 increased its power output to balance the connected loads. From Step 2 to Step 5, DG18 increased power output as more loads were restored at each step. At Step 4, DG25 and DG47 were started. The three-phase power generated by DG25 and DG47 were coordinated with DG18 to balance the load demand at each step.

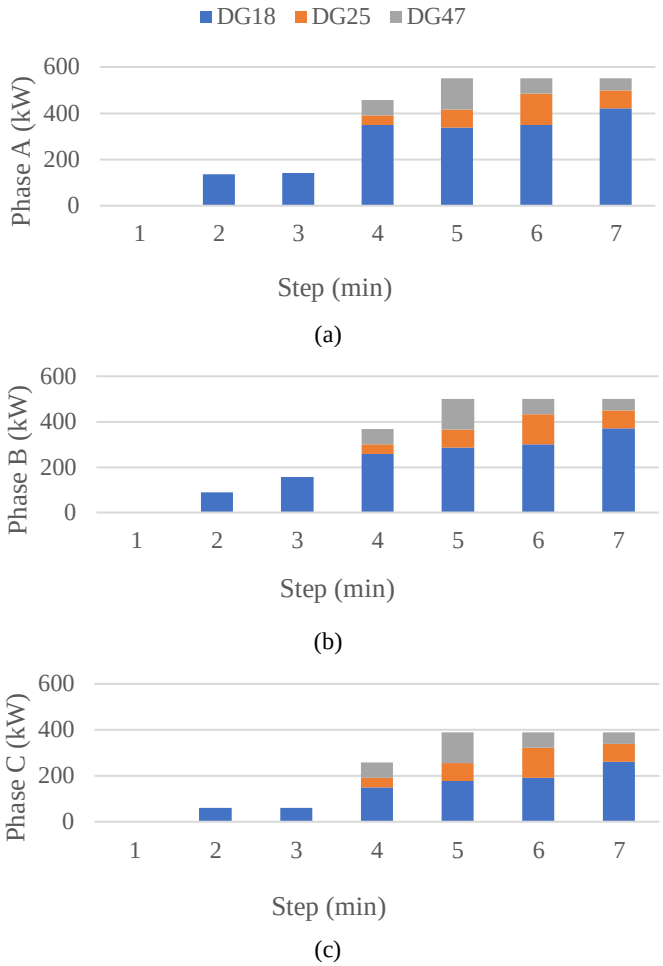

Figure 4.41. Three phase active power output by DG18, DG25, and DG47 in Scenario III.2. (a): Phase A, (b): Phase B, (C): Phase C

In the BSR model, the DG current unbalance constraints are defined for all the black start DGs. TABLE 4.47 lists the CUI values for all the DGs at each time step. It can be observed that the CUI values for DG18 at Step 3 was larger than the threshold 20% by 1.3%. This is due to the linearization technique used for approximating CUI. However, this error was small and can be tolerated. To address this problem, the system operator can use a conservative CUI limit in the BSR model. From TABLE 4.43, DG13 was started at step 1 with three loads (L16, L17, and L34) on phase C. Therefore, the CUI value for DG13 at step 1 was 100%. Since the maximum CUI value for DG18 and DG60 is 20%, no loads were restored at step 1 in Microgrid 2 and Microgrid 3 to avoid violating the DG current unbalance constraints. For dispatchable DGs (DG25, DG47 and DG105), which outputted same amount of power at each phase, the CUI values were 0% at each step.

TABLE 4.47. CUI VALUES FOR ALL THE DGS IN SCENARIO III.1

Step (min)	DG13	DG18	DG25	DG47	DG60	DG77	DG105
1	1.0	0.000	0.0	0.0	0.000	0.0	1.0
2	0.37	0.000	0.0	0.0	0.143	0.0	0.165
3	0.36	0.211	0.0	0.0	0.093	0.0	0.439
4	0.36	0.181	0.0	0.0	0.093	0.0	0.139
5	0.36	0.194	0.0	0.0	0.093	0.0	0.039
6	0.36	0.182	0.0	0.0	0.093	0.0	0.145
7	0.36	0.205	0.0	0.0	0.093	0.0	0.098

Voltage-dependent ZIP loads change load demands in response to their terminal voltage magnitudes. The load demands for two voltage dependent loads, constant current load L45 and constant impedance load L22, are listed in TABLE 4.48 and TABLE 4.49,

respectively. It can be seen that the voltage magnitudes were different at each step, the equivalent load demands for both L45 and L22 were approximated accordingly. The errors between the reference values and the approximated values were very close. Note the voltage at each step was quite close to 1.0 p.u., which helped reduce the approximation error, since the ZIP load was linearized using the Tylor series and expanded at 1.0 p.u.

TABLE 4.48. VOLTAGE DEPENDENT LOAD: CONSTANT CURRENT LOAD L45

Step (min)	Phase A Voltage (p.u.)	Active Power (kW)			Reactive Power (kVar)		
		Ref.	Approx.	error	Ref.	Approx.	error
1	0	0	0	0	0	0	0
2	0	0	0	0	0	0	0
3	0.9987	19.974	19.97441	0.000415	9.987	9.987207	0.000207
4	0.9946	19.892	19.8928	0.000801	9.946	9.9464	0.0004
5	1.0037	20.074	20.07334	0.00066	10.037	10.03667	0.00033
6	1.0025	20.05	20.04966	0.000337	10.025	10.02483	0.000168
7	1.0025	20.05	20.04966	0.000337	10.025	10.02483	0.000168

TABLE 4.49. VOLTAGE DEPENDENT LOAD: CONSTANT IMPEDANCE LOAD L22

Step (min)	Phase B Voltage (p.u.)	Active Power (kW)			Reactive Power (kVar)		
		Ref.	Approx.	error	Ref.	Approx.	error
1	0	0	0	0	0	0	0
2	0.9982	39.85613	39.85574	0.000385	19.92806	19.92787	0.000193
3	0.998	39.84016	39.83984	0.000322	19.92008	19.91992	0.000161
4	0.9996	39.96801	39.9681	9.45E-05	19.984	19.98405	4.73E-05
5	0.9995	39.96001	39.95813	0.001875	19.98001	19.97907	0.000938
6	0.9996	39.96801	39.96635	0.001653	19.984	19.98318	0.000826
7	0.9996	39.96801	39.96635	0.001653	19.984	19.98318	0.000826

The maximum step load constraint defined in the BSR model prevents excessive frequency dip due to restoring loads. The frequency responses during the restoration process for each isolated microgrid are shown in Figure 4.42. It be can observed that each time a black start DG changed its active power output due to restoring a group of loads or coordinating with other dispatchable DGs within the same microgrid, the frequency changed accordingly. The frequency for each isolated microgrid was maintained between 59.5Hz and 60.5Hz.

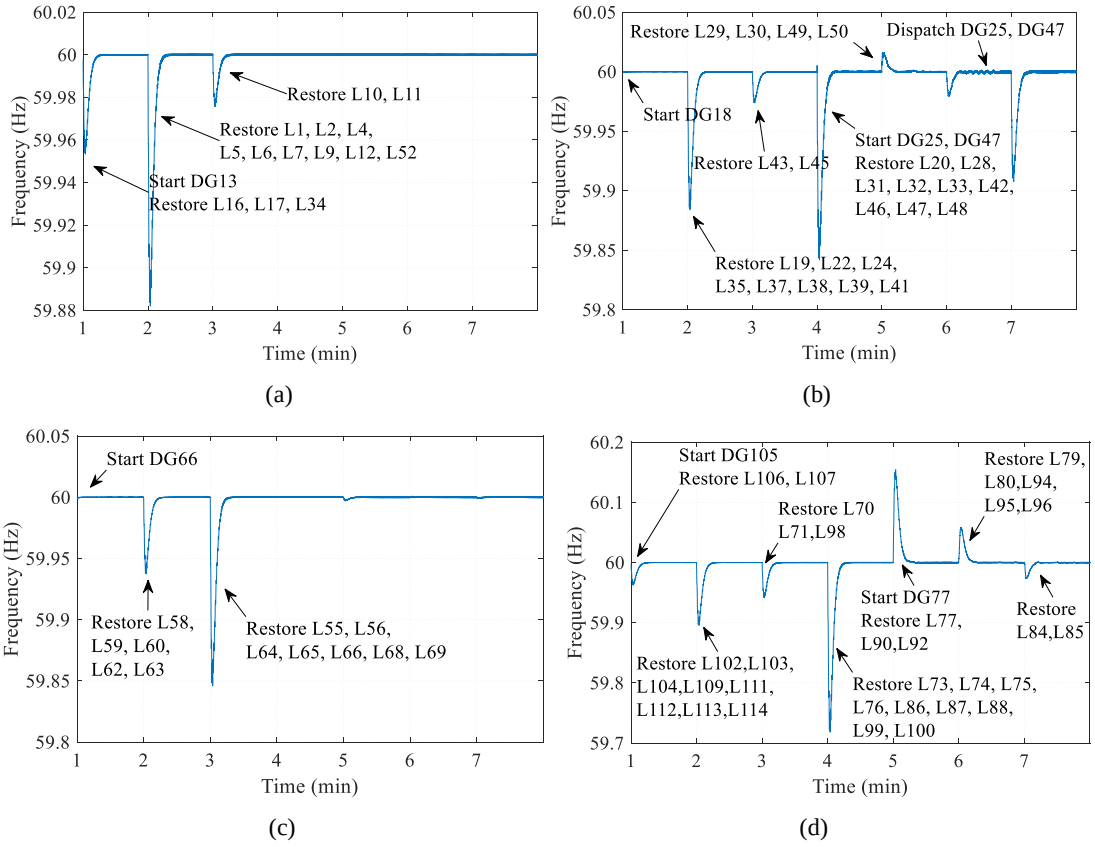

Figure 4.42. Frequency response during the restoration process for each isolated microgrid. (a): Microgrid No.1, (b): Microgrid No.2, (c): Microgrid No.3, (d): Microgrid No.4

4.3.3.2 Scenario III.2: Unbalanced System with CLPU Loads

In Scenario III.2, all the loads were assumed to be under CLPU conditions.

Figure 4.43 shows the total restored load demand at each step. The peak load demand was around 4600 kW at Step 6. It can be observed that at from Step 7 to Step 12, the total load demand decreased due to CLPU effects.

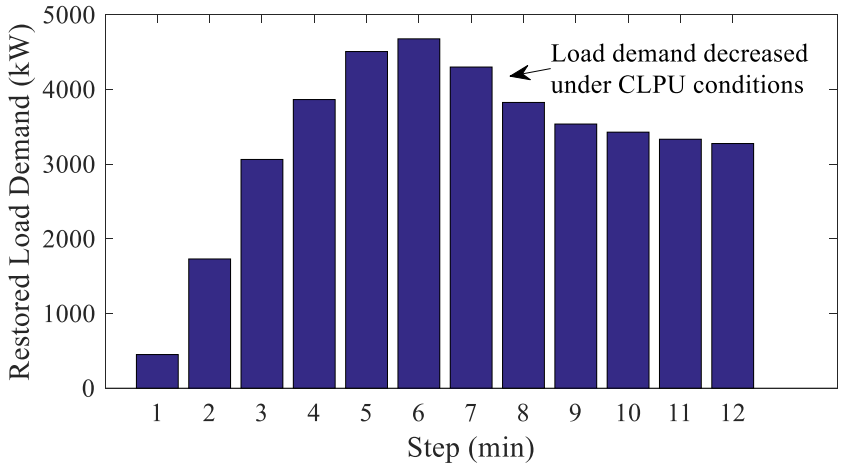

Figure 4.43. Scenario III.2: Total restored load

The restoration sequences for switchable lines and loads are listed in TABLE 4.50. Comparing to TABLE 4.43, it can be observed that some loads were restored later in Scenario III.2. For example, in Scenario III.1, it took 5 steps for microgrid No.2 to restore all the loads, whereas 10 steps were used in this scenario. This is because the initial load demand under CLPU conditions will be much higher than normal demand. Restoring a group of loads was limited by various constraints defined in the BSR model (e.g., line capacity, voltage, DG ramp, and DG current unbalance). Therefore, some load can only be restored when previously-energized loads decreased due to reaching diversity [117].

TABLE 4.50. SCENARIO III.2: SWITCHABLE LINES AND LOADS ENERGIZED AT EACH STEP

Step	Energized Switchable Lines	Restored Loads and DGs
	$x_{ij,t}^{BR} = 1$	$x_{g,t}^{G} = 1, x_{l,t}^{L} = 1$
1	None	{DG13, $L_{1/0}$16, $L_{1/0}$17, $L_{1/0}$34}[1], {DG18}[2], {DG66}[3], {DG105, $L_{1/0}$106, $L_{1/0}$107}[4]
2	$\{S_{152}^{13}\}^1$, $\{S_{21}^{18}, S_{135}^{18}\}^2$, $\{S_{60}^{57}, S_{61}^{60}, S_{62}^{60}\}^3$, $\{S_{105}^{101}\}^4$	{$L_1$52}[1], {$L_{1/0}$19, $L_1$22,$L_1$24, $L_1$35,$L_1$37,$L_1$38,$L_1$39,$L_1$41, }[2], {$L_1$58,$L_1$59, $L_{1/0}$60, $L_1$62, $L_1$63}[3], {$L_1$102, $L_1$103, $L_1$104}[4]
3	$\{S_{13}^{8}\}^1$, $\{S_{25}^{23}\}^2$, $\{S_{64}^{63}, S_{61}^{56}, S_{160}^{60}\}^3$, $\{S_{197}^{97}\}^4$	{$L_1$1,$L_1$2,$L_1$4,$L_1$5,$L_1$6,$L_1$7,$L_1$9,$L_1$12, }[1], {$L_{1/0}$55, $L_{1/0}$56, $L_{1/0}$64, $L_1$65, $L_1$66}[3] {$L_1$68,$L_1$69, $L_1$70, $L_1$71, $L_1$98}[4]
4	$\{S_{14}^{9}\}^1$,$\{S_{26}^{25}, S_{42}^{40}\}^2$, $\{S_{72}^{67}\}^4$	{$L_1$10, $L_1$11}[1], {$L_1$31,$L_1$32,$L_1$33, $L_1$43,$L_1$45}[2], {$L_1$73, $L_1$74, $L_1$75, $L_1$76, $L_1$86, $L_1$87, $L_1$88, $C_{1/0}$88 }[4]
5	$\{S_{47}^{44}\}^2$, $\{S_{77}^{76}, S_{89}^{87}, S_{99}^{98}, S_{108}^{105}\}^4$	{DG25, DG47, $L_1$47,$L_1$48}[2], {DG77, $L_1$77, $L_1$90, $L_1$92, $L_1$99, $L_1$100, $L_1$109, $L_1$111, $L_1$112, $L_1$113, $L_1$114}[4]
6	$\{S_{48}^{30}\ S_{49}^{47}\}^2$, $\{S_{78}^{77}, S_{93}^{91}\}^4$	{$L_1$29, $L_1$30, $L_1$49, $L_1$50}[2], { $L_1$79, $L_1$80, $L_1$94, $L_1$95, $L_1$96}[4]
7	$\{S_{81}^{80}\}^3$	{$L_{1/0}$20 }[2], {$L_1$84, $L_1$85}[4]
8	None	None
9	None	None
10	None	{$L_{1/0}$42}[4]
11	None	None
12	None	None
Loads Not Restored:		$L_0$51, $L_0$53, $L_0$82, $L_0$83, $L_1$28, $L_{1/0}$46

The values of decision variables, $x_{ij,t}^{BR}$, $x_{g,t}^{G}$, and $x_{l,t}^{L}$ could be determined from TABLE 4.50. In addition, DG three-phase power output for scenario III.2 are summarized in TABLE 4.51, TABLE 4.52, and TABLE 4.53.

TABLE 4.51. SCENARIO III.1: DG POWER OUTPUT ON PHASE A

Step	$P_{g,t}^{A}\ (kW) + jQ_{g,t}^{A}(kVar)$						
	DG13	DG18	DG25	DG47	DG60	DG77	DG105
1	0+j0	0+j0	0+j0	0+j0	0+j0	0+j0	0+j0
2	100+j50	300+j150	0+j0	0+j0	150+j75	0+j0	0+j0
3	334+j167	253+j127	0+j0	0+j0	229+j126	0+j0	400+j200
4	426+j213	343+j172	0+j0	0+j0	187+j104	0+j0	543+j244
5	341+j171	224+j188	40+j0	180+j68	154+j86	200+j100	588+j265
6	277+j139	411+j297	74+j0	50+j12	137+j77	215+j100	643+j297
7	242+j121	471+j323	40+j0	60+j0	127+j71	267+j100	448+j224
8	223+j112	415+j287	40+j0	50+j0	122+j69	67+j100	547+j173
9	213+j106	368+j261	40+j0	50+j0	119+j67	267+j100	291+j144
10	207+j104	392+j272	40+j0	50+j0	117+j66	267+j100	261+j129
11	204+j102	370+j260	40+j0	50+j0	116+j66	267+j100	244+j120
12	202+j101	352+j251	40+j0	50+j0	116+j65	267+j100	235+j116

TABLE 4.52. SCENARIO III.1: DG POWER OUTPUT ON PHASE B

Step	$P_{g,t}^{B}\ (kW) + jQ_{g,t}^{B}(kVar)$						
	DG13	DG18	DG25	DG47	DG60	DG77	DG105
1	0+j0	0+j0	0+j0	0+j0	0+j0	0+j0	200+j100
2	0+j0	200+j100	0+j0	0+j0	100+j50	0+j0	169+j84
3	100+j50	169+j84	0+j0	0+j0	374+j192	0+j0	129+j64
4	84+j42	229+j114	0+j0	0+j0	313+j161	0+j0	362+j203
5	64+j32	128+j140	40+j0	180+j68	248+j129	200+j100	417+j179
6	53+j27	231+j207	74+j0	50+j12	213+j112	215+j100	507+j229
7	47+j24	216+j195	40+j0	60+j0	194+j102	267+j100	338+j169
8	44+j22	201+j179	40+j0	50+j0	183+j96	67+j100	450+j124
9	42+j21	187+j171	40+j0	50+j0	177+j94	267+j100	202+j100
10	41+j21	179+j166	40+j0	50+j0	174+j92	267+j100	175+j86
11	41+j20	175+j163	40+j0	50+j0	172+j91	267+j100	161+j79
12	40+j20	173+j162	40+j0	50+j0	171+j91	267+j100	153+j75

TABLE 4.53. SCENARIO III.1: DG POWER OUTPUT ON PHASE C

Step	$P_{g,t}^{C}\ (kW) + jQ_{g,t}^{C}(kVar)$						
	DG13	DG18	DG25	DG47	DG60	DG77	DG105
1	250+j125	0+j0	0+j0	0+j0	0+j0	0+j0	0+j0
2	211+j106	150+j75	0+j0	0+j0	100+50j	0+j0	250+125j
3	411+j205	127+j63	0+j0	0+j0	324+j167	0+j0	211+j106
4	345+j172	197+j98	0+j0	0+j0	271+j140	0+j0	566+j305
5	279+j140	102+j126	40+j0	180+j68	216+j113	200+j100	483+j262
6	244+j122	408+j296	74+j0	50+j12	186+j98	215+j100	350+j200
7	224+j112	363+j269	40+j0	60+j0	170+j90	267+j100	360+j230
8	213+j107	308+j233	40+j0	50+j0	161+j85	67+j100	489+j194
9	207+j104	273+j214	40+j0	50+j0	156+j83	267+j100	232+j115
10	204+j102	254+j203	40+j0	50+j0	153+j82	267+j100	201+j99
11	202+j101	243+j197	40+j0	50+j0	152+j81	267+j100	184+j91
12	201+j101	237+j194	40+j0	50+j0	151+j80	267+j100	175+j86

Based on the switching sequence listed in TABLE 4.50, the system was eventually partitioned into four isolated microgrid, as shown in Figure 4.44. Except microgrid No.2, all the other three microgrids had similar final configurations with the microgrids formed in Scenario III.1 (see Figure 4.39). However, the restoration sequence for each microgrid was different.

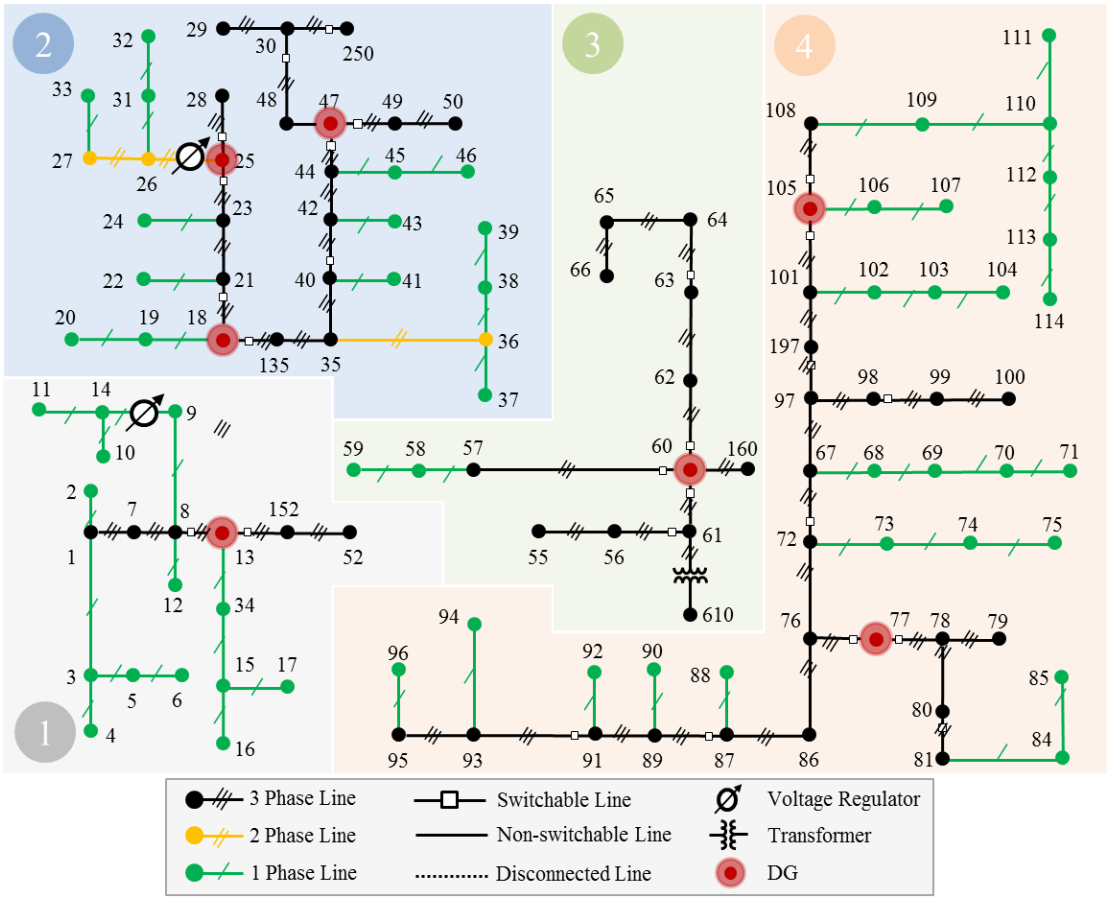

Figure 4.44. Scenario III.2: Energized system at the last step. De-energized components are removed

The restoration sequence specified in TABLE 4.50 for microgrid No.2 is shown in Figure 4.45. The restoration sequence generated by the BSR method was different from that in Scenario III.1 (see Figure 4.40) starting from Step 2. DG25 and DG47 were started at Step 5. The three DGs in microgrid No.2 were coordinated to provide power for the changing load demand under CLPU conditions.

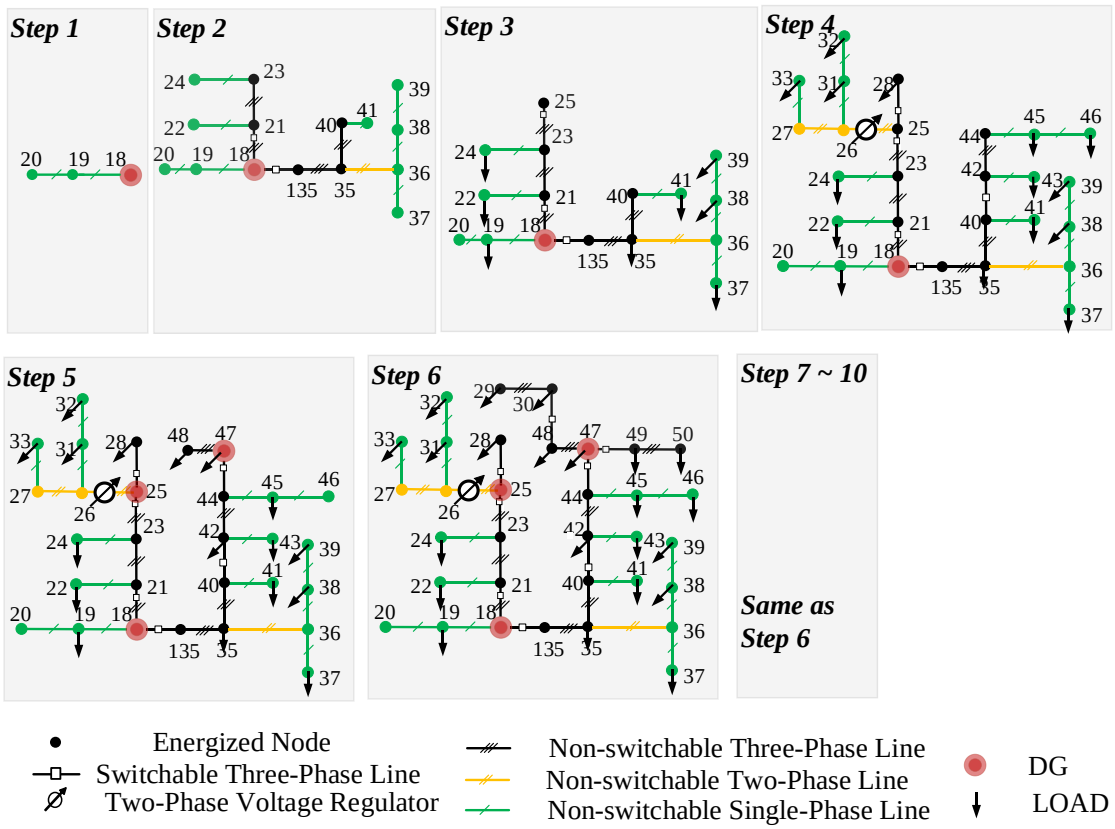

Figure 4.45. Scenario III.2: Restoration sequence showing how microgrid No.2 was developed step-by-step.

The CUI factors for all the DG in Scenario II.2 are listed in TABLE 4.54. The CUI values for DG18 at Step 2 and Step 3 were slightly beyond the CUI limit (20%). Since DG13 was started at step 1 together with L16 L17 and L34, the CUI value for DG13 at step 1 was 100%. Then, as more loads were restored from step 3 to step 6, the CUI values for DG13 were maintained between 30% and 40%. From step 7 to step 12, although no more loads were restored in Microgrid 1, the CUI values continued to change at each step since all the energized loads were under CLPU conditions. Similar observations were made for other black start DGs. The CUI values for non-black start DGs were 0%, since their three-phase power output were balanced.

TABLE 4.54. CUI FACTORS FOR ALL THE DGS IN SCENARIO II.2

Step (min)	DG13	DG18	DG25	DG47	DG60	DG77	DG105
1	1.000	0.000	0	0	0.000	0	1.000
2	0.588	0.204	0	0	0.143	0	0.527
3	0.332	0.204	0	0	0.132	0	0.326
4	0.361	0.174	0	0	0.139	0	0.101
5	0.367	0.194	0	0	0.128	0	0.073
6	0.364	0.151	0	0	0.120	0	0.147
7	0.363	0.189	0	0	0.114	0	0.049
8	0.363	0.179	0	0	0.110	0	0.032
9	0.363	0.167	0	0	0.108	0	0.109
10	0.363	0.200	0	0	0.107	0	0.119
11	0.363	0.191	0	0	0.106	0	0.126
12	0.364	0.180	0	0	0.106	0	0.130

In summary, the proposed BSR method was applied to an unbalanced three-phase system in Case III. The capability of handling ZIP load, CLPU load, and generating corresponding restoration sequences was demonstrated.

4.3.4 Case IV: Rolling-Horizon Procedure

Case IV was performed to show how the rolling-horizon functionality works. The balanced modified IEEE 123 node test system was used in Case IV. The system information of the test system can be found in APPENDIX A. All the lines of the test system were switchable, and there was only one black start DG13 in the system. The system was completely de-energized due to a major blackout caused by extreme weather events. All the loads were under CLPU conditions. The objective function and constraints were the same as that used in Case I. Different lengths of prediction horizon (3, 5, 12, and 30 minutes) were studied. The decision time step (Δt) was 1 minute. The implementation

framework is introduced in Section 3. For each prediction horizon (*T*) value, the control horizon (*C*) was selected as *T-1*. The total scheduled horizon (*H*) was 30 minutes. For each prediction horizon, the total number of rolling-horizon iterations (*K*) was determined, so that all the control actions were generated over the total scheduled horizon.

TABLE 4.55 summarizes the total number of restored loads, total restored energy by Step 30, and computation time for different horizons. The system can be fully restored within 30 minutes. When *T* was 12 minutes, 114 out of 123 loads were restored within 3 iterations, indicating the rolling-horizon procedure may generate a suboptimal solution. Similarly, when *T* was 5, 114 loads were restored within 7 iterations, while the computation time was a fraction of previous cases. Note that only 17 loads were restored when $T = 3$, implying that the rolling-horizon procedure using a very small window length may generate low-quality solutions.

TABLE 4.55. RESULTS OF BSR USING ROLLING-HORIZON PROCEDURE IN CASE IV

T (min)	*C* (min)	*H* (min)	*Iteration (K)*	No. of Restored Loads	Restored Energy by Step 30 (kWh)	Computation Time (s)
30	30	30	1	123	835.27	16.200
12	11	30	3	114	785.85	12.225
5	4	30	7	114	644.01	9.432
3	2	30	12	17	133.55	8.813

Figure 4.46 shows the total restored load at each step. In Figure 4.46, different window lengths generated solutions of varying quality. Although $T = 5$ can restore 114 loads eventually, the restored energy (644.01 kWh) during the process was less than the cases using $T = 12$ or $T = 30$ (785.85 kWh and 835.27 kWh). This is because at each iteration,

the proposed formulation will maximize the restored energy within the given horizon. For example, if $T = 3$, the method will try to restore as much energy as possible within the prediction horizon during each iteration. Using a very short window will easily get trapped into a local optimal solution. This is why when $T = 3$, the restoration plan in Figure 4.46 restored more energy than other cases from Step 1 to Step 6, but restored no more loads after Step 6 to avoid violating constraints. Whereas other cases can successfully energize other DGs along the energization paths, then restored more loads using local DGs. Regarding the computation time, since the proposed MILP model defines variables and constraints for each controllable component at each step, longer window lengths will result in more computation time. Therefore, the window length should be selected carefully, and a properly tuned rolling-horizon BSR method can generate an acceptable solution within a reasonable time. The system operator should select window lengths as large as possible, while ensuring the computation time is acceptable.

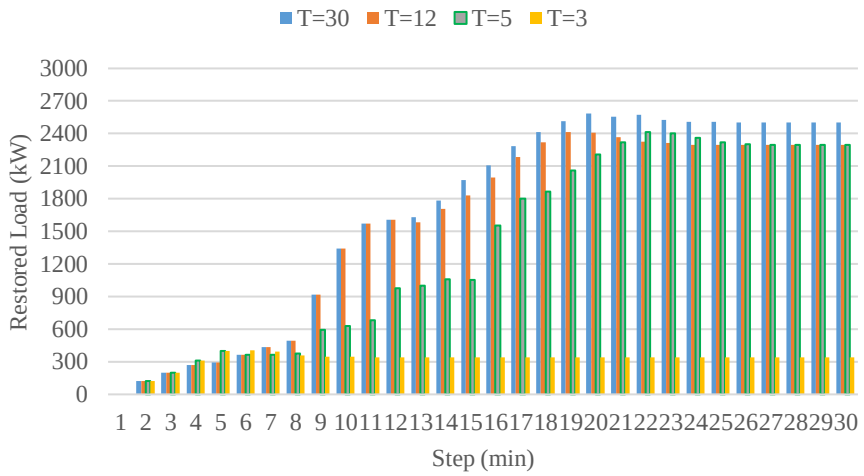

Figure 4.46. Restored load demand (kW) at each step for different prediction horizons

Figure 4.47 shows a zoomed-in view of restored load from Step 3 to Step 10, when the horizon was 3 and 5, respectively. For convenience, we named both sequences as horizon-3 sequence and horizon-5 sequence. We can see that from Step 5 to Step 7, horizon-3 sequence restored more energy than horizon-5 sequence. However, starting from Step 8, the horizon-5 sequence started restoring more demand than the horizon-3 sequence. TABLE 4.56 lists the horizon-3 and horizon-5 sequences. It can be seen that from Step 1 to Step 5, the sequences were the same. However, at Step 6, the horizon-3 sequence energized line 18-19, and line 18-21 (see Figure 4.48). This is because there were two loads connected to Node 19 and Node 21. Restoring these two loads will maximize the restored load for the considered horizon. However, by checking the line capacity constraints, it is not possible to restore any other loads. Otherwise, some line will be overloaded. On the contrary, the horizon-5 sequence energized lines 18-135, 135-35, 35-40, and 40-42, then eventually started the DG at Node 42 (see Figure 4.48).

TABLE 4.56. RESTORATION SEQUENCE WHEN T WAS 3 AND 5

Step	T =3	T = 5
1	None	None
2	1-3, 1-7	1-3, 1-7
3	3-4, 3-5, 7-8	3-4, 3-5, 7-8
4	5-6, 8-9, 8-12,8-13	5-6, 8-9, 8-12,8-13
5	9-14, 13-34, 13-18, 13-152	9-14, 13-34, 13-18, 13-152
6	18-19, 18-21	18-135
7	None	135-35
8	None	35-40
9	None	40-41, 40-42 (42 is DG node)
…	…	…

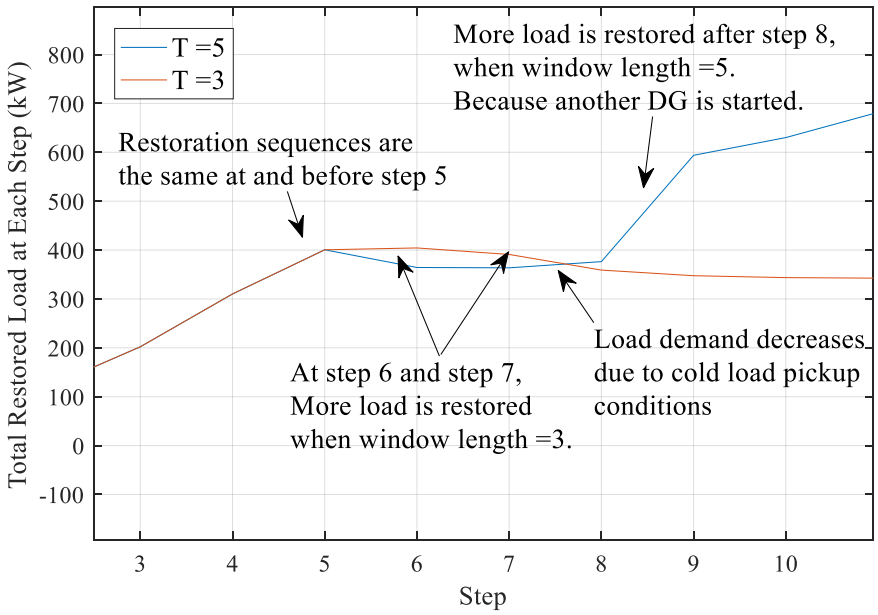

Figure 4.47. Total restored load at each step, when *T* was 3 and 5, respectively

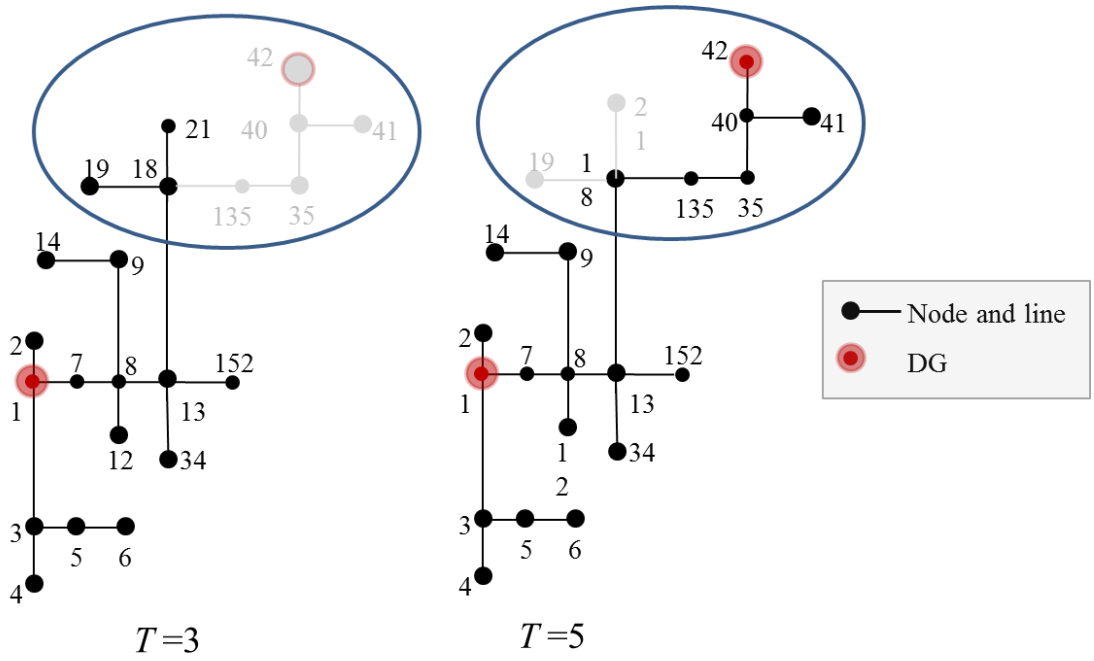

Figure 4.48. System configuration at Step 9. Horizon-3 sequence restored loads at node 19 and node 21. Horizon-5 sequence picked loads on nodes 35, 40, and 41, and eventually started the DG on node 42

Note the control horizon (*C*) used in the rolling-horizon procedure was set to *T-1*. That is to say, during each iteration, a restoration sequence for a total of *T* steps was generated, then only the first *T-1* steps were implemented. In some applications (e.g., model predictive control for stabilization control), the control horizon is normally set as 1 [117]. Next, for the same test system, different control horizons were tested for two different prediction horizons (e.g., *T*=12 and *T*=5). For each selected control horizon, a maximum iteration number was assigned to ensure the solution can be generated for the entire scheduled horizon, which was 30 minutes in this case. Restored load demand at each step for different control horizons when the prediction horizon was 12 minutes and 5 minutes are shown in Figure 4.49 and Figure 4.50, respectively. It can be observed that when the horizon was large (e.g., *T=12*), all the selected control horizons, except *C=1*, can be used to achieve similar results. However, small control horizons require more iterations to generate the solution for the scheduled horizon (e.g., 30 minutes). When *C=1*, the horizon will move forward 1 step every iteration. Thus, it can be trapped in the local optimal solution as well. For example, when *C=1*, starting from Step 7, no more loads were restored until Step 23. For short prediction horizons (e.g., *T=5*), a satisfying solution was generated only when *C=4*. Using smaller control horizons (e.g., 1, 2, and 3) can only generate poor quality solutions.

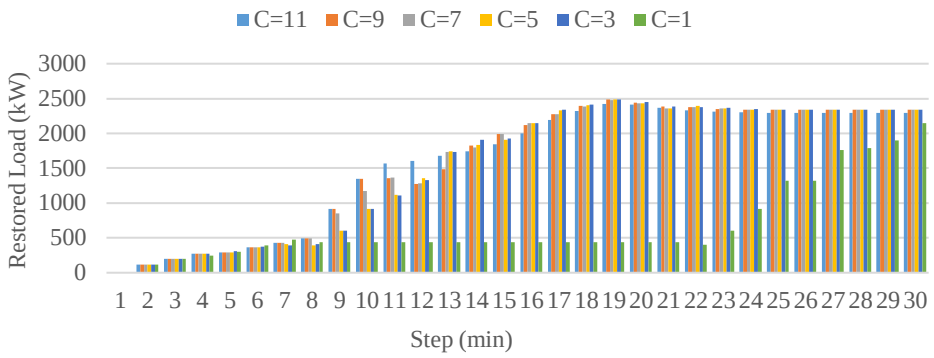

Figure 4.49. Restored load demand at each step for different control horizons when the prediction horizon is 12

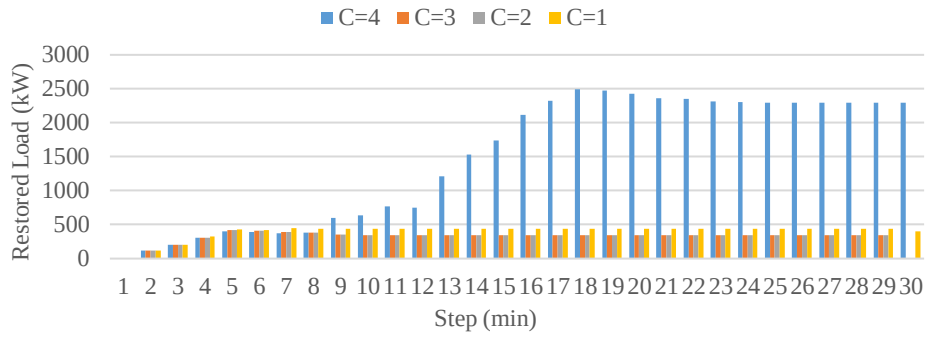

Figure 4.50. Restored load demand at each step for different control horizons when the prediction horizon is 5

Next, the rolling-horizon procedure was applied to the same test system under light loading conditions (50% of the original loading demand) using the same rolling-horizon settings. The results were shown in TABLE 4.55. It can be observed that for all the cases, all the loads were restored. However, the total restored energy over the horizon of 30 minutes was different for each case. Again, this was because using shorter horizons can only schedule operations over fewer steps than using long horizons. Thus, different sequences were generated, which can be observed in Figure 4.51. When the horizon was 3 minutes, similar observations as discussed for Figure 4.46 can be made from Step 1 to

Step 7, where the total restored energy was maximized. However, from the long run, using 30-minute horizon obviously had restored more energy over the entire 30-minute horizon.

TABLE 4.57. RESULTS OF BSR USING ROLLING-HORIZON PROCEDURE UNDER LIGHT LOADING CONDITION

T (min)	*C* (min)	*H* (min)	*Iteration (K)*	No. of Restored Loads	Restored Energy by Step 30 (kWh)	Computation Time (s)
30	30	30	1	123	419.5	18.603
12	11	30	3	123	416.5	12.306
5	4	30	7	123	394.7	10.530
3	2	30	12	123	393.7	9.155

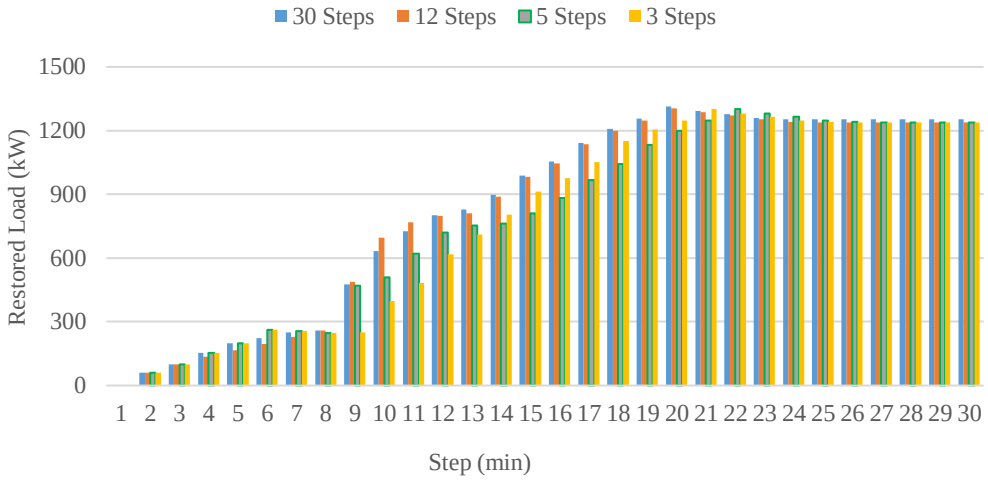

Figure 4.51. Restored load demand (kW) at each step for different windows lengths

In summary, the rolling-horizon procedure with different rolling-horizon parameters were studied. In some cases, the solutions generated using very short horizons were trapped into local low-quality solutions, because short horizon length will significantly reduce the capability of coordinating various control actions across multiple time steps. In

addition, different lengths of control horizons were studied. It has been shown that small control horizons may result in poor solutions.

4.3.5 Case V: Renewable DGs and ESS

In Case V, the restoration solutions were studied when PV and ESS were added to the unbalanced modified IEEE 123 node test system. In this case, it was assumed that each load node has a certain penetration of PV and ESS. The PV profiles and load profiles were retrieved by sampling the PV curves and load curves starting from 10:00pm, June 1st 2016, from the Pecan Street project database (see subsection 4.1.3). All the loads were assumed to be under CLPU conditions. The system was fully de-energized. The test system was the unbalanced modified IEEE 123 node test system introduced in section 4.1.2. The system parameters can be found in APPENDIX B. The rolling-horizon parameters were selected as: $\Delta t = 2$ minutes, $C = 8$ minutes, $T = 10$ minutes, and $H = 60$ minutes.

Figure 4.52 shows one of the PV profiles used in Case V. The horizontal axis represents the hours, and the vertical axis represents the PV output in kW. It can be seen that the PV only outputs power during day time. The PV output is fluctuating in response to the sunlight radiation over solar panels. The peak PV output is reached around 2:00pm. Similarly, three sample load profiles are shown in Figure 4.53. The horizontal axis represents the hours, and the vertical axis represents the aggregated load demand in kW. The three curves represent the load profiles of 10 houses, 50 houses, and 80 houses.

By grouping different number of individual residential/commercial/industrial load profiles, each load in the test system was represented by a unique profile. Since each load in the system was assumed to be installed with a certain percentage of PV and ESS, it was

assumed that a PV will be energized immediately when its load is restored, and ESS can be controlled separately.

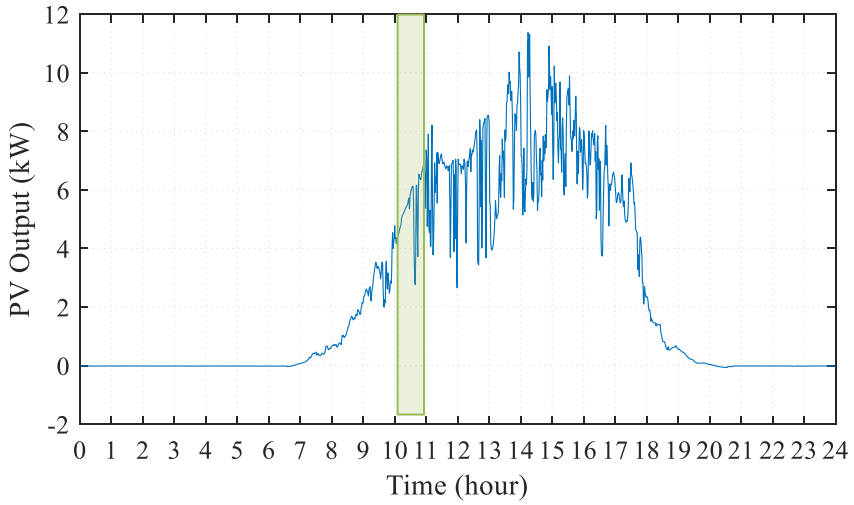

Figure 4.52. A PV profile used in Case V sampled starting from 10:00am

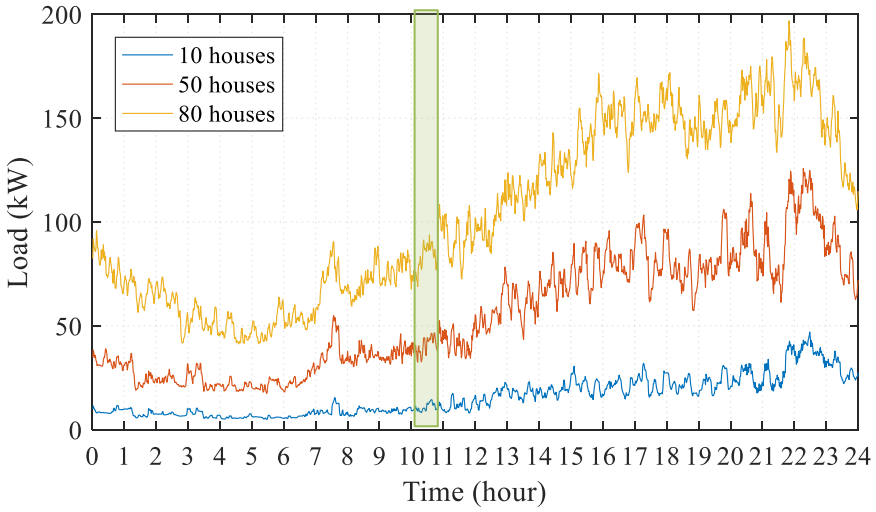

Figure 4.53. A load profile used in Case V sampled starting from 10:00am

Three scenarios with different penetrations of PV and ESS were studied in Case V. The scenario information and the values of the objective function are summarized in TABLE 4.58. In Scenario V.1, there were no renewable DGs or ESS in the system. The restoration solution generated by the BSR method can restore 2230.4 kWh of energy. In Scenario V.2, 10% of PV was installed at each load node and no ESS in system. The total restored energy was 2720.5 kWh, which was higher than in Scenario V.1. In Scenario V.3, both 10% of PV and 10% of ESS were installed at each load node. The total restored energy was 2888.4 kWh. From the values of restored energy, installing both PV and ESS can help restore more energy.

TABLE 4.58. SCENARIOS OF DIFFERENT PV AND ESS PENETRATIONS USED IN CASE V

Scenario No.	PV (%)	ESS Penetration (%)	Restored Energy (kWh)
V.1	0%	0%	2230.4
V.2	10%	0%	2720.5
V.3	10%	10%	2888.4

Figure 4.54 shows the total restored load at each step in each scenario. Scenario V.3 clearly has restored more energy than the other two scenarios, which can also be observed in TABLE 4.58. Most loads were energized during the first 10 minutes. In Scenario V.1, some loads restored in Scenario V.3 cannot be restored without using PV and ESS. In Scenario V.2, some loads restored within first 8 steps in Scenario V.3 were restored from Step 18 to Step 24. For each scenario, the CLPU effects can be observed when the total amount of restored load demand decreased after being restored and gaining diversity. For example, the load demand decreased from 4000 kW to 3000 kW from Step 8 to Step 18 because the loads restored before Step 7 started gaining diversity.

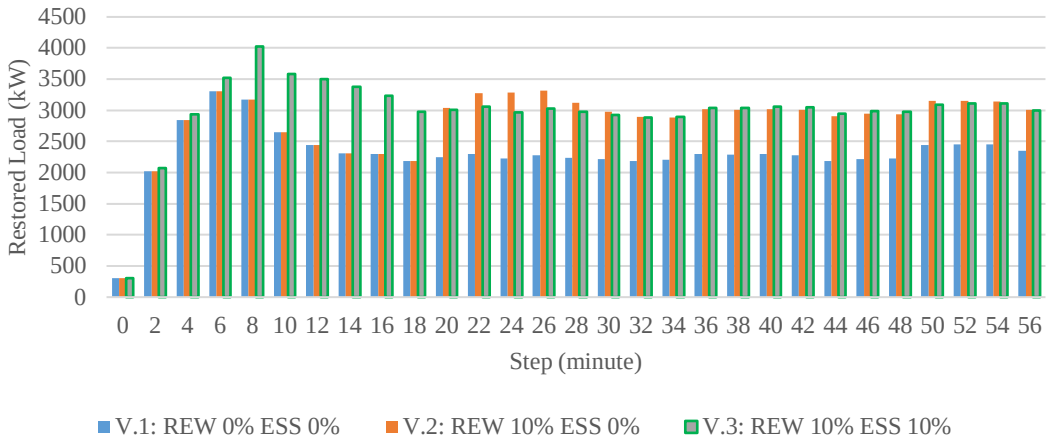

Figure 4.54. Case V: Total restored load at each step in each scenario

As an example, Figure 4.55 shows the ESS charging/discharging actions and PV profiles at node 78. It can be observed that ESS at node 78 was discharged from Step 2 to Step 9, when most loads were restored. Indeed, providing active power locally during these steps was most helpful for alleviating various operational constraints. This is because ESS can directly reduce the load demand on its terminal node, hence directly reduce the line power and prevent the node voltage from dropping too much. Furthermore, when PV output dropped around Step 20, ESS can compensate the dropped power immediately.

In summary, three scenarios with different penetrations of PV and ESS were studied and discussed in Case V. The BSR method is shown to be able to incorporate time-varying PV profiles and load profiles into the BSR model. The ESS at each node can be effectively dispatched to help with restoration and compensate the PV outputs.

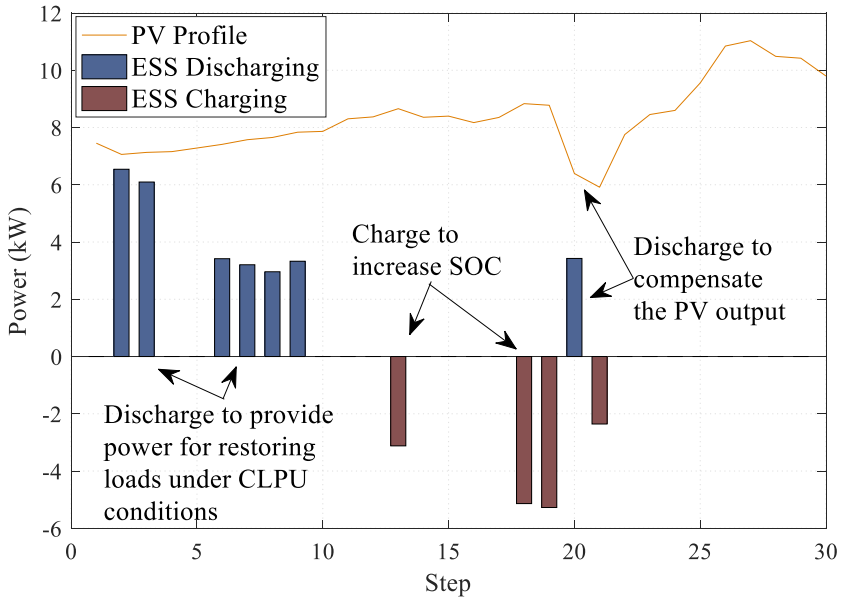

Figure 4.55. Scenario V.3: ESS charging/discharging and PV profile at node 78

4.3.6 Case VI: Validation of Linear Power Flow Models

Two linear power flow models are formulated in the BSR model for approximating the voltage magnitude and line power for balanced and unbalanced three-phase systems. The linearized models will inevitably introduce approximation errors. Therefore, the restoration solutions generated by the BSR method should be validated to ensure the approximation errors are acceptable. In Case VI, the linear power flow models for balanced systems and unbalanced systems were validated in OpenDSS, which is an open-source software developed by the Electric Power Research Institute (EPRI) [142]. To validate each linear power flow model, multiple scenarios were generated. For each scenario, a restoration solution was generated.

4.3.6.1 Validation of Power Flow Model for Balanced Systems

The test system used for validating the linear power flow model for balanced systems was the balanced modified IEEE 123 node test system. The horizon was set to 10 minutes. The interval was set to 1 minute. Rolling-horizon procedure was disabled. All the loads were under CLPU conditions. No faults were applied to the system. The system was fully de-energized. The objective function and constraints were the same as that used for Case I. A total of 20 scenarios were generated for validation purposes. The load demand for each load was multiplied by a scale factor from 1.0 to 1.5.

The voltage magnitude and line power values ($V_{i,t}$ and $P_{ij,t}^{BR} + jQ_{ij,t}^{BR}$) solved by the BSR method were compared with the OpenDSS results in the correlation plots, as shown in Figure 4.56. In Figure 4.56 (a), voltage magnitudes were compared with OpenDSS results. It shows that the voltage magnitudes were always maintained between 0.97 p.u. and 1.04 p.u., and that they were closely correlated with the OpenDSS results. The maximum error was around 0.002 p.u. In Figure 4.56 (b), the line apparent powers approximated by the linear power flow were compared with the OpenDSS results. The maximum error was around 20 kVA. This is mainly due to the fact that the nonlinear terms, which represent the system losses, are neglected in the linear power flow model.

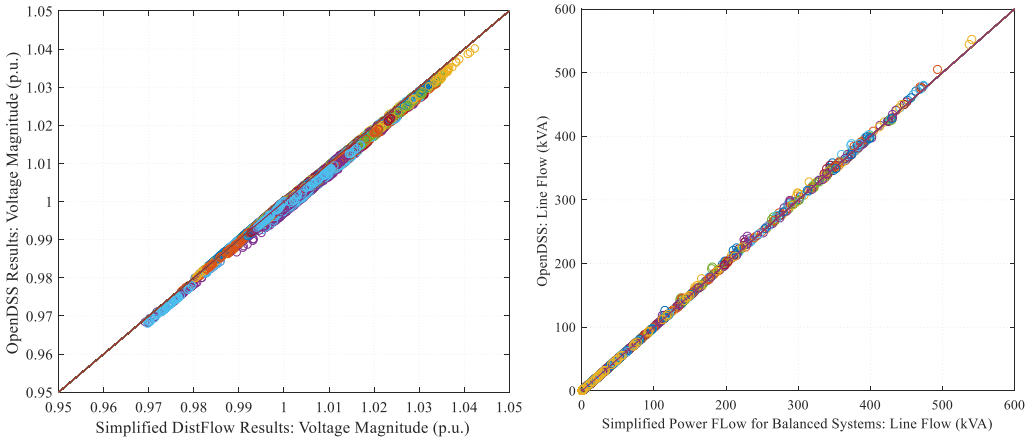

(a) (b)

Figure 4.56. Correlation between linear power flow results and OpenDSS results under balanced conditions. (a): Voltage magnitude. (b): Line apparent power

4.3.6.2 Validation of Power Flow Model for Unbalanced Systems

The unbalanced modified IEEE 123 node test system was used for validating the linear power flow model for unbalanced systems. The horizon was set to 10 minutes. The interval was set to 1 minute. Rolling-horizon procedure was disabled. All the loads were ZIP loads. The system was fully de-energized. The objective function and constraints were the same as that used for Case III. A total of 20 scenarios were generated for validation purposes. The load demand for each load was multiplied by a scale factor, from 1.0 to 1.5.

The voltage magnitude and line power values approximated by the linear power flow were compared with the OpenDSS results in Figure 4.57. In Figure 4.57(a), three-phase voltage magnitudes were compared with the OpenDSS results. The maximum error was around 0.002 p.u. The voltage on each node was maintained between 0.98 p.u. and 1.015 p.u. Figure 4.57(b) compares the line apparent power between the approximated values

and the OpenDSS results. The maximum error was around 80 kVA. This was mainly resulted by the assumptions that was made to derive the linear power flow formulation. In practice, system operator can use a conservative limit to avoid overloading on the lines.

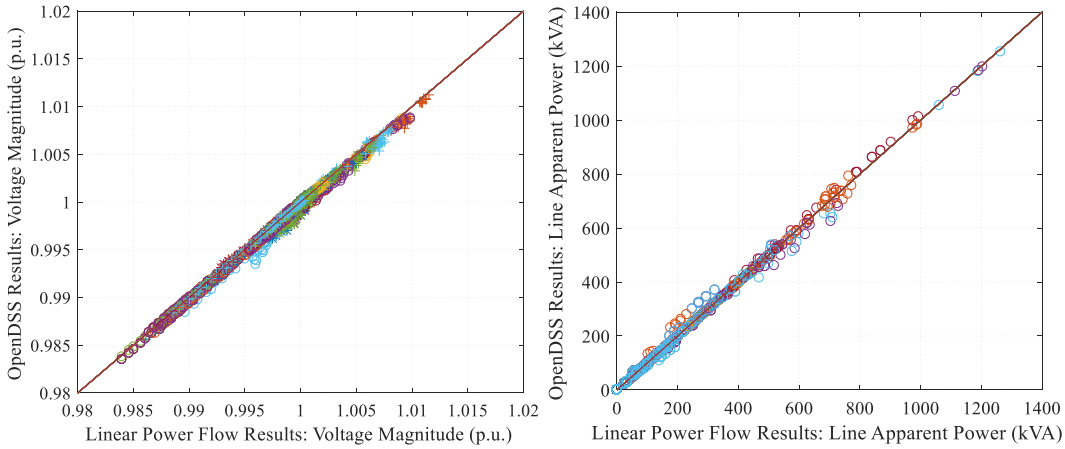

(a) (b)

Figure 4.57. Correlation between linear power flow results and OpenDSS results under unbalanced condtions. (a): Voltage magnitude. (b): Line apparent power

In summary, the voltage magnitudes and line powers approximated by the linear system models were validated against the OpenDSS results. The results showed that the approximation errors for both balanced system model and unbalanced system model were within acceptable ranges from the engineering perspective.

4.4 Performance Analysis

As concluded in the case studies, the BSR method can generate black start solutions in response to different system operating conditions. The results of case studies showed that a proper selection of rolling-horizon parameters is critical for generating high-quality solutions. In addition, the computation time, which is important for the BSR method to be implemented in a near-real time manner, requires further studies under different system operating conditions and rolling-horizon parameters. In this section, the performance of the BSR method applied to different system conditions is analyzed. First, performance indices are defined to measure the quality of the solutions. Next, the impact of rolling-horizon parameters is studied. Finally, the performance of the BSR method applied to various system operating conditions is studied.

4.4.1 Performance Indices

To quantitatively analyze the performance of the proposed BSR method, three performance indices are introduced in this subsection.

1) Total restored energy: The total restored energy (E) is the objective function of the BSR method. It an important index to measure the performance of the BSR method under different operating conditions. The load weight factors were set to 1 for all cases studied in this subsection. E can be mathematically defined as:

$$E = \sum_{l \in \mathcal{L}} \sum_{t \in \mathcal{T}} \left(P_{l,t}^{A} + P_{l,t}^{B} + P_{l,t}^{C} \right) \cdot \Delta t \tag{4.24}$$

where $\mathcal{L}$ is the set of loads, $P_{l,t}^{A}$, $P_{l,t}^{B}$, and $P_{l,t}^{C}$ are load demand on each phase of load l at step t. The load demand on a phase will be zero if this phase is not present. In addition, the load demand will be zero if it is not restored.

2) *Optimal solution gap:* Optimal solution gap is defined as the difference between the reference solution generated using single-horizon procedure (e.g., the rolling-horizon parameters are set as *C=T=H, K=1*) and the solution generated using rolling-horizon procedure [133, 136]. This index can be mathematically defined as [133, 136]:

$$G = \frac{E^* - E}{E^*} \times 100\% \tag{4.25}$$

where E^* is the total restored energy solved using single-horizon procedure; E is the total restored energy solved using rolling-horizon procedure.

3) *Computation* time: Computation time is the duration used for solving the BSR model. In this dissertation research, the MILP model was solved by CPLEX 12.6, on an Intel Core i7-4600U, 2.1 GHz CPU, 12 GB RAM, and 64-bit operating system PC.

4.4.2 Test System

The test system used for performance analysis was the three-phase unbalanced modified IEEE 123 node test system, which is introduced in APPENDIX B. The single-line diagram of the test system is shown in Figure 4.58. The DG on node 13 was the only black start DG. All the other DGs were non-black start dispatchable DGs. No faults were applied to the system. This configuration greatly increases the system complexity comparing with the configuration used in the case studies, since it contains more switches

and will take more steps to fully energize the system starting from the only black start DG. The system was fully de-energized.

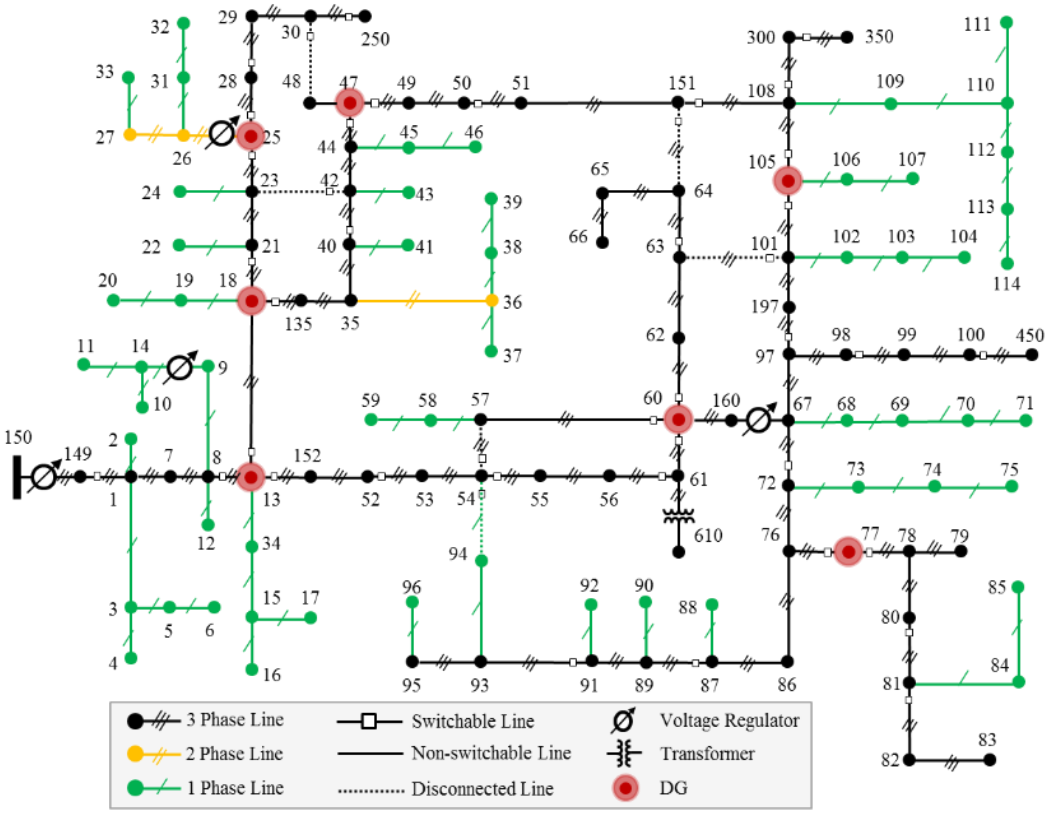

Figure 4.58. Single-line diagram of the test system

4.4.3 Rolling-Horizon Parameters

In this subsection, the impact of using different rolling-horizon parameters is studied. First of all, the impact of different decision time steps (Δt) was studied. Then, the impact of total scheduled horizons (H) were studied. Next, different combinations of prediction (T) and control (C) horizons were studied.

4.4.3.1 Impact of Decision Time Step

A black start restoration solution contains control actions over multiple time steps. A decision time step specifies the duration between two consecutive discrete time steps. It can be expected that if a system can be fully energized using different decision time steps, smaller steps can enable the control actions to be implemented faster, hence accelerating the black start process. Therefore, properly selecting a decision time step for the BSR model is important. The rolling-horizon procedure was enabled to study the impact of using different rolling-horizon parameters on the test system introduced in section 4.4.2. The total scheduled horizon (H) was 30 minutes. The decision time steps (Δt) were selected from 0.5 minutes to 4 minutes in intervals of 0.5 minutes. The prediction horizon (T) and control horizon (C) were 10 steps and 9 steps, with each step being equal to the selected decision time step. The BSR method was applied to different system operating conditions (e.g., DG ramp rate, DG capacity, maximum step load, and loading level).

The values of two performance indices, total restored energy and computation time, are listed in TABLE 4.59 and TABLE 4.60, respectively. Multiple scenarios representing different system operating conditions were created by scaling the DG ramp rate, DG capacity, maximum step load, and loading level. The scaling factors are shown in both tables.

TABLE 4.59. RESTORED ENERGY FOR DIFFERENT DECISION TIME STEPS

Δt (min)	Restored Energy (kWh)								
	Original	Fast DG Ramp Rate (5x)	Slow DG Ramp Rate (0.2x)	Large DG Cap. (5x)	Small DG Cap. (0.5x)	Large Step Loads (100%)	Small Step Loads (10%)	Heavy Loading (2x)	Light Loading (0.5x)
0.5	0	1844.26	0.00	0.00	0.00	0	0.00	0	372.31
1.0	1591.58	1598.57	0.00	1591.58	0.00	1631.56	0.00	0	820.21
1.5	1265.65	1265.67	1244.99	1265.68	438.88	1297.48	0.00	1302.49	647.18
2.0	1561.64	1561.64	1555.55	1561.64	571.31	1600.88	0.00	1642.61	789.94
2.5	1483.78	1483.78	1477.71	1483.79	551.26	1521.08	0.00	1595.65	749.88
3.0	1423.02	1423.02	1419.38	1423.02	489.02	1458.78	0.00	1519.88	717.45

TABLE 4.60. COMPUTATION TIME FOR DIFFERENT DECISION TIME STEPS

Δt (min)	Computation Time (seconds)								
	Original	Fast DG Ramp Rate (5x)	Slow DG Ramp Rate (0.2x)	Large DG Cap. (5x)	Small DG Cap. (0.5x)	Large Step Loads (100%)	Small Step Loads (10%)	Heavy Loading (2x)	Light Loading (0.5x)
0.5	74.19	332.23	67.62	85.55	48.78	80.42	64.34	152.22	58.46
1.0	945.3	200.46	79.25	973.24	43.09	934.43	893.45	209.66	47.57
1.5	156.2	143.97	580.43	148.95	140.66	136.55	106.98	2428.51	51.64
2.0	64.96	76.23	99.24	66.98	185.39	64.14	83.76	408.33	56.49
2.5	62.65	61.72	67.40	62.94	143.53	59.36	78.66	618.32	49.10
3.0	68.52	72.84	63.43	67.47	208.40	58.65	108.42	2178.67	54.30

From TABLE 4.59, when $\Delta t = 0.5$ minutes, it can be observed that for the original system operating condition, no loads were restored. This is because the ramp rate of DGs was insufficient to restore any loads within a short amount of time to support any loads, if the decision time step is too small. The maximum power output of a DG increased/decreased between two consecutive steps is formulated as $P_{t \to t+1} = P^{ramp} \cdot \Delta t$. However, if a DG has sufficient ramping capacity, it can restore a load by increasing its power output within a short time step. This can be observed in TABLE 4.59 when $\Delta t =$

0.5 minutes, 332.23 kWh of load demand was restored when DG ramp rate was enlarged by 5 times and 58.46 kWh of load demand was restored when loading level was halved. In TABLE 4.59, for the original system operating condition, more energy was restored using $\Delta t = 1$ minute than using larger decision time steps, since control actions were implemented faster than using larger intervals. When the ramp rate was scaled by 0.5, it can be seen that no loads were restored when Δt=0.5 or 1.0 minutes. This is because lower ramp rates prevented DGs from outputting enough power to supply any loads within the specified decision time steps.

Regarding the DG capacity, enlarging DG capacity by 5 times did not show significant impact on the performance indices, in terms of total restored energy and computation time. When the DG capacity was scaled by 0.5, only a small amount of energy was restored (e.g., 439 kWh restored when $\Delta t = 1.5$, 571 kWh restored when $\Delta t = 2.0$), since less power could be outputted by DGs and the maximum load step determined by equation (3.84) became smaller accordingly. The computation time was increased by around three times, as shown in TABLE 4.60.

Enlarging the maximum step load coefficient to 100% did not show a major impact on the computation time as shown in TABLE 4.60. In TABLE 4.59, more energy (e.g., 1631 kWh restored when $\Delta t = 1$, compared to 1591 kWh restored under original operating conditions) was restored for each selected decision time step. This is because large maximum step load coefficients allowed DGs to restore more loads within a decision time step. When the maximum step load coefficient was lowered to 10%, no loads were restored for all selected decision time steps.

As shown in TABLE 4.59, when the system loading was doubled, no loads were restored (i.e., total restored energy was 0 kWh) when 0.5 and 1.0 minutes were used as decision time steps. This is because under heavy loading conditions, restoring a load may require DGs to output more power, hence requiring the DGs to have sufficient ramp rates. When the system was lightly loaded, 372.3 kWh of energy were restored when $\Delta t = 0.5$ minutes, even though the DGs were operated with limited ramp rate capacity.

Regarding the computation time, it can be observed in TABLE 4.60 that using large decision time steps resulted less computation time, except when the system was under heavy loading conditions. For the original operating condition, the BSR method took 945 seconds to solve the MILP model when Δt=1 minute. For heavily loaded condition, the computation time increased significantly. When Δt =1.5 and 3 minutes, the BSR method took around 35 ~ 40 minutes to solve the MILP model. This is because by stressing the system, many constraints (e.g., DG related constraints, line kVA capacity constraint) could be potentially violated if too much loads were restored. Therefore, the MILP solver would execute more branch-and-bound iterations to find the optimal solution [131].

4.4.3.2 Impact of Total Scheduled Horizon

In order to study the impact of total scheduled horizon (*H*), different horizons were tested under various system operating conditions. In this subsection, *H* were selected as 6, 10, 14, 18, 22, 26, and 30 minutes. The decision time step was set to 2 minutes. In order to compare the performance of different horizons, the total restored energy within 30 minutes was analyzed. For a smaller *H* (e.g., 6 minutes), the rolling-horizon procedure was enabled to generate the solutions over 30 minutes by assuming $T = H$. As observed

in Case IV, a large control horizon (C) could achieve better solutions given a fixed T. Therefore, the control horizon (C) was selected as $T - 1$. The impact of selecting different vales of T and C is studied in section 4.4.3.3.

The total restored energy and computation time for each scenario are listed in TABLE 4.61 and TABLE 4.62, respectively. Multiple scenarios representing different system operating conditions were created by scaling the DG ramp rate, DG capacity, maximum step load, and loading level. The scaling factors are shown in both tables.

TABLE 4.61. TOTAL RESTORED ENERGY USING DIFFERENT TOTAL SCHEDULED HORIZONS

H (min)	Original	Fast DG Ramp Rate (5x)	Slow DG Ramp Rate (0.2x)	Large DG Cap. (5x)	Small DG Cap. (0.5x)	Large Step Loads (100%)	Small Step Loads (10%)	Heavy Loading (2x)	Light Loading (0.5x)
6	1514.50	1514.50	1374.17	1519.43	882.06	1514.50	1514.50	1760.05	609.83
10	1518.75	1518.75	1456.47	1524.97	1033.43	1518.75	1518.75	1797.92	765.19
14	1551.11	1551.11	1450.70	1551.11	1124.25	1551.11	1551.11	1854.31	765.19
18	1551.11	1551.11	1491.36	1555.92	1095.68	1551.11	1551.11	1944.70	777.96
22	1561.64	1561.64	1491.36	1566.45	1171.13	1561.64	1561.64	N/A	777.96
26	1561.64	1561.64	1491.36	1566.45	N/A	1561.64	1561.64	N/A	783.22
30	1561.64	1561.64	1491.36	1566.45	N/A	1561.64	1561.64	N/A	783.22

TABLE 4.62. COMPUTATION TIME USING DIFFERENT TOTAL SCHEDULED HORIZONS

H (min)	Original	Fast DG Ramp Rate (5x)	Slow DG Ramp Rate (0.2x)	Large DG Cap. (5x)	Small DG Cap. (0.5x)	Large Step Loads (100%)	Small Step Loads (10%)	Heavy Loading (2x)	Light Loading (0.5x)
6	32.73	33.04	44.20	30.68	31.86	34.25	31.41	34.16	30.10
10	25.95	26.42	50.15	29.57	32.27	27.60	28.09	33.12	24.05
14	26.55	24.77	88.68	25.66	113.03	28.77	37.96	56.86	24.79
18	26.10	23.47	700.59	19.80	286.69	23.70	31.25	76.33	24.58
22	50.88	47.18	525.35	31.77	2508.53	38.40	42.16	>1 hour	29.58
26	78.44	80.06	901.02	33.75	>1 hour	60.38	50.59	>1 hour	37.76
30	123.70	129.70	1146.72	56.06	>1 hour	60.11	79.43	>1 hour	49.57

In TABLE 4.62, it can be observed that for the original system operating condition, the black start solutions generated using all the selected schedule horizons restored the system within around 2 minutes. However, as the system was stressed by reducing the operational margin (e.g., low DG ramp rate condition and heavy loading condition), the computation time increased dramatically. Specifically, when the DG capacity was halved, it took around 40 minutes to solve the MILP model when $H = 22$ minutes. When $H = 26$ minutes and $H = 30$ minutes, the MILP model could not be solved within 1 hour. Similarly, when the system was heavily loaded, a black start solution could not be generated when a long horizon was used (e.g., 22, 26, or 30 minutes). Furthermore, as shown in TABLE 4.61, using short horizons generated less-optimal solutions comparing with using longer horizons (e.g., 1514 kWh of energy restored when $H = 6$ minutes, 1561 kWh of energy restored when $H = 30$ minutes). This is because the BSR method will only search for the optimal solution within the given horizon length. Therefore, smaller H values may lead to less optimal solutions, due to lack of coordination across more steps. However, using small H values in the rolling-horizon procedure requires much less computation time than solving the problem within a single horizon using a large horizon.

4.4.3.3 Impact of Prediction Horizon and Control Horizon

In this subsection, the performance of the rolling-horizon procedure using different combinations of prediction and control horizons is discussed. The decision time step was 2 minutes, and the total scheduled horizon was 30 minutes. The PV and load profiles introduced in 4.1.3 were generated using the data at 10:00am. Both the PV penetration and ESS penetration were 10%. All loads were ZIP loads. The prediction horizons (T)

changed from 4 minutes to 14 minutes, and control horizons (C) changed from 2 minutes to 12 minutes. Note the control horizon should always be smaller than the prediction horizon. The objective value generated by single-horizon procedure was 1772.33 kWh, which took 1858 seconds to be solved. Two performance indices, optimal solution gap and reduced computation time, were used to compare different combinations of prediction and control horizons.

The performance values for different prediction and control horizons are listed in TABLE 4.63 and TABLE 4.64, respectively. It can be seen that the optimal solution gap was always zero, when the prediction horizon was 14 minutes. However, when the prediction horizons were 4 minutes, 8 minutes, and 10 minutes, poor-quality solutions were generated when the control horizon was 2 minutes or 4 minutes. When the prediction horizon was 12 minutes, using control horizons of 2 minutes or 4 minutes achieved 0.84% of optimal solution gap, which was smaller than using larger control horizons. However, regarding the computation time, using larger control horizons always resulted in less computation time. Generally, the computation time was reduced by more than 90% in most cases. Less computation time was saved when the prediction horizon was 14 minutes and the control horizon was 2 minutes. This is because the small control horizons need more iterations to cover the entire scheduled horizon. During each iteration, the MILP model must be formulated and translated to CPLEX. Therefore, more time was spent on problem formulation and translating. In conclusion, selecting the prediction and control horizons is also a trade-off between the solution quality and computation time. For this particular operating condition, the prediction horizon can be selected between 10 ~ 14

minutes, and the control horizon can be selected between 6 ~ 12 minutes. Because the optimal solutions gap can always be maintained within 2%, and the computation time can be reduced by at least 93%.

TABLE 4.63. OPTIMAL SOLUTION GAP FOR DIFFERENT PREDICTION AND CONTROL HORIZONS

	Optimal Solution Gap (%)					
	T=4 min	T=6 min	T=8 min	T=10 min	T=12 min	T=14 min
C=2 min	99.25	1.58	65.63	46.39	0.84	0.00
C=4 min		1.58	2.00	46.12	0.84	0.00
C=6 min			2.00	0.90	1.58	0.00
C=8 min				0.90	1.58	0.00
C=10 min					1.58	0.00
C=12 min						0.00

TABLE 4.64. REDUCED COMPUTATION TIME FOR DIFFERENT PREDICTION AND CONTROL HORIZONS

	Reduced Computation Time (%)					
	T=4 min	T=6 min	T=8 min	T=10 min	T=12 min	T=14 min
C=2 min	97.17	95.64	93.41	89.16	86.60	82.74
C=4 min		97.78	97.14	94.83	93.75	91.68
C=6 min			98.24	96.976	95.57	93.63
C=8 min				97.57	96.42	94.43
C=10 min					96.75028	95.14
C=12 min						95.11

In summary, the selection of the rolling-horizon parameters showed an apparent impact on the performance of the BSR method. Specifically, using small decision time steps can limit the DG ramping capability, hence only allowing small step loads to be restored. Similarly, heavily loaded conditions required the system to be operated with limited margins, hence needing more computation time for solving the MILP problem in CPLEX. Regarding the total scheduled horizon, it should be long enough to ensure the

solution optimality. Using small scheduled horizons may generate sub-optimal solutions. Again, the DG ramping capacity, DG capacity, and system loading condition are three major factors that affect the computation time. The computation time significantly increased under limited DG ramping capacity and heavily loaded condition, when single-horizon procedure was implemented. If the rolling-horizon procedure was used to reduce the computation time, the prediction and control horizons should be selected properly. Low-quality solutions were generated when both horizons were short. However, using longer prediction and control horizons resulted in longer computation time. The overall reduced computation time using rolling-horizon procedure was around 90%. Note the rolling-horizon parameters were selected for a particular operating condition. For different operating conditions, the rolling-horizon parameters should be properly selected in order to achieve a better trade-off between the solution quality and computation time.

4.4.4 Performance Under Various System Conditions

4.4.4.1 Impact of CLPU Conditions

In this subsection, the performance of the BSR method was studied under different peak load magnitudes and durations of CLPU conditions, which can be represented by S^U and α as defined in equation (3.13). Both S^U and α were changed from 0.6 to 1.5. Only black start DGs and dispatchable DGs were considered. PV and ESS were not considered. The total scheduled horizon was 30 minutes. The decision time step was set to 2 minutes. Two sets of rolling-horizon parameters were tested. The first set used 10 minutes as the

prediction horizon and 8 minutes as the control horizon. The second set used 14 minutes as the prediction horizon and 12 minutes as the control horizon.

The values of total restored energy generated by the single-horizon procedure and the computation time for all the scenarios are listed in TABLE 4.65 and TABLE 4.66, respectively. Smaller objective values or shorter computation times are marked with a shade of green. Larger objective values or longer computation times are marked with a shade of red. These values will be used as reference values for comparing with the results generated by rolling-horizon procedures.

From TABLE 4.65, it can be observed that as S^U increased, which means the peak CLPU load demand gets higher, the objective values increased accordingly. Similarly, as α increased, which means it will take more time for the peak CLPU load demand to drop gradually to the diversified loading level, the objective values increased. The minimal restored energy was 1343 kWh when $S^U = 0.6$ and $\alpha = 1.5$. The maximum restored energy was 1937 kWh when $S^U = 1.5$ and $\alpha = 0.6$.

Regarding the computation time shown in TABLE 4.66, larger S^U values and lower α values took more time to solve the MILP model. Indeed, increasing the peak CLPU load demand and CLPU duration stressed the system such that generating a feasible black start solution became more difficult, hence required more computation time. The longest computation time was around 209 seconds when $S^U = 1.5$, $\alpha = 0.8$, which was almost 6 times longer than the shortest computation time when $S^U = 0.6$, $\alpha = 0.6$. Note that this study was only conducted based on the original loading level.

TABLE 4.65. OBJECTIVE VALUES USING SINGLE-HORIZON PROCEDURE: CLPU PARAMETER STUDY

	Objective Values (kWh)									
	Su=0.6	Su=0.7	Su=0.8	Su=0.9	Su=1.0	Su=1.1	Su=1.2	Su=1.3	Su=1.4	Su=1.5
a=0.6	1401	1471	1539	1608	1675	1742	1799	1866	1903	1937
a=0.7	1388	1451	1513	1575	1637	1696	1747	1807	1840	1897
a=0.8	1378	1435	1492	1550	1606	1661	1707	1762	1790	1842
a=0.9	1369	1423	1476	1530	1581	1633	1675	1727	1750	1798
a=1.0	1363	1413	1463	1513	1562	1610	1659	1698	1745	1763
a=1.1	1357	1405	1452	1500	1546	1593	1637	1674	1718	1734
a=1.2	1353	1398	1443	1489	1533	1577	1619	1653	1696	1710
a=1.3	1349	1393	1435	1479	1521	1564	1604	1636	1677	1689
a=1.4	1346	1387	1430	1471	1512	1552	1591	1622	1661	1687
a=1.5	1343	1383	1424	1464	1503	1543	1580	1619	1647	1671

TABLE 4.66. COMPUTATION TIME USING SINGLE-HORIZON PROCEDURE: CLPU PARAMETER STUDY

	Computation Time (second)									
	Su=0.6	Su=0.7	Su=0.8	Su=0.9	Su=1.0	Su=1.1	Su=1.2	Su=1.3	Su=1.4	Su=1.5
a=0.6	30.02	31.89	35.00	28.93	54.86	55.82	90.68	121.92	116.55	203.26
a=0.7	28.64	32.16	29.83	29.01	46.22	54.88	97.39	61.77	175.77	81.98
a=0.8	34.39	30.26	31.29	31.52	81.73	56.60	57.85	58.46	137.63	209.28
a=0.9	32.42	35.62	32.61	23.79	47.07	61.51	94.76	72.65	140.79	178.91
a=1.0	45.66	32.51	40.93	47.42	49.80	54.15	60.94	86.72	65.91	157.31
a=1.1	56.12	32.57	39.58	28.27	39.38	37.34	37.42	65.37	97.82	167.40
a=1.2	26.88	49.41	57.73	30.14	53.08	42.51	67.70	71.44	63.02	168.40
a=1.3	24.59	34.60	41.92	31.14	42.00	37.86	47.70	91.61	86.20	141.76
a=1.4	26.03	32.80	26.89	25.70	51.45	54.61	68.39	115.37	75.82	51.64
a=1.5	31.88	39.41	36.13	25.63	59.55	65.49	85.67	54.29	82.75	122.71

The optimal solution gaps compared with the reference values, when the prediction horizons (T) were 10 minutes and 14 minutes, are listed in TABLE 4.67 and TABLE 4.68, respectively. “X” represents an infeasible solution was generated in the corresponding scenario. Smaller optimal solution gap values are marked with a shade of green. Larger optimal solution gap values are marked with a shade of red.

It can be seen from both TABLE 4.67 and TABLE 4.68 that as S^U increased and α decreased, the optimal solution gap became larger, meaning the rolling-horizon procedure generated less sub-optimal solutions when the peak CLPU load demand and CLPU duration increased. Using $T = 10$ minutes achieved up to 36.60% of optimal solution gap, which was much bigger than 8.74% when using $T = 14$ minutes. Note that many infeasible solutions were generated when $T = 10$ minutes. No infeasible solutions were generated when α was 0.6 or 0.7. When $T = 14$ minutes, only one infeasible solution was generated. A reason for the generation of infeasible solutions is that during each iteration of rolling-horizon procedure, the formulated BSR model only maximizes the objective value over the current prediction horizon. Since the BSR model requires that a load cannot be tripped after being restored and all the restored loads will change load demand under CLPU conditions, some operational constraints may be violated when moving to the next iteration, hence resulting in infeasible solutions.

TABLE 4.67. OPTIMAL SOLUTION GAP WHEN PREDICTION HORIZON WAS 10 MINUTES

	Optimal Solution Gap (%)									
	Su=0.6	Su=0.7	Su=0.8	Su=0.9	Su=1.0	Su=1.1	Su=1.2	Su=1.3	Su=1.4	Su=1.5
a=0.6	18.14	18.61	19.00	19.37	19.68	20.12	20.32	20.70	36.49	35.73
a=0.7	18.06	18.51	18.88	19.22	19.64	19.94	20.12	20.54	25.61	36.60
a=0.8	X	18.42	X	19.10	X	19.78	19.96	X	23.55	36.44
a=0.9	17.94	18.34	18.67	19.02	19.37	X	19.81	20.16	22.47	36.32
a=1.0	X	18.27	18.5	18.90	19.26	X	19.88	X	20.34	36.15
a=1.1	17.85	X	18.50	18.82	X	X	19.79	X	20.27	36.04
a=1.2	17.81	18.17	18.44	18.75	19.05	19.28	19.69	19.80	20.13	35.90
a=1.3	17.78	18.13	X	18.69	X	19.21	19.59	19.70	X	35.85
a=1.4	17.76	18.07	18.38	18.64	18.93	19.14	X	19.65	X	20.2
a=1.5	17.73	18.04	X	18.59	18.87	X	X	19.69	19.87	20.14

TABLE 4.68. OPTIMAL SOLUTION GAP WHEN PREDICTION HORIZON WAS 14 MINUTES

	Optimal Solution Gap (%)									
	Su=0.6	Su=0.7	Su=0.8	Su=0.9	Su=1.0	Su=1.1	Su=1.2	Su=1.3	Su=1.4	Su=1.5
a=0.6	2.84	3.86	X	5.62	6.36	7.12	7.62	8.28	8.58	8.74
a=0.7	2.66	3.62	4.48	5.29	6.06	6.72	7.21	7.83	8.11	8.71
a=0.8	2.51	3.41	4.23	5.01	5.74	6.37	6.84	7.46	7.69	8.31
a=0.9	2.39	3.24	4.02	4.77	5.45	6.06	6.52	7.10	7.34	7.93
a=1.0	2.2	3.10	3.84	4.55	5.21	5.80	6.39	6.81	7.38	7.59
a=1.1	2.19	2.97	3.68	4.36	5.01	5.57	6.15	6.56	7.06	7.26
a=1.2	2.12	2.87	3.54	4.86	4.83	5.38	5.95	6.33	6.81	7.01
a=1.3	2.06	2.78	3.39	4.07	4.68	5.22	5.76	6.13	6.60	6.77
a=1.4	2.00	2.69	3.35	3.96	4.55	5.07	5.58	5.95	6.42	6.78
a=1.5	1.95	2.62	3.26	3.86	4.42	4.97	5.44	5.93	6.27	6.60

The reduced computation times for each scenario, when the prediction horizons were 10 minutes and 14 minutes, were listed in TABLE 4.69 and TABLE 4.70. Larger values of reduced computation time (i.e., less computation time) are marked with a shade of green. Smaller values of reduced computation time (i.e., longer computation time) are marked with a shade of red. Reduced computation time reflects how much time can be saved by using rolling-horizon procedure, comparing to the computation time using single-horizon procedure shown in TABLE 4.66.

From both TABLE 4.69 and TABLE 4.70, it can be observed that when $T = 10$ minutes or 14 minutes, the computation time was reduced significantly by implementing the rolling-horizon procedure, for most of the tested scenarios. In TABLE 4.66, when $S^U = 1.5$, most scenarios (except for $\alpha = 0.7$ or 1.4) required more than 100 seconds to solve the MILP models using single-horizon procedure. Whereas in TABLE 4.69 and TABLE 4.70, the computation times for solving these scenarios using rolling-horizon procedure could be reduced by 80% ~ 90% when $T = 10$ minutes and 50% ~ 80% when

$T = 12$ minutes. Similar observations can be made for other scenarios. The average reduced computation time was around 50% to 80%. For some cases (e.g., the scenario with $T = 14$, $S^U = 1.4$, $\alpha = 1.0$), only a small amount of computation time was reduced.

TABLE 4.69. REDUCED COMPUTATION TIME WHEN HORIZON WAS 10 MINUTES

	Reduced Computation Time (%)									
	Su=0.6	Su=0.7	Su=0.8	Su=0.9	Su=1.0	Su=1.1	Su=1.2	Su=1.3	Su=1.4	Su=1.5
a=0.6	73.20	73.74	71.89	73.44	87.03	80.22	80.04	77.46	84.19	94.99
a=0.7	76.94	72.69	66.93	69.28	85.91	83.22	80.15	78.73	92.07	80.24
a=0.8	75.70	71.50	73.35	63.78	93.25	76.44	65.82	81.96	84.65	88.40
a=0.9	74.52	81.18	71.41	67.94	84.76	85.66	87.26	81.51	85.82	89.50
a=1.0	72.87	73.22	75.58	79.85	87.69	85.72	83.14	84.83	73.29	84.38
a=1.1	87.72	57.66	79.67	69.35	78.16	79.94	68.86	80.56	83.45	87.31
a=1.2	75.42	78.52	86.85	72.83	86.56	84.72	80.35	80.21	80.57	85.98
a=1.3	44.80	71.36	82.98	79.90	85.11	83.84	60.71	84.58	88.41	84.86
a=1.4	42.13	78.10	69.05	74.14	85.13	85.84	83.45	89.18	82.02	50.65
a=1.5	74.20	74.44	74.32	76.92	88.95	85.93	88.58	79.44	84.69	85.40

TABLE 4.70. REDUCED COMPUTATION TIME WHEN HORIZON WAS 14 MINUTES

	Reduced Computation Time (%)									
	Su=0.6	Su=0.7	Su=0.8	Su=0.9	Su=1.0	Su=1.1	Su=1.2	Su=1.3	Su=1.4	Su=1.5
a=0.6	67.02	70.19	70.99	44.47	46.91	67.64	80.03	71.92	66.99	74.36
a=0.7	66.42	68.92	63.74	60.72	55.77	69.81	80.80	54.92	70.74	40.96
a=0.8	70.63	74.10	67.12	67.99	82.69	64.64	56.53	64.52	64.96	74.09
a=0.9	65.30	62.20	56.96	17.33	67.22	65.18	82.16	59.07	64.50	82.81
a=1.0	51.86	62.71	72.75	61.59	71.01	67.52	68.97	77.71	14.67	52.86
a=1.1	82.19	49.30	68.38	63.47	63.07	59.52	52.16	49.93	80.19	71.71
a=1.2	61.12	75.13	80.52	64.88	43.91	61.30	75.55	53.39	40.61	78.67
a=1.3	60.03	56.45	80.24	56.66	37.08	65.58	61.87	66.90	78.72	65.84
a=1.4	52.93	69.64	71.28	64.97	54.97	58.09	55.48	80.71	65.54	41.02
a=1.5	73.94	71.93	77.03	67.91	69.04	74.68	76.96	68.58	74.97	76.57

In summary, the rolling-horizon parameters selected for a particular operating point cannot guarantee the solution quality and feasibility when being applied to other operating conditions. In this study, when applying the BSR method to different operating conditions defined by CLPU parameters, using longer prediction horizon (14 minutes) achieved relatively small optimal solution gaps and acceptable computation times, comparing with using short prediction horizon (10 minutes). Under certain CLPU conditions, infeasible solutions were observed. This is due to the lack of coordination of dispatching DERs between iterations. Even though using longer prediction horizon can reduce the number of infeasible solutions, a theoretical method should be developed to introduce the coordination among iterations when implementing the BSR method in the rolling-horizon procedure.

4.4.4.2 Impact of PV and ESS

In this subsection, the black start solutions are compared when different penetrations of PV and ESS were considered. The PV profiles were retrieved by sampling the PV curves from the Pecan Street project database introduced in section 4.1.3.1. The total scheduled horizon was 30 minutes. The interval was set to 2 minutes. Two sets of rolling-horizon parameters were used. The first set used 10 minutes as the prediction horizon and 8 minutes as the control horizon. The second set used 14 minutes as the prediction horizon and 12 minutes as the control horizon.

To generate different test scenarios, samples were taken starting from different time instances. For example, if the studied time horizon was 30 minutes, multiple PV profiles can be generated by retrieving data from the profile segments from 8:00am to 8:30am,

9:00am to 9:30am, and so on. The definitions for PV penetration and ESS penetration can be found in sections 4.1.3.1 and 4.3.5, respectively. In this subsection, the PV and load profiles were generated every two hours from 8:00am to 6:00pm using the profiles on June 1st 2016. The PV penetration was selected as 0%, 20%, 40%, 60%, 80%, and 100%. The ESS penetration was selected as 0% and 20%, respectively.

The total restored energy for each scenario, when the ESS penetration was 0%, is listed in TABLE 4.71 for $T = 10$ minutes and TABLE 4.72 for $T = 14$ minutes. Smaller values of restored energy were marked in a shade of green. Larger values of restored energy were marked in a shade of red.

From TABLE 4.71, it can be observed that when $T = 10$ minutes, many infeasible solutions were generated under different PV profiles and load profiles. When the BSR method was applied to the load demand sampled starting from 18:00, no feasible solutions could be generated for all the selected PV penetrations. This is because the rolling-horizon procedure was implemented in an iterative manner, and the BSR method only schedules the control actions for the current iteration without considering how the load and PV change in the following iterations. If the PV profiles and load profiles change in a way that they cannot be continuously supported during the following iterations, then the BSR method will generate an infeasible solution. A larger horizon can be used to address this concern. As shown in TABLE 4.72, when $T = 14$ minutes, using rolling-horizon procedure can solve all the scenarios without generating infeasible solutions, except the scenario when the load demand was generated starting from 10:00 and PV penetration was 100%.

TABLE 4.71. TOTAL RESTORED ENERGY WHEN PREDICTION HORIZON WAS 10 AND ESS PENETRATION WAS 0%

Time	Total Restored Energy (kWh)					
	PV=0%	PV=20%	PV=40%	PV=60%	PV=80%	PV=100%
8:00	610.12	610.12	X	610.12	610.12	610.12
10:00	650.69	X	X	650.69	X	650.69
12:00	X	748.26	X	748.26	748.26	748.26
14:00	X	X	872.66	872.66	872.66	872.668
16:00	X	1053.41	1058.96	X	X	1058.96
18:00	X	X	X	X	X	X

TABLE 4.72. TOTAL RESTORED ENERGY WHEN PREDICTION HORIZON WAS 14 AND ESS PENETRATION WAS 0%

Time	Total Restored Energy (kWh)					
	PV=0%	PV=20%	PV=40%	PV=60%	PV=80%	PV=100%
8:00	609.4194	609.4194	609.4194	609.4194	609.4194	609.4194
10:00	647.661	648.7231	648.7231	648.7231	648.7231	X
12:00	745.7201	747.0828	747.0828	747.0828	747.0828	747.0828
14:00	853.4847	860.1896	868.8174	870.0477	870.1211	871.1851
16:00	832.7079	1008.198	1022.245	1045.938	1050.961	1051.11
18:00	916.2309	926.8641	927.3392	939.8982	943.1473	944.9616

The total restored energy for each scenario, when the ESS penetration was 20%, is listed in TABLE 4.73 for $T = 10$ minutes and TABLE 4.74 for $T = 14$ minuts. Smaller values of restored energy were marked in a shade of green. Larger values of restored energy were marked in a shade of red.

In TABLE 4.71, there were a total of 17 infeasible solutions generated, when the ESS penetration was 0%. Whereas in TABLE 4.73 ($T = 10$ minutes), only 4 infeasible solutions were generated, since the ESS at each load node strategically supplemented PV

fluctuations and load profiles. In TABLE 4.74 ($T = 14$ minutes), all the scenarios were successfully solved. Comparing TABLE 4.74 with TABLE 4.72, it can be seen that extra energy was restored for each scenario due to the ESS coordination.

TABLE 4.73. TOTAL RESTORED ENERGY WHEN PREDICTION HORIZON WAS 10 AND ESS PENETRATION WAS 20%

Time	Total Restored Energy (kWh)					
	PV=0%	PV=20%	PV=40%	PV=60%	PV=80%	PV=100%
8:00	609.3572	609.3572	609.3572	609.3572	609.3572	609.3572
10:00	648.4042	649.5512	649.5512	649.5512	649.5512	649.5512
12:00	X	748.2624	748.2624	748.2624	748.2624	748.2624
14:00	694.9578	X	862.7774	X	868.161	871.0832
16:00	829.8757	841.746	849.6762	850.626	1044.623	1055.277
18:00	818.1535	821.0928	X	823.5453	829.0518	829.2401

TABLE 4.74. TOTAL RESTORED ENERGY WHEN PREDICTION HORIZON WAS 14 AND ESS PENETRATION WAS 20%

Time	Total Restored Energy (kWh)					
	PV=0%	PV=20%	PV=40%	PV=60%	PV=80%	PV=100%
8:00	610.1206	610.1206	610.1206	610.1206	610.1206	610.1206
10:00	650.6978	650.6978	650.6978	650.6978	650.6978	650.6978
12:00	748.2624	748.2624	748.2624	748.2624	748.2624	748.2624
14:00	872.6684	872.6684	872.6684	872.6684	872.6684	872.6684
16:00	1049.093	1061.994	1064.447	1064.447	1064.447	1064.447
18:00	1145.221	1152.141	1155.947	1160.627	1164.642	1168.325

In summary, introducing renewable DGs into the BSR model could generate infeasible solutions if the rolling-horizon parameters were not properly selected. However, coordinating ESSs with the renewable DGs can reduce the number of infeasible solutions.

4.4.4.3 Impact of DG Parameters and Loading Conditions

As observed in section 4.4.3, applying the BSR method on the heavily loaded system resulted in significantly increased computation time. In addition, smaller DG capacity and lower DG ramp rate also stressed the system and resulted in extended computation time. In this subsection, the performance of the BSR method applied to operating conditions with different DG capacity, DG ramp rate and system loading conditions is discussed. The total scheduled horizon was 30 minutes. The prediction and control horizons were 14 minutes and 12 minutes, respectively. The decision time step was 2 minutes. Note this set of rolling-horizon parameters works well when studying the impact of CLPU conditions. The scaling factors for both DG ramp rate and DG capacity were scaled from 0.2 to 2.0. The system loading conditions were scaled by a scalar changed from 1.0 to 2.0.

The values of total restored energy for all the operating conditions are listed in TABLE 4.75, TABLE 4.76, and TABLE 4.77.

From TABLE 4.75, it can be observed that when the DG capability scalar was 0.2, no loads were restored. As the DG capacity scalar increased to 0.4, some loads were restored and continuously supported when the ramping rate scalar was between 0.6 and 1.4. Note there were a total of 4 operating conditions that made the BSR method generate infeasible solutions, which are represented by 'x'. This is because when the DG ramp rate scalar was low (e.g., 0.2), some loads restored during the first iteration would decrease under CLPU conditions. However, DGs could not decrease the output power to balance the load demand due to limited DG ramp rate. When the capacity scalars were larger than 0.6, the BSR method was able to find a feasible solution.

TABLE 4.75. TOTAL RESTORED ENERGY FOR DG PARAMETER STUDY WITH LOADING SCALAR BEING 1.0

	Objective Values (kWh)									
	Cap=0.2	Cap=0.4	Cap=0.6	Cap=0.8	Cap=1.0	Cap=1.2	Cap=1.4	Cap=1.6	Cap=1.8	Cap=2.0
Ramp=0.2	0	x	x	1837	1900	1916	1968	1982	1983	1993
Ramp=0.4	0	0	1795	1970	1995	1997	1999	1999	1999	1999
Ramp=0.6	0	1147	1860	1984	1999	1999	1999	1999	1999	1999
Ramp=0.8	0	1140	1867	1984	1999	1999	1999	1999	1999	1999
Ramp=1.0	0	1140	1865	1980	1999	1999	1999	1999	1999	1999
Ramp=1.2	0	1148	1865	1980	1999	1999	1999	1999	1999	1999
Ramp=1.4	0	1132	1861	1980	1999	1999	1999	1999	1999	1999
Ramp=1.6	0	x	1867	1980	1999	1999	1999	1999	1999	1999
Ramp=1.8	0	x	1861	1980	1999	1999	1999	1999	1999	1999
Ramp=2.0	0	1139	1861	1980	1999	1999	1999	1999	1999	1999

TABLE 4.76. TOTAL RESTORED ENERGY FOR DG PARAMETER STUDY WITH LOADING SCALAR BEING 2.0

	Objective Values (kWh)									
	Cap=0.2	Cap=0.4	Cap=0.6	Cap=0.8	Cap=1.0	Cap=1.2	Cap=1.4	Cap=1.6	Cap=1.8	Cap=2.0
Ramp=0.2	138	0	0	0	0	0	0	0	0	x
Ramp=0.4	138	0	0	0	0	0	x	x	x	0
Ramp=0.6	138	0	0	0	2322	x	x	x	x	x
Ramp=0.8	138	0	0	x	0	2834	x	0	0	x
Ramp=1.0	138	0	0	0	x	2439	x	0	2443	x
Ramp=1.2	138	0	0	x	2625	x	x	x	x	x
Ramp=1.4	138	0	0	x	x	x	x	x	x	x
Ramp=1.6	138	0	0	x	0	x	2434	x	x	x
Ramp=1.8	138	0	0	x	0	x	x	x	x	x
Ramp=2.0	138	0	0	x	0	x	x	x	x	2443

TABLE 4.77. TOTAL RESTORED ENERGY FOR DG PARAMETER STUDY WITH LOADING SCALAR BEING 3.0

	Objective Values (kWh)									
	Cap=0.2	Cap=0.4	Cap=0.6	Cap=0.8	Cap=1.0	Cap=1.2	Cap=1.4	Cap=1.6	Cap=1.8	Cap=2.0
Ramp=0.2	46	x	x	x	x	x	x	0	x	0
Ramp=0.4	46	x	x	x	x	x	x	2590	x	x
Ramp=0.6	46	x	0	x	x	x	x	x	x	x
Ramp=0.8	46	x	0	1812	x	x	x	x	x	x
Ramp=1.0	46	x	1413	x	x	x	x	x	x	x
Ramp=1.2	46	0	x	1839	0	x	x	x	x	2731
Ramp=1.4	46	0	1430	1924	2255	x	x	x	x	2727
Ramp=1.6	46	0	1430	1922	2225	2502	x	x	x	x
Ramp=1.8	46	0	x	x	2275	x	x	x	x	2731
Ramp=2.0	46	0	x	1922	2134	x	x	2731	x	x

From TABLE 4.76, it can be seen that when the system loading was doubled, many infeasible solutions were generated. This indicates that the rolling-horizon parameters were not suitable for relatively heavily loaded operating conditions. When the DG capacity scalar was 0.2, a small number of loads was restored. When the DG capacity scalar was 0.4 or 0.6, no loads were restored. This is because the minimal power output constraint required each DG must maintain its output power above a certain level. DGs with higher minimal power output limits were not be able to maintain the minimal power out, when the load demand starts to decrease under CLPU conditions. From TABLE 4.77, it can be observed that most of the solutions were infeasible, when the system loading level was tripled. Another set of rolling-horizon parameters should be developed accordingly.

TABLE 4.78, TABLE 4.79, and TABLE 4.80 summarize the computation time for each studied operating condition. It can be seen that except for several operating conditions in TABLE 4.78 that took 15-20 minutes, all the other operating conditions can be solved within 3 minutes. Whereas using single-horizon procedure took more than an hour when the system was heavily loaded or the DG capacity was lowered, as shown in TABLE 4.62.

TABLE 4.78. COMPUTATION TIME FOR DG PARAMETER STUDY WITH LOADING SCALAR BEING 1.0

	Computation Time (seconds)									
	Cap=0.2	Cap=0.4	Cap=0.6	Cap=0.8	Cap=1.0	Cap=1.2	Cap=1.4	Cap=1.6	Cap=1.8	Cap=2.0
Ramp=0.2	32	44	55	83	65	40	37	33	37	35
Ramp=0.4	33	26	274	34	32	32	32	33	34	35
Ramp=0.6	32	54	659	38	31	33	31	33	34	34
Ramp=0.8	27	53	207	40	31	34	32	33	34	34
Ramp=1.0	27	54	193	35	31	34	33	34	34	34
Ramp=1.2	28	60	188	36	31	33	32	35	34	36
Ramp=1.4	27	992	63	37	32	34	32	33	33	31
Ramp=1.6	26	217	141	40	31	33	32	34	34	32
Ramp=1.8	26	1378	60	39	31	33	32	35	34	32
Ramp=2.0	27	1572	62	34	31	35	32	34	35	32

TABLE 4.79. COMPUTATION TIME FOR DG PARAMETER STUDY WITH LOADING SCALAR BEING 2.0

	Computation Time (seconds)									
	Cap=0.2	Cap=0.4	Cap=0.6	Cap=0.8	Cap=1.0	Cap=1.2	Cap=1.4	Cap=1.6	Cap=1.8	Cap=2.0
Ramp=0.2	28	46	43	28	33	29	30	27	32	84
Ramp=0.4	28	40	46	31	30	32	33	48	49	29
Ramp=0.6	28	35	52	29	135	40	40	62	36	58
Ramp=0.8	28	29	51	32	29	46	55	28	32	34
Ramp=1.0	28	37	30	28	58	44	39	28	41	30
Ramp=1.2	29	32	28	36	61	41	41	32	41	35
Ramp=1.4	28	40	30	32	43	46	34	29	32	29
Ramp=1.6	33	38	29	46	26	40	48	37	52	34
Ramp=1.8	31	55	28	51	27	40	37	31	42	34
Ramp=2.0	36	44	30	36	27	42	43	33	33	43

TABLE 4.80. COMPUTATION TIME FOR DG PARAMETER STUDY WITH LOADING SCALAR BEING 3.0

	Computation Time (seconds)									
	Cap=0.2	Cap=0.4	Cap=0.6	Cap=0.8	Cap=1.0	Cap=1.2	Cap=1.4	Cap=1.6	Cap=1.8	Cap=2.0
Ramp=0.2	27	30	41	31	38	38	87	28	62	30
Ramp=0.4	27	30	36	76	45	51	58	42	49	143
Ramp=0.6	27	35	28	41	54	42	52	38	158	201
Ramp=0.8	28	33	28	36	46	42	131	130	46	42
Ramp=1.0	28	32	35	52	35	159	138	49	88	83
Ramp=1.2	28	35	36	38	30	54	61	88	92	103
Ramp=1.4	27	33	51	45	46	85	126	43	66	54
Ramp=1.6	28	36	42	47	38	59	112	46	140	52
Ramp=1.8	27	49	34	41	46	57	94	42	76	46
Ramp=2.0	28	29	33	47	38	65	160	93	43	66

4.5 Summary of Findings

In this section, the proposed BSR method was applied to both balanced and unbalanced test systems, and its performance under various operating conditions was analyzed.

First, six case studies were presented to show how the proposed BSR method works. In Case I and Case II, the BSR method was applied to a balanced modified IEEE 13 node system with one black start DG and multiple dispatchable DGs and an ESS. In Case III, the test system was an unbalanced modified IEEE 123 node system with multiple black start DGs and dispatchable DGs. The rolling-horizon procedure was implemented in Case IV and Case V. The linear power flow models were validated in Case VI. It was observed that the proposed BSR method could generate restoration sequences and coordinate dispatchable DGs, ESS, and switches during the restoration process, in response to various operating conditions.

Next, the performance of the proposed BSR method were analyzed through a series of extensive studies. Three performance indices (total restored energy, optimal solution gap, and computation time) were introduced to evaluate the performance of the BSR method. The BSR method was applied to the unbalanced modified IEEE 123 node system with various rolling-horizon parameters (decision time step (Δt), total scheduled horizon (H), prediction horizon (T), and control horizon (C)) and system parameters (DG ramp rate, DG capacity, maximum load step, system loading, CLPU conditions, and PV and ESS penetrations). The findings on the impact of aforementioned parameters are summarized as follows.

The decision time step (Δt) determines how fast a black start sequence can be implemented. A large Δt (e.g., 2 minutes to 3 minutes) allowed a dispatchable DG to output more power between two consecutive time steps, so as to restore more loads. Using a small Δt allowed to carry out black start control actions faster than using large Δt. For example, under original system operating conditions, 1591 kWh of energy was restored when $\Delta t = 1$ minute and 1423 kWh of energy was restored when Δt =3 minutes. However, small Δt values could limit the DG ramp rate capacity. If Δt was too small (e.g., 0.5 minutes), no loads could be restored. In addition, under heavy system loading conditions, much more computation time (up to 40 minutes) was needed.

The total scheduled horizon (*H*) determines how many time steps that are considered in the BSR model, given a fixed decision time step. Ideally, *H* should be large enough to ensure the black start process could be completed and the solution optimality could be guaranteed. Small *H* values could not ensure all the loads were restored within the limited time steps. However, large *H* values could result in longer computation time. Under certain stressed system operating conditions (e.g., limited DG capacity, heavy loading condition), it took more than 1 hour to solve the MILP model in CPLEX. For a particular system operating condition, an optimal *H* value could be determined to achieve a trade-off between the solution quality and computation time. For example, under the low ramp rate system operating condition, using $H = 30$ minutes could restore 1491 kWh of energy. Whereas using $H = 14$ minutes could restore 1450 kWh of energy, which was a little bit smaller than using $H = 30$. However, it took 1.5 minutes for $H = 14$ minutes, and 20

minutes for $H = 30$ minutes. Using $H = 14$ minutes could both generate a near-optimal solution within an acceptable computation time.

The prediction horizon (*T*) and control horizon (*C*) affect the performance of the BSR method given fixed *H* and Δt values. Even if *H* was large enough, an improper selection of prediction and control horizon values could result in poor-quality solutions. It was observed that given $H = 30$ minutes and $\Delta t = 2$ minutes, the computation time could be reduced by more than 90% on average. In addition, using small *C* values required more iterations to cover the entire scheduled horizon, thus more time was spent on formulating and translating the MILP model. In some cases with short *T* and/or *C* values, the optimal solutions gap was unacceptable (i.e., more than 40%). Therefore, selecting the prediction and control horizons is also a trade-off between the solution quality and computation time.

DG parameters, especially the DG ramp rate and DG capacity, also play an important role in affecting the BSR method performance. Sufficient DG ramp rate and DG capacity would not affect the computation time. However, low DG ramp rate and limited DG capacity could stress the system operating condition and result in extended computation time, because in order to avoid violating these constraints, the MILP solver would execute more branch-and-bound iterations to find the optimal solution. The maximum computation time observed was more than 1 hour when DG capacity was halved.

System loading conditions, including the base loading levels and CLPU conditions, showed a significant impact on the BSR performance. Given a fixed set of rolling-horizon parameters, different CLPU parameters could lead to infeasible solutions when short *T* and *C* values (e.g., $T = 10$ minutes and $C = 8$ minutes) were used. It was observed that

using larger T and C values (e.g., $T = 14$ minutes and $C = 12$ minutes) could reduce the total number of infeasible solutions. However, as the system loading level increased, the total number of infeasible solutions increased significantly, even if $T = 14$ minutes and $C = 12$ minutes were used. It could be concluded that the rolling-horizon parameters determined for a particular system operating condition may not be suitable for other operating conditions. A method that could determine the rolling-horizon parameters for a system operating condition without performing exhaustive studies is needed.

The PV and ESS penetrations also affect the BSR performance. Since the BSR method only generated optimal solutions for the current iteration without considering the PV output and load fluctuations, infeasible solutions could be generated. Specifically, when the ESS penetration was 0%, infeasible solutions were generated when $T = 10$ minutes. Less infeasible solutions were observed when $T = 14$ minutes. The PV output and load fluctuations could be supplemented by ESS, such that less infeasible solutions were generated when ESS penetration was 20%.

4.6 Section Summary

In this section, a set of case studies were presented and discussed to show how the proposed BSR method works. The BSR method was applied to both balanced systems and unbalanced systems under various operating conditions. The results showed that the BSR method could generate optimal black start solutions in response to varying system operating conditions. The rolling-horizon procedure could reduce the computation time while sub-optimal solutions were generated. Then, the performance of the BSR method was evaluated through a series of extensive studies. The impact of selection of rolling-

horizon parameters was presented and discussed. Finally, the BSR method was applied to various system operating conditions to quantitatively investigate the performance using three performance indices.

5 CONCLUSIONS AND FUTURE WORK

5.1 Summary and Conclusions

This dissertation presented and discussed a new black start restoration methodology, which can be applied to distribution systems and microgrids with distributed energy resources (DERs). The proposed black start service (BSR) method has several features that distinguish it from the existing methods. First, it formulates the black start restoration problem as a dynamic optimization problem, which allows to generate the black start sequence that can be implemented to restore a system sequentially. Second, it allows to form multiple microgrids in the system by grouping multiple DERs and loads and coordinate DERs within a same microgrid over a time period. Third, it addresses several practical concerns that are normally ignored in many of the existing methods, such as cold load pick up (CLPU) issues, unbalanced three-phase condition, ZIP load models, and DG unbalanced operating conditions.

The new BSR method was formulated as a dynamic optimization problem with both continuous variables and discrete variables defined for multiple discrete time steps over a horizon. Both the objective function and constraints were formulated in the linear form, so the BSR model is a typical mixed-integer linear programming (MILP) model which can be effectively solved by commercial solvers. Furthermore, several linear models were developed and integrated into the BSR model to address the aforementioned practical issues. Specifically, the linear models CLPU loads and ZIP loads were proposed to approximate the load demand; A set of topological constraints were proposed to ensure

the physical connections among different components, as well as the tree topology during the restoration process; A linear model for approximating the current unbalance index was developed to ensure the three-phase DGs will not be overheated by the negative sequence current induced by unbalanced operating conditions.

A framework was introduced to show how to implement the BSR model using various tools and software. In this dissertation research, the MILP problems were solved by the IBM CPLEX MILP solver. Since the BSR problem was formulated as a dynamic optimization problem, decision variables, state variables and constraints must be defined at each time step. Therefore, the problem size will become intractable when solving large-scale systems over a long horizon. In order to reduce the computation time, the rolling-horizon procedure was introduced.

To illustrate how the new BSR method works, a set of case studies were presented and discussed. The new BSR method was applied to both balanced and unbalanced systems in response to varying system operating conditions. The capability of the BSR method to generate black start sequences and coordinate DERs was presented. The rolling-horizon procedure was shown to be able to reduce the computation time, while achieving optimal or suboptimal solutions. However, low-quality solutions were generated when the prediction horizon and the control horizon were not properly selected.

To evaluate the performance of the BSR method under various operating conditions, a series of extensive studies were performed in this dissertation research. The extensive studies included evaluating the impact of the rolling-horizon parameters and the performance under varying system operating conditions, such as different loading

conditions, PV and ESS penetrations, and DG parameters. Three performance indices were introduced, namely, total restored energy, optimal solution gap, and computation time. Firstly, the impact of rolling-horizon parameters was studied. It was found that the selection of the rolling-horizon parameters presented a significant impact on the performance of the BSR method. Specifically, using small decision time steps could limit the DG ramping capability, hence only allowing small loads to be restored. Similarly, heavily loading conditions required the system to be operated with limited margins, hence more computation time was needed for solving the MILP problem in CPLEX. The computation time was significantly reduced by using rolling-horizon procedure. Using rolling-horizon procedure with longer prediction horizons could achieve sub-optimal solutions and require much less computation time compared with single-horizon procedure.

However, the rolling-horizon procedure cannot guarantee the feasibility of solutions. Stressed system operating conditions (e.g., slow DG ramp rate, small DG capacity, and heavy loaded system operating condition) resulted in not only extended computation time, but also infeasible solutions in some cases.

5.2 Future Work

As observed in the performance analysis, the BSR method implemented based on the rolling-horizon procedure generated infeasible solutions in some scenarios. Further studies should be conducted to propose a method for properly selecting the rolling-horizon parameters without conducting exhaustive case studies.

The BSR method could control DERs over multiple discrete time steps. This type of control could be seen as the secondary control for DER controllers, since the control signals were received periodically [100]. If the decision time step was large, the PV output and load demand fluctuations could result in infeasible solutions. Therefore, an integrated scheme that can coordinate primary control and secondary control for all controllable DERs should be developed.

In this work, the BSR method can be applied to radial distribution systems and microgrids with DERs. However, some distribution systems are operated in mesh topology. A new system model formulation can be developed to enable the BSR method to handle meshed systems.

REFERENCES

[1] C. Abbey, D. Cornforth, N. Hatziargyriou, K. Hirose, A. Kwasinski, E. Kyriakides, *et al.,* "Powering Through the Storm: Microgrids Operation for More Efficient Disaster Recovery," *IEEE Power and Energy Magazine,* vol. 12, pp. 67-76, 2014.

[2] M. Panteli and P. Mancarella, "Influence of Extreme Weather and Climate Change on the Resilience of Power Systems: Impacts and Possible Mitigation Strategies," *Electric Power Systems Research,* vol. 127, pp. 259-270, 10, 2015.

[3] President's Council of Economic Advisers, Economic benefits of increasing electric grid resilience to weather outages. [Online]. Available: http://energy.gov/

[4] Y. Wang, C. Chen, J. Wang, and R. Baldick, "Research on Resilience of Power Systems Under Natural Disasters: A Review," *IEEE Transactions on Power Systems,* vol. PP, pp. 1-10, 2015.

[5] USA Today. Over 1 Million Without Power as Hurricane Matthew Lashes Florida [Online]. Available: http://www.usatoday.com

[6] National Climatic Data Center. Billion-Dollar Weather and Climate Disasters: Overview [Online]. Available: https://www.ncdc.noaa.gov/billions/overview

[7] D.W. Cooke, "The Sesilience of the Electric Power Delivery System in Response to Terrorism and Natural Disasters: Summary of a Workshop," *Division on Engineering and Physical Sciences* 2013.

[8] S. Tamronglak, S. H. Horowitz, A. G. Phadke, and J. S. Thorp, "Anatomy of Power System Blackouts: Preventive Relaying Strategies," *IEEE Transactions on Power Delivery*, vol. 11, pp. 708-715, Apr 1996.

[9] N. R. Council, *Terrorism and the Electric Power Delivery System*. The National Academies Press, 2012.

[10] L. Shan, C. Bo, T. Zourntos, D. Kundur, and K. Butler-Purry, "A Coordinated Multi-Switch Attack for Cascading Failures in Smart Grid," *IEEE Transactions on Smart Grid*, vol. 5, pp. 1183-1195, 2014.

[11] A. Kwasinski. "Lessons from field damage assessments about communication networks power supply and infrastructure performance during natural disasters with a focus on Hurricane Sandy." *FCC Workshop on Network Resiliency* 2013.

[12] R. J. Campbell, *Weather-Related Power Outages and Electric System Resiliency*. Library of Congress, 2012.

[13] A. Schwarzenegger and H. R. Renteria. Electric Power Disruption: Toolkit for Local Government [Online]. Available: http://www.caloes.ca.gov/

[14] K. H. LaCommare and J. H. Eto. Understanding the Cost of Power Interruptions to U.S. Electricity Consumers [Online]. Available: http://certs.lbl.gov

[15] C. Chen, J. Wang, F. Qiu, and D. Zhao, "Resilient Distribution System by Microgrids Formation After Natural Disasters," *IEEE Transactions on Smart Grid*, vol. 7, p. 9, 2016.

[16] J. A. P. Lopes, C. L. Moreira, and A. G. Madureira, "Defining Control Strategies for MicroGrids Islanded Operation," *IEEE Transactions on Power Systems,* vol. 21, pp. 916-924, 2006.

[17] M. Vadari and G. StokeS, "Utility 2.0 and the Dynamic Microgrid," *Public Utilities Fortnightly,* 2013.

[18] B. Lasseter, "Microgrids [distributed power generation]," in *Power Engineering Society Winter Meeting,* vol.1. pp. 146-149, 2001

[19] R. H. Lasseter, "Smart Distribution: Coupled Microgrids," *Proceedings of the IEEE,* vol. 99, pp. 1074-1082, 2011.

[20] G. Strbac, N. Hatziargyriou, J. P. Carvalho Lopes, C. Moreira, A. Dimeas, and D. Papadaskalopoulos, "Microgrids: Enhancing the Resilience of the European Megagrid," *Power and Energy Magazine, IEEE,* vol. 13, pp. 35-43, 2015.

[21] S. Mohagheghi and Y. Fang, "Applications of Microgrids in Distribution System Service Restoration," in *IEEE PES Innovative Smart Grid Technologies (ISGT),* pp. 1-7, 2011

[22] K. Schneider, F. Tuffner, M. Elizondo, C. C. Liu, Y. Xu, and D. Ton, "Evaluating the Feasibility to Use Microgrids as a Resiliency Resource," *IEEE Transactions on Smart Grid,* vol. PP, pp. 1-1, 2016.

[23] X. Yu, H. Jia, C. Wang, W. Wei, Y. Zeng, and J. Zhao, "Network Reconfiguration for Distribution System with Micro-Grids," in *International Conference on Sustainable Power Generation and Supply,* pp. 1-4, 2009

[24] T. Sicong, X. Jian-Xin, and S. K. Panda, "Optimization of Distribution Network Incorporating Distributed Generators: An Integrated Approach," *IEEE Transactions on Power Systems,* vol. 28, pp. 2421-2432, 2013.

[25] J. Li, X. Y. Ma, C. C. Liu, and K. P. Schneider, "Distribution System Restoration With Microgrids Using Spanning Tree Search," *IEEE Transactions on Power Systems,* vol. 29, pp. 3021-3029, Nov 2014.

[26] A. Castillo, "Microgrid Provision of Blackstart in Disaster Recovery for Power System Restoration," in *IEEE International Conference on Smart Grid Communications (SmartGridComm),* pp. 534-539, 2013

[27] F. E. Ricketts, "The Restoration of Service After a Necessary Interruption," *Transactions of the American Institute of Electrical Engineers,* vol. XXXV, pp. 635-654, 1916.

[28] P. Kundur, *Power System Stability And Control*. New York: McGraw-Hill, 1994.

[29] G. Venkataramanan and C. Marnay, "A Larger Role for Microgrids," *Power and Energy Magazine, IEEE,* vol. 6, pp. 78-82, 2008.

[30] B. Beihof, T. Jahns, R. Lasseter, and G. Radlof. Transforming the Grid from the Distribution System Out: The Potential for Dynamic Distribution Systems to Create a New Energy Marketplace [Online]. Available: https://energy.wisc.edu

[31] P. Asmus. Distributed Generation Leads Microgrid Investment Opportunities [Online]. Available: http://www.navigantresearch.com

[32] R. Arghandeh, M. Brown, A. Del Rosso, G. Ghatikar, E. Stewart, A. Vojdani, *et al.*, "The Local Team Leveraging Distributed Resources to Improve Resilience," *IEEE Power & Energy Magazine,* vol. 12, pp. 76-83, Sep-Oct 2014.

[33] C. S. Holling, "Resilience and Stability of Ecological Systems," *Annual review of ecology and systematics,* pp. 1-23, 1973.

[34] EPRI. Enhancing Distribution Resiliency Opportunities for Applying Innovative Technologies [Online]. Available: Available: http://www.epri.com

[35] Y. Xu, C. C. Liu, K. P. Schneider, and D. T. Ton, "Placement of Remote-Controlled Switches to Enhance Distribution System Restoration Capability," *IEEE Transactions on Power Systems,* vol. 31, pp. 1139-1150, 2016.

[36] D. Pinney. Costs and Benefits of Smart Feeder Switching: Quantifying the Operating Value of SFS [Online]. Available: https://www.smartgrid.gov

[37] R. Billinton, *Power system reliability evaluation*: Taylor & Francis, 1970.

[38] M. Panteli and P. Mancarella, "The Grid: Stronger, Bigger, Smarter?: Presenting a Conceptual Framework of Power System Resilience," *IEEE Power and Energy Magazine,* vol. 13, pp. 58-66, 2015.

[39] Y. Jiang, C.-C. Liu, M. Diedesch, E. Lee, and A. K. Srivastava, "Outage Management of Distribution Systems Incorporating Information From Smart Meters," *IEEE Transactions on Power Systems,* vol. PP, pp. 1-11, 2015.

[40] Y. Jiang, C.-C. Liu, and Y. Xu, "Smart Distribution Systems," *Energies,* vol. 9, p. 297, 2016.

[41] J. A. Momoh, *Electric Power Distribution, Automation, Protection, And Control*. CRC Press, 2007.

[42] T. Gonen, *Electric Power Distribution Engineering, Third Edition*. Taylor & Francis, 2014.

[43] A. Zidan, M. Khairalla, A. M. Abdrabou, T. Khalifa, K. Shaban, A. Abdrabou, *et al.*, "Fault Detection, Isolation, and Service Restoration in Distribution Systems: State-of-the-Art and Future Trends," *IEEE Transactions on Smart Grid,* vol. PP, pp. 1-16, 2016.

[44] D. Lubkeman and D. E. Julian, "Large Scale Storm Outage Management," in *IEEE Power Engineering Society General Meeting,* pp. 16-22 Vol.1, 2014

[45] Y. Ming-Jong and K. J. Min, "Repair-Unit Location Models for Power Failures," *IEEE Transactions on Engineering Management,* vol. 45, pp. 57-65, 1998.

[46] Y. Liu, R. Fan, and V. Terzija, "Power System Restoration: a Literature Review from 2006 to 2016," *Journal of Modern Power Systems and Clean Energy,* vol. 4, pp. 332-341, 2016.

[47] J. Stoupis, Z. Wang, F. Yang, V. Donde, F. Mekic, and W. Peterson, "Restoring Confidence," *ABB Review,* vol. 3, p. 6, 2009.

[48] A. Arab, A. Khodaei, S. K. Khator, K. Ding, V. A. Emesih, and Z. Han, "Stochastic Pre-hurricane Restoration Planning for Electric Power Systems Infrastructure," *Smart Grid, IEEE Transactions on,* vol. 6, pp. 1046-1054, 2015.

[49] S. Chowdhury, S. P. Chowdhury, and P. Crossley, *Microgrids and Active Distribution Networks*. The Institution of Engineering and Technology, 2009.

[50] M. E. Baran and F. F. Wu, "Network Reconfiguration in Distribution Systems for Loss Reduction and Load Balancing," *IEEE Transactions on Power Delivery,* vol. 4, pp. 1401-1407, 1989.

[51] A. M. Cuomo, R. L. Kauffman, J. B. Rhodes, A. Zibelman and J. M. Hauer, "Microgrids for Critical Facility Resiliency in New York State. Final report," New York State Energy Research and Development Authority, 2014.

[52] Line Protection Subcommittee of IEEE PES. Cold Load Pickup Issues [Online]. Available: http://www.pes-psrc.org/

[53] E. Agneholm, *Cold Load Pick-up.* Chalmers University of Technology, 1999.

[54] C. Ucak and A. Pahwa, "An Analytical Approach for Step-by-Step Restoration of Distribution-Systems Following Extended Outages," *IEEE Transactions on Power Delivery,* vol. 9, pp. 1717-1723, Jul 1994.

[55] S. Chavali, A. Pahwa, and S. Das, "A Genetic Algorithm Approach for Optimal Distribution Feeder Restoration During Cold Load Pickup," in *Proceedings of the 2002 Congress on Evolutionary Computation*, pp. 1816-1819, 2002.

[56] Y. Y. Hsu, H. M. Huang, H. C. Kuo, S. K. Peng, C. W. Chang, K. J. Chang, *et al.*, "Distribution System Service Restoration Using a Heuristic Search Approach," *IEEE Transactions on Power Delivery,* vol. 7, pp. 734-740, 1992.

[57] S. Wang and H. D. Chiang, "Multi-Objective Service Restoration of Distribution Systems Using Group-Based Two-Stage Methodology," in *2014 IEEE PES T&D Conference and Exposition*, pp. 1-5. 2014.

[58] M. S. Tsai, "Development of an Object-Oriented Service Restoration Expert System With Load Variations," *IEEE Transactions on Power Systems,* vol. 23, pp. 219-225, 2008.

[59] C. Chao-Shun, L. Chia-Hung, and T. Hung-Ying, "A Rule-Based Expert System with Colored Petri Net Models for Distribution System Service Restoration," *IEEE Transactions on Power Systems,* vol. 17, pp. 1073-1080, 2002.

[60] P. L. Cavalcante, J. C. López, J. F. Franco, M. J. Rider, A. V. Garcia, M. R. R. Malveira, *et al.*, "Centralized Self-Healing Scheme for Electrical Distribution Systems," *IEEE Transactions on Smart Grid,* vol. 7, pp. 145-155, 2016.

[61] J. C. López, J. F. Franco, and M. J. Rider, "Optimisation-Based Wwitch Allocation to Improve Energy Losses and Service Restoration in Radial Electrical Distribution Systems," *IET Generation, Transmission & Distribution,* vol. 10, pp. 2792-2801, 2016.

[62] New York ISO. A Review of Distributed Energy Resources [Online]. Available: www.nyiso.com

[63] New York DPS. Reforming the Energy Vision [Online]. Available: http://www3.dps.ny.gov/

[64] F. Katiraei, C. Abbey, S. Tang, and M. Gauthier, "Planned Islanding on Rural Feeders - Utility Perspective," in *IEEE Power and Energy Society General Meeting,* pp. 1-6, 2008.

[65] NERC. Glossary of Terms Used in NERC Reliability Standards [Online]. Available: http://www.nerc.com/files/glossary_of_terms.pdf

[66] C. L. Moreira, F. O. Resende, and J. A. Peas Lopes, "Using Low Voltage MicroGrids for Service Restoration," *IEEE Transactions on Power Systems,* vol. 22, pp. 395-403, 2007.

[67] R. J. Yinger, "Behavior of Capstone and Honeywell Microturbine Generators during Load Changes," California Energy Commission, 2004.

[68] NYSERDA, N. Y. DPS, and N. Y. DHSES. Microgrids for Critical Facility Resiliency in New York State [Online]. Available: www.nyserda.ny.gov

[69] L. Shanshan, H. Yunhe, L. Chen-Ching, and R. Podmore, "The Healing Touch: Tools and Challenges for Smart Grid Restoration," *IEEE Power and Energy Magazine,* vol. 12, pp. 54-63, 2014.

[70] ISO New England, ISO New England Operating Procedure No. 11: Blackstart Resource Administration [Online]. Available: http://www.iso-ne.com/

[71] M. D. Galus, S. Koch, and G. Andersson, "Provision of Load Frequency Control by PHEVs, Controllable Loads, and a Cogeneration Unit," *IEEE Transactions on Industrial Electronics,* vol. 58, pp. 4568-4582, 2011.

[72] FERC, Staff Issue Assessment of Demand Response and Advanced Metering Report [Online]. Available: http://www.ferc.gov

[73] M. H. Albadi and E. F. El-Saadany, "Demand Response in Electricity Markets: An Overview," in *IEEE Power Engineering Society General Meeting,* pp. 1-5, 2007

[74] Bower, Ward Isaac, et al. The Advanced Microgrid. Integration and Interoperability. Sandia National Laboratories, Albuquerque, NM, 2014.

[75] IEEE, "IEEE Guide for Design, Operation, and Integration of Distributed Resource Island Systems with Electric Power Systems," in *IEEE Std 1547.4-2011*, ed, pp. 1-54. 2011

[76] O. Ting-Chia, L. Whei-Min, H. Cong-Hui, and C. Fu-Sheng, "A Hybrid Programming for Distribution Reconfiguration of DC Microgrid," in *2009 IEEE PES/IAS Conference on Sustainable Alternative Energy (SAE)*, pp. 1-7. 2009.

[77] Z. Y. Wang and J. H. Wang, "Self-Healing Resilient Distribution Systems Based on Sectionalization Into Microgrids," *IEEE Transactions on Power Systems*, vol. 30, pp. 3139-3149, Nov 2015.

[78] M. E. Nassar and M. M. A. Salama, "Adaptive Self-Adequate Microgrids Using Dynamic Boundaries," *IEEE Transactions on Smart Grid*, vol. 7, pp. 105-113, 2016.

[79] S. A. Arefifar, Y. A. R. I. Mohamed, and T. H. M. El-Fouly, "Comprehensive Operational Planning Framework for Self-Healing Control Actions in Smart Distribution Grids," *IEEE Transactions on Power Systems*, vol. 28, pp. 4192-4200, 2013.

[80] H. Gao, Y. Chen, Y. Xu, and C. C. Liu, "Resilience-Oriented Critical Load Restoration Using Microgrids in Distribution Systems," *IEEE Transactions on Smart Grid*, vol. PP, pp. 1-1, 2016.

[81] A. Sharma, D. Srinivasan, and A. Trivedi, "A Decentralized Multiagent System Approach for Service Restoration Using DG Islanding," *IEEE Transactions on Smart Grid*, vol. 6, pp. 2784-2793, 2015.

[82] B. Ansari and S. Mohagheghi, "Electric service restoration using microgrids," in *2014 IEEE PES General Meeting*, pp. 1-5. 2014.

[83] W. Zhaoyu, C. Bokan, W. Jianhui, and C. Chen, "Networked Microgrids for Self-Healing Power Systems," *IEEE Transactions on Smart Grid*, vol. 7, pp. 310-319, 2016.

[84] S. A. Arefifar, Y. A. R. I. Mohamed, and T. El-Fouly, "Optimized Multiple Microgrid-Based Clustering of Active Distribution Systems Considering Communication and Control Requirements," *IEEE Transactions on Industrial Electronics*, vol. 62, pp. 711-723, 2015.

[85] M. Adibi, P. Clelland, L. Fink, H. Happ, R. Kafka, J. Raine, *et al.*, "Power System Restoration - A Task Force Report," *IEEE Transactions on Power Systems*, vol. 2, pp. 271-277, 1987.

[86] V. Kumar, H. C. R. Kumar, I. Gupta, and H. O. Gupta, "DG Integrated Approach for Service Restoration Under Cold Load Pickup," *IEEE Transactions on Power Delivery*, vol. 25, pp. 398-406, 2010.

[87] A. M. El-Zonkoly, "Power system single step restoration incorporating cold load pickup aided by distributed generation," *International Journal of Electrical Power & Energy Systems*, vol. 35, pp. 186-193, 2012.

[88] R. Perez-Guerrero, G. T. Heydt, N. J. Jack, B. K. Keel, and A. R. Castelhano, "Optimal Restoration of Distribution Systems Using Dynamic Programming," *IEEE Transactions on Power Delivery*, vol. 23, pp. 1589-1596, Jul 2008.

[89] C. C. Liu, V. Vittal, G. T. Heydt, and K. Tomsovic, "Development and Evaluation of System Restoration Strategies from a Blackout," PSERC Tehnical Report 2009.

[90] S. Thiébaux, C. Coffrin, H. Hijazi, and J. Slaney, "Planning with MIP for supply restoration in power distribution systems," *Proceedings of the Twenty-Third international joint conference on Artificial Intelligence*, Beijing, China, 2013.

[91] C. Coffrin and P. Van Hentenryck, "Transmission system restoration with co-optimization of repairs, load pickups, and generation dispatch," *International Journal of Electrical Power & Energy Systems*, vol. 72, pp. 144-154, 11// 2015.

[92] Y. Xu, C. C. Liu, K. Schneider, F. Tuffner, and D. Ton, "Microgrids for Service Restoration to Critical Load in a Resilient Distribution System," *IEEE Transactions on Smart Grid*, vol. PP, pp. 1-1, 2016.

[93] M. H. M. Camillo, R. Z. Fanucchi, M. E. V. Romero, T. W. d. Lima, L. T. Marques, J. A. D. Massignan, *et al.*, "Determination of switching sequence of Service Restoration in Distribution Systems: Application and analysis on a real and large-scale radial system," in *2016 IEEE/PES Transmission and Distribution Conference and Exposition (T&D)*, 2016, pp. 1-5.

[94] I. Watanabe and M. Nodu, "A Genetic Algorithm for Optimizing Switching Sequence of Service Restoration in Distribution Systems," in *Congress on Evolutionary Computation*, 2004, pp. 1683-1690 Vol.2.

[95] J. P. Lopes, C. Moreira, and F. Resende, "Microgrids black start and islanded operation," in *Proc. 15th Power System Computation Conference*, Liege, Belgium, 2005.

[96] F. Katiraei and C. Abbey, "Diesel Plant Sizing and Performance Analysis of a Remote Wind-Diesel Microgrid," in *IEEE Power Engineering Society General Meeting*, pp. 1-8. 2007.

[97] J. A. Peas Lopes, C. L. Moreira, A. G. Madureira, F. O. Resende, X. Wu, N. Jayawarna, *et al.*, "Control Strategies for Microgrids Emergency Operation," in *2005 International Conference on Future Power Systems*, pp. 6 pp.-6. 2005.

[98] S. Thale and V. Agarwal, "A Smart Control Strategy for the Black Start of a Microgrid Based on PV and Other Auxiliary Sources Under Islanded Condition," in *2011 37th IEEE Photovoltaic Specialists Conference (PVSC)*,pp. 002454-002459. 2011.

[99] E. Zare and M. Shahabi, "Microgrid Restoration after Major Faults in Main Grid with Automatic and Constant Time Switching," *IJISA,* vol. 5, p. 9, 2013.

[100] C. Liang, M. Khodayar, and M. Shahidehpour, "Only Connect: Microgrids for Distribution System Restoration," *IEEE Power and Energy Magazine,* vol. 12, pp. 70-81, 2014.

[101] C. Niannian, X. Xufeng, and J. Mitra, "A Hierarchical Multi-Agent Control Scheme for a Black Start-Capable Microgrid," in *IEEE Power and Energy Society General Meeting*, pp. 1-7. 2011.

[102] D. Jie and R. G. Harley, "Islanded Microgrids Black Start Procedures with Wind Power Integration," in *IEEE Power and Energy Society General Meeting (PES)*, pp. 1-5. 2013.

[103] F. O. Resende, N. J. Gil, and J. A. P. Lopes, "Service Sestoration on Distribution Systems Using Multi-MicroGrids," *European Transactions on Electrical Power,* vol. 21, pp. 1327-1342, 2011.

[104] C. Gouveia, C. Leal Moreira, J. A. Pecas Lopes, D. Varajao, and R. Esteves Araujo, "Microgrid Service Restoration: The Role of Plugged-in Electric Vehicles," *IEEE Industrial Electronics Magazine,* vol. 7, pp. 26-41, 2013.

[105] J. A. P. Lopes, C. L. Moreira, and F. O. Resende, "Control Strategies for Microgrids Black Start and Islanded Operation," *Journal of Distributed Energy Resource,* 2005.

[106] M. M. Adibi, *Power System Restoration: Methodologies & Implementation Strategies*. Wiley, 2000.

[107] A. Chiang, *Elements of dynamic optimization*, Illinois: Waveland Press Inc, 2000.

[108] T. Nagata, H. Sasaki, and R. Yokoyama, "Power system restoration by joint usage of expert system and mathematical programming approach," *IEEE Transactions on Power Systems,* vol. 10, pp. 1473-1479, 1995.

[109] Y. Kumar, B. Das, and J. Sharma, "Multiobjective, Multiconstraint Service Restoration of Electric Power Distribution System With Priority Customers," *IEEE Transactions on Power Delivery,* vol. 23, pp. 261-270, 2008.

[110] S. Wencong, W. Jianhui, and R. Jaehyung, "Stochastic Energy Scheduling in Microgrids With Intermittent Renewable Energy Resources," *IEEE Transactions on Smart Grid,* vol. 5, pp. 1876-1883, 2014.

[111] W. H. Kersting, *Distribution System Modeling and Analysis*. CRC Press, 2001.

[112] A. Garces, "A Linear Three-Phase Load Flow for Power Distribution Systems," *IEEE Transactions on Power Systems*, vol. PP, pp. 1-2, 2015.

[113] H. Ahmadi, J. R. Mart´, and A. v. Meier, "A Linear Power Flow Formulation for Three-Phase Distribution Systems," *IEEE Transactions on Power Systems*, vol. PP, pp. 1-10, 2016.

[114] L. Gan and S. H. Low, "Convex Relaxations and Linear Approximation for Optimal Power Flow in Multiphase Radial Networks," in *Power Systems Computation Conference (PSCC)*, pp. 1-9. 2014.

[115] B. A. Robbins and A. D. Domínguez-García, "Optimal Reactive Power Dispatch for Voltage Regulation in Unbalanced Distribution Systems," *IEEE Transactions on Power Systems*, vol. PP, pp. 1-11, 2015.

[116] A. Borghetti, F. Napolitano, and C. A. Nucci, "Volt/Var Optimization of Unbalanced Distribution Feeders via Mixed Integer Linear Programming," *International Journal of Electrical Power & Energy Systems*, vol. 72, pp. 40-47, 11, 2015.

[117] K. P. Schneider, E. Sortomme, S. S. Venkata, M. T. Miller, and L. Ponder, "Evaluating the Magnitude and Duration of Cold Load Pick-up on Residential Distribution Feeders Using Multi-State Load Models," *IEEE Transactions on Power Systems*, vol. PP, pp. 1-10, 2015.

[118] W. W. Lang, M. D. Anderson, and D. R. Fannin, "An Analytical Method for Quantifying the Electrical Space Heating Component of a Cold Load Pick Up,"

IEEE Transactions on Power Apparatus and Systems, vol. PAS-101, pp. 924-932, 1982.

[119] B. A. Robbins, H. Zhu, and A. D. Domínguez-García, "Optimal Tap Setting of Voltage Regulation Transformers in Unbalanced Distribution Systems," *IEEE Transactions on Power Systems,* vol. 31, pp. 256-267, 2016.

[120] J. F. Franco, M. J. Rider, M. Lavorato, and R. Romero, "A Mixed-Integer LP Model for the Optimal Allocation of Voltage Regulators and Capacitors in Radial Distribution Systems," *International Journal of Electrical Power & Energy Systems,* vol. 48, pp. 123-130, 2013.

[121] E. Acha, H. Ambriz-Perez, and C. R. Fuerte-Esquivel, "Advanced Transformer Control Modeling in an Optimal Power Flow Using Newton's Method," *IEEE Transactions on Power Systems,* vol. 15, pp. 290-298, 2000.

[122] M. M. Adibi, R. A. Polyak, I. A. Griva, L. Mili, and S. Ammari, "Optimal Transformer Tap Selection Using Modified Barrier-Augmented Lagrangian Method," *IEEE Transactions on Power Systems,* vol. 18, pp. 251-257, 2003.

[123] H. Ahmadi and J. R. Marti, "Linear Current Flow Equations With Application to Distribution Systems Reconfiguration," *IEEE Transactions on Power Systems,* vol. 30, pp. 2073-2080, Jul 2015.

[124] M. M. Adibi, J. N. Borkoski, R. J. Kafka, and T. L. Volkmann, "Frequency Response of Prime Movers During Restoration," *IEEE Transactions on Power Systems,* vol. 14, pp. 751-756, May 1999.

[125] B. Y. Zhao, X. D. Dong, and J. Bornemann, "Service Restoration for a Renewable-Powered Microgrid in Unscheduled Island Mode," *IEEE Transactions on Smart Grid,* vol. 6, pp. 1128-1136, May 2015.

[126] G. Chicco, F. Corona, R. Porumb, and F. Spertino, "Experimental Indicators of Current Unbalance in Building-Integrated Photovoltaic Systems," *IEEE Journal of Photovoltaics,* vol. 4, pp. 924-934, 2014.

[127] Z. Wang, J. Wang, and C. Chen, "A Three-Phase Microgrid Restoration Model Considering Unbalanced Operation of Distributed Generation," *IEEE Transactions on Smart Grid,* vol. submitted.

[128] M. Allie and R. Lyons, "A Root of Less Evil," *IEEE Signal processing magazine,* vol. 22, pp. 93-96, 2005.

[129] L. H. Macedo, J. F. Franco, M. J. Rider, and R. Romero, "Optimal Operation of Distribution Networks Considering Energy Storage Devices," *IEEE Transactions on Smart Grid,* vol. 6, pp. 2825-2836, 2015.

[130] P. P. Barker and R. W. D. Mello, "Determining the Impact of Distributed Generation on Power Systems. I. Radial Distribution Systems," in *2000 Power Engineering Society Summer Meeting (Cat. No.00CH37134)*, 2000, pp. 1645-1656 vol. 3.

[131] IBM ILOG CPLEX, "V12. 1: User's Manual for CPLEX," *International Business Machines Corporation,* vol. 46, p. 157, 2009.

[132] Gurubi Optimization, "Gurobi Optimizer Reference Manual," vol. 2, pp. 1.3-3.3, 2012.

[133] J. F. Marquant, R. Evins, and J. Carmeliet, "Reducing Computation Time with a Rolling Horizon Approach Applied to a MILP Formulation of Multiple Urban Energy Hub System," *Procedia Computer Science,* vol. 51, pp. 2137-2146, 2015.

[134] W. B. Powell, *Approximate Dynamic Programming: Solving the curses of dimensionality*. John Wiley & Sons, 2007.

[135] M. Morari and J. H. Lee, "Model Predictive Control: Past, Present and Future," *Computers & Chemical Engineering,* vol. 23, pp. 667-682, 1999.

[136] A. Dimitriadis, N. Shah, and C. Pantelides, "RTN-Based Rolling Horizon Algorithms for Medium Term Scheduling of Multipurpose Plants," *Computers & Chemical Engineering,* vol. 21, pp. S1061-S1066, 1997.

[137] H. Wang, K. Meng, Z. Y. Dong, Z. Xu, F. Luo, and K. P. Wong, "Efficient Real-Time Residential Energy Management Through MILP Based Rolling Horizon Optimization," in *IEEE Power & Energy Society General Meeting,* pp. 1-6. 2015.

[138] The Mathworks, "MATLAB User Guide," *Natick, MA,* vol. 5, p. 333, 1998.

[139] J. Lofberg, "YALMIP: A Toolbox for Modeling and Optimization in MATLAB," in *Computer Aided Control Systems Design, 2004 IEEE International Symposium on,* 2005, pp. 284-289.

[140] IEEE, IEEE PES Distribution Test Feeders. [Online]. Available: http://www.ewh.ieee.org/

[141] Kersting, William H. "Radial Distribution Test Feeders." I*EEE Power Engineering Society Winter Meeting,* Vol. 2. 2001.

[142] R. C. Dugan, "Reference Guide: The Open Distribution System Simulator (OPENDSS)," *Electric Power Research Institute, Inc*, vol. 7, 2012.

[143] C.A.Smith, Pecan Street Project Database [Online]. Available: https://dataport.pecanstreet.org/

[144] P. Lilienthal and G. I. Power, "High Penetrations of Renewable Energy for Island Grids," *Power Engineering*, vol. 111, pp. 90, 2007.

[145] IEEE, "IEEE Guide for Loading Mineral-Oil-Immersed Transformers and Step-Voltage Regulators," *IEEE Std C57.91-2011 (Revision of IEEE Std C57.91-1995)*, pp. 1-123, 2012.

APPENDIX A BALANCED MODIFIED IEEE 123 NODE SYSTEM

The balanced modified IEEE 123 node test system was modified based on the original IEEE 123 node system, which is a three-phase unbalanced system operated at 4.16 kV. The original system data is available in [140]. The original test system was modified using the similar method for the IEEE 13 node test system. The line impedances were modified by assuming perfectly transposed. For three-phase lines, the off-diagonal terms in the line impedance matrix were ignored, and the diagonal terms were equal to the average value of original diagonal values. For single-phase and two-phase lines, the missing phase(s) were added with the impedance being equal to the other phase(s). The voltage regulators were removed from the system. N150 was the slack bus. The voltage at N150 was regulated at 1.0 p.u. The transformers were replaced with lines, with the kVA capacity being equal to the kVA capacity of the original transformers, and the impedance being equal to the winding impedance of the transformers. All the lines were switchable. The single-line diagram and system parameters of the balanced modified IEEE 123 node test system are shown below.

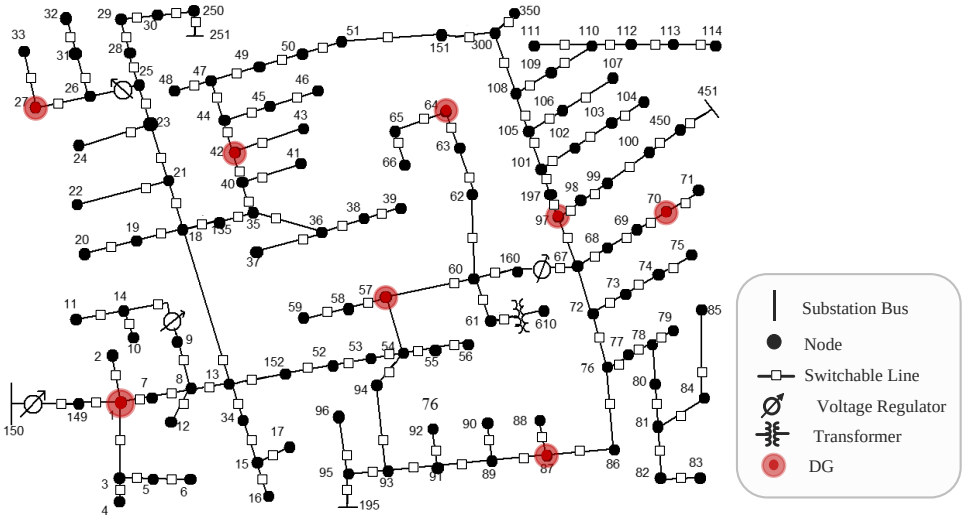

Figure A.1. Single-line diagram of the balanced IEEE 123 Node Test System

TABLE A.0.1. DG PARAMETERS OF BALANCED MODIFIED 123 NODE TEST SYSTEM

Parameter	DG1	DG2	DG3	DG3	DG3	DG3	DG3	DG3
Node position	1	27	42	57	64	70	87	97
FRR	5%	5%	5%	5%	5%	5%	5%	5%
P_g^{max} (kW)	8e5	1000	1000	1000	1000	1000	1000	1000
P_g^{min} (kW)	0	100	100	100	100	100	100	100
Q_g^{max} (kVar)	8e5	1000	1000	1000	1000	1000	1000	1000
Q_g^{min} (kVar)	-8e5	-800	-800	-800	-800	-800	-800	-800
P_g^{RAMP} (kW/min)	1000	500	500	500	500	500	500	500
Status	1	1/0	1/0	1/0	1/0	1/0	1/0	1/0

TABLE A.0.2. LINE CONFIGURATION OF BALANCED MODIFIED 123 NODE TEST SYSTEM

Configuration No.	Resistance per mile (ohm)	Reactance per mile (ohm)
1	0.4576	1.078
2	0.4666	1.0482
3	0.4615	1.0651
4	0.4615	1.0651
5	0.4666	1.0482
6	0.4576	1.0780
7	0.4576	1.0780
8	0.4576	1.0780
9	1.3292	1.3475
10	1.3292	1.3475
11	1.3292	1.3475
12	1.5209	0.7521
13	0.01	0.01

TABLE A.0.3. LINE SEGMENT DATA OF BALANCED MODIFIED 123 NODE TEST SYSTEM

From	To	Length (ft.)	Config.	From	To	Length (ft.)	Config.	From	To	Length (ft.)	Config.
1	2	175	10	40	42	250	1	80	81	475	6
1	3	250	11	42	43	500	10	81	82	250	6
1	7	300	1	42	44	200	1	81	84	675	11
3	4	200	11	44	45	200	9	82	83	250	6
3	5	325	11	44	47	250	1	84	85	475	11
5	6	250	11	45	46	300	9	86	87	450	6
7	8	200	1	47	48	150	4	87	88	175	9
8	12	225	10	47	49	250	4	87	89	275	6
8	9	225	9	49	50	250	4	89	90	225	10
8	13	300	1	50	51	250	4	89	91	225	6
9	14	425	9	51	15	500	4	91	92	300	11
13	34	150	11	52	53	200	1	91	93	225	6
13	18	825	2	53	54	125	1	93	94	275	9
14	11	250	9	54	55	275	1	93	95	300	6
14	10	250	9	54	57	350	3	95	96	200	10
15	16	375	11	55	56	275	1	97	98	275	3
15	17	350	11	57	58	250	10	98	99	550	3
18	19	250	9	57	60	750	3	99	10	300	3
18	21	300	2	58	59	250	10	100	45	800	3
19	20	325	9	60	61	550	5	101	10	225	11
21	22	525	10	60	62	250	12	101	10	275	3
21	23	250	2	62	63	175	12	102	10	325	11
23	24	550	11	63	64	350	12	103	10	700	11
23	25	275	2	64	65	425	12	105	10	225	10
25	26	350	7	65	66	325	12	105	10	325	3
25	28	200	2	67	68	200	9	106	10	575	10
26	27	275	7	67	72	275	3	108	10	450	9
26	31	225	11	67	97	250	3	108	30	1000	3
27	33	500	9	68	69	275	9	109	11	300	9
28	29	300	2	69	70	325	9	110	11	575	9
29	30	350	2	70	71	275	9	110	11	125	9
30	25	200	2	72	73	275	11	112	11	525	9
31	32	300	11	72	76	200	3	113	11	325	9
34	15	100	11	73	74	350	11	135	35	375	4
35	36	650	8	74	75	400	11	150	14	100	1
35	40	250	1	76	77	400	6	149	1	300	1
36	37	300	9	76	86	700	3	152	52	400	1
36	38	250	10	77	78	100	6	160	67	350	6
38	39	325	10	78	79	225	6	197	10	250	3
40	41	325	11	78	80	475	6				

TABLE A.0.4. SPOT LOAD DATA OF BALANCED MODIFIED 123 NODE TEST SYSTEM

Node	P(kW)	Q(kVar)	Node	P(kW)	Q(kVar)	Node	P(kW)	Q(kVar)	Node	P(kW)	Q(kVar)
1	13	6.67	33	35	25	65	13.3	6.67	97	13.3	6.67
2	13	6.67	34	70	50	66	13.3	6.67	98	6.67	3.33
3	13	6.67	35	35	25	67	13.3	6.67	99	13.3	6.67
4	13	6.67	36	13.3	6.67	68	13.3	6.67	100	105	80
5	13	6.67	37	6.67	3.33	69	6.67	3.33	101	6.67	3.33
6	6.67	3.33	38	13.3	6.67	70	6.67	3.33	102	13.3	6.67
7	13	6.67	39	13.3	6.67	71	6.67	3.33	103	13.3	6.67
8	6.67	3.33	40	6.67	3.33	72	6.67	3.33	104	13.3	6.67
9	13	6.67	41	6.67	3.33	73	13.3	6.67	105	13.3	6.67
10	6.67	3.33	42	6.67	3.33	74	6.67	3.33	106	6.67	3.33
11	13	6.67	43	6.67	3.33	75	13.3	6.67	107	6.67	3.33
12	6.67	3.33	44	6.67	3.33	76	6.67	3.33	108	13.3	6.67
13	13	6.67	45	13.3	6.67	77	13.3	6.67	109	13.3	6.67
14	13	6.67	46	13.3	6.67	78	13.3	6.67	110	13.3	6.67
15	13	6.67	47	13.3	6.67	79	6.67	3.33	111	13.3	6.67
16	13	6.67	48	35	25	80	6.67	3.33	112	6.67	3.33
17	13	6.67	49	13.3	6.67	81	6.67	3.33	113	13.3	6.67
18	13	6.67	50	6.67	3.33	82	6.67	3.33	114	13.3	6.67
19	13	6.67	51	13.3	6.67	83	6.67	3.33	135	6.67	3.33
20	6.67	3.33	52	6.67	3.33	84	6.67	3.33	149	6.67	3.33
21	6.67	3.33	53	13.3	6.67	85	6.67	3.33	150	13.3	6.67
22	13	6.67	54	13.3	6.67	86	13.3	6.67	151	13.3	6.67
23	13	6.67	55	6.67	3.33	87	6.67	3.33	152	13.3	6.67
24	13	6.67	56	13.3	6.67	88	13.3	6.67	160	13.3	6.67
25	13	6.67	57	105	80	89	13.3	6.67	197	6.67	3.33
26	6.67	3.33	58	6.67	3.33	90	13.3	6.67	250	6.67	3.33
27	6.67	3.33	59	13.3	6.67	91	35	25	251	6.67	3.33
28	6.67	3.33	60	13.3	6.67	92	13.3	6.67			
29	6.67	3.33	61	13.3	6.67	93	6.67	3.33			
30	13	6.67	62	13.3	6.67	94	13.3	6.67			
31	6.67	3.33	63	6.67	3.33	95	6.67	3.33			
32	6.67	3.33	64	6.67	3.33	96	13.3	6.67			

TABLE A.0.5. CAPACITOR DATA OF BALANCED MODIFIED 123 NODE TEST SYSTEM

Node	kVAr
83	200
88	16.67
90	16.67
92	16.67

TABLE A.0.6. POWER FLOW FOR BALANCED MODIFIED 13 NODE SYSTEM: VOLTAGE MAGNITUDE AND ANGLE

Node	Magnitude (p.u.)	Angle (degree)	Node	Magnitude (p.u.)	Angle (degree)	Node	Magnitude (p.u.)	Angle (degree)
1	1	0	42	0.97702	-1.1	81	0.95793	-2
2	0.99976	0	43	0.97687	-1.1	82	0.95786	-2
3	0.99955	0	44	0.97671	-1.1	84	0.95728	-2
7	0.99382	-0.3	45	0.9765	-1.1	83	0.95783	-2
4	0.99943	0	47	0.97649	-1.1	85	0.95709	-2
5	0.99932	0	46	0.97634	-1.1	87	0.95723	-2.1
6	0.99917	0	48	0.97646	-1.1	88	0.95719	-2.1
8	0.98976	-0.5	49	0.97633	-1.1	89	0.95686	-2.1
12	0.98962	-0.5	50	0.9762	-1.1	90	0.95673	-2.1
9	0.98935	-0.5	51	0.97613	-1.1	91	0.95667	-2.1
13	0.98406	-0.8	117	0.9761	-1.1	92	0.95656	-2.1
14	0.98865	-0.5	52	0.9794	-1	93	0.95656	-2.1
34	0.98384	-0.8	53	0.97712	-1.1	94	0.95655	-2.1
18	0.979	-1	54	0.97571	-1.2	95	0.95643	-2.1
11	0.98849	-0.5	55	0.97564	-1.2	96	0.95632	-2.1
10	0.98856	-0.5	57	0.97196	-1.3	98	0.96018	-1.9
15	0.98369	-0.8	56	0.97562	-1.2	99	0.9598	-1.9
16	0.98356	-0.8	58	0.97172	-1.3	100	0.95966	-1.9
17	0.9835	-0.8	60	0.96435	-1.7	124	0.9594	-2
19	0.97878	-1	59	0.97155	-1.3	101	0.95984	-1.9
21	0.97816	-1	61	0.96424	-1.7	102	0.95964	-1.9
20	0.97858	-1	62	0.96396	-1.7	105	0.95936	-2
22	0.97782	-1	63	0.96371	-1.7	103	0.95942	-1.9
23	0.97761	-1.1	64	0.96338	-1.7	104	0.95904	-2
24	0.9776	-1.1	65	0.96305	-1.7	106	0.95926	-2
25	0.97706	-1.1	66	0.9629	-1.7	108	0.95892	-2
26	0.97669	-1.1	67	0.96127	-1.9	107	0.95919	-2
28	0.97693	-1.1	68	0.96102	-1.9	109	0.95802	-2
27	0.97657	-1.1	72	0.96008	-1.9	122	0.95873	-2
31	0.97657	-1.1	97	0.96038	-1.9	110	0.95748	-2
33	0.97633	-1.1	69	0.96086	-1.9	111	0.95721	-2
29	0.97681	-1.1	70	0.9608	-1.9	112	0.95737	-2
30	0.97675	-1.1	71	0.96077	-1.9	113	0.95718	-2
121	0.97675	-1.1	73	0.95972	-1.9	114	0.95716	-2
32	0.97653	-1.1	76	0.95936	-2	115	0.979	-1
35	0.97797	-1	74	0.95946	-1.9	116	0.99988	0
36	0.97761	-1.1	75	0.95924	-1.9	118	0.98406	-0.8
40	0.97744	-1.1	77	0.95874	-2	119	0.96435	-1.7
37	0.97759	-1.1	86	0.95801	-2	120	0.96038	-1.9
38	0.97735	-1.1	78	0.95861	-2	125	0.96424	-1.7
39	0.9772	-1.1	79	0.9586	-2	123	0.95873	-2
41	0.97723	-1.1	80	0.95811	-2			

TABLE A.0.7. POWER FLOW FOR BALANCED MODIFIED 13 NODE SYSTEM: VOLTAGE MAGNITUDE AND ANGLE

From	To	Current (A)	Angle (degree)	From	To	Current (A)	Angle (degree)	From	To	Current (A)	Angle (degree)
1	2	304.412	-26.58	40	42	24.0554	-27.69	80	81	13.8891	-28.61
1	3	12.86	-26.58	42	43	2.09071	-27.66	81	82	4.00902	-28.6
1	7	287.305	-28.03	42	44	21.8006	-27.69	81	84	6.88651	-28.61
3	4	4.21891	-26.58	44	45	7.44056	-27.68	82	83	1.709	-28.6
3	5	4.84684	-26.58	44	47	12.5415	-27.7	84	85	2.84649	-28.61
5	6	4.25531	-26.58	45	46	3.79134	-27.68	86	87	24.823	-28.66
7	8	284.344	-28.04	47	48	2.33479	-27.69	87	88	1.39006	-28.63
8	12	4.53869	-27.05	47	49	9.31592	-27.7	87	89	18.9727	-28.66
8	9	12.9647	-27.07	49	50	7.19143	-27.7	89	90	3.66721	-28.65
8	13	266.384	-28.11	50	51	4.10951	-27.7	89	91	11.6219	-28.67
9	14	11.6543	-27.07	51	151	0.72668	-27.7	91	92	2.76319	-28.66
13	34	10.7651	-27.33	52	53	159.875	-28.45	91	93	7.00762	-28.67
13	18	87.5125	-27.65	53	54	158.56	-28.45	93	94	0.262538	-28.67
14	11	4.5091	-27.07	54	55	3.90146	-27.73	93	95	6.37595	-28.67
14	10	2.5752	-27.07	54	57	151.417	-28.49	95	96	3.79259	-28.67
15	16	2.29717	-27.33	55	56	0.775864	-27.73	97	98	10.3323	-28.51
15	17	3.7878	-27.33	57	58	6.98575	-27.91	98	99	9.70256	-28.51
18	19	6.36189	-27.57	57	60	143.861	-28.52	99	100	6.94385	-28.52
18	21	40.063	-27.65	58	59	4.59836	-27.91	100	450	4.66703	-28.52
19	20	4.35604	-27.57	60	61	2.84778	-28.28	101	102	6.27736	-28.51
21	22	4.56771	-27.61	60	62	11.7672	-28.27	101	105	24.5136	-28.56
21	23	31.7252	-27.66	62	63	10.6865	-28.27	102	103	4.64208	-28.52
23	24	0.170047	-27.63	63	64	7.05768	-28.27	103	104	3.85521	-28.52
23	25	28.4328	-27.67	64	65	5.82509	-28.27	105	106	3.36865	-28.53
25	26	14.9936	-27.68	65	66	3.37953	-28.27	105	108	19.6349	-28.57
25	28	9.39377	-27.66	67	68	8.69246	-28.44	106	107	0.803883	-28.53
26	27	6.60163	-27.68	67	72	61.4619	-28.6	108	109	14.0456	-28.58
26	31	3.94047	-27.67	67	97	50.5363	-28.53	108	300	2.66715	-28.56
27	33	3.36632	-27.68	68	69	4.04593	-28.44	109	110	12.7678	-28.58
28	29	5.78322	-27.67	69	70	1.39494	-28.44	110	111	3.35163	-28.58
29	30	2.24183	-27.67	70	71	0.723325	-28.44	110	112	6.23631	-28.58
30	250	0.372568	-27.67	72	73	9.26287	-28.5	112	113	2.59869	-28.58
31	32	0.816019	-27.67	72	76	50.9506	-28.62	113	114	0.407642	-28.58
34	15	10.6145	-27.33	73	74	5.18515	-28.5	135	35	39.3243	-27.67
35	36	7.91424	-27.63	74	75	3.95148	-28.51	150	149	4.25212	153.43
35	40	30.0919	-27.68	76	77	22.2749	-28.59	149	1	163.461	-28.43
36	37	0.462512	-27.63	76	86	27.4941	-28.65	152	52	125.005	-28.55
36	38	7.23188	-27.63	77	78	17.7631	-28.6	160	67	30.8487	-28.55
38	39	3.30988	-27.64	78	79	0.954658	-28.56	197	101	167.367	-28.4
40	41	4.52632	-27.64	78	80	15.109	-28.6				

APPENDIX B UNBALANCED MODIFIED IEEE 123 NODE SYSTEM

Three-phase unbalanced modified IEEE 123 node system was modified based on the original IEEE 123 node test feeder. The system has some voltage drop problems, which can be potentially caused by heavily loading conditions [140]. A set of switches and DGs were added to the system. All the original lines, nodes, transformers, regulators, capacitor banks, and unbalanced loads were kept. The single-line diagram is shown in Figure B.1. Buses are represented by dots, and the substation bus (bus 150) is represented by a bar. Three-phase, two-phase, and single-phase lines are represented by black, yellow, and green wires, respectively. There are a total of 46 switchable lines and 4 voltage regulators in the system. Each voltage regulator was equipped with switches on both sides. A line is switchable by installing a switch, which is represented by a square on the line. All the component parameters are given in TABLE B.0.1 to TABLE B.0.7. TABLE B.0.8 lists the CLPU parameters for different types of loads. The parameters were derived from the guided CLPU ratio specified in IEEE Standard C57.91-2011 [145].

Seven DGs were added to the system, and their parameters are summarized in TABLE B.0.1. “Status” indicates the type of DGs, where “1” indicates that the DG is a black start DG; “1/0” indicates that the DG is a non-black start DG but can be started by external sources; and “0” represents that the DG is not available for participating in the service restoration. The locations of DGs and switchable lines are arbitrarily assigned.

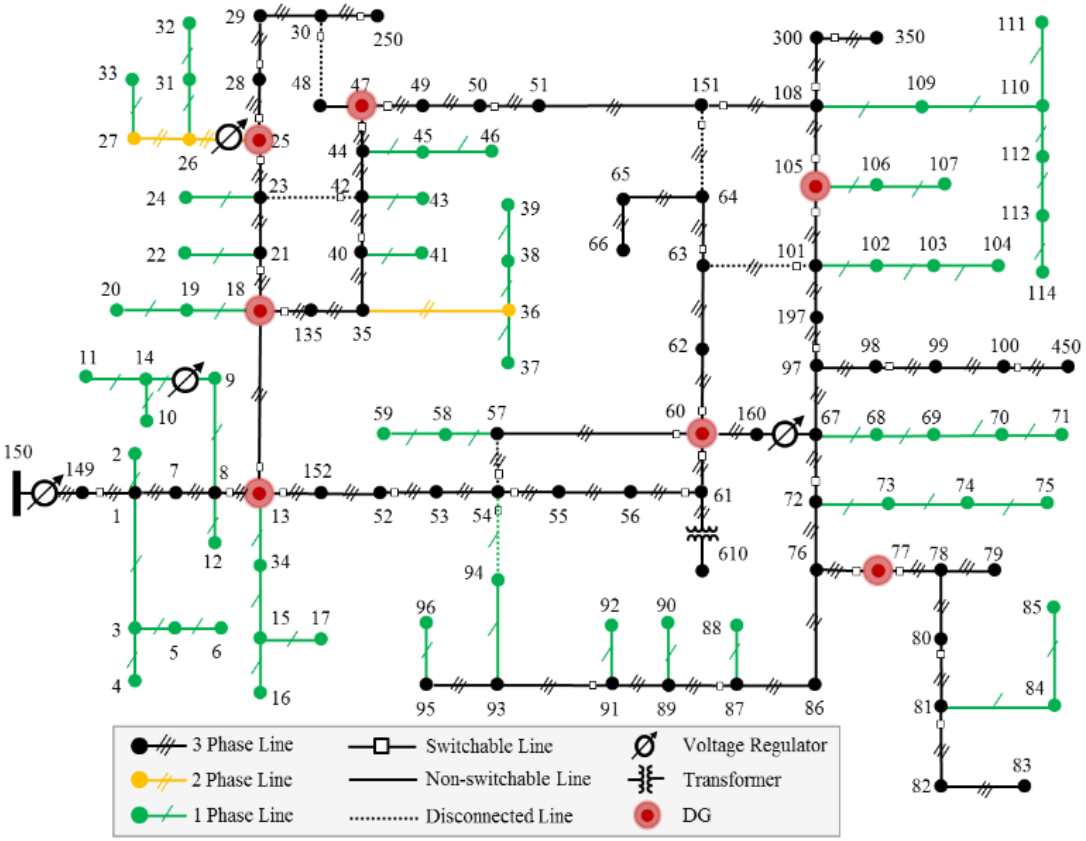

Figure B.1. Single-line diagram of unbalanced IEEE 123 Node Test System

TABLE B.0.1. PARAMETERS OF DGS ADDED TO THE UNBALANCED MODIFIED 123 NODE TEST SYSTEM

Parameters	DG13	DG18	DG25	DG47	DG60	DG77	DG105
Node position	13	18	25	47	60	77	105
P_g^{max} (MW)	0.9	1.05	1.2	1.5	1.2	0.8	1.5
P_g^{min} (MW)	0.09	0.1	0.12	0.15	0.12	0.12	0.15
Q_g^{max} (MVar)	0.7	0.8	0.9	1.2	0.9	0.3	1.2
Q_g^{min} (MVar)	-0.5	-0.5	-0.6	-0.9	-0.6	-0.3	-0.9
P_g^R(MW/sec)	0.5	0.4	0.3	0.2	0.3	0.5	0.6
CUF (%)	100%	20%	10%	10%	20%	10%	100%
MLS (%)	80%	70%	80%	60%	50%	60%	80%
Status	1	1	0	1/0	1	1/0	1

There are a total of 85 loads and 4 capacitors in the test system. The controllability is indicated in TABLE B.0.2, where a load is named by the letter “L” followed by a subscript

and a bus number, and a capacitor is named by the letter "C" followed by a subscript and the bus number. For simplicity's sake, the weight factor is assumed to be 1.0 for each load. If there are critical loads in the system, larger weight factors must be assigned to these critical loads, in order to restore them prior to other loads. The subscript "1" indicates that the load is directly connected to the bus, "1/0" indicates that the load can be remotely switched on or off, and "0" indicates that the load cannot be restored for some reasons. Switchable lines are named by the letter "S" with the superscript and the subscript as the "from bus" and "to bus", respectively.

TABLE B.0.2. CONTROLLABILITY OF COMPONENTS IN THE UNBALANCED MODIFIED IEEE 123 NODE TEST SYSTEM

Controllability of Components	Components
Switchable Lines	S_{13}^{8}, S_{18}^{13}, S_{21}^{18}, S_{25}^{23}, S_{28}^{25}, S_{29}^{28}, S_{250}^{30}, S_{42}^{40}, S_{47}^{44}, S_{49}^{47}, S_{60}^{57}, S_{61}^{60}, S_{62}^{60}, S_{64}^{63}, S_{72}^{67}, S_{77}^{76}, S_{78}^{77}, S_{81}^{80}, S_{89}^{87}, S_{93}^{91}, S_{99}^{98}, S_{450}^{100}, S_{105}^{101}, S_{108}^{105}, S_{300}^{108}, S_{48}^{30}, S_{42}^{23}, S_{151}^{64}, S_{101}^{63}, S_{61}^{56}, S_{152}^{13}, S_{135}^{18}, S_{160}^{60}, S_{197}^{97}, S_{350}^{300}, S_{51}^{50}, S_{151}^{51}, S_{53}^{52}, S_{54}^{53}, S_{55}^{54}, S_{57}^{54}, S_{82}^{81}, S_{149}^{1}, S_{610}^{76}, S_{94}^{54}, S_{151}^{108}
Loads	$L_1$1, $L_1$2, $L_2$4, $L_1$5, $L_1$6, $L_1$7, $L_1$9, $L_1$10, $L_1$11, $L_1$12, $L_{1/0}$16, $L_{1/0}$17, $L_{1/0}$19, $L_{1/0}$20, $L_1$22, $L_1$24, $L_1$28, $L_1$29, $L_1$30, $L_1$31, $L_1$32, $L_1$33, $L_{1/0}$34, $L_1$35, $L_1$37, $L_1$38, $L_1$39, $L_1$41, $L_{1/0}$42, $L_1$43, $L_1$45, $L_{1/0}$46, $L_1$47, $L_1$48, $L_1$49, $L_1$50, $L_1$51, $L_1$52, $L_1$53, $L_{1/0}$55, $L_{1/0}$56, $L_1$58, $L_1$59, $L_{1/0}$60, $L_1$62, $L_1$63, $L_1$64, $L_1$65, $L_1$66, $L_1$68, $L_1$69, $L_1$70, $L_1$71, $L_1$73, $L_1$74, $L_1$75, $L_1$76, $L_1$77, $L_1$79, $L_1$80, $L_1$82, $L_1$83, $L_1$84, $L_1$85, $L_1$86, $L_1$87, $L_1$88, $L_1$90, $L_1$92, $L_{1/0}$94, $L_{1/0}$95, $L_{1/0}$96, $L_1$98, $L_1$99, $L_1$100, $L_1$102, $L_1$103, $L_1$104, $L_{1/0}$106, $L_{1/0}$107, $L_1$109, $L_1$111, $L_1$112, $L_1$113, $L_1$114,
Capacitor Banks	$C_{1/0}$83, $C_{1/0}$88, $C_{1/0}$90, $C_{1/0}$92

TABLE B.0.3. LINE SEGMENT DATA OF UNBALANCED MODIFIED 123 NODE TEST SYSTEM

From	To	Length (ft.)	Config.	From	To	Length (ft.)	Config.	From	To	Length (ft.)	Config.
1	2	175	10	40	42	250	1	80	81	475	6
1	3	250	11	42	43	500	10	81	82	250	6
1	7	300	1	42	44	200	1	81	84	675	11
3	4	200	11	44	45	200	9	82	83	250	6
3	5	325	11	44	47	250	1	84	85	475	11
5	6	250	11	45	46	300	9	86	87	450	6
7	8	200	1	47	48	150	4	87	88	175	9
8	12	225	10	47	49	250	4	87	89	275	6
8	9	225	9	49	50	250	4	89	90	225	10
8	13	300	1	50	51	250	4	89	91	225	6
9	14	425	9	51	15	500	4	91	92	300	11
13	34	150	11	52	53	200	1	91	93	225	6
13	18	825	2	53	54	125	1	93	94	275	9
14	11	250	9	54	55	275	1	93	95	300	6
14	10	250	9	54	57	350	3	95	96	200	10
15	16	375	11	55	56	275	1	97	98	275	3
15	17	350	11	57	58	250	10	98	99	550	3
18	19	250	9	57	60	750	3	99	10	300	3
18	21	300	2	58	59	250	10	100	45	800	3
19	20	325	9	60	61	550	5	101	10	225	11
21	22	525	10	60	62	250	12	101	10	275	3
21	23	250	2	62	63	175	12	102	10	325	11
23	24	550	11	63	64	350	12	103	10	700	11
23	25	275	2	64	65	425	12	105	10	225	10
25	26	350	7	65	66	325	12	105	10	325	3
25	28	200	2	67	68	200	9	106	10	575	10
26	27	275	7	67	72	275	3	108	10	450	9
26	31	225	11	67	97	250	3	108	30	1000	3
27	33	500	9	68	69	275	9	109	11	300	9
28	29	300	2	69	70	325	9	110	11	575	9
29	30	350	2	70	71	275	9	110	11	125	9
30	25	200	2	72	73	275	11	112	11	525	9
31	32	300	11	72	76	200	3	113	11	325	9
34	15	100	11	73	74	350	11	135	35	375	4
35	36	650	8	74	75	400	11	150	14	100	1
35	40	250	1	76	77	400	6	149	1	300	1
36	37	300	9	76	86	700	3	152	52	400	1
36	38	250	10	77	78	100	6	160	67	350	6
38	39	325	10	78	79	225	6	197	10	250	3
40	41	325	11	78	80	475	6				

TABLE B.0.4. LOAD DATA OF UNBALANCED MODIFIED 123 NODE TEST SYSTEM

Node	Load Model	Ph-1 kW	Ph-1 kVAr	Ph-2 kW	Ph-2 kVAr	Ph-3 kW	Ph-4 kVAr	Node	Load Model	Ph-1 kW	Ph-1 kVAr	Ph-2 kW	Ph-2 kVAr	Ph-3 kW	Ph-4 kVAr
1	Y-PQ	40	20	0	0	0	0	60	Y-PQ	20	10	0	0	0	0
2	Y-PQ	0	0	20	10	0	0	62	Y-Z	0	0	0	0	40	20
4	Y-PQ	0	0	0	0	40	20	63	Y-PQ	40	20	0	0	0	0
5	Y-I	0	0	0	0	20	10	64	Y-I	0	0	75	35	0	0
6	Y-Z	0	0	0	0	40	20	65	D-Z	35	25	35	25	70	50
7	Y-PQ	20	10	0	0	0	0	66	Y-PQ	0	0	0	0	75	35
9	Y-PQ	40	20	0	0	0	0	68	Y-PQ	20	10	0	0	0	0
10	Y-I	20	10	0	0	0	0	69	Y-PQ	40	20	0	0	0	0
11	Y-Z	40	20	0	0	0	0	70	Y-PQ	20	10	0	0	0	0
12	Y-PQ	0	0	20	10	0	0	71	Y-PQ	40	20	0	0	0	0
16	Y-PQ	0	0	0	0	40	20	73	Y-PQ	0	0	0	0	40	20
17	Y-PQ	0	0	0	0	20	10	74	Y-Z	0	0	0	0	40	20
19	Y-PQ	40	20	0	0	0	0	75	Y-PQ	0	0	0	0	40	20
20	Y-I	40	20	0	0	0	0	76	D-I	105	80	70	50	70	50
22	Y-Z	0	0	40	20	0	0	77	Y-PQ	0	0	40	20	0	0
24	Y-PQ	0	0	0	0	40	20	79	Y-Z	40	20	0	0	0	0
28	Y-I	40	20	0	0	0	0	80	Y-PQ	0	0	40	20	0	0
29	Y-Z	40	20	0	0	0	0	82	Y-PQ	40	20	0	0	0	0
30	Y-PQ	0	0	0	0	40	20	83	Y-PQ	0	0	0	0	20	10
31	Y-PQ	0	0	0	0	20	10	84	Y-PQ	0	0	0	0	20	10
32	Y-PQ	0	0	0	0	20	10	85	Y-PQ	0	0	0	0	40	20
33	Y-I	40	20	0	0	0	0	86	Y-PQ	0	0	20	10	0	0
34	Y-Z	0	0	0	0	40	20	87	Y-PQ	0	0	40	20	0	0
35	D-PQ	40	20	0	0	0	0	88	Y-PQ	40	20	0	0	0	0
37	Y-Z	40	20	0	0	0	0	90	Y-I	0	0	40	20	0	0
38	Y-I	0	0	20	10	0	0	92	Y-PQ	0	0	0	0	40	20
39	Y-PQ	0	0	20	10	0	0	94	Y-PQ	40	20	0	0	0	0
41	Y-PQ	0	0	0	0	20	10	95	Y-PQ	0	0	20	10	0	0
42	Y-PQ	20	10	0	0	0	0	96	Y-PQ	0	0	20	10	0	0
43	Y-Z	0	0	40	20	0	0	98	Y-PQ	40	20	0	0	0	0
45	Y-I	20	10	0	0	0	0	99	Y-PQ	0	0	40	20	0	0
46	Y-PQ	20	10	0	0	0	0	100	Y-Z	0	0	0	0	40	20
47	Y-I	35	25	35	25	35	25	102	Y-PQ	0	0	0	0	20	10
48	Y-Z	70	50	70	50	70	50	103	Y-PQ	0	0	0	0	40	20
49	Y-PQ	35	25	70	50	35	20	104	Y-PQ	0	0	0	0	40	20
50	Y-PQ	0	0	0	0	40	20	106	Y-PQ	0	0	40	20	0	0
51	Y-PQ	20	10	0	0	0	0	107	Y-PQ	0	0	40	20	0	0
52	Y-PQ	40	20	0	0	0	0	109	Y-PQ	40	20	0	0	0	0
53	Y-PQ	40	20	0	0	0	0	111	Y-PQ	20	10	0	0	0	0
55	Y-Z	20	10	0	0	0	0	112	Y-I	20	10	0	0	0	0
56	Y-PQ	0	0	20	10	0	0	113	Y-Z	40	20	0	0	0	0
58	Y-I	0	0	20	10	0	0	114	Y-PQ	20	10	0	0	0	0
59	Y-PQ	0	0	20	10	0	0								

TABLE B.0.5. LINE CONFIGURATION OF UNBALANCED MODIFIED IEEE 123 NODE TEST SYSTEM

Config.	Impedance (ohm per mile)			Config.	Impedance (ohm per mile)		
1	0.4576+j1.0780	0.1560+j0.5017 0.4666+j1.0482	0.1535+j0.3849 0.1580+j0.4236 0.4615+j1.0651	7	0.4576+j1.0780	0.0000+j 0.0000 0.0000+j 0.0000	0.1535+j 0.3849 0.0000+j 0.0000 0.4615+j 1.0651
2	0.4666+j1.0482	0.1580+j 0.4236 0.4615+j 1.0651	0.1560+j 0.5017 0.1535+j 0.3849 0.4576+j 1.0780	8	0.4576+j1.0780	0.1535+j 0.3849 0.4615+j 1.0651	0.0000+j 0.0000 0.0000+j 0.0000 0.0000+j 0.0000
3	0.4615+j1.0651	0.1535+j 0.3849 0.4576+j 1.0780	0.1580+j 0.4236 0.1560+j 0.5017 0.4666+j 1.0482	9	1.3292+j1.3475	0.0000+j 0.0000 0.0000+j 0.0000	0.0000+j 0.0000 0.0000+j 0.0000 0.0000+j 0.0000
4	0.4615+j1.0651	0.1580+j0.4236 0.4666+j 1.0482	0.1535+j 0.3849 0.1560+j 0.5017 0.4576+j 1.0780	10	0.0000+j0.0000	0.0000+j 0.0000 1.3292+j 1.3475	0.0000+j 0.0000 0.0000+j 0.0000 0.0000+j 0.0000
5	0.4666+j1.0482	0.1560+j 0.5017 0.4576+j 1.0780	0.1580+j 0.4236 0.1535+j 0.3849 0.4615+j 1.0651	11	0.0000+j0.0000	0.0000+j 0.0000 0.0000+j 0.0000	0.0000+j 0.0000 0.0000+j 0.0000 1.3292+j 1.3475
6	0.4576+j1.0780	0.1535+j 0.3849 0.4615+j 1.0651	0.1560+j 0.5017 0.1580+j 0.4236 0.4666+j 1.0482	12	1.5209+j0.7521	0.5198+j 0.2775 1.5329+j 0.7162	0.4924+j 0.2157 0.5198+j 0.2775 1.5209+j 0.7521

TABLE B.0.6. TRANSFORMER (XFM) AND REGULATOR (RG) DATA OF UNBALANCED MODIFIED 123 NODE TEST SYSTEM

	kVA	kV-high	kV-low	R - %	X - %	Tap Position (Phase A,B,C)
Substation	5,000	115 - D	4.16 Gr-W	1	8	N/A
XFM - 1	150	4.16 - D	.480 - D	1.27	2.72	N/A
RG 150-149	-	4.16	4.16	3	7.5	7,7,7
RG 9-14	-	4.16	4.16	1	2	8,1,5
RG 25-26	-	4.16	4.16	1	2	0, N/A, -1
RG 160-67	-	4.16	4.16	1	2	-1, N/A, N/A

TABLE B.0.7. CAPACITOR DATA OF UNBALANCED MODIFIED 123 NODE TEST SYSTEM

Node	Ph-A (kVAr)	Ph-B (kVAr)	Ph-C (kVAr)
83	200	200	200
88	50	–	–
90	–	50	–
92	–	–	50
Total	250	250	250

TABLE B.0.8. LOAD PARAMETERS OF UNBALANCED MODIFIED IEEE 13 NODE TEST FEEDER

Load Type	S_l^U/S_l^D	D_l(min)	α_l
Residential	2.5/1.0	3	0.3
Commercial	2.0/1.0	3	0.5
Industrial	1.5/1.0	3	0.8

TABLE B.0.9. ESS PARAMETERS OF UNBALANCED MODIFIED IEEE 123 NODE TEST FEEDER

Parameter	ESS
Node position	On each load
$E_e^{ESS\_R}$	40 kWh
ρ_e^{min}	10 %
ρ_e^{max}	100 %
η_e^C	0.90
η_e^D	0.90
$P_e^{C\_min}/P_e^{C\_max}$	0/400 kW
$Q_e^{C\_min}/Q_e^{C\_max}$	0/200 kVar
$P_e^{D\_min}/P_e^{D\_max}$	0/400 kW
$Q_e^{D\_min}/Q_e^{D\_max}$	0/200 kVar

APPENDIX C SIMULATION SETUP

Restoration solutions can be validated in OpenDSS, which is an open-source three-phase AC power flow simulator developed by The Electric Power Research Institute (EPRI) [142]. The simulation setup is illustrated in Figure C.1. The information of the test distribution systems (e.g., DG data, line data, load data, transformer data) is stored in Microsoft Office Excel documents and OpenDSS documents. Additional Excel documents containing solar data, wind data and CLPU parameters can be accessed by both MATLAB and OpenDSS. MATLAB runs the BSR algorithm after importing the system information from the Excel documents. The restoration solution, which represents a sequence of control actions, will be translated into the OpenDSS commands through the component object model (COM) interface. Then OpenDSS solves a sequence of steady-state power flow problems specified by restoration solutions, and export power flow results (e.g., voltage magnitude and line power) to Excel documents. Next, various steady-state constraints can be validated in MATLAB.

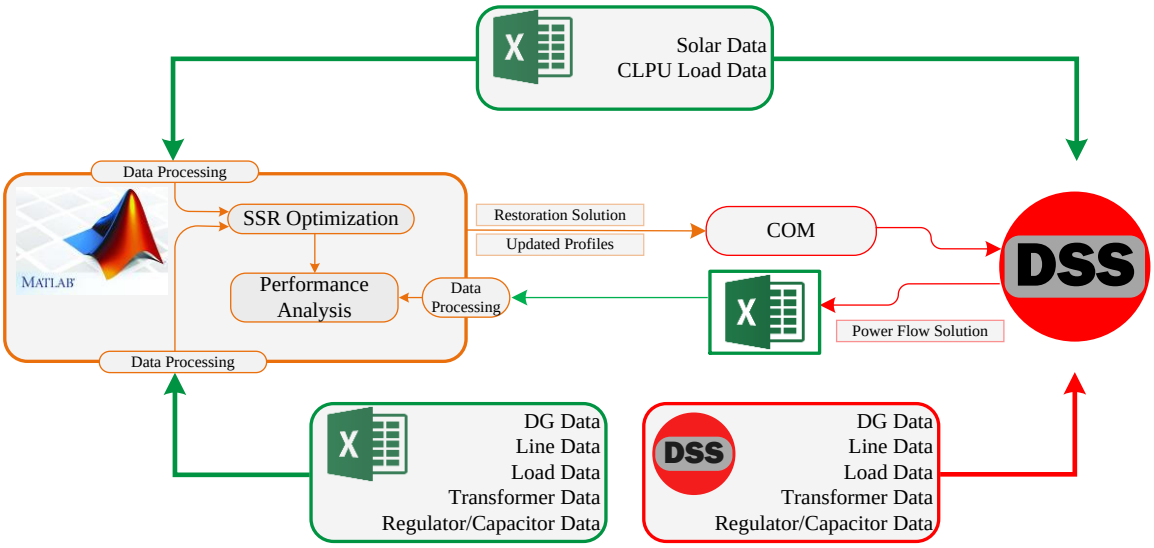

Figure C.1. Simulation setup for validating steady-state constraints

Dynamic security constraints can be checked in PSCAD/EMTDC, which is a time domain simulation program for simulating electromagnetic behaviors of power systems. PSCAD can simulate three-phase unbalanced systems with capability of convenient data input/output, and complete component library, which include typical DER models such as diesel generator, wind turbine, solar panel, and energy storage. The simulation setup for checking dynamic security constraints is shown in Figure C.2. Similar to the simulation setup in Figure C.1, MATLAB will import system information from Excel documents, and generate restoration solutions. Various control actions in the restoration solutions can be exported to Excel documents, and executed in PSCAD.

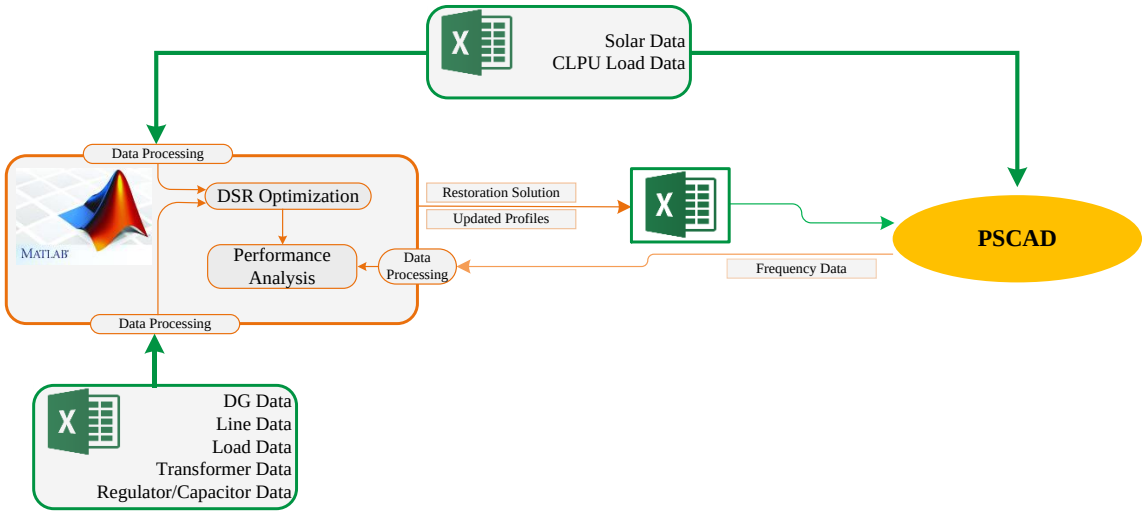

Figure C.2. Simulation setup for validating dynamic security constraints